Finite Element Micromechanics Modeling of Inelastic Deformation of Unidirectionally Fiber-Reinforced Composites

by

Su-Yuen Hsu

Dissertation submitted to the Faculty of the

Virginia Polytechnic Institute and State University

in partial fulfillment of the requirements for the degree of

Doctor of Philosophy

in

Engineering Mechanics

APPROVED:

O. H. Griffin, Jr., Chairman

R. M. Barker

M. W. Hyer

J. N. Reddy

K. L. Reifsnider

July, 1992

Blacksburg, Virginia

Finite Element Micromechanics Modeling of Inelastic Deformation of Unidirectionally Fiber-Reinforced Composites

by

Su-Yuen Hsu

O. H. Griffin, Jr., Chairman

Engineering Mechanics

(ABSTRACT)

This dissertation contains two parts.

Part I (Efficient Endochronic Finite Element Analysis: an Example of a Cyclically Loaded Boron/Aluminum Composite): A convenient and efficient algorithmic tangent matrix approach has been developed for 3-D finite element (FE) analysis using the endochronic theory without a yield surface. The underlying algorithm for integrating the endochronic constitutive equation was derived by piecewise linearization of the plastic strain path. The approach was employed to solve a micromechanics boundary value problem of a cyclically loaded unidirectional boron/6061 aluminum composite. All the FE results consistently demonstrate superior numerical stability and efficiency of the proposed method. Extensions of the method to endochronic plasticity with a yield surface and to the plane stress case are also presented.

Part II (Simple and Unified Finite Element Formulation for Doubly Periodic Models: Applications to Boron/Aluminum Composites): A simple and unified weak formulation and its convenient FE implementation have been proposed. The weak formulation is valid for any doubly periodic model under uniform 3-D macro-stress, and serves as a common rational foundation of different FE approaches. The algorithmic tangent matrix approach for the endochronic theory has been incorporated into the FE formulation to model isothermal, rate-independent plastic macro-deformation of unidirectional fibrous composites with idealized two-phase micro-structure and backed-out inelastic matrix properties. Methods for determining inelastic

material parameters of the matrix have been established. Numerical results for a B/6061 Al composite subjected to on-axis and off-axis monotonic tensile loadings are in good agreement with experimental data. The micromechanics model also shows the potential for quantitative characterization of complicated cyclic behavior. Finally, some effects of model geometry on overall plastic response of the B/6061 Al composite are discussed from the viewpoint of theoretical-experimental correlation.

Acknowledgements

I would like to thank my advisor, Dr. O. H. Griffin, Jr., for his guidance and encouragement. He assisted in keeping my research on the track with timely advice, while I felt free in my own exploration. His friendly encouragement, showing confidence to my capability, was an important support for me throughout frustrations.

I am very grateful to Dr. R. M. Barker, Dr. M. W. Hyer, Dr. J. N. Reddy, and Dr. K. L. Reifsnider for serving on my advisory committee and reviewing the manuscript.

The financial support provided by Virginia Institute for Material Systems, directed by Dr. K. L. Reifsnider, is particularly acknowledged.

I shall dedicate my achievements to my grandfather and parents. They have encouraged and supported me to pursue a Ph.D. degree since I was a young boy. Without them, I could have neither realized the value of education nor appreciated the pleasure in study. Finally, I can never thank Shu-Man enough for her sacrifice. She deserves a Ph.T. (Push Husband Through) degree.

Table of Contents

Overview

This dissertation is aimed at establishing an engineering method for inelastic micromechanics analysis of unidirectionally continuous-fiber-reinforced composites.

An engineering method usually has to be convenient and efficient; the theories behind an engineering method are expected to be as simple and as unified as possible. Facing these requirements for a suitable method for inelastic micromechanics analysis of unidirectional fibrous composites, we have been concerned with two issues: (1) the constitutive model for the inelastic matrix of a composite, and (2) the finite element formulation for composite geometric models. Although there has been substantial advancement over the past years, this work represents a significant step toward fitting a rational approach in our engineering environment. The dissertation contains two parts. The title of each manifests its attribute.

I. Efficient Endochronic Finite Element Analysis: an Example of a Cyclically Loaded Boron/Aluminum Composite

II. Simple and Unified Finite Element Formulation for Doubly Periodic Models: Applications to Boron/Aluminum Composites

Each part contains its own sections of introduction, theoretical development, application, and concluding remarks. Indeed, the two parts can be considered either connected or separate, depending on a reader's interest.

I. Efficient Endochronic Finite Element Analysis: an Example of a Cyclically Loaded Boron/Aluminum Composite

1. Introduction

Since Valanis [1] modified the original endochronic theory by redefining the intrinsic time increment as a scaled plastic strain increment, the new version of the endochronic theory has been examined extensively in the aspect of constitutive modeling (e.g., [2 - 6]). The intrinsic time of the endochronic theory is in itself a material property, and is used for description of the thermomechanical history of a material in order to determine its response. The prior studies, which cover theoretical investigation and experimental verification, have shown the new theory versatile in predicting nonproportional cyclic behavior of isotropic materials. However, in the aspect of structural application, very limited progress is seen in the literature.

Lin et al. [7] implemented the original endochronic theory in their finite element (FE) simulation of dynamic inelastic response of structures by an initial stress scheme. Valanis and Fan [8] developed an initial strain FE algorithm for the incrementally nonlinear stress-strain relation of the new endochronic theory without a yield surface. As discussed in Hsu et al. [9], the Valanis-Fan scheme fails in convergence under the requirement of accurately reproducing instantaneous elastic response to initial load-

ing or subsequent unloading. Watanabe and Atluri [10] showed that the new endochronic theory with a yield surface reduces to having a mathematical structure similar to those of the classical plasticity theories of combined kinematic-isotropic hardening. Thus, their resulting incrementally linear stress-strain relation is no more difficult or expensive to implement in FE computation than those of classical plasticity. More recently, as a consequence of an improved scheme for updating plastic strain increments, Sengupta and Saxena [11] successfully applied the incrementally nonlinear constitutive equation of the new endochronic theory to solve an axi-symmetric geomechanics problem by an initial strain FE method. Therefore, it appears that the current methods for implementation of the new endochronic theory in numerical structural analysis are limited to the conventional type. Besides, the initial strain method hardly ever performs well when local structural response has a complicated nonproportional cyclic nature, or is dominated by plasticity.

The objective of this paper is to present a convenient and efficient method for endochronic FE analysis in line with the approach of algorithmic tangent moduli [12]. The underlying algorithm for integrating the endochronic constitutive equation was derived by piecewise linearization of the plastic strain path. The 3-D strain-controlled integration algorithm for the new endochronic theory without a yield surface, developed by Hsu et al. [6], is reviewed in Section 2. Then, the corresponding algorithmic tangent matrix and discussion on its numerical implementation is presented in Section 3. To demonstrate the superior stability and efficiency of the proposed method, we performed FE micromechanics analyses for a cyclically loaded unidirectional boron/6061 aluminum composite. The solution to the micromechanics boundary value problem is examined in detail in Section 4. Finally, extensions of the method-

ology to endochronic plasticity with a yield surface and to the plane stress case are addressed in Section 5.

2. 3-D Strain-Controlled Integration Algorithm

Valanis [1] showed that the new endochronic constitutive equation for plastically incompressible, rate-independent isotropic materials can be expressed as follows:

$$s_{ij} = \int_0^z \rho(z - z') \frac{d\varepsilon_{ij}^p}{dz'} dz' \tag{1}$$

where

$$dz = \frac{d\zeta}{f} \tag{2}$$

and

$$d\zeta = (d\varepsilon_{ij}^p d\varepsilon_{ij}^p)^{1/2} \tag{3}$$

$\rho(z)$ is a material function called the hereditary function. The other material function, f, is called the hardening function, and is assumed to depend on z herein. The symbols s_{ij} and ε_{ij}^p are the deviatoric stress and plastic strain tensors, respectively. The

parameter z is referred to as the intrinsic time. The kernel function $\rho(z)$ may be represented by an n-term Dirichlet series,

$$\rho(z) = \sum_{r=1}^{n} C_r e^{-\alpha_r z} \tag{4}$$

with the requirement that $\rho(0)$ be sufficiently large in order to produce instantaneous elastic response at the onset of initial loading or subsequent unloading. C_r and α_r are material constants such that $\alpha_1 = 0$, $C_1 \geq 0$, and α_r and C_r are positive for $r \geq 2$.

Eqs. 1 and 4 suggest that the deviatoric stress, s_{ij}, may be resolved into n stress-like internal variables, s^r_{ij}. Namely,

$$s_{ij} = \sum_{r=1}^{n} s^r_{ij} \tag{5}$$

where

$$s^r_{ij} = \int_0^z C_r e^{-\alpha_r (z - z')} \frac{d\varepsilon^p_{ij}}{dz'} dz' \tag{6}$$

or, equivalently,

$$\frac{ds^r_{ij}}{dz} + \alpha_r s^r_{ij} = C_r \frac{d\varepsilon^p_{ij}}{dz} \tag{7}$$

$$= C_r f \frac{d\varepsilon^p_{ij}}{d\zeta} \tag{8}$$

Eqs. 2 and 3 have been used in deriving the last equation. Let us consider a loading path in plastic strain space, and divide the path into segments. Further, let $(\bullet)_{m-1}$ and $(\bullet)_m$ denote quantities of a variable at the beginning and end of the mth segment, respectively, and $(\Delta\bullet)_m$ the difference between the quantities. We assume the segments are so small that the following approximation can be made:

1. According to Eq. 2,

$$\Delta z_m = \frac{\Delta\zeta_m}{f(z_{m-1} + \beta\Delta z_m)} \tag{9}$$

where β is an assigned numerical parameter.

2. Each segment of the plastic strain path is linearized. Thus, Eq. 3 leads to

$$\Delta\zeta_m = [(\Delta\varepsilon_{ij}^p)_m(\Delta\varepsilon_{ij}^p)_m]^{1/2} \tag{10}$$

for the mth segment. In addition,

$$\frac{d\varepsilon_{ij}^p}{d\zeta} = \frac{(\Delta\varepsilon_{ij}^p)_m}{\Delta\zeta_m} \tag{11}$$

3. As Eq. 8 will be used for an accurate estimate of $(s_{ij}^r)_m$, but not for the continuous variation from $(s_{ij}^r)_{m-1}$ to $(s_{ij}^r)_m$, it may be reasonable to simplify Eq. 8 as follows:

$$\frac{ds_{ij}^r}{dz} + \alpha_r s_{ij}^r = C_r f(z_{m-1} + \beta\Delta z_m)\frac{d\varepsilon_{ij}^p}{d\zeta} \tag{12}$$

Eqs. 9, 11, and 12 imply

$$\frac{ds_{ij}^r}{dz} + \alpha_r s_{ij}^r = C_r \frac{(\Delta\varepsilon_{ij}^p)_m}{\Delta z_m} \tag{13}$$

Now, it is possible to determine $(s_{ij}^r)_m$ in terms of $(\Delta\varepsilon_{ij}^p)_m$, Δz_m, and the initial condition, $s_{ij}^r = (s_{ij}^r)_{m-1}$ at $z = z_{m-1}$. We note that the driving term of Eq. 13, which is a first-ordered linear differential equation with constant coefficients, is independent of z in the interval (z_{m-1}, z_m). As a result, Eq. 13 can be easily solved, and s_{ij}^r at $z = z_m$, i.e., $(s_{ij}^r)_m$, for $r \geq 2$ turns out to be

$$(s_{ij}^r)_m = (s_{ij}^r)_{m-1} e^{-\alpha_r \Delta z_m} + \frac{C_r}{\alpha_r} \frac{(\Delta\varepsilon_{ij}^p)_m}{\Delta z_m} (1 - e^{-\alpha_r \Delta z_m}) \tag{14}$$

Eq. 13 can be integrated more simply for $r = 1$ due to $\alpha_1 = 0$. Alternatively, L'Hospital's rule can be applied to Eq. 14. No separate mathematical treatment is given in the following for the case of $r = 1$. The simplification of Eq. 8 to Eq. 13 follows the idea proposed by Zienkiewicz et al. [13] for integrating linear viscoelastic constitutive equations. Eq. 14 serves for precise approximation of $(s_{ij}^r)_m$ since the exponential nonlinearity of material behavior, as reflected by Eqs. 4 and 8, has been appropriately dealt with. Note that the integrated endochronic relation, Eq. 14, is exact if there is no transient hardening ($f =$ constant) and the loading event traces a piecewise linear path in the plastic strain space.

Having Eqs. 5, 9, 10, and 14, we may proceed to review the 3-D strain-controlled integration scheme [6]. Its excellent numerical efficiency regarding constitutive simulation has been demonstrated in [14].

For a plastically incompressible material,

$$(\Delta s_{ij})_m = 2G[(\Delta e_{ij})_m - (\Delta \varepsilon_{ij}^p)_m] \tag{15}$$

where G is the elastic shear modulus, and e_{ij} is the deviatoric strain tensor. On the other hand, Eqs. 5 and 14 result in

$$(\Delta s_{ij})_m = \frac{(\Delta \varepsilon_{ij}^p)_m}{\Delta z_m} \sum_{r=1}^{n} \frac{C_r}{\alpha_r}(1 - e^{-\alpha_r \Delta z_m}) - \sum_{r=1}^{n} (s_{ij}^r)_{m-1}(1 - e^{-\alpha_r \Delta z_m}) \tag{16}$$

Combining Eqs. 15 and 16 and omitting the subscripts m and m − 1 for convenience, we obtain

$$\Delta \varepsilon_{ij}^p = \frac{A_{ij} \Delta z}{B} \tag{17}$$

where

$$A_{ij}(\Delta z) = 2G\Delta e_{ij} + \sum_{r=1}^{n} s_{ij}^r (1 - e^{-\alpha_r \Delta z}) \tag{18}$$

and

$$B(\Delta z) = 2G\Delta z + \sum_{r=1}^{n} \frac{C_r}{\alpha_r}(1 - e^{-\alpha_r \Delta z}) \tag{19}$$

Substitution of Eq. 17 into Eq. 10 gives

$$(\Delta \zeta)^2 = A_{ij} A_{ij} \frac{(\Delta z)^2}{B^2} \tag{20}$$

Substituting $\Delta \zeta$ from Eq. 9 into Eq. 20, we obtain

$$R(\Delta z) \equiv (CB)^2 - A_{ij}A_{ij} = 0 \tag{21}$$

where

$$C(\Delta z) = f(z + \beta\Delta z) \tag{22}$$

For a given strain increment, this equation can be solved for Δz by the Newton-Raphson technique using the following expressions for the derivatives:

$$R'(\Delta z) = 2[CB(C'B + CB') - A_{ij}A_{ij}'] \tag{23}$$

$$A_{ij}'(\Delta z) = \sum_{r=1}^{n} \alpha_r s_{ij}^r e^{-\alpha_r \Delta z} \tag{24}$$

$$B'(\Delta z) = 2G + \sum_{r=1}^{n} C_r e^{-\alpha_r \Delta z} \tag{25}$$

$$C'(\Delta z) = \beta f'(z + \beta\Delta z) \tag{26}$$

Then Δz is used in Eq. 17 to calculate the plastic strain increments. Finally, stress can be computed from the elastic stress-strain relation, and the internal variable s_{ij}^r is updated in accordance with Eq. 14.

It has been shown by Hsu and Griffin [14] that for hardening materials ($f' \geq 0$), the existence and uniqueness of a positive root of Eq. 21 is guaranteed regardless of the size of $\Delta\varepsilon_{ij}$ experienced in the past or specified at present. Further, by utilizing the fact of $R' > 0$ at the positive root, a reliable and efficient Newton-Raphson solver for Eq. 21 can be easily coded.

3. Algorithmic Tangent Matrix Approach

The 3-D strain-controlled integration algorithm of Section 2 "defines" an incrementally nonlinear stress-strain relation. Application of such a stress-strain relation to mixed-type constitutive simulation or structural analysis, by using the Newton-Raphson method, entails the so-called algorithmic tangent matrix [12], **C**, whose elements are defined for the mth increment as

$$(C_{ij})_m = \frac{\partial(\Delta\sigma_i)_m}{\partial(\Delta\varepsilon_j)_m} \qquad i, j = 1, 2, ..., 6 \tag{27}$$

In the above, $(\Delta\sigma_i)_m$ is an element of the column matrix of the mth stress increment, $\Delta\boldsymbol{\sigma}_m^T = [(\Delta\sigma_{11})_m\,(\Delta\sigma_{22})_m\,(\Delta\sigma_{33})_m\,(\Delta\sigma_{23})_m\,(\Delta\sigma_{13})_m\,(\Delta\sigma_{12})_m]$, and $(\Delta\varepsilon_j)_m$ is an element of the column matrix of the mth strain increment, $\Delta\boldsymbol{\epsilon}_m^T = [(\Delta\varepsilon_{11})_m\,(\Delta\varepsilon_{22})_m\,(\Delta\varepsilon_{33})_m\,2(\Delta\varepsilon_{23})_m\,2(\Delta\varepsilon_{13})_m\,2(\Delta\varepsilon_{12})_m]$. σ_{ij} and ε_{ij} represent the stress and strain tensors, respectively. Likewise, we have $(\Delta s_i)_m$, $(\Delta\varepsilon_i^e)_m$, and $(\Delta\varepsilon_i^p)_m$ denote elements of $\Delta\mathbf{s}_m$, $\Delta\boldsymbol{\epsilon}_m^e$, and $\Delta\boldsymbol{\epsilon}_m^p$, respectively, which represent the respective matrices of the mth deviatoric stress, elastic strain, and plastic strain increments. Note that $(\Delta\varepsilon_i)_m$, $(\Delta\varepsilon_i^e)_m$, and $(\Delta\varepsilon_i^p)_m$,

$i = 4, 5, 6$, are the engineering shear strains. The subscripts m and m − 1 are omitted in the following whenever ambiguity should not occur.

To achieve an expression of **C** (the algorithmic tangent matrix), we first derive the plastic algorithmic tangent matrix, $\mathbf{C}^p$, from Eq. 16. Its elements are written as

$$C_{ij}^p = \frac{\partial \Delta s_i}{\partial \Delta \varepsilon_j^p} + \frac{\partial \Delta s_i}{\partial \Delta z} \frac{\partial \Delta z}{\partial \Delta \zeta} \frac{\partial \Delta \zeta}{\partial \Delta \varepsilon_j^p} \qquad i, j = 1, 2, ..., 6 \tag{28}$$

by viewing Δs_{ij} of Eq. 16 a function of $\Delta \varepsilon_j^p$ and Δz. The $\partial \Delta z / \partial \Delta \zeta$ and $\partial \Delta \zeta / \partial \Delta \varepsilon_j^p$ can be easily found from Eqs. 9 and 10, respectively. The resulting C_{ij}^p, a function of ε_j^p, is then cast into the following computationally suitable form:

$$C_{ij}^p = L\left[(P - Q)\frac{\Delta \bar{\varepsilon}_i^p}{\Delta z} - R_i\right]\Delta \bar{\varepsilon}_j^p + Qk_{ij} \tag{29}$$

where

$$L = \frac{1}{\Delta \zeta (C + \Delta z C')} \tag{30}$$

$$P = \sum_{r=1}^{n} C_r e^{-\alpha_r \Delta z} \tag{31}$$

$$Q = \frac{1}{\Delta z} \sum_{r=1}^{n} \frac{C_r}{\alpha_r} (1 - e^{-\alpha_r \Delta z}) \tag{32}$$

$$R_i = \sum_{r=1}^{n} \alpha_r s_i^r e^{-\alpha_r \Delta z} \tag{33}$$

and

$$k_{ij} = \begin{cases} 1 & i = j = 1, 2, 3 \\ 1/2 & i = j = 4, 5, 6 \\ 0 & i \neq j \end{cases} \tag{34}$$

The $\Delta\bar{\varepsilon}_i^p$ of Eq. 29 are the tensorial plastic strain increments, $\Delta\varepsilon_{ij}^p$ (i.e., $\Delta\bar{\varepsilon}_i^p = k_{ij}\Delta\varepsilon_j^p$); the s_i^r of Eq. 33 are the internal variables s_{ij}^r (i.e., $s_1^r = s_{11}^r$, $s_2^r = s_{22}^r$, $s_3^r = s_{33}^r$, $s_4^r = s_{23}^r$, etc.). The C and C′ of Eq. 30 have been defined by Eqs. 22 and 26, respectively. Associated with $\mathbf{C}^p$ is the algorithmic differential deviatoric-stress-plastic-strain relation,

$$d\Delta\mathbf{s} = \mathbf{C}^p d\Delta\boldsymbol{\epsilon}^p \tag{35}$$

Eq. 16 implies plastic incompressibility in agreement with Eq. 1. Accordingly,

$$\mathbf{0} = \mathbf{A}\Delta\boldsymbol{\epsilon}^p \tag{36}$$

and

$$\Delta\boldsymbol{\epsilon}^p = \mathbf{B}\Delta\boldsymbol{\epsilon}^p \tag{37}$$

where

$$\mathbf{A} = \begin{bmatrix} 1/3 & 1/3 & 1/3 & 0 & 0 & 0 \\ 1/3 & 1/3 & 1/3 & 0 & 0 & 0 \\ 1/3 & 1/3 & 1/3 & 0 & 0 & 0 \\ 0 & 0 & 0 & 0 & 0 & 0 \\ 0 & 0 & 0 & 0 & 0 & 0 \\ 0 & 0 & 0 & 0 & 0 & 0 \end{bmatrix} \tag{38}$$

and

$$\mathbf{B} = \begin{bmatrix} 2/3 & -1/3 & -1/3 & 0 & 0 & 0 \\ -1/3 & 2/3 & -1/3 & 0 & 0 & 0 \\ -1/3 & -1/3 & 2/3 & 0 & 0 & 0 \\ 0 & 0 & 0 & 1 & 0 & 0 \\ 0 & 0 & 0 & 0 & 1 & 0 \\ 0 & 0 & 0 & 0 & 0 & 1 \end{bmatrix} \tag{39}$$

The use of Eq. 37 in Eq. 35 gives

$$\mathbf{B}\mathrm{d}\Delta\boldsymbol{\sigma} = \mathbf{C}^{\mathrm{p}}\mathbf{B}\mathrm{d}\Delta\boldsymbol{\epsilon}^{\mathrm{p}} \tag{40}$$

On the other hand, the incremental elastic stress-strain relation is

$$\Delta\boldsymbol{\sigma} = (3\mathrm{K}\mathbf{A} + 2\mathrm{G}\mathbf{B}\mathbf{k})\Delta\boldsymbol{\epsilon}^{\mathrm{e}} \tag{41}$$

where K is the elastic bulk modulus, and **k** is a 6 x 6 matrix whose elements are defined by Eq. 34. Premultiplications of Eq.41 by **A** and by **B**, respectively, result in

$$\mathbf{A}\Delta\boldsymbol{\sigma} = 3\mathrm{K}\mathbf{A}\Delta\boldsymbol{\epsilon}^{\mathrm{e}} \tag{42}$$

and

$$\mathbf{B}\Delta\boldsymbol{\sigma} = 2\mathrm{G}\mathbf{B}\mathbf{k}\Delta\boldsymbol{\epsilon}^{\mathrm{e}} = 2\mathrm{G}\mathbf{k}\mathbf{B}\Delta\boldsymbol{\epsilon}^{\mathrm{e}} \tag{43}$$

Eqs. 36 and 42 lead to

$$\frac{1}{3\mathrm{K}}\mathbf{A}\mathrm{d}\Delta\boldsymbol{\sigma} = \mathbf{A}(\mathrm{d}\Delta\boldsymbol{\epsilon}^{\mathrm{e}} + \mathrm{d}\Delta\boldsymbol{\epsilon}^{\mathrm{p}}) \tag{44}$$

Similarly, due to Eqs. 40 and 43,

$$\left[\frac{1}{2G}\mathbf{k}^{-1} + (\mathbf{C}^p)^{-1}\right]\mathbf{B}d\Delta\boldsymbol{\sigma} = \mathbf{B}(d\Delta\boldsymbol{\epsilon}^e + d\Delta\boldsymbol{\epsilon}^p) \tag{45}$$

Finally, summing up $\mathbf{A}d\Delta\boldsymbol{\sigma}$, obtained from Eq. 44, and $\mathbf{B}d\Delta\boldsymbol{\sigma}$, from Eq. 45, gives $d\Delta\boldsymbol{\sigma}$.

$$d\Delta\boldsymbol{\sigma} = \{3K\mathbf{A} + \left[\frac{1}{2G}\mathbf{k}^{-1} + (\mathbf{C}^p)^{-1}\right]^{-1}\mathbf{B}\}(d\Delta\boldsymbol{\epsilon}^e + d\Delta\boldsymbol{\epsilon}^p) \tag{46}$$

A comparison between Eqs. 27 and 46 immediately indicates the desired expression of the algorithmic tangent matrix,

$$\begin{aligned}\mathbf{C} &= 3K\mathbf{A} + \left[\frac{1}{2G}\mathbf{k}^{-1} + (\mathbf{C}^p)^{-1}\right]^{-1}\mathbf{B} \\ &= 3K\mathbf{A} + \mathbf{C}^p\left(\frac{1}{2G}\mathbf{k}^{-1}\mathbf{C}^p + \mathbf{I}\right)^{-1}\mathbf{B}\end{aligned} \tag{47}$$

where $\mathbf{I}$ is the 6×6 identity matrix, and

$$\mathbf{k}^{-1} = \begin{bmatrix} 1 & 0 & 0 & 0 & 0 & 0 \\ 0 & 1 & 0 & 0 & 0 & 0 \\ 0 & 0 & 1 & 0 & 0 & 0 \\ 0 & 0 & 0 & 2 & 0 & 0 \\ 0 & 0 & 0 & 0 & 2 & 0 \\ 0 & 0 & 0 & 0 & 0 & 2 \end{bmatrix} \tag{48}$$

It is evident in Eq.47 that whenever the matrix $\mathbf{I}$ is negligible in comparison to the matrix $\mathbf{C}^p$, which is possible if $\sum_{r=1}^{n} C_r$ is large, $\mathbf{C}$ approximates the matrix of elastic moduli.

The holonomic relation suggested by Eq. 27,

$$d\Delta\boldsymbol{\sigma} = \mathbf{C}d\Delta\boldsymbol{\epsilon} \tag{49}$$

can be used in a straightforward Newton-Raphson procedure for mixed-type constitutive simulation, or for solving boundary value problems by the displacement formulation FE method. Each specified loading increment usually necessitates several Newton-Raphson iterations, each of which generates a sub-incremental solution. In case of the FE analysis, a Newton-Raphson iteration begins with construction of the global stiffness matrix using: (1) Eqs. 29 and 47, (2) the internal variables z and s^f_{ij} obtained at the end of the preceding loading increment, and (3) the intrinsic time increment, Δz, and the plastic strain increment, $\Delta\varepsilon^p_{ij}$, of the preceding iteration (of the current loading increment). Eq. 29 indicates that $\mathbf{C}^p$ is indeterminate at $\Delta\bar{\varepsilon}^p_i = 0$ unless $R_i = 0$. This is because the material behavior for both continuous loading and unloading is characterized by a unified endochronic constitutive equation without a loading-unloading criterion. Thus, the elastic constitutive matrix is used for every first iteration as a general rule. On the other hand, the global residual load vector is calculated as the difference between the desired incremental load and the part which is contributed by the stress increment, $\Delta\sigma_{ij}$, of the preceding iteration. The global stiffness matrix and residual load vector constitute a linear system of equations, from which we intend to determine the displacement "sub-increment" by imposing a proper displacement boundary condition. In case of the first iteration, the desired displacement increment is applied to the linear system; otherwise, the corresponding homogeneous displacement boundary condition is applied. The displacement "sub-increment" is added to the displacement "increment" of the preceding iteration to form the updated displacement "increment," from which the strain increment, $\Delta\varepsilon_{ij}$, can be determined at every integration point. Finally, $\Delta\varepsilon_{ij}$ is input into the 3-D strain-controlled integration algorithm to calculate Δz, $\Delta\varepsilon^p_{ij}$, and $\Delta\sigma_{ij}$

for their future use in calculation of the global stiffness matrix and residual load vector during the next iteration.

The Newton-Raphson iteration is repeated and all the internal variables (i.e., z, ε_{ij}^{p}, and s_{ij}^{r}) remain unchanged until convergence is achieved. Afterward, the displacement increment is used to update the total displacement, and the total strain ensues. In addition, Δz and $\Delta\varepsilon_{ij}^{p}$ are employed to update all the internal variables. We finally call in the elastic stress-strain relation to compute the total stress, so the determination of structural response to a specified loading increment comes to an end.

The plastic algorithmic tangent matrix, $\mathbf{C}^{p}$, is generally unsymmetric because of the term $LR_i\Delta\bar{\varepsilon}_i^{p}$ of Eq. 29. Symmetry occurs if and only if $R_i = 0$, or the vectors R_i and $\Delta\bar{\varepsilon}_i^{p}$ are parallel. The first situation is true for an annealed material or a material whose memory of kinematic hardening has been judiciously erased through a cyclic unloading process with a gradually decreasing amplitude. Regarding the latter case, if the plastic strain path has become linear for such a long intrinsic time that $\mathbf{s}^{r}$, $\mathbf{s}$, and $\mathbf{R}$ turn parallel with the linear segment of the plastic strain path, and if the tentative deviatoric strain increment, $\mathbf{Bk}\Delta\boldsymbol{\epsilon}$, of the preceding Newton-Raphson iteration lies in the same direction, then so does the corresponding plastic strain increment, $\mathbf{k}\Delta\boldsymbol{\epsilon}^{p}$. Therefore, the $\mathbf{C}^{p}$ used for the current iteration is symmetric. It can be shown that if an algorithmic tangent matrix approach, similar to that for FE analysis, is applied to constitutive simulation of stress-controlled proportional loading, $\mathbf{C}^{p}$ is symmetric whenever it should be calculated.

$\mathbf{C}^{p}$ is akin to the classical plastic constitutive tangent matrix for the following identities, which can be deduced from Eqs. 29 and 36:

$$\sum_{i=1}^{3} C_{i1}^{p} = \sum_{i=1}^{3} C_{i2}^{p} = \sum_{i=1}^{3} C_{i3}^{p} = Q \neq 0 \tag{50}$$

$$\sum_{i=1}^{3} C_{i4}^{p} = \sum_{i=1}^{3} C_{i5}^{p} = \sum_{i=1}^{3} C_{i6}^{p} = 0 \tag{51}$$

$$\sum_{j=1}^{3} C_{1j}^{p} = \sum_{j=1}^{3} C_{2j}^{p} = \sum_{j=1}^{3} C_{3j}^{p} = Q \neq 0 \tag{52}$$

$$\sum_{j=1}^{3} C_{4j}^{p} = \sum_{j=1}^{3} C_{5j}^{p} = \sum_{j=1}^{3} C_{6j}^{p} = 0 \tag{53}$$

Eqs. 35, 50, and 51 imply $\mathbf{A}d\Delta\epsilon^{p} = 0$, which is not surprising at all if we recall the earlier use of Eq. 36. However, the same reasoning toward plastic incompressibility is essential for the case of the classical plastic constitutive tangent matrix. Using Eqs. 50 - 53, we can show that the matrix $\mathbf{F} \equiv (\mathbf{k}^{-1}\mathbf{C}^{p}/2G + \mathbf{I})^{-1}$ of Eq. 47 possesses characteristics similar to Eqs. 50 - 53. Particularly, the similarity to Eqs. 52 and 53 allows one to efficiently construct the matrix **FB** of Eq. 47 in a computer implementation.

We make our final remark on the presented algorithmic tangent matrix approach by considering a structure under monotonic loading. Let us assume $f \equiv$ constant (a constant hardening function) and $\mathbf{s}^{r} = \mathbf{0}$ everywhere initially. According to the present approach, if the total load is applied in a single marching step, then the solution is identical to that based on a deformation theory of plasticity with the following deviatoric-stress-plastic-strain relation:

$$s_{ij} = \frac{\varepsilon_{ij}^{p}}{z} \sum_{r=1}^{n} \frac{C_r}{\alpha_r} (1 - e^{-\alpha_r z}) \tag{54}$$

where $z = (\varepsilon_{ij}^{p}\varepsilon_{ij}^{p})^{1/2}/f$. Note that the algorithmic tangent matrix of such a one-step approximation is identical to the constitutive tangent matrix of the deformation theory, and is symmetric and determinate. On the other hand, if the total load is applied in more than one step, and the internal variables are updated in accordance, then the well-known path-dependent effect enters our solution, while the material model retains the same stress-strain curve (Eq. 54) for proportional monotonic loading. Therefore, the influence of path-dependent material behavior on structural response can be examined simply by varying the number of marching steps.

4. FE Solution for a Cyclically Loaded Unidirectional Boron/Aluminum Composite

The proposed numerical method was subjected to crucial tests to demonstrate its superior stability and efficiency. The method was applied to a micromechanics boundary value problem of a cyclically loaded unidirectional B/6061 Al composite. Even if the macro-stress is in a plane stress state, the severe mismatch in constituent properties induces very complicated 3-D micro-stress.

Shown in Fig. 1 is the idealized micro-structure of the B/6061 Al composite. The 6061 aluminum alloy matrix is reinforced by a periodic diamond array of boron fibers in the x_1 direction. We note that nearly periodic packing is not unusual for metal matrix composites with thicker fibers due to their fabrication methods. Fissures, voids, and interfacial reaction zones are excluded from the present consideration. Besides, the computation of this numerical illustration started with a homogeneous stress-free state in each constituent; this simplification renders our illustration of the proposed method simpler to be understood. Both the boron fibers and the aluminum matrix

are assumed to be isotropic; the fibers are elastic, while the matrix is elastoplastic. The elastic bulk and shear moduli of the fibers are $K_f = 222.22 \times 10^3$ MPa and $G_f = 166.67 \times 10^3$ MPa, respectively, and those of the matrix are $K_m = 70.98 \times 10^3$ MPa and $G_m = 27.22 \times 10^3$ MPa, respectively. The plastic behavior of the matrix is represented by the endochronic constitutive equations, Eqs. 1 - 4, with $f \equiv 1$, $n = 4$, $C_1 = 2.8 \times 10^2$ MPa, $\alpha_1 = 0$, $C_2 = 6.0 \times 10^3$ MPa, $\alpha_2 = 3.36 \times 10^2$, $C_3 = 7.0 \times 10^4$ MPa, $\alpha_3 = 2.46 \times 10^3$, $C_4 = 9.8 \times 10^6$ MPa, and $\alpha_4 = 4.00 \times 10^5$. We take a constant hardening function because the 6061 aluminum alloy does not show considerable cyclic hardening. Using the material parameters of the matrix, we generated its initial monotonic stress-strain curve (the continuous line in Fig. 2) and cyclic stress-strain curve (the squares in Fig. 2). In terms of the endochronic theory, the "initial" monotonic curve obtained with $f \equiv$ constant is identical to the "subsequent" monotonic curve obtained from a specimen whose memory of kinematic hardening has been carefully erased, and its f has grown to the same stable constant. Nevertheless, the initial monotonic curve obtained with $f \equiv$ constant differs from the cyclic stress-strain curve even though the difference may be small (Fig. 2). The fiber volume fraction of the composite is 0.45, and the fiber diameter is 0.142 mm. These numbers together with the monolayer thickness, $h = 0.194$ mm, completely define the micro-geometry (Fig. 1).

According to Hashin [15], local-theory stress-strain relations of a macroscopically homogeneous composite are determined by imposing the following displacement condition on the boundary of a composite volume to induce a uniform macroscopic strain field, ε_{ij}^o, and a uniform macroscopic stress field, σ_{ij}^o:

$$u_j = \varepsilon_{ij}^o x_i \tag{55}$$

where u_j is the displacement vector, and x_i are the coordinate variables. The macro-stress, σ^o_{ij}, is calculated as the volume average of the micro-stress field corresponding to the boundary condition, Eq. 55. The geometry of the composite volume should be such that local-theory constitutive relations between macro-stress and macro-strain can be established. In view of the boundary condition, and the x_1-independence and double periodicity of micro-structure of the present composite model, we consider a composite volume whose geometry leads to dominant generalized plane strain deformation and a stress field dominated by the double periodicity. Therefore, the displacement field can be approximately expressed in the following form regardless of irrelevant rigid-body motion:

$$u_1 = \bar{u}_1(x_2, x_3) + \varepsilon^o_{11} x_1 \tag{56}$$

$$u_2 = \bar{u}_2(x_2, x_3) \tag{57}$$

$$u_3 = \bar{u}_3(x_2, x_3) \tag{58}$$

In case of $\varepsilon^o_{23} = \varepsilon^o_{13} = 0$, we further infer from symmetry that $\sigma^o_{23} = \sigma^o_{13} = 0$ and the trapezoid region OHIJ shown in Fig. 1 is the smallest for sufficient analysis with boundary conditions described below. Let $\int(\bullet)dl$ and $\int(\bullet)ds$ denote the line integral and double integral on the $x_1 = 0$ plane, respectively, t_i denote the traction vector, and w denote half the fiber spacing (Fig.1).

1. Boundary conditions on the edge IJ: $\bar{u}_i$ is antisymmetric, but t_i is symmetric about the midpoint G.

2. Boundary conditions on the edges HI and JO:

(1)

$$\bar{u}_1 = \begin{cases} \frac{w}{2}\varepsilon_{12}^{o} & \text{on HI} \\ -\frac{w}{2}\varepsilon_{12}^{o} & \text{on JO} \end{cases}$$

$$\int_{HI} t_1 dl - \int_{JO} t_1 dl = h\sigma_{12}^{o}$$

(2)

$$\bar{u}_2 = \begin{cases} \frac{w}{2}\varepsilon_{22}^{o} & \text{on HI} \\ -\frac{w}{2}\varepsilon_{22}^{o} & \text{on JO} \end{cases}$$

$$\int_{HI} t_2 dl - \int_{JO} t_2 dl = h\sigma_{22}^{o}$$

(3)

$$t_3 = \begin{cases} 0 & \text{on HI} \\ 0 & \text{on JO} \end{cases}$$

3. Boundary conditions on the edge OH:

(1)

$$t_1 = 0$$

(2)

$$t_2 = 0$$

(3)

$$\bar{u}_3 = -\frac{h}{2}\varepsilon_{33}^{o}$$

$$\int_{OH} t_3 dl = -w\sigma_{33}^{o}$$

4. Axial force condition:

$$\int_{OHIJ} \sigma_{11} ds = \frac{hw}{2}\sigma_{11}^{o}$$

According to the foregoing argument, plane-stress loading of the composite model ($\sigma_{33}^{o} = \sigma_{23}^{o} = \sigma_{13}^{o} = 0$) can be simulated by dividing the trapezoid region, OHIJ, into 2-D finite elements with three variables ($\bar{u}_1$, $\bar{u}_2$, and $\bar{u}_3$) allocated at each node. Shown in Fig. 3 is the FE grid of the present numerical illustration, which contains 216 constant-strain triangles and 126 nodes. It should be borne in mind that the nodes on the sloping boundary, IJ (Fig. 1), are allocated symmetrically about the midpoint G. One extra degree of freedom must be added to the FE formulation to account for the uniform longitudinal normal strain, ε_{11}^{o}. The incorporation of the additional variable, ε_{11}^{o}, leads to an arrow-shaped global stiffness matrix. The boundary conditions are specified in incremental form. Among the eight incremental macroscopic vari-

ables ($\Delta\varepsilon^{\circ}_{11}$, $\Delta\varepsilon^{\circ}_{22}$, $\Delta\varepsilon^{\circ}_{33}$, $\Delta\varepsilon^{\circ}_{12}$, $\Delta\sigma^{\circ}_{11}$, $\Delta\sigma^{\circ}_{22}$, $\Delta\sigma^{\circ}_{33}$, $\Delta\sigma^{\circ}_{12}$), $\Delta\sigma^{\circ}_{33}$ is always specified to be zero, three out of the six in-plane components are specified as desired, and the remaining four incremental macroscopic variables are determined from the FE computation. Boundary conditions 2(3), 3(1) and (2), and 4 are imposed on the global system of FE equations in the usual way. On the other hand, simultaneous reductions of the numbers of the unknowns and of the FE equations can be carried out at the global level by respective correlations of boundary nodal variables and of boundary force vectors according to boundary conditions 1, 2(1) and (2), and 3(3).

There are three types of iteration performed in the present illustration, the initial iteration, constant-stiffness iteration, and Newton-Raphson iteration. The initial iteration is the first iteration of a specified loading increment, and is always based on the elastic constitutive matrix. Therefore, the global elastic stiffness matrix is calculated only once and then stored for repeated use. In a constant-stiffness iteration, the triangularized global stiffness matrix of the preceding iteration is reserved for the current iteration. The Newton-Raphson iteration, which involves updating of the global stiffness matrix as explained in Section 3, consumes more time than the constant-stiffness iteration, but provides a better convergence rate. Besides, the Newton-Raphson iteration works well as a primary iteration (e.g., the 2nd or 3rd iteration) for loading increments of a complicated history, while the constant-stiffness iteration usually does not. At the end of an iteration, an error measure called ERROR and a performance logical indicator called CHECK are set up, and effectiveness of the iteration is assessed. If an iteration is considered effective, then the "incremental" solution vector is updated with the "sub-incremental" solution vector generated during the iteration; otherwise, no "actual" updating is performed. For the initial iteration, ERROR and CHECK are set as $\text{ERROR}_1 = 1$ and $\text{CHECK}_1 =$ "false", respectively.

For a subsequent iteration, e.g., the mth iteration ($m \geq 2$), $ERROR_m$ is calculated as the ratio of the norm of the "sub-incremental" solution vector to that of the "tentatively" (not actually) updated "incremental" solution vector. On the other hand, "true" is assigned to $CHECK_m$ ($m \geq 2$) if $ERROR_m$ is not smaller than the ERROR of the last effective iteration or $ERROR_m$ is not smaller than $TOLERN^{(m-1)/(NITRB-1)}$; otherwise, "false" is assigned to $CHECK_m$. TOLERN is a predefined tolerance value, and $NITRB > 1$ is a predefined integer representing the expected number of iterations taken to reach convergence. The mth iteration ($m \geq 1$) is considered ineffective if and only if the mth iteration is not a Newton-Raphson iteration and $CHECK_m$ = "true". Therefore, the initial iteration is always considered effective. Three possibilities exist at the end of an iteration, e.g., the mth iteration ($m \geq 1$): (1) Convergence is deemed to have occured if $ERROR_m < TOLERN$. (2) Program execution is terminated if the total number of iterations (m) reaches a predefined limit, NITR3, or the number of Newton-Raphson iterations reaches its predefined limit, NITRA ($NITR3 \geq 1$ and $NITRA \geq 1$). (3) Otherwise, a new iteration, i.e., the $(m+1)$th iteration ($m + 1 \geq 2$), should be initiated. To obtain the best numerical efficiency, rules are established to decide whether the new iteration is a constant-stiffness iteration or a Newton-Raphson iteration.

1. If the new iteration is in the primary stage of iteration, i.e., $2 \leq m + 1 \leq NITR1$, or in the emergent stage, i.e., $NITR2 \leq m + 1 \leq NITR3$, then the new iteration is a Newton-Raphson iteration. NITR1 and NITR2 are predefined integers.

2. If the new iteraiton is in the secondary stage of iteration, i.e., $NITR1 < m + 1 < NITR2$, and its preceding iteration (i.e., the mth iteration, $m \geq 1$) is effective, then a constant-stiffness iteration is chosen as the priority. On the

contrary, if the mth iteration is ineffective, then a Newton-Raphson iteration is triggered.

We note that the primary and the emergent stages of iteration may be set null by predefining NITR1 < 2 and NITR3 $<$ NITR2, respectively. The secondary stage becomes null likewise by predefining NITR2 $\leq$ NITR1. In addition, a software switch has been installed so that declaration of an ineffective iteration is prevented if the switch is off. Therefore, it is possible to implement the full Newton-Raphson method for all the subsequent iterations and the initial-strain method as two special cases. In the numerical experiments to be reviewed, those parameters regarding convergence monitoring were predefined as follows: TOLERN $= 1 \times 10^{-3}$, NITR1 $= 2$, NITR2 $= 11$, NITR3 $= 15$, NITRA $= 10$, and NITRB $=$ NITR2 $- 1 = 10$.

A cyclic loading history of transverse normal stress was applied to the B/Al composite in the first numerical experiment. As shown in Figs. 4 and 5, the loading consisted of three events, an initial straining to $\varepsilon^{g}_{22} = 0.2\%$, a reverse loading to 0.1%, and a final straining to 0.4%. $\sigma^{g}_{11} = \varepsilon^{g}_{12} = 0$ and increments of ε^{g}_{22} were specified as the boundary conditions. To examine numerical efficiency and stability, we tested six cases of different numbers of increments in each loading event, (1, 1, 1), (2, 1, 3), (5, 3, 8), (10, 5, 15), (20, 10, 30), and (50, 25, 75), on an IBM 3090-300E. Three parenthesized numbers of increments correspond to the three loading events, respectively. The calculated macroscopic response is presented in Figs. 4 and 5. The microscopic response in three crucial elements, elements 52, 72, and 216, is shown in Figs. 6 - 8 for the cases of (1, 1, 1), (2, 1, 3), (5, 3, 8), and (50, 25, 75) increments. The continuous lines in Figs. 4 - 8 represent the prediction with (50, 25, 75) increments, and the discrete symbols represent the predictions with less increments. Due to the fact of

$\sigma^{\circ}_{13} = \sigma^{\circ}_{12} = 0$ in this numerical experiment, micro-stresses σ_{13} and σ_{12} vanish in the analyzed region; and σ_{23} is negligibly small in elements 72 and 216 because the boundary edge OH (Fig. 1) is free of traction in the x_2 direction. Computational time and records of numerical iterations are summarized in Tables 1 - 4. In the tables, a record like (9, 1) x 4 means in each of "4" consecutive loading increments, "9" iterations were executed to attain convergence, and "1" of them is a Newton-Raphson iteration. The records of numerical iterations appear in the tables in the same sequence as they occurred in the simulation.

The present approach was further tested for another loading history. Fig. 9 indicates the biaxial strain cycle (1-2-3, ..., 7-8-1) of the second numerical experiment, where $\sigma^{\circ}_{11} = 0$ and increments of ε°_{22} and ε°_{12} were specified as the boundary conditions. The loading history comprised the initial tensile loading to point 1 (Fig. 9) and two strain cycles, and was restarted for changing the number of increments per linear segment of the imposed macro-strain path. Four cases were studied, the cases of 1, 2, 5, and 50 increments per linear segment. Since the quality of the predictions is very stable throughout the loading history, only the response during the 2nd cycle is shown in the figures for clarity. The macro-response and micro-response are presented in Fig. 10 and Figs. 11 - 13, respectively. The continuous lines in Figs. 9 - 13 represent the simulation with 50 increments per linear segment, and the discrete symbols represent the simulations with less increments. σ_{23} and σ_{13} are negligibly small in elements 72 and 216 because the boundary edge OH (Fig. 1) is free of traction in the x_1 and x_2 directions. We note that apparently closed loops were observed at the macro-level but little openings were seen at the micro-level. Numerical statistics recorded during the 2nd cycle and computational time spent over the entire loading history (the initial loading plus two cycles) are summarized in Tables 5 - 8.

It is evident that all the results consistently demonstrate excellent numerical efficiency and stability of the proposed method. The unconditional stability is particularly valuable for complex plasticity analyses. With the advantage of unconditional stability, one can considerably cut down the cost of preliminary analysis of a complicated engineering problem by using a small number of marching steps for a satisfactorily accurate solution. Finally, we close this section with a general report on error monitoring. We recall that Eq. 21 has to be solved numerically. The equation was considered satisfied in the foregoing numerical experiments if $|R(\Delta z)| < 1 \times 10^{-10}\,\mathrm{MPa}^2$. Secondly, it has been stated that an incremental solution is accepted if $\mathrm{ERROR} < \mathrm{TOLERN} = 1 \times 10^{-3}$. We found that generally, $\mathrm{ERROR} < 5 \times 10^{-4}$ when only one Newton-Raphson iteration was invoked during a loading increment, and $\mathrm{ERROR} < 5 \times 10^{-5}$ when more Newton-Raphson iterations were necessary.

5. Extensions to Endochronic Plasticity with a Yield Surface and to the Plane Stress Case

The formulations and numerical algorithms presented in Sections 2 and 3 can be extended to the endochronic theory with the Mises yield surface of combined kinematic-isotropic hardening. This version of the endochronic theory was derived by Valanis [1] by incorporation of the Dirac δ function into the kernel, $\rho(z)$. Namely, Eq. 4 is rewritten as

$$\rho(z) = \sum_{r=1}^{n-1} C_r e^{-\alpha_r z} + \tau_y^o \delta(z) \tag{59}$$

where τ_y^o is a positive material constant. Then, substitution of Eqs. 2 and 59 into Eq. 1 gives the following constitutive equations:

$$s_{ij} - \alpha_{ij} = \tau_y \frac{d\varepsilon_{ij}^p}{d\zeta} \tag{60}$$

where

$$\alpha_{ij} = \sum_{r=1}^{n-1} \int_{o}^{z} C_r e^{-\alpha_r(z-z')} \frac{d\varepsilon_{ij}^{p}}{dz'} dz' \tag{61}$$

and

$$\tau_y = \tau_y^o f \tag{62}$$

In terms of classical plasticity theory, α_{ij} represents the center of the Mises yield surface, and τ_y the size of the yield surface. Eq. 60 is the associated normality flow rule. The evolution of the yield surface is governed by the kinematic hardening rule Eq. 61 and the isotropic hardening rule Eq. 62. Moreover, in view of Eq. 3, Eq. 60 implies that the condition,

$$(s_{ij} - \alpha_{ij})(s_{ij} - \alpha_{ij}) = \tau_y^2 \tag{63}$$

is satisfied during a plastic event. Following the common methodology of classical plasticity theory, one can easily combine the differential forms of Eqs. 61 - 63 to derive a linear relation between $d\zeta$ and ds_{ij}, and thus a differential deviatoric-stress-plastic-strain relation in the classical form.

To establish a 3-D strain-controlled integration algorithm, we start with the following equations which account for Eqs. 60 - 62 (for a plastic event) and a pure elastic event:

$$s_{ij} = \alpha_{ij} + s_{ij}^{n} \tag{64}$$

where

$$\alpha_{ij} = \sum_{r=1}^{n-1} s_{ij}^r \tag{65}$$

$$\begin{cases} \dfrac{ds_{ij}^r}{dz} + \alpha_r s_{ij}^r = C_r f \dfrac{d\varepsilon_{ij}^p}{d\zeta} & \text{if } d\varepsilon_{ij}^p \neq 0 \\ ds_{ij}^r = 0 & \text{if } d\varepsilon_{ij}^p = 0 \end{cases} \tag{66a, b}$$

for $r = 1, 2, \ldots, n-1$, and

$$\begin{cases} s_{ij}^n = \tau_y^o f \dfrac{d\varepsilon_{ij}^p}{d\zeta} & \text{if } d\varepsilon_{ij}^p \neq 0 \\ ds_{ij}^n = 2G de_{ij} & \text{if } d\varepsilon_{ij}^p = 0 \end{cases} \tag{67a, b}$$

The technique of piecewise linearization of the plastic strain path in Section 2 equally applies to the current case. However, a convenient means to an end is to take the limit of the resulting equations of Section 2 by letting $C_n \to \infty$, $\alpha_n \to \infty$, and keeping $C_n/\alpha_n = \tau_y^o$ at the same time. For example, Eqs. 66a and 67a can be obtained from Eq. 8. We only summarize the results below because the connection with those equations of Section 2 is so evident.

1.

$$(s_{ij}^r)_m = \begin{cases} (s_{ij}^r)_{m-1} e^{-\alpha_r \Delta z_m} + \dfrac{(\Delta\varepsilon_{ij}^p)_m}{\Delta z_m} \dfrac{C_r}{\alpha_r} (1 - e^{-\alpha_r \Delta z_m}) & \text{if } (\Delta\varepsilon_{ij}^p)_m \neq 0 \\ (s_{ij}^r)_{m-1} & \text{if } (\Delta\varepsilon_{ij}^p)_m = 0 \end{cases}$$

(68a, b)

for $r = 1, 2, \ldots, n-1$, and

$$(s_{ij}^n)_m = \begin{cases} \tau_y^o \dfrac{(\Delta\varepsilon_{ij}^p)_m}{\Delta z_m} & \text{if } (\Delta\varepsilon_{ij}^p)_m \neq 0 \\ (s_{ij}^n)_{m-1} + 2G(\Delta e_{ij})_m & \text{if } (\Delta\varepsilon_{ij}^p)_m = 0 \end{cases} \tag{69a, b}$$

2.

$$(\Delta s_{ij})_m = (\Delta\alpha_{ij})_m + (\Delta s_{ij}^n)_m \tag{70}$$

where

$$(\Delta\alpha_{ij})_m = \begin{cases} \dfrac{(\Delta\varepsilon_{ij}^p)_m}{\Delta z_m} \displaystyle\sum_{r=1}^{n-1} \frac{C_r}{\alpha_r}(1 - e^{-\alpha_r \Delta z_m}) - \sum_{r=1}^{n-1} (s_{ij}^r)_{m-1}(1 - e^{-\alpha_r \Delta z_m}) & \text{if } (\Delta\varepsilon_{ij}^p)_m \neq 0 \\ 0 & \text{if } (\Delta\varepsilon_{ij}^p)_m = 0 \end{cases}$$

(71a, b)

and

$$(\Delta s_{ij}^n)_m = \begin{cases} \tau_y^o \dfrac{(\Delta\varepsilon_{ij}^p)_m}{\Delta z_m} - (s_{ij}^n)_{m-1} & \text{if } (\Delta\varepsilon_{ij}^p)_m \neq 0 \\ 2G(\Delta e_{ij})_m & \text{if } (\Delta\varepsilon_{ij}^p)_m = 0 \end{cases} \tag{72a, b}$$

3.

$$\Delta\varepsilon_{ij}^p = \begin{cases} \dfrac{A_{ij}\Delta z}{B} & \text{if } \Delta z \neq 0 \\ 0 & \text{if } \Delta z = 0 \end{cases} \tag{73a, b}$$

where

$$A_{ij}(\Delta z) = 2G\Delta e_{ij} + \sum_{r=1}^{n-1} s_{ij}^{r}(1 - e^{-\alpha_r \Delta z}) + s_{ij}^{n} \tag{74}$$

and

$$B(\Delta z) = 2G\Delta z + \sum_{r=1}^{n-1} \frac{C_r}{\alpha_r}(1 - e^{-\alpha_r \Delta z}) + \tau_y^o \tag{75}$$

4.

$$\begin{cases} R(\Delta z) \equiv (CB)^2 - A_{ij}A_{ij} = 0 & \text{if } R(0) < 0 \\ \Delta z = 0 & \text{if } R(0) \geq 0 \end{cases} \tag{76a, b}$$

where $C(\Delta z)$ has been defined by Eq. 22, and

$$R(0) = (f\tau_y^o)^2 - (2G\Delta e_{ij} + s_{ij}^{n})(2G\Delta e_{ij} + s_{ij}^{n}) \tag{77}$$

5. The derivatives of R, A_{ij}, B, and C are used to solve Eq. 76a by the Newton-Raphson method. R′ and C′ are given by Eqs. 23 and 26, respectively.

$$A_{ij}'(\Delta z) = \sum_{r=1}^{n-1} \alpha_r s_{ij}^{r} e^{-\alpha_r \Delta z} \tag{78}$$

$$B'(\Delta z) = 2G + \sum_{r=1}^{n-1} C_r e^{-\alpha_r \Delta z} \tag{79}$$

It is obvious at this moment that the 3-D strain-controlled integration algorithm for the endochronic theory with a yield surface should be parallel with that of Section 2. Most importantly, pay additional attention to Eq. 77. The physical meaning of Eq. 77 is clear; $R(0) < 0$ means the assumption of purely elastic Δe_{ij} results in penetration of the yield surface. Mathematically, $R(0) < 0$ guarantees the existence of a positive root of Eq. 76a. It should be noted that whether $R(0) < 0$ or not influences the solution for Δz (Eq. 76), calculation of $\Delta\varepsilon_{ij}^{p}$ (Eq. 73), and updating of the internal variables (Eqs. 68 and 69).

The algorithmic tangent matrix for the current case is identical to that of Section 3 except that Eqs. 29 and 47 are now under the same restriction of $\Delta\varepsilon_{ij}^{p} \neq 0$ as Eqs. 71a and 72a, and that Eqs. 31 - 33 should be modified by the limit operation ($C_n \rightarrow \infty$, $\alpha_n \rightarrow \infty$, and $C_n/\alpha_n = \tau_y^o$). Therefore,

$$P = \sum_{r=1}^{n-1} C_r e^{-\alpha_r \Delta z} \tag{80}$$

$$Q = \frac{1}{\Delta z} \sum_{r=1}^{n-1} \frac{C_r}{\alpha_r} (1 - e^{-\alpha_r \Delta z}) + \frac{\tau_y^o}{\Delta z} \tag{81}$$

$$R_i = \sum_{r=1}^{n-1} \alpha_r s_i^r e^{-\alpha_r \Delta z} \tag{82}$$

and

$$\mathbf{C} = \begin{cases} 3K\mathbf{A} + \mathbf{C}^p\left(\frac{1}{2G}\mathbf{k}^{-1}\mathbf{C}^p + \mathbf{I}\right)^{-1}\mathbf{B} & \text{if } \Delta\varepsilon_{ij}^p \neq 0 \\ 3K\mathbf{A} + 2G\mathbf{B}\mathbf{k} & \text{if } \Delta\varepsilon_{ij}^p = 0 \end{cases} \tag{83a, b}$$

The algorithmic tangent matrix approach, developed in Section 3 for solving boundary value problems, can be applied in connection with the above formulations for the theory with a yield surface. In addition to following the procedure described in Section 3, one needs to handle logical bifurcations such as appear in Eqs. 76 and 83. We recall that basically, $\mathbf{C}^p$ originates from Eqs. 70, 71a, and 72a. These equations concisely reveal piecewise linearization of the plastic strain path, and are geometrically interpreted in Fig. 14. As shown in the figure, if the mth loading event causes linear growth of plastic strain, the loading must consist of two sub-loading events. One is either an elastic loading or a neutral loading, depending on the size of $(s_{ij}^{\eta})_{m-1}$. The other is a plastic loading, and induces expansion and translation of the yield surface such that the orientation of s_{ij}^{η} is fixed and plastic strain grows linearly during the sub-loading event.

All the foregoing 3-D formulations can be slightly tailored for plane strain or axisymmetric problems. Still, formulations for the important plane stress problems require further manipulation, and are presented in the following only for the case without a yield surface. Extension to the case with a yield surface can be made in the same way as in the first part of this section.

We consider plane stress loading, i.e.,

$$\sigma_{33} = 0 \tag{84}$$

and

$$\sigma_{23} = \sigma_{13} = 0 \tag{85}$$

As a consequence,

$$\varepsilon_{33}^{e} = -\frac{\nu}{1-\nu}(\varepsilon_{11}^{e} + \varepsilon_{22}^{e}) \tag{86}$$

and

$$\varepsilon_{23}^{p} = \varepsilon_{13}^{p} = 0 \tag{87}$$

where ν is the Poisson's ratio. In addition,

$$\varepsilon_{33}^{p} = -\varepsilon_{11}^{p} - \varepsilon_{22}^{p} \tag{88}$$

due to plastic incompressibility. Therefore,

$$\begin{aligned} \varepsilon_{33} &= \varepsilon_{33}^{e} + \varepsilon_{33}^{p} \\ &= -\frac{\nu}{1-\nu}(\varepsilon_{11} + \varepsilon_{22}) - \frac{1-2\nu}{1-\nu}(\varepsilon_{11}^{p} + \varepsilon_{22}^{p}) \end{aligned} \tag{89}$$

as a result of Eqs. 86 and 88. Thus, expressions of the deviatoric strains e_{11} and e_{22} in terms of ε_{11}, ε_{22}, ε_{11}^{p}, and ε_{22}^{p} are obtained by utilizing Eq. 89.

$$e_{ii} = \bar{e}_{ii} + \phi(\varepsilon_{11}^{p} + \varepsilon_{22}^{p}) \qquad i = 1, 2; \text{ no sum on } i \tag{90}$$

where

$$\bar{e}_{11} = \frac{2-\nu}{3(1-\nu)}\varepsilon_{11} - \phi\varepsilon_{22} \tag{91}$$

$$\bar{e}_{22} = -\phi\varepsilon_{11} + \frac{2-\nu}{3(1-\nu)}\varepsilon_{22} \tag{92}$$

and

$$\phi = \frac{1 - 2\nu}{3(1 - \nu)} \tag{93}$$

Substituting Eq. 90 into Eq. 15 with (i, j) = (1, 1), (2, 2), and then combining the two resulting equations and Eq. 16 with (i, j) = (1, 1), (2, 2), respectively, we obtain

$$\begin{cases} \overline{B}\Delta\varepsilon_{11}^{p} + B^{*}\Delta\varepsilon_{22}^{p} = \overline{A}_{11}\Delta z \\ B^{*}\Delta\varepsilon_{11}^{p} + \overline{B}\Delta\varepsilon_{22}^{p} = \overline{A}_{22}\Delta z \end{cases} \tag{94}$$

where

$$\overline{A}_{ii}(\Delta z) = 2G\Delta\overline{e}_{ii} + \sum_{r=1}^{n} s_{ii}^{r}(1 - e^{-\alpha_r \Delta z}) \qquad i = 1, 2;\ \text{no sum on i} \tag{95}$$

$$\overline{B}(\Delta z) = 2G(1 - \phi)\Delta z + \sum_{r=1}^{n} \frac{C_r}{\alpha_r}(1 - e^{-\alpha_r \Delta z}) \tag{96}$$

and

$$B^{*}(\Delta z) = -2G\phi\Delta z \tag{97}$$

Eq. 94 can be solved for $\Delta\varepsilon_{11}^{p}$ and $\Delta\varepsilon_{22}^{p}$ in terms of Δz.

$$\Delta\varepsilon_{ii}^{p} = \frac{\eta_{ii}\Delta z}{B} \qquad i = 1, 2;\ \text{no sum on i} \tag{98}$$

where B has been defined by Eq. 19,

$$\eta_{11}(\Delta z) = \frac{\overline{A}_{11}\overline{B} - \overline{A}_{22}B^*}{\overline{B} + B^*} \tag{99}$$

and

$$\eta_{22}(\Delta z) = \frac{\overline{A}_{22}\overline{B} - \overline{A}_{11}B^*}{\overline{B} + B^*} \tag{100}$$

Besides, a similar expression of $\Delta\varepsilon^p_{12}$ has been available from Eq. 17.

$$\Delta\varepsilon^p_{12} = \frac{A_{12}\Delta z}{B} \tag{101}$$

where A_{12} has been defined by Eq. 18. Finally, substituting $\Delta\varepsilon^p_{ij}$ from Eqs. 87, 88, 98, and 101, and $\Delta\zeta$ from Eq. 9 into Eq. 10 gives

$$\overline{R}(\Delta z) \equiv (CB)^2 - 2(\eta_{11}^2 + \eta_{22}^2 + \eta_{11}\eta_{22} + A_{12}^2) = 0 \tag{102}$$

where C has been defined by Eq. 22. Obviously, Eq. 102 plays the same role as Eq. 21. The derivatives needed for solving Eq. 102 are given below for completeness.

$$\overline{R}'(\Delta z) = 2\{CB(C'B + CB') - [(2\eta_{11} + \eta_{22})\eta_{11}' + (\eta_{11} + 2\eta_{22})\eta_{22}' + 2A_{12}A_{12}']\} \tag{103}$$

where A_{12}', B', and C' have been defined by Eqs. 24 - 26, respectively,

$$\eta_{11}'(\Delta z) = \frac{(\overline{A}_{11}'\overline{B} + \overline{A}_{11}\overline{B}' - \overline{A}_{22}'B^* - \overline{A}_{22}B^{*\prime})(\overline{B} + B^*) - (\overline{A}_{11}\overline{B} - \overline{A}_{22}B^*)(\overline{B}' + B^{*\prime})}{(\overline{B} + B^*)^2} \tag{104}$$

and

$$\eta_{22}'(\Delta z) = \frac{(\overline{A}_{22}'\overline{B} + \overline{A}_{22}\overline{B}' - \overline{A}_{11}'B^* - \overline{A}_{11}B^{*\prime})(\overline{B} + B^*) - (\overline{A}_{22}\overline{B} - \overline{A}_{11}B^*)(\overline{B}' + B^{*\prime})}{(\overline{B} + B^*)^2}$$

(105)

In Eqs. 104 and 105, $\overline{A}_{ii}' = A_{ii}'$ ($i = 1, 2$; no sum on i), which has been defined by Eq. 24,

$$\overline{B}'(\Delta z) = 2G(1 - \phi) + \sum_{r=1}^{n} C_r e^{-\alpha_r \Delta z} \tag{106}$$

and

$$B^{*\prime}(\Delta z) = -2G\phi \tag{107}$$

Having the necessary equations for the strain-controlled integration algorithm for the plane stress case, we commence to derive the corresponding algorithmic tangent matrix. As a direct result of Eq. 84,

$$\Delta\sigma_{11} = 2\Delta s_{11} + \Delta s_{22} \tag{108}$$

and

$$\Delta\sigma_{22} = \Delta s_{11} + 2\Delta s_{22} \tag{109}$$

In addition,

$$\Delta\sigma_{12} = \Delta s_{12} \tag{110}$$

Substitution of Δs_{11}, Δs_{22}, and Δs_{12} from Eq. 16 into Eqs. 108 - 110 gives $\Delta\sigma_{11}$, $\Delta\sigma_{22}$, and $\Delta\sigma_{12}$ in terms of $\Delta\varepsilon_{ij}^{p}$ and Δz. Therefore, the elements (i.e., $\tilde{C}_{ij}^{p}$) of the 3×3, plane stress, plastic algorithmic tangent matrix (i.e., $\tilde{\mathbf{C}}^{p}$) are written as follows:

$$\tilde{C}_{ij}^{p} = \frac{\partial \Delta\tilde{\sigma}_i}{\partial \Delta\tilde{\varepsilon}_j^{p}} + \frac{\partial \Delta\tilde{\sigma}_i}{\partial \Delta z}\frac{\partial \Delta z}{\partial \Delta\zeta}\frac{\partial \Delta\zeta}{\partial \Delta\tilde{\varepsilon}_j^{p}} \tag{111}$$

where $\Delta\tilde{\sigma}_i$ is an element of $\Delta\tilde{\boldsymbol{\sigma}}^{T} = [\Delta\sigma_{11}\, \Delta\sigma_{22}\, \Delta\sigma_{12}]$, and $\Delta\tilde{\varepsilon}_j^{p}$ is an element of $\Delta\tilde{\boldsymbol{\epsilon}}^{p^T} = [\Delta\varepsilon_{11}^{p}\, \Delta\varepsilon_{22}^{p}\, 2\Delta\varepsilon_{12}^{p}]$. As before, $\partial\Delta z/\partial\Delta\zeta$ and $\partial\Delta\zeta/\partial\Delta\tilde{\varepsilon}_j^{p}$ can be easily found from Eqs. 9 and 10, respectively. However, the $\Delta\zeta$ of Eq. 111 is currently considered a function of only $\Delta\varepsilon_{11}^{p}$, $\Delta\varepsilon_{22}^{p}$, and $\Delta\varepsilon_{12}^{p}$ because of Eqs. 87 and 88. The plane stress, plastic algorithmic tangent matrix $\tilde{\mathbf{C}}^{p}$ may be also obtained by modifying Eq. 35 with Eqs. 87 and 88, and the following equations resulting from Eq. 84:

$$\Delta\sigma_{11} = \Delta s_{11} - \Delta s_{33} \tag{112}$$

$$\Delta\sigma_{22} = \Delta s_{22} - \Delta s_{33} \tag{113}$$

The straightforward modification of Eq. 35 leads to the following algorithmic differential stress-plastic-strain relation:

$$d\Delta\tilde{\boldsymbol{\sigma}} = \tilde{\mathbf{C}}^{p} d\Delta\tilde{\boldsymbol{\epsilon}}^{p} \tag{114}$$

where $\tilde{\mathbf{C}}^{p}$ is expressed in terms of C_{ij}^{p}, defined by Eq. 29, as follows:

$$\tilde{\mathbf{C}}^{p} = \begin{bmatrix} 1 & 0 & -1 & 0 \\ 0 & 1 & -1 & 0 \\ 0 & 0 & 0 & 1 \end{bmatrix} \begin{bmatrix} C_{11}^{p} & C_{12}^{p} & C_{13}^{p} & C_{16}^{p} \\ C_{21}^{p} & C_{22}^{p} & C_{23}^{p} & C_{26}^{p} \\ C_{31}^{p} & C_{32}^{p} & C_{33}^{p} & C_{36}^{p} \\ C_{61}^{p} & C_{62}^{p} & C_{63}^{p} & C_{66}^{p} \end{bmatrix} \begin{bmatrix} 1 & 0 & 0 \\ 0 & 1 & 0 \\ -1 & -1 & 0 \\ 0 & 0 & 1 \end{bmatrix} \tag{115}$$

Looking back to Eqs. 29 and 33, we find that calculation of C^p_{i3} and C^p_{3i}, $i = 1, 2, 3, 6$, of Eq. 115 requires two out-of-plane components, $\Delta\bar{\varepsilon}^p_3$ (i.e., $\Delta\varepsilon^p_{33}$) and R_3. $\Delta\varepsilon^p_{33}$ can be calculated from Eq. 88, and $R_3 = -R_1 - R_2$ as a result of Eqs. 14, 33, and 88. Collectively, $\tilde{\mathbf{C}}^p$ can be conveniently constructed in computer implementation. We finally call in the incremental elastic stress-strain relation,

$$\Delta\tilde{\epsilon}^e = \tilde{\mathbf{S}}^e \Delta\tilde{\sigma} \tag{116}$$

where $\Delta\tilde{\epsilon}^{e^T} = [\Delta\varepsilon^e_{11}\ \Delta\varepsilon^e_{22}\ 2\Delta\varepsilon^e_{12}]$, and $\tilde{\mathbf{S}}^e$ is the plane stress elastic compliance matrix, which is expressed in terms of the Young's modulus, E, and the Poisson's ratio, ν, as follows:

$$\tilde{\mathbf{S}}^e = \begin{bmatrix} 1/E & -\nu/E & 0 \\ -\nu/E & 1/E & 0 \\ 0 & 0 & 2(1+\nu)/E \end{bmatrix} \tag{117}$$

Eqs. 114 and 116, and $\Delta\tilde{\epsilon} = \Delta\tilde{\epsilon}^e + \Delta\tilde{\epsilon}^p$, where $\Delta\tilde{\epsilon}^T = [\Delta\varepsilon_{11}\ \Delta\varepsilon_{22}\ 2\Delta\varepsilon_{12}]$, produce a linear system of three matrix equations in terms of $d\Delta\tilde{\sigma}$, $d\Delta\tilde{\epsilon}^p$, $d\Delta\tilde{\epsilon}^e$, and $d\Delta\tilde{\epsilon}$. The desired relation between $d\Delta\tilde{\sigma}$ and $d\Delta\tilde{\epsilon}$ is easily derived from the system.

$$d\Delta\tilde{\sigma} = \tilde{\mathbf{C}} d\Delta\tilde{\epsilon} \tag{118}$$

where $\tilde{\mathbf{C}}$ is the plane stress algorithmic tangent matrix,

$$\tilde{\mathbf{C}} = (\tilde{\mathbf{C}}^p\tilde{\mathbf{S}}^e + \tilde{\mathbf{I}})^{-1}\tilde{\mathbf{C}}^p \tag{119}$$

The matrix $\tilde{\mathbf{I}}$ of Eq. 119 is the 3×3 identity matrix.

6. Concluding Remarks

The convenient and efficient algorithmic tangent matrix approach has been developed for endochronic FE analysis. It is wished that the approach may significantly alleviate the long-standing difficulties in computational cyclic plasticity. The method of piecewise linearization of the plastic strain path has the potential for application to other advanced plasticity models and for extension to viscoplasticity; further investigation is recommended to exploit the potential.

References

1. Valanis, K. C., "Fundamental Consequences of a New Intrinsic Time Measure: Plasticity as a Limit of the Endochronic Theory," *Archives of Mechanics*, Vol. 32, 1980, pp. 171 - 191.

2. Valanis, K. C. and Lee, C. F., "Endochronic Theory of Cyclic Plasticity with Applications," *Journal of Applied Mechanics*, Vol. 51, 1984, pp. 367 - 374.

3. Valanis, K. C., "Continuum Foundations of Endochronic Plasticity," *Journal of Engineering Materials and Technology*, Vol. 106, 1984, pp. 367 - 375.

4. Wu, H. C., Yao, J. C., and Chu, S. C., "Investigation of Endochronic Constitutive Equation Subject to Plastic Strain-Controlled Axial-Torsional Deformation," *Journal of Engineering Materials and Technology*, Vol. 108, 1986, pp. 262 - 269.

5. Murakami, H. and Read, H. E., "Endochronic Plasticity: Some Basic Properties of Plastic Flow and Failure," *International Journal of Solids and Structures*, Vol. 23, 1987, pp. 133 - 151.

6. Hsu, S. Y., Jain, S. K., and Griffin, O. H., Jr., "Verification of Endochronic Theory for Nonproportional Loading Paths," *Journal of Engineering Mechanics*, Vol. 117, 1991, pp. 110 - 131.

7. Lin, H. C., Hsieh, B. J., and Valentin, R. A., "The Application of Endochronic Plasticity Theory in Modeling the Dynamic Inelastic Response of Structural Systems," *Nuclear Engineering and Design*, Vol. 66, 1981, pp. 213 - 221.

8. Valanis, K. C. and Fan, J., "Endochronic Analysis of Cyclic Elastoplastic Strain Fields in a Notched Plate," *Journal of Applied Mechanics*, Vol. 50, 1983, pp. 789 - 794.

9. Hsu, S. Y., Jain, S. K., and Griffin, O. H., Jr., "A Procedure for Determining Endochronic Material Functions and Verification of Endochronic Theory for Nonproportional Loading Paths," Technical Report VPI-E-89-25, College of Engineering, Virginia Polytechnic Institute and State University, Blacksburg, Virginia, 1989.

10. Watanabe, O. and Atluri, S. N., "A New Endochronic Approach to Computational Elastoplasticity: Example of a Cyclically Loaded Cracked Plate," *Journal of Applied Mechanics*, Vol. 52, 1985, pp. 857 - 864.

11. Sengupta, A. and Saxena, S. K., "Performance of a Numerical Algorithm Based on a Thermodynamic Constitutive Theory in Solving Elasto-Plastic Boundary Value Problems," *Numerical Models in Geomechanics: NUMOG III*, Pietruszczak, S. and Pande, G. N., eds., Elsevier Science Publishers, London, 1989.

12. Lubliner, J., Section 4.5, *Plasticity Theory*, Macmillan Publishing Company, New York, 1990.

13. Zienkiewicz, O. C., Watson, M., and King, I. P., "A Numerical Method of Visco-Elastic Stress Analysis," *International Journal of Mechanical Science*, Vol. 10, 1968, pp. 807 - 827.

14. Hsu, S. Y. and Griffin, O. H., Jr., "On Stability and Efficiency of Numerical Integration of Endochronic Constitutive Equations," *Computers and Structures*, Vol. 44, 1992, pp. 657 - 665.

15. Hashin, Z., "Analysis of Composite Materials - A Survey," *Journal of Applied Mechanics*, Vol. 50, 1983, pp. 481 - 505.

Figures

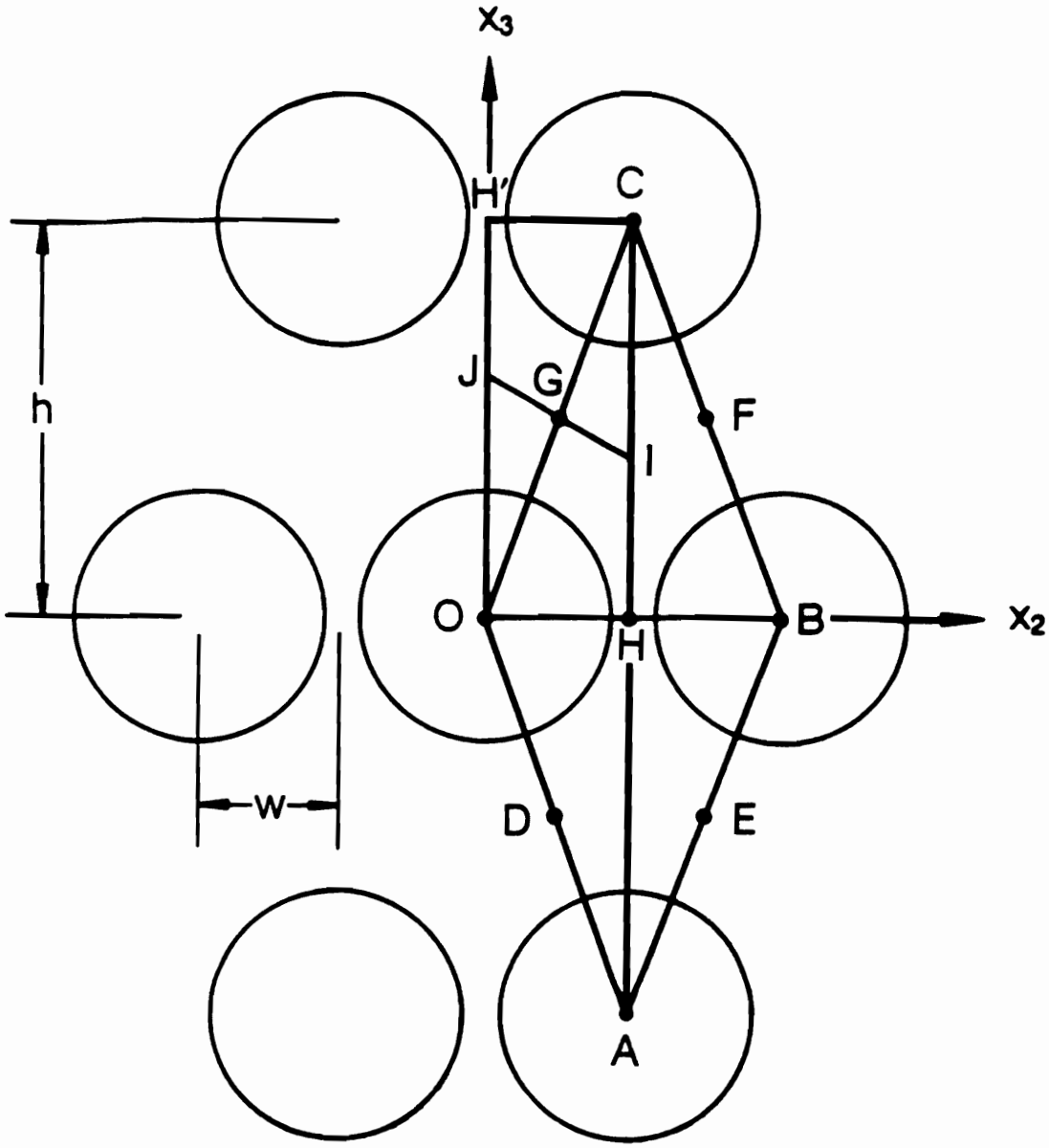

Figure 1. Composite Reinforced with Periodic Diamond Array of Fibers

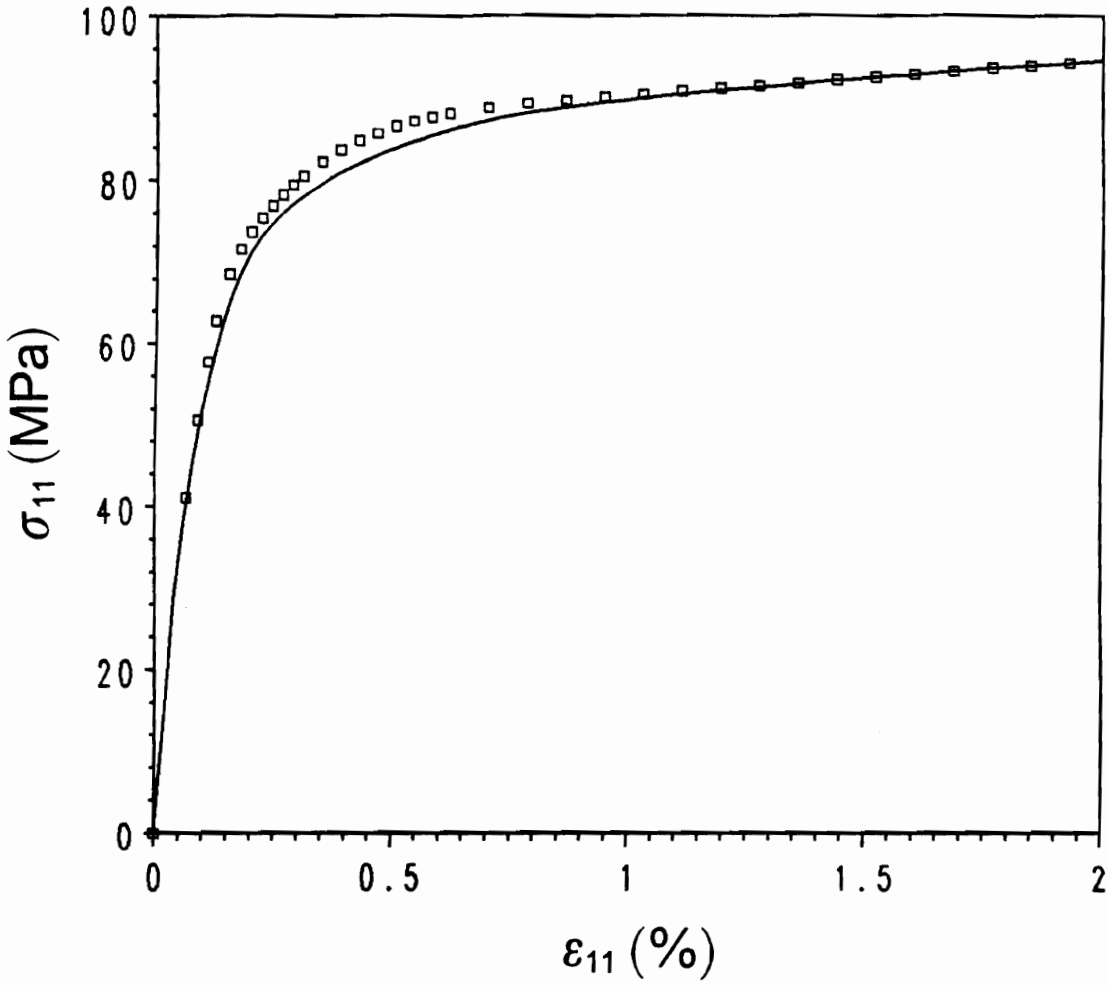

Figure 2. Initial Monotonic Stress-Strain Curve and Cyclic Stress-Strain Curve of 6061 Aluminum Alloy: The continuous line represents the monotonic curve, and the squares the cyclic curve.

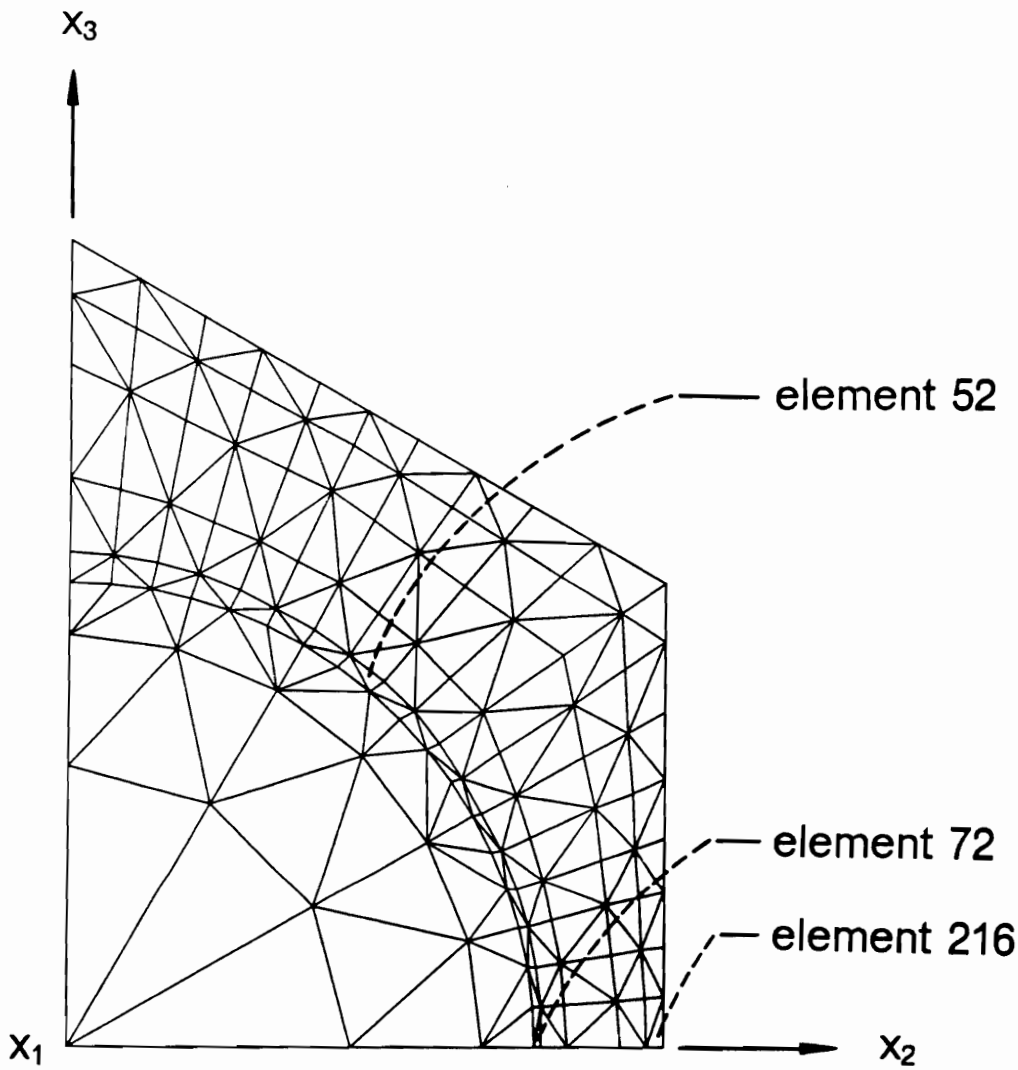

Figure 3. Finite Element Grid for Periodic Diamond Model

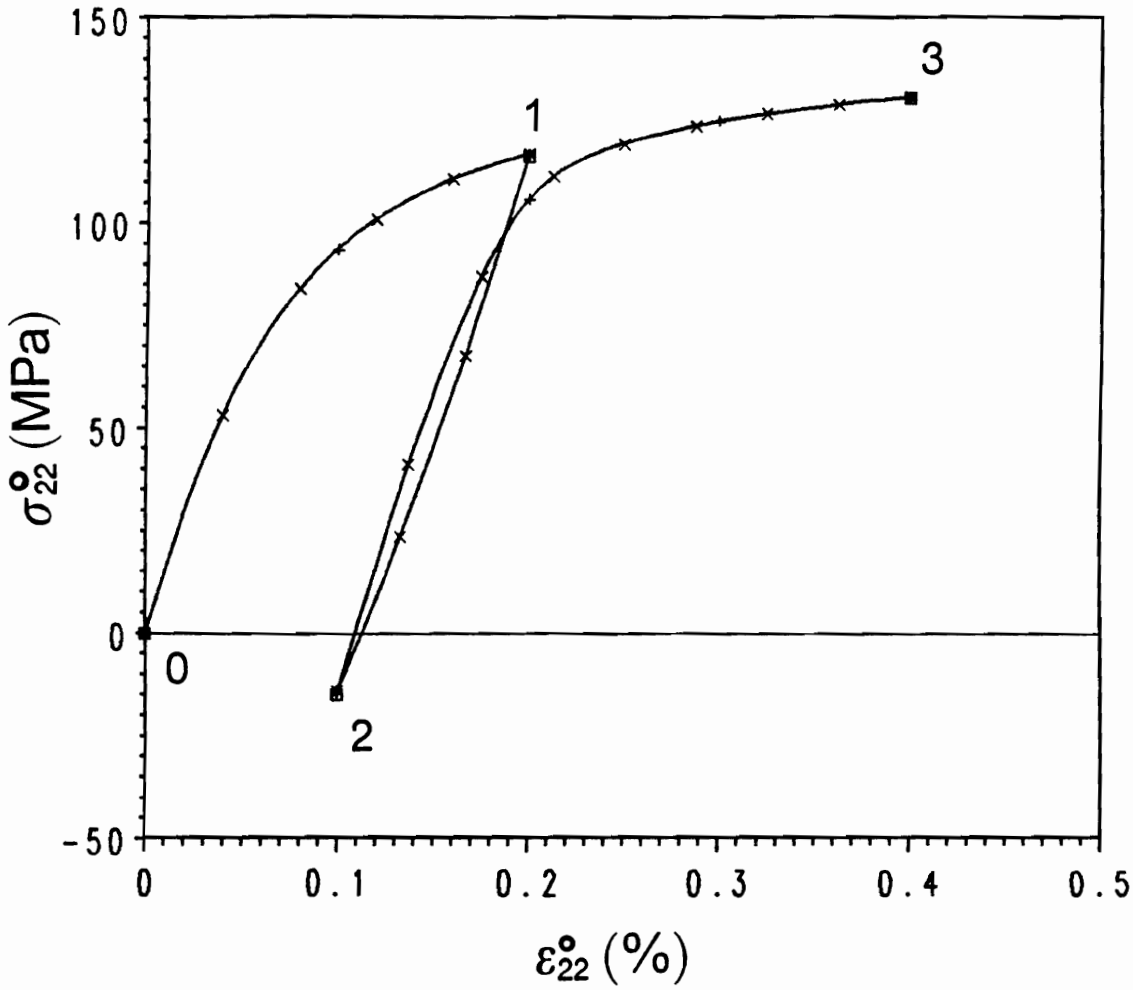

Figure 4. Macro-Response to Transverse Normal Cyclic Loading: The predictions using (1, 1, 1), (2, 1, 3), (5, 3, 8), and (50, 25, 75) increments are represented by the square, +, x, and continuous line, respectively.

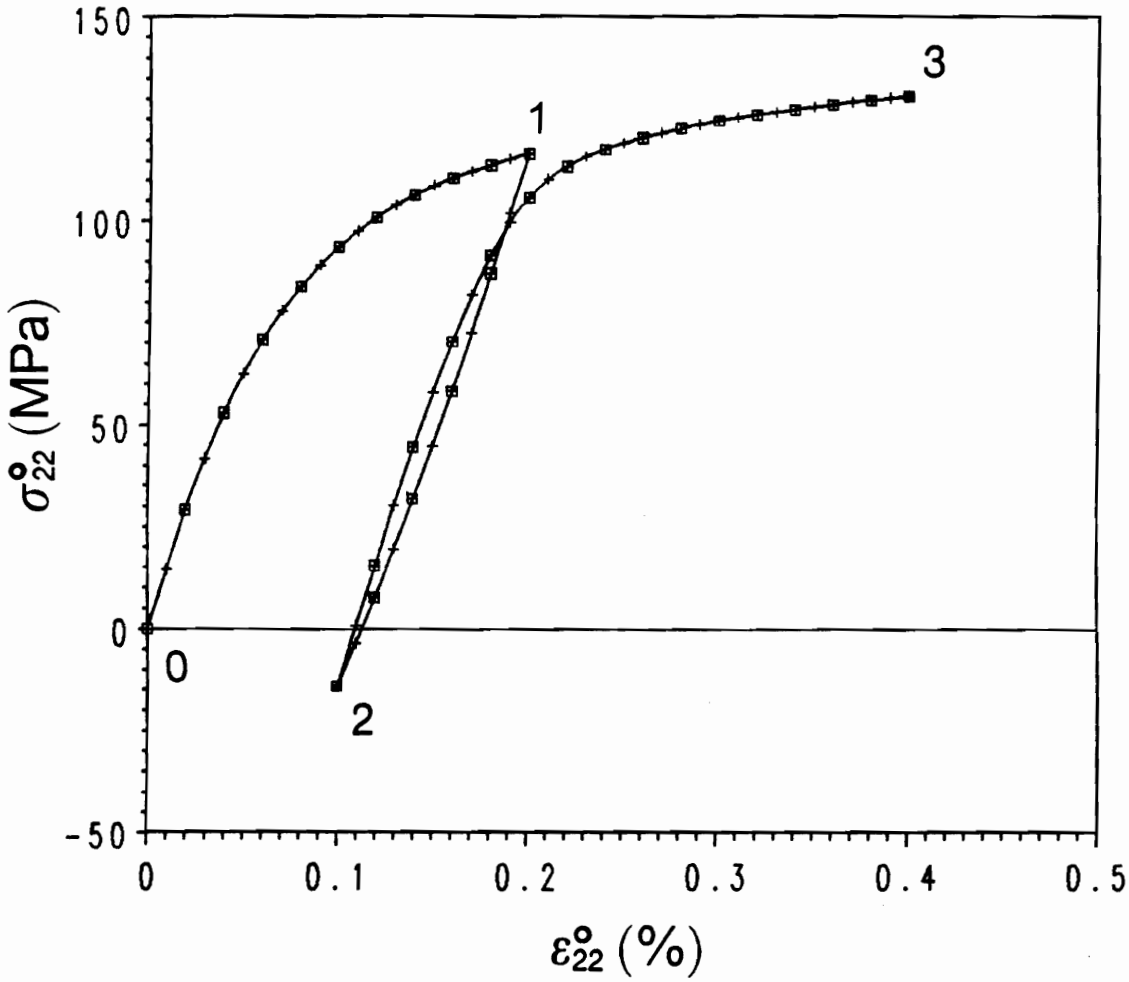

Figure 5. Macro-Response to Transverse Normal Cyclic Loading: The predictions using (10, 5, 15), (20, 10, 30), and (50, 25, 75) increments are represented by the square, +, and continuous line, respectively.

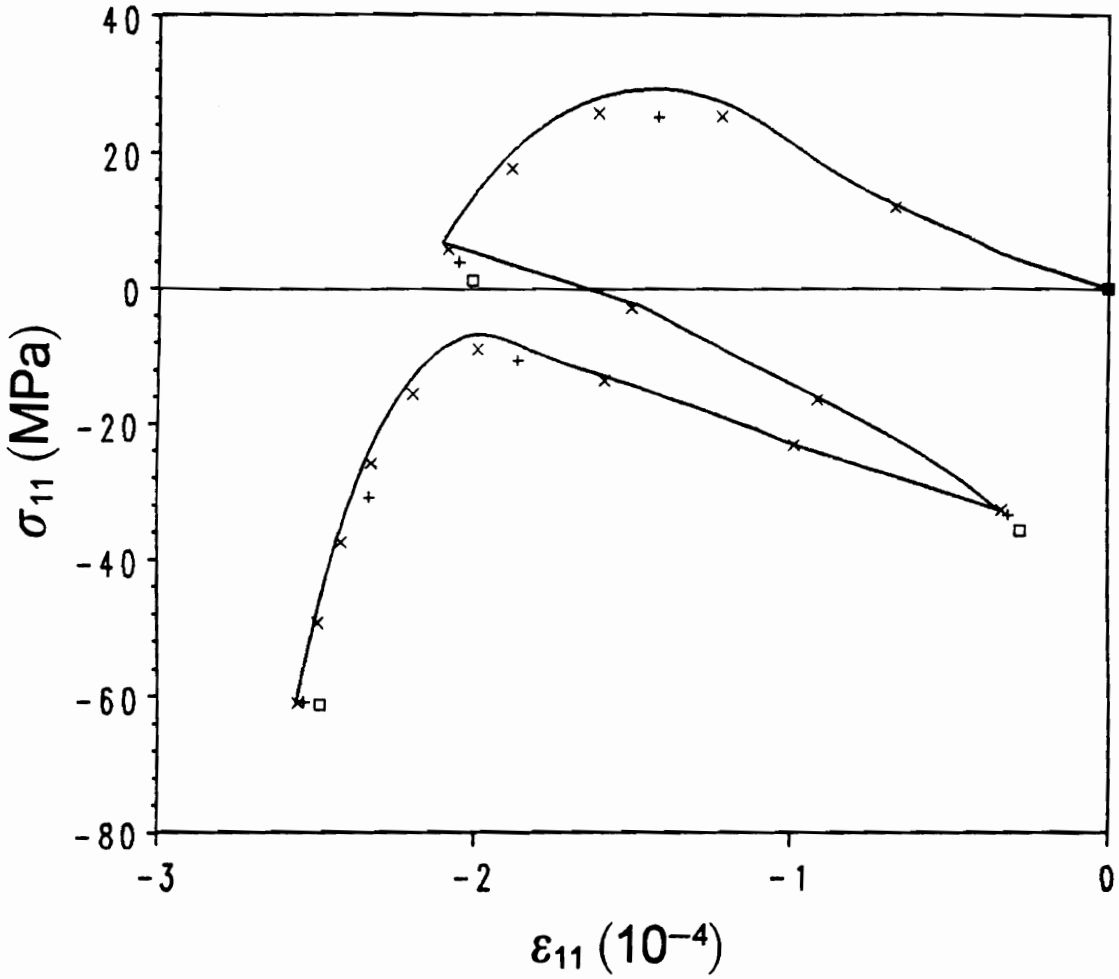

Figure 6a. Micro-Response to Transverse Normal Cyclic Loading in Element 52: The predictions using (1, 1, 1), (2, 1, 3), (5, 3, 8), and (50, 25, 75) increments are represented by the square, +, x, and continuous line, respectively.

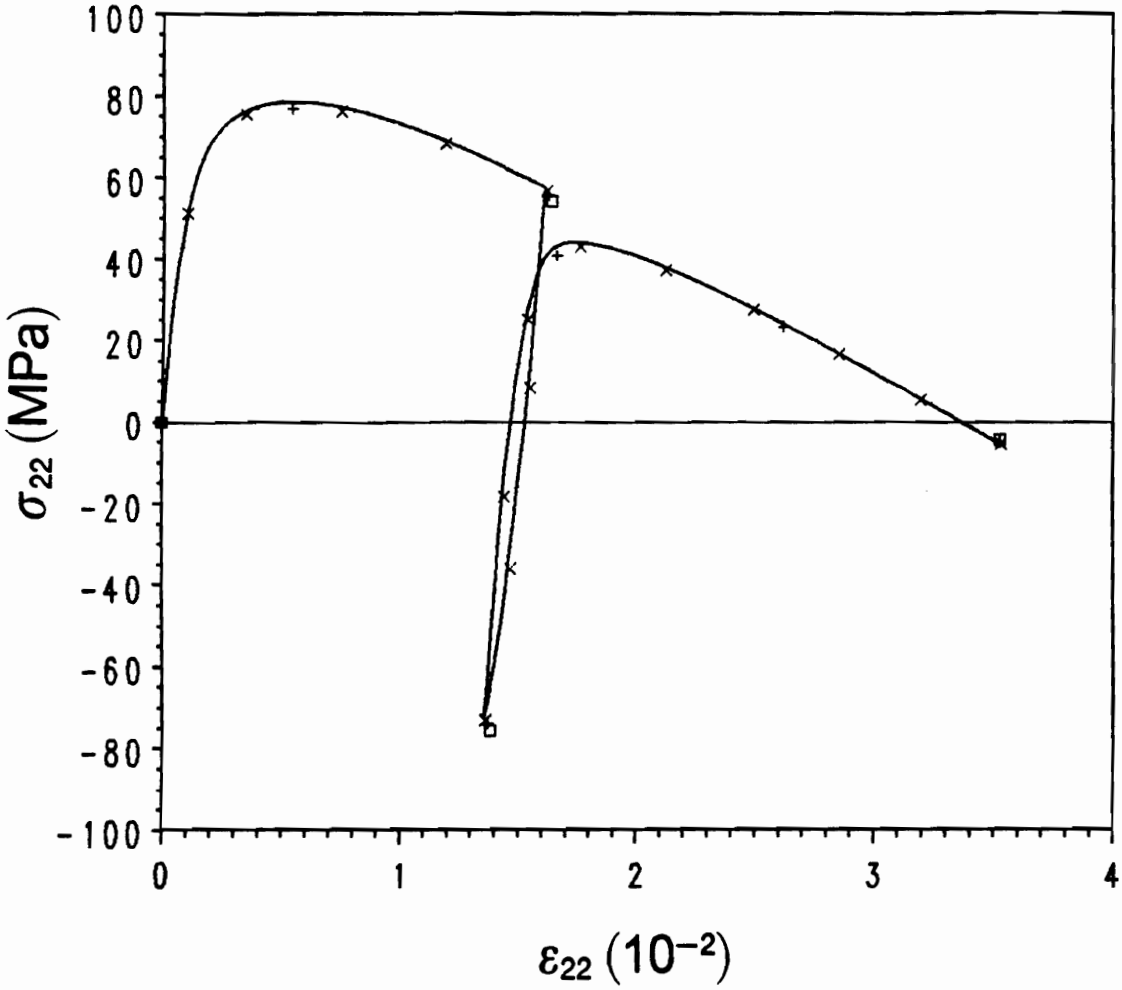

Figure 6b. Micro-Response to Transverse Normal Cyclic Loading in Element 52: The predictions using (1, 1, 1), (2, 1, 3), (5, 3, 8), and (50, 25, 75) increments are represented by the square, +, x, and continuous line, respectively.

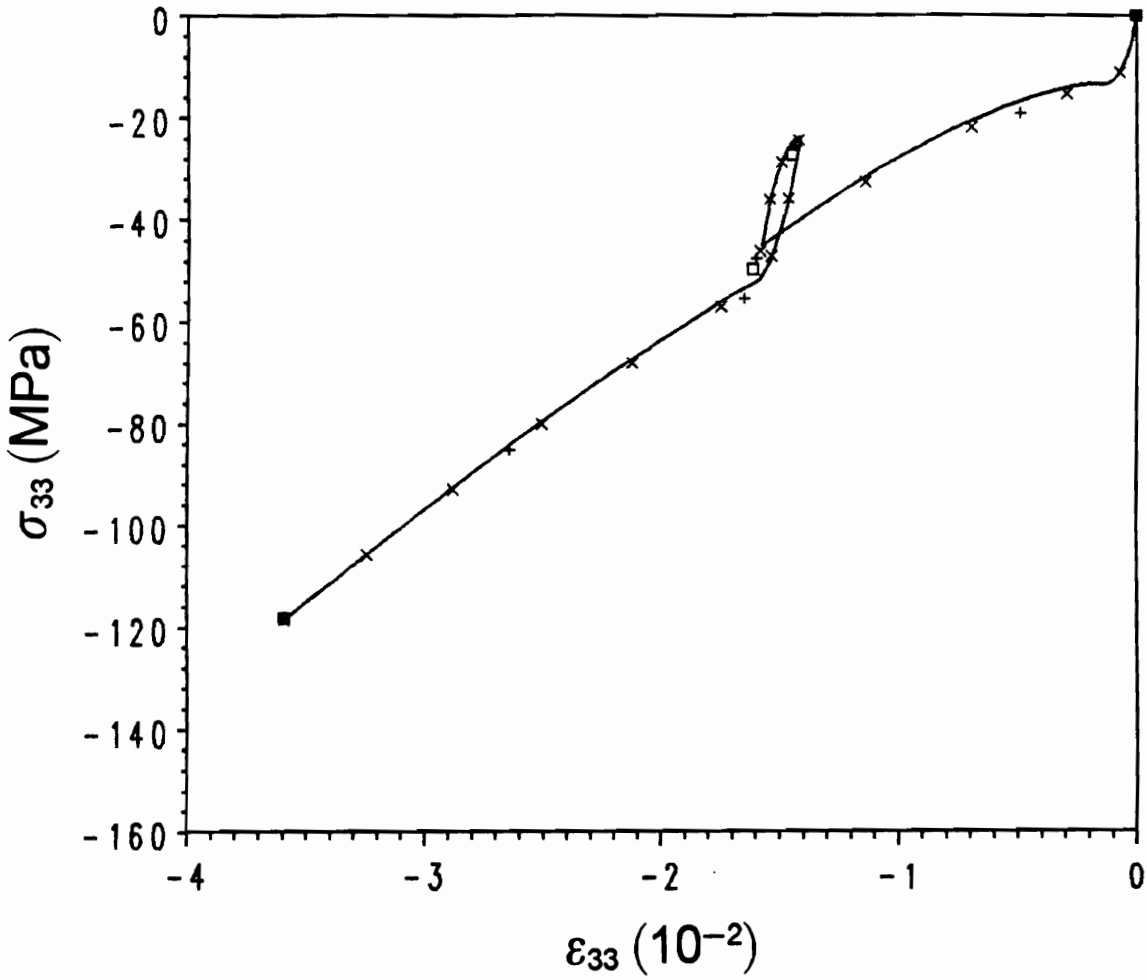

Figure 6c. Micro-Response to Transverse Normal Cyclic Loading in Element 52: The predictions using (1, 1, 1), (2, 1, 3), (5, 3, 8), and (50, 25, 75) increments are represented by the square, +, x, and continuous line, respectively.

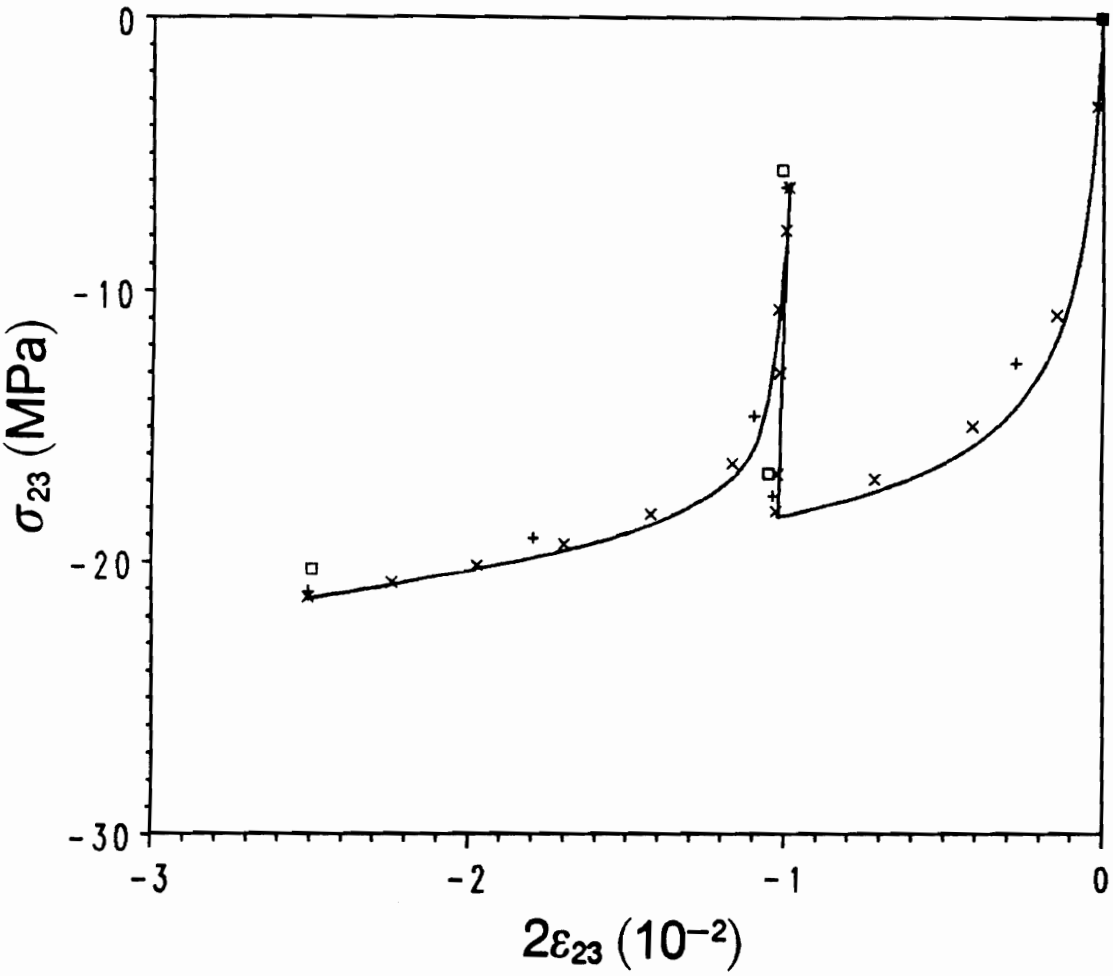

Figure 6d. Micro-Response to Transverse Normal Cyclic Loading in Element 52: The predictions using (1, 1, 1), (2, 1, 3), (5, 3, 8), and (50, 25, 75) increments are represented by the square, +, x, and continuous line, respectively.

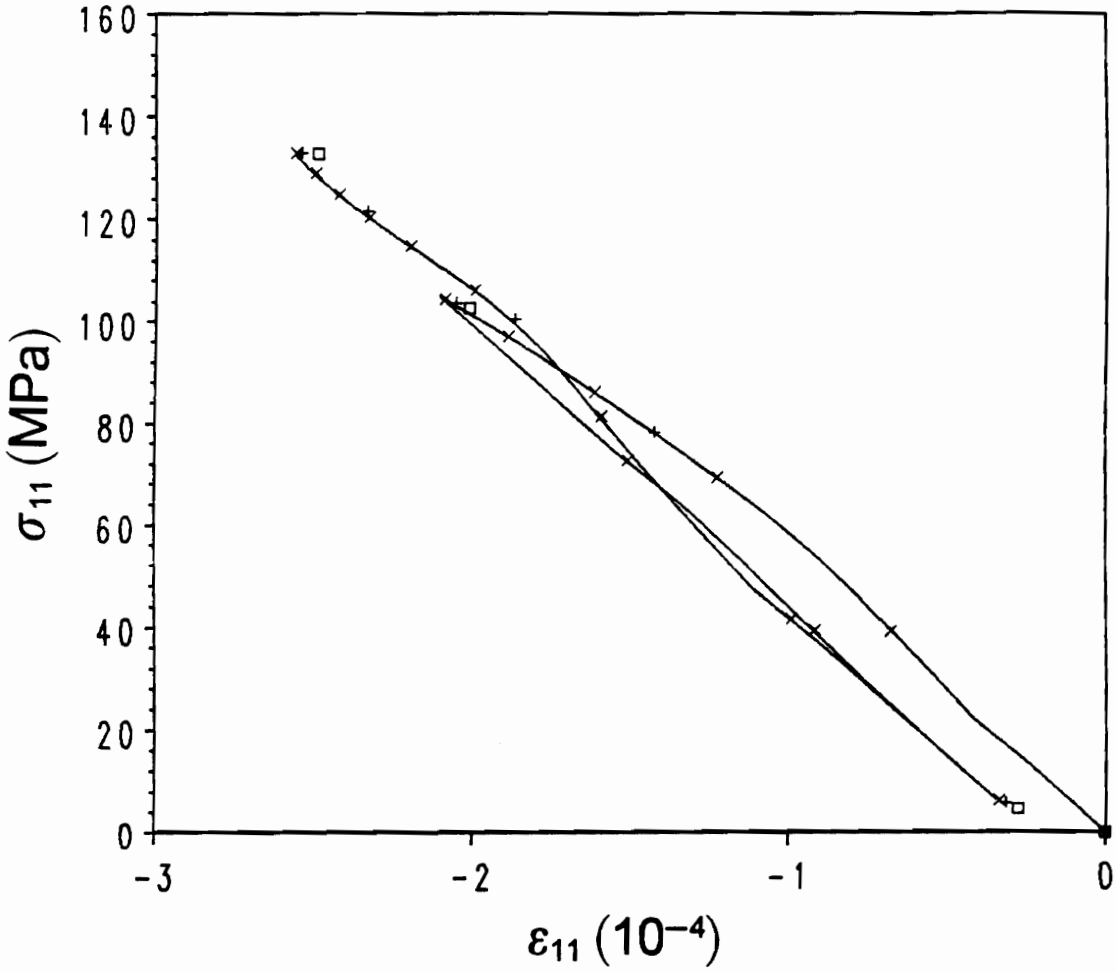

Figure 7a. Micro-Response to Transverse Normal Cyclic Loading in Element 72: The predictions using (1, 1, 1), (2, 1, 3), (5, 3, 8), and (50, 25, 75) increments are represented by the square, +, x, and continuous line, respectively.

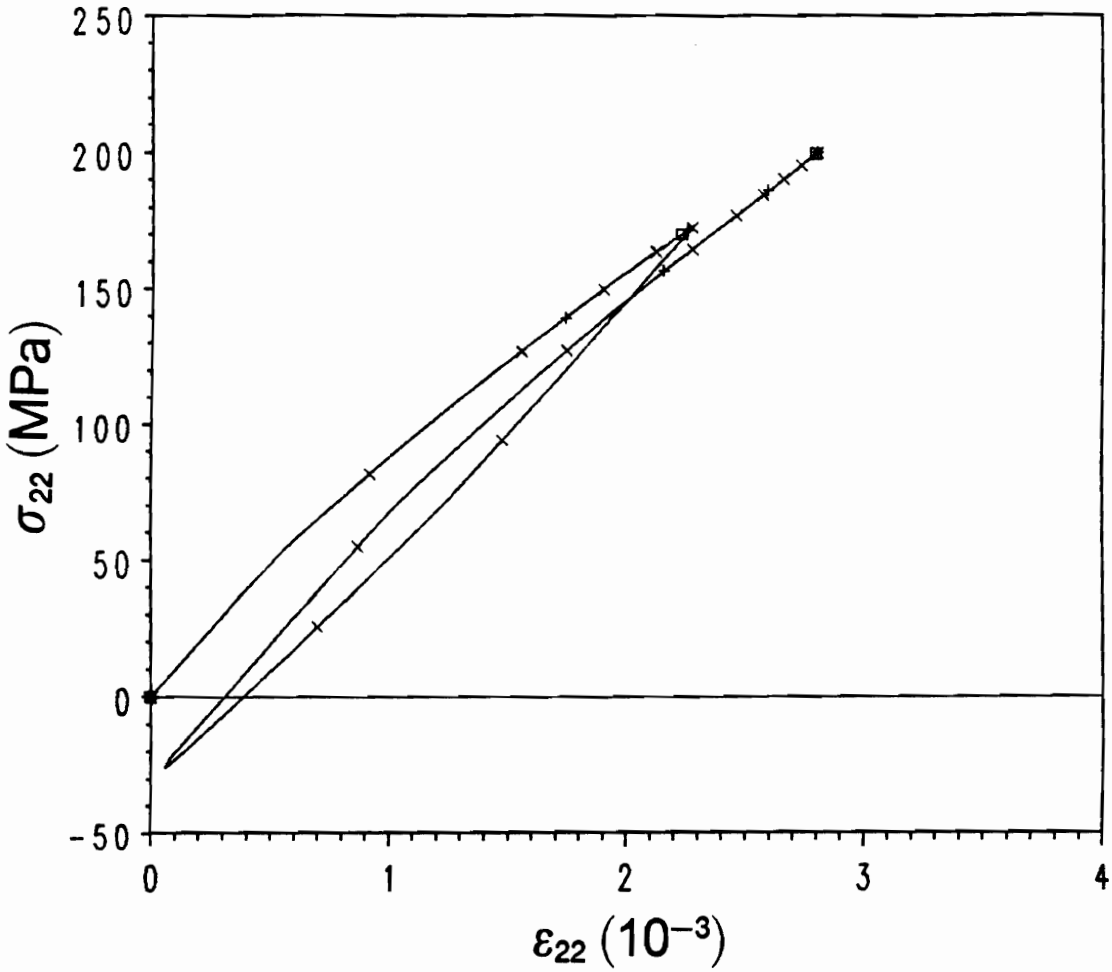

Figure 7b. Micro-Response to Transverse Normal Cyclic Loading in Element 72: The predictions using (1, 1, 1), (2, 1, 3), (5, 3, 8), and (50, 25, 75) increments are represented by the square, +, x, and continuous line, respectively.

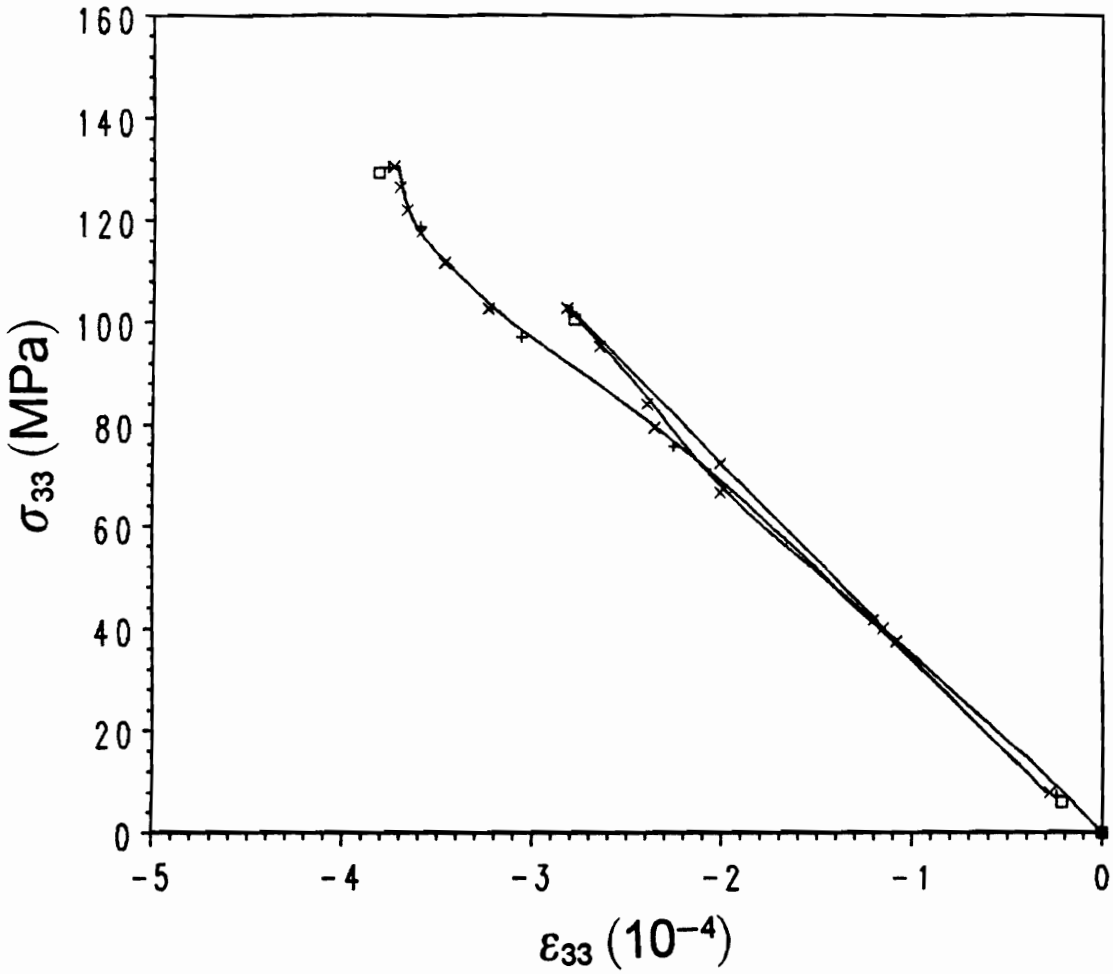

Figure 7c. Micro-Response to Transverse Normal Cyclic Loading in Element 72: The predictions using (1, 1, 1), (2, 1, 3), (5, 3, 8), and (50, 25, 75) increments are represented by the square, +, x, and continuous line, respectively.

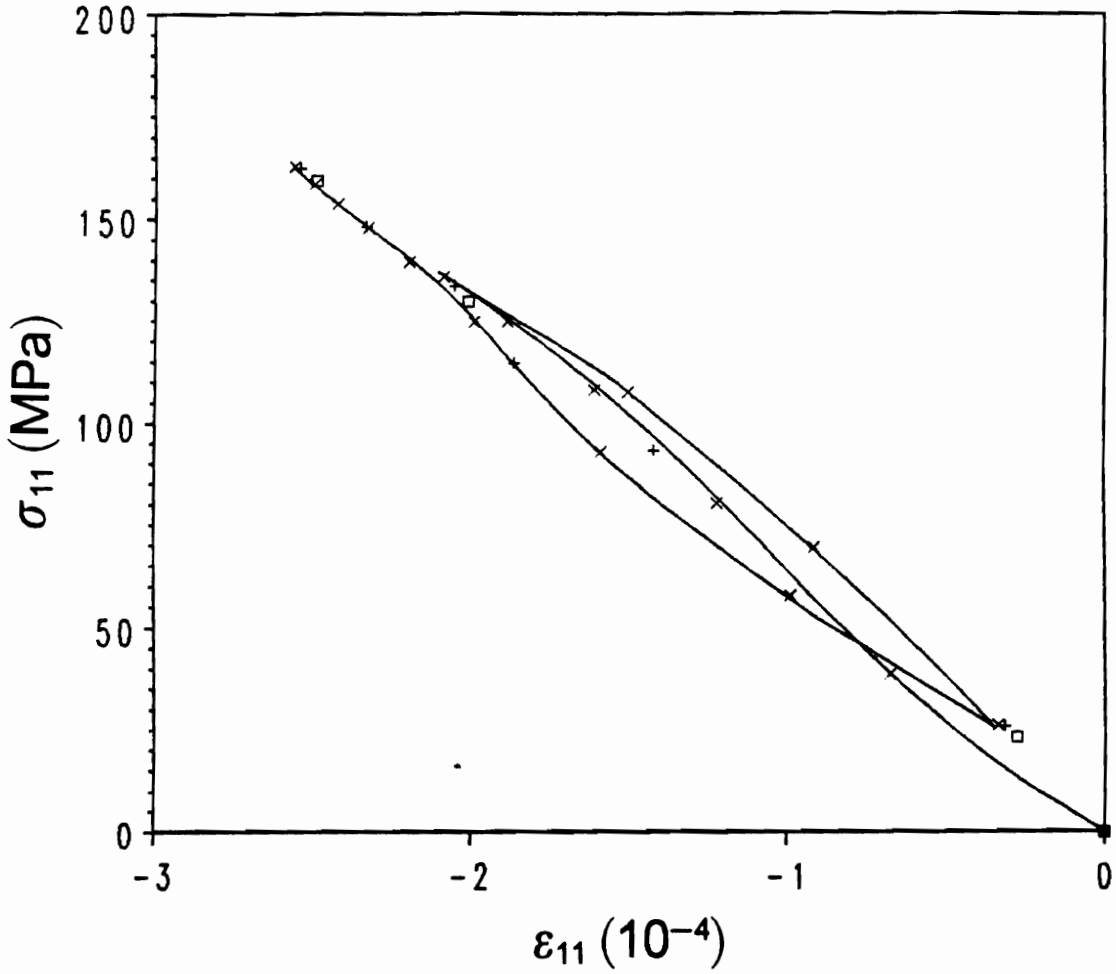

Figure 8a. Micro-Response to Transverse Normal Cyclic Loading in Element 216: The predictions using (1, 1, 1), (2, 1, 3), (5, 3, 8), and (50, 25, 75) increments are represented by the square, +, x, and continuous line, respectively.

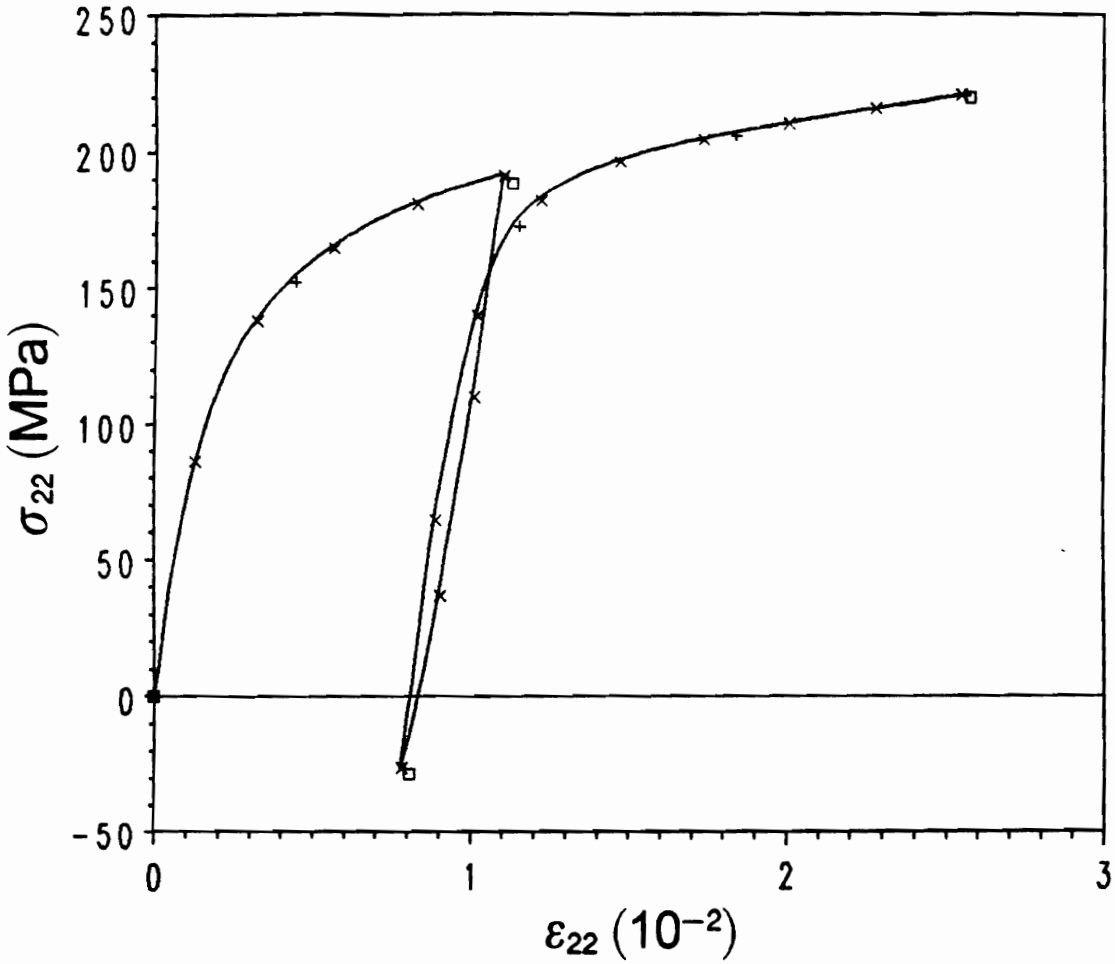

Figure 8b. Micro-Response to Transverse Normal Cyclic Loading in Element 216: The predictions using (1, 1, 1), (2, 1, 3), (5, 3, 8), and (50, 25, 75) increments are represented by the square, +, x, and continuous line, respectively.

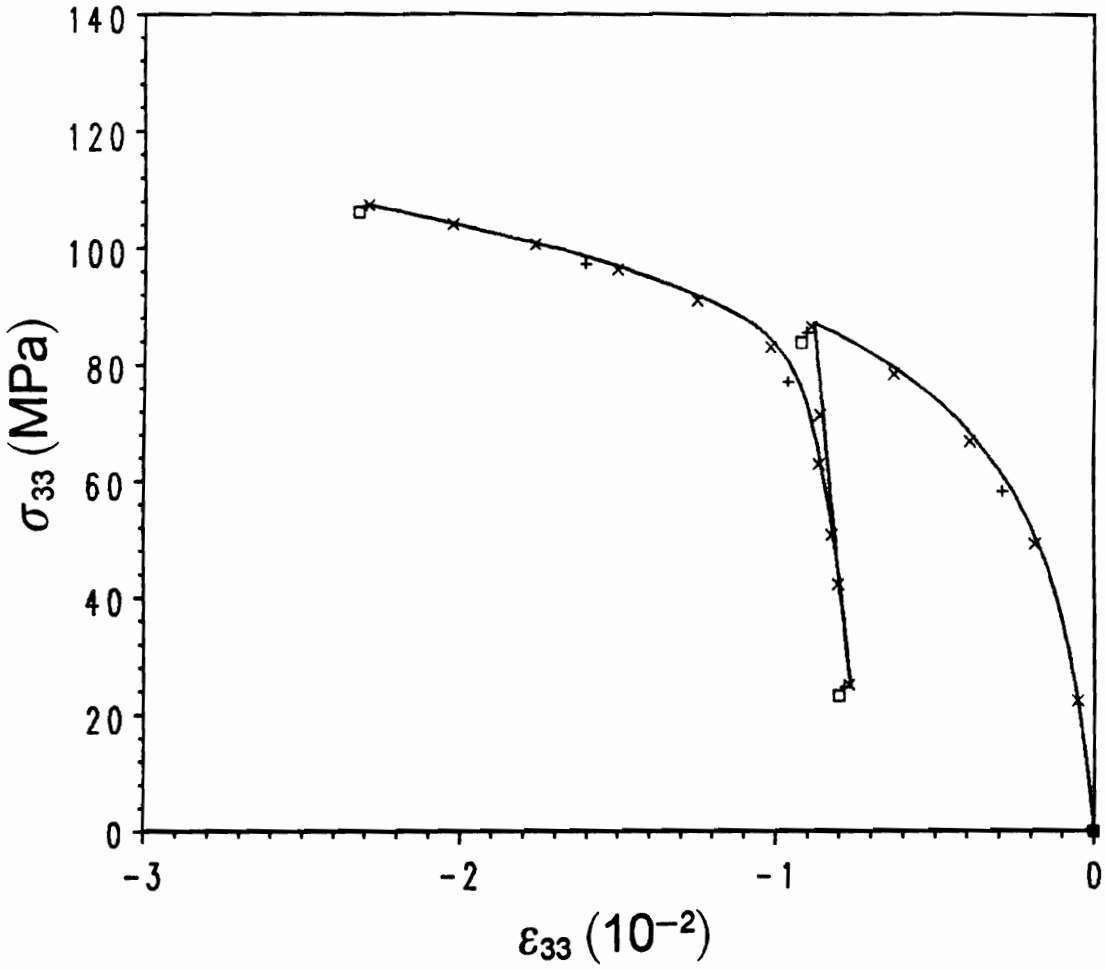

Figure 8c. Micro-Response to Transverse Normal Cyclic Loading in Element 216: The predictions using (1, 1, 1), (2, 1, 3), (5, 3, 8), and (50, 25, 75) increments are represented by the square, +, x, and continuous line, respectively.

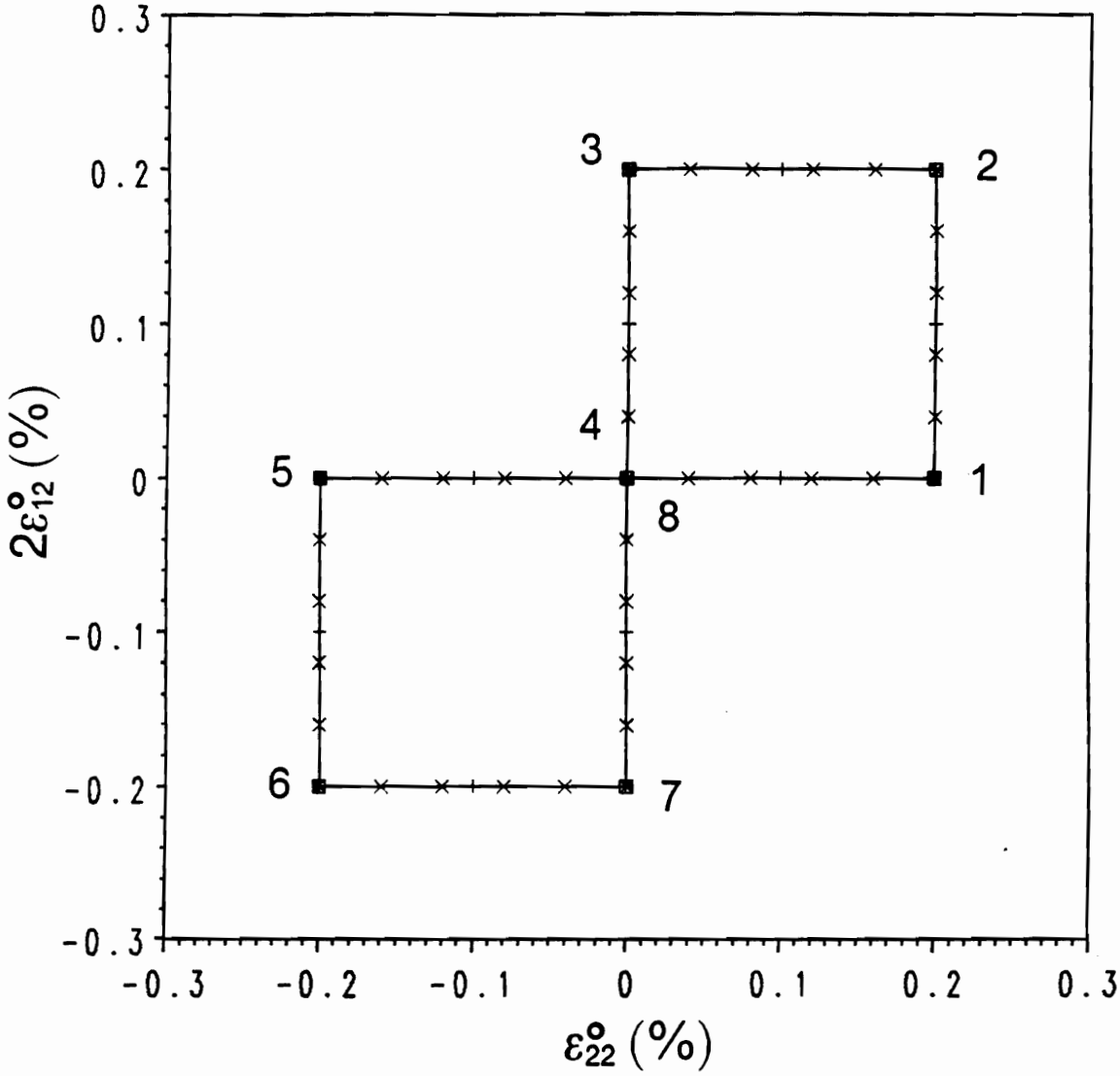

Figure 9. Transverse-Normal Longitudinal-Shear Cyclic Loading Path: The loading path was traced for the cases of 1, 2, 5, and 50 increments/segment as represented by the square, +, x, and continuous line, respectively.

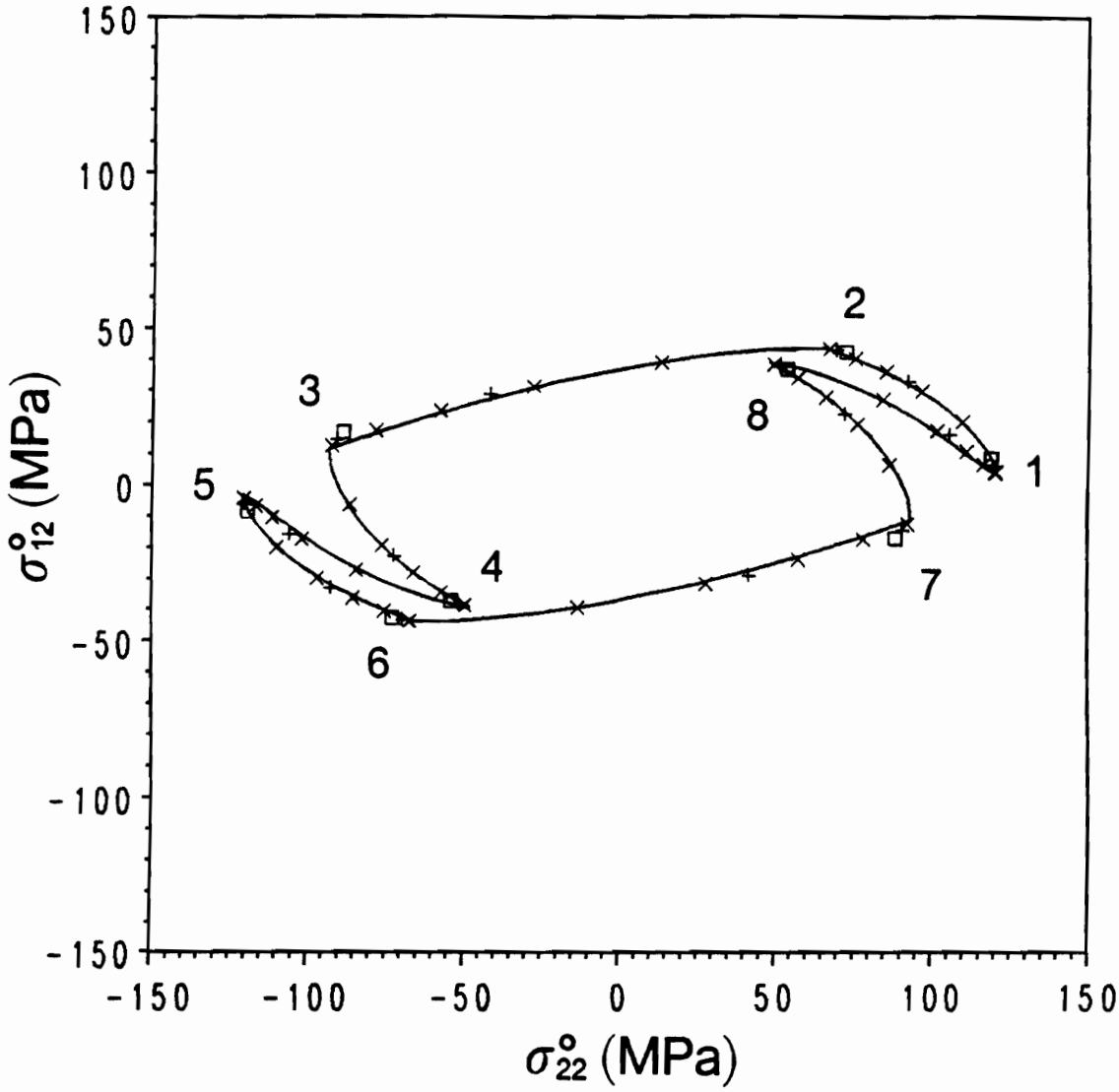

Figure 10a. Macro-Response to Transverse-Normal Longitudinal-Shear Cyclic Loading: The predictions using 1, 2, 5, and 50 increments/segment are represented by the square, +, x, and continuous line, respectively.

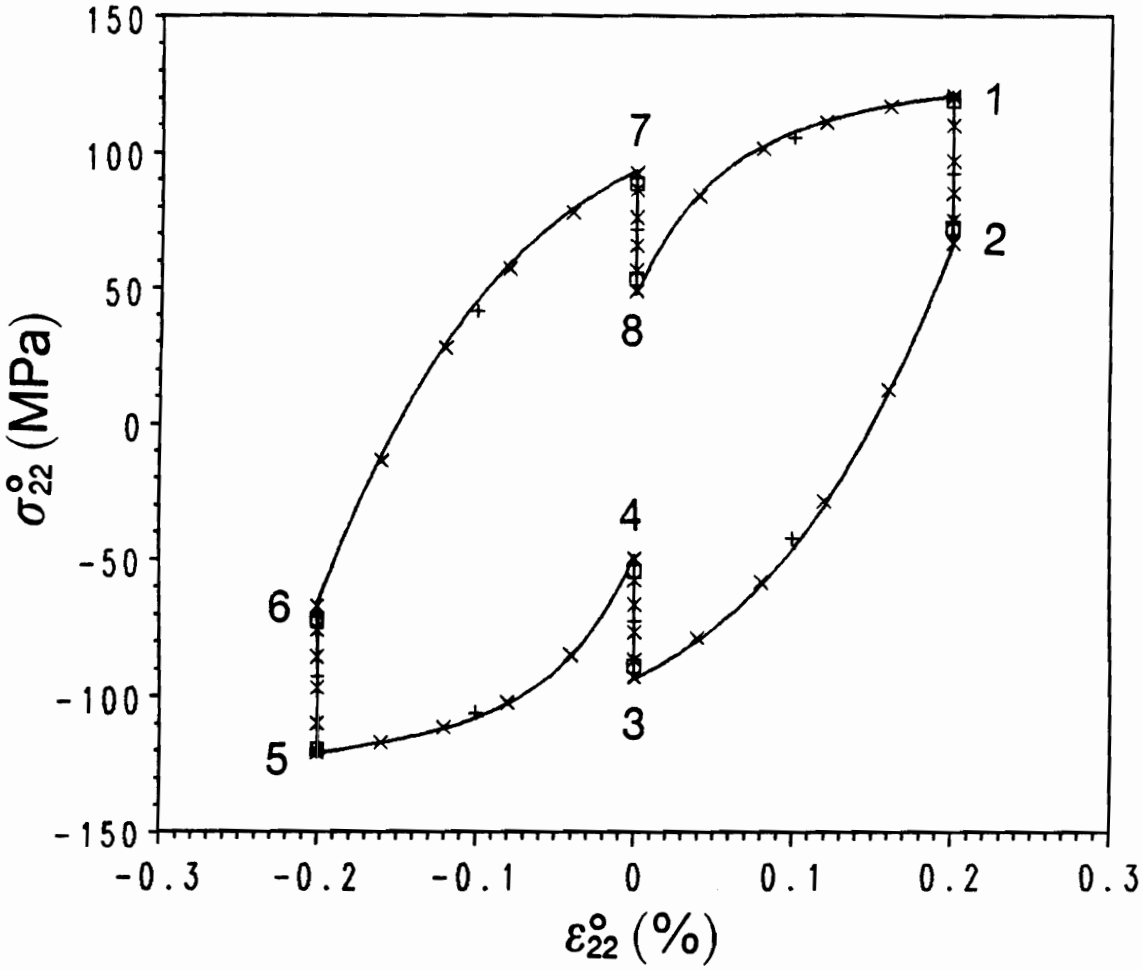

Figure 10b. Macro-Response to Transverse-Normal Longitudinal-Shear Cyclic Loading: The predictions using 1, 2, 5, and 50 increments/segment are represented by the square, +, x, and continuous line, respectively.

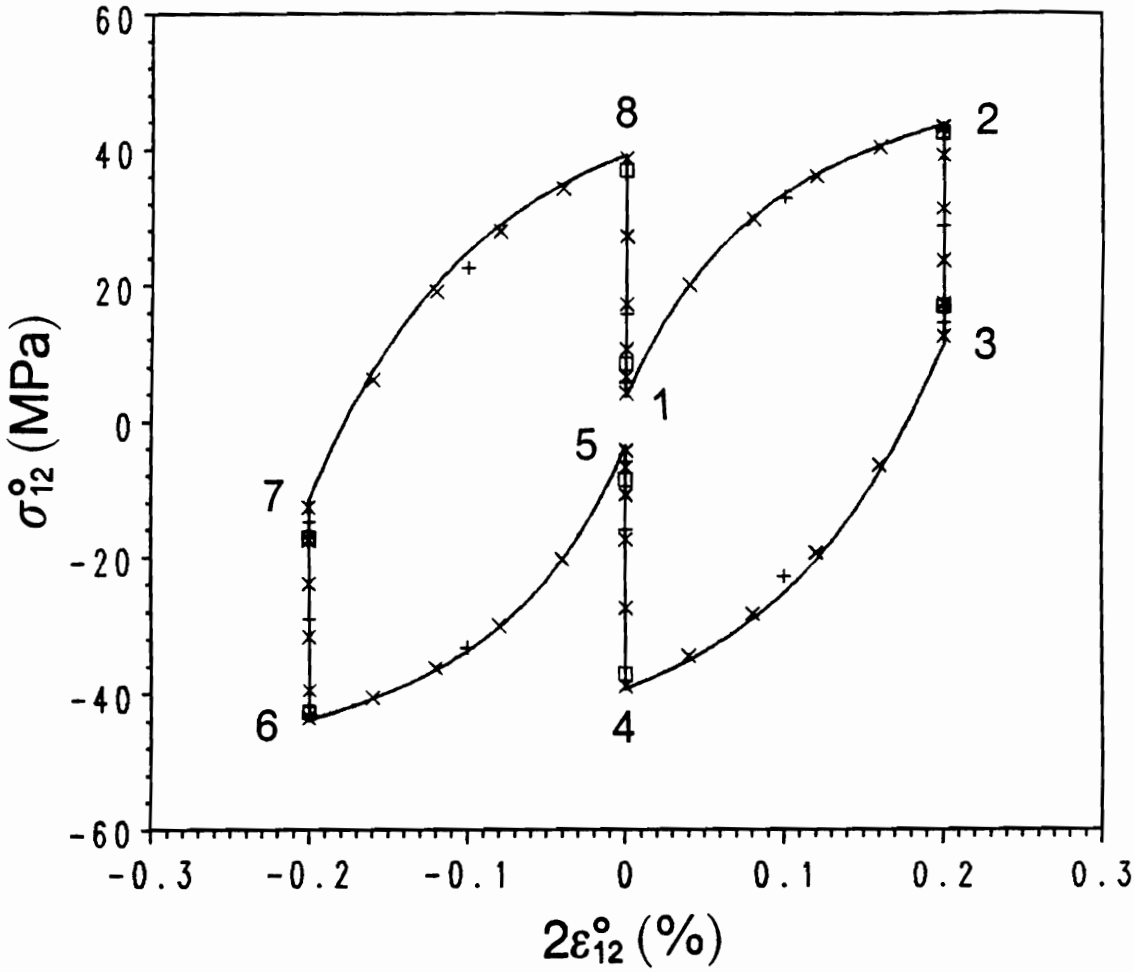

Figure 10c. Macro-Response to Transverse-Normal Longitudinal-Shear Cyclic Loading: The predictions using 1, 2, 5, and 50 increments/segment are represented by the square, +, x, and continuous line, respectively.

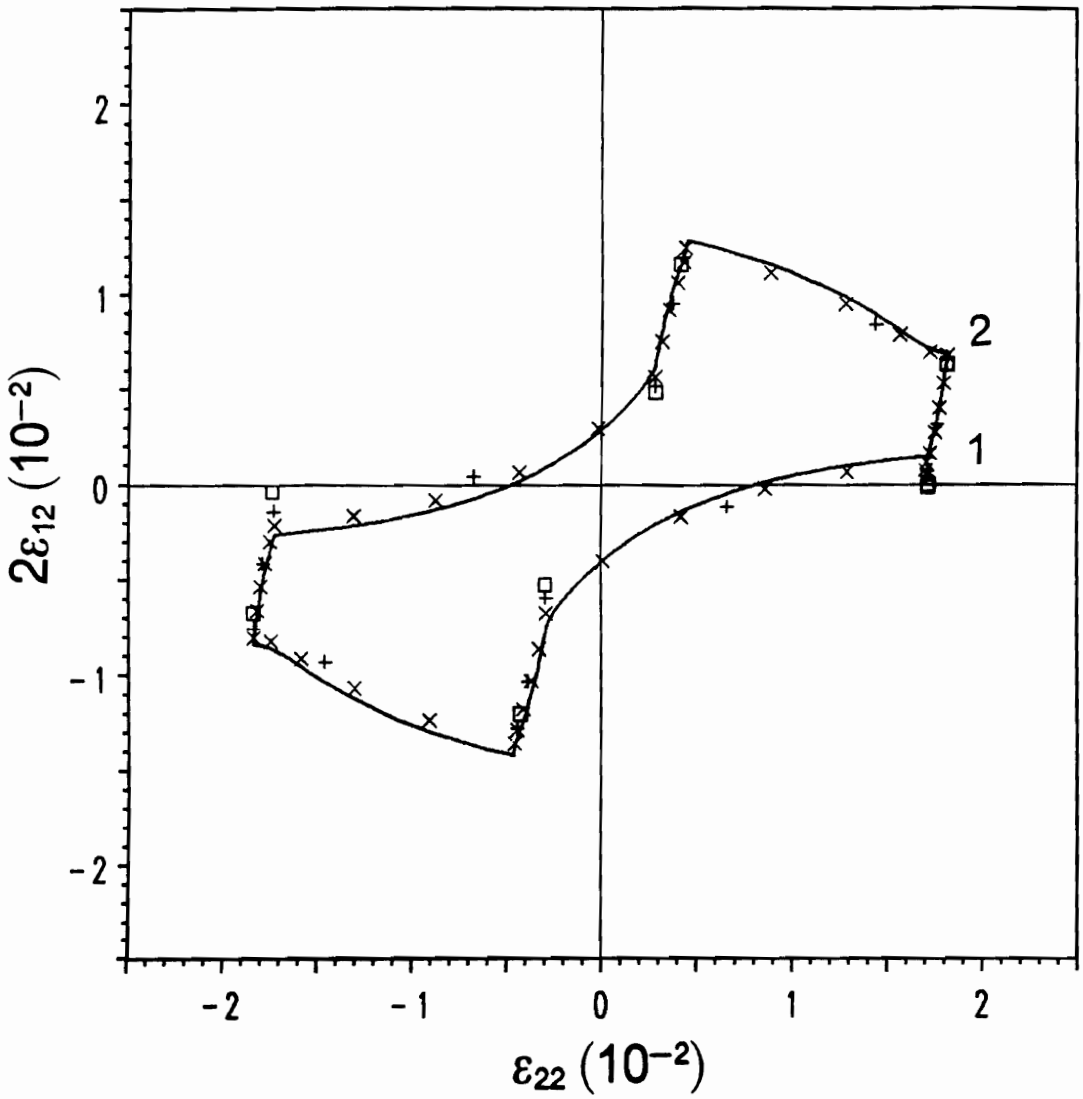

Figure 11a. Micro-Response to Transverse-Normal Longitudinal-Shear Cyclic Loading in Element 52: The predictions using 1, 2, 5, and 50 increments/segment are represented by the square, +, x, and continuous line, respectively.

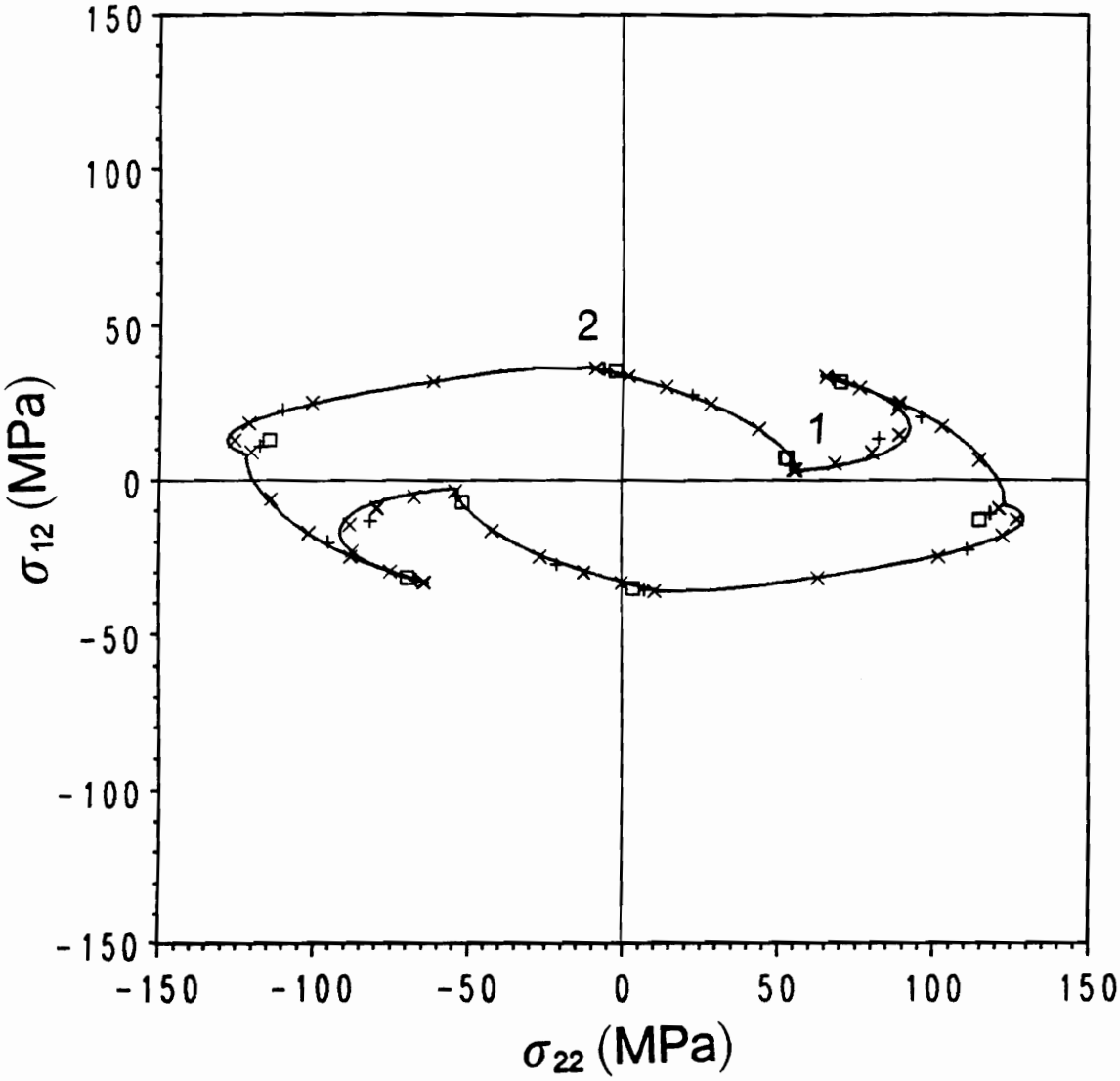

Figure 11b. Micro-Response to Transverse-Normal Longitudinal-Shear Cyclic Loading in Element 52: The predictions using 1, 2, 5, and 50 increments/segment are represented by the square, +, x, and continuous line, respectively.

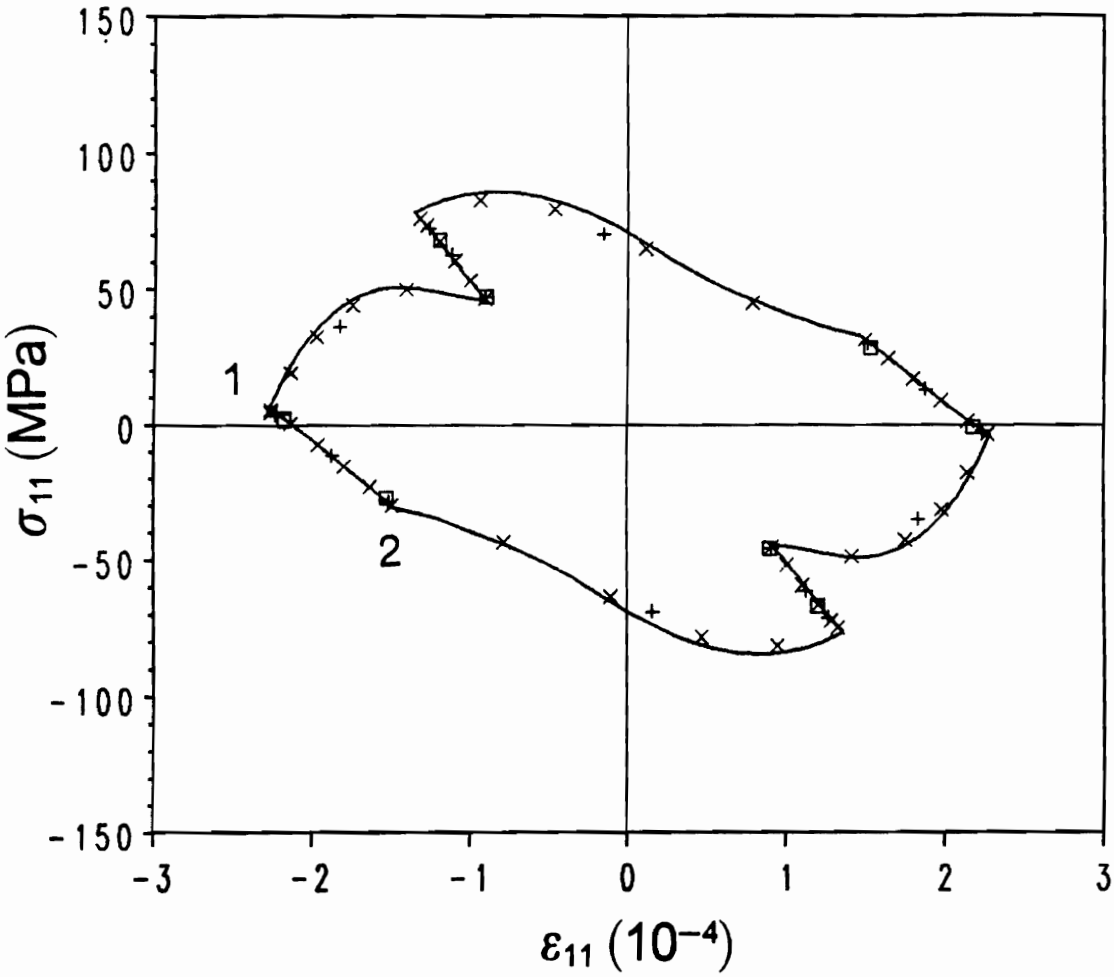

Figure 11c. Micro-Response to Transverse-Normal Longitudinal-Shear Cyclic Loading in Element 52: The predictions using 1, 2, 5, and 50 increments/segment are represented by the square, +, x, and continuous line, respectively.

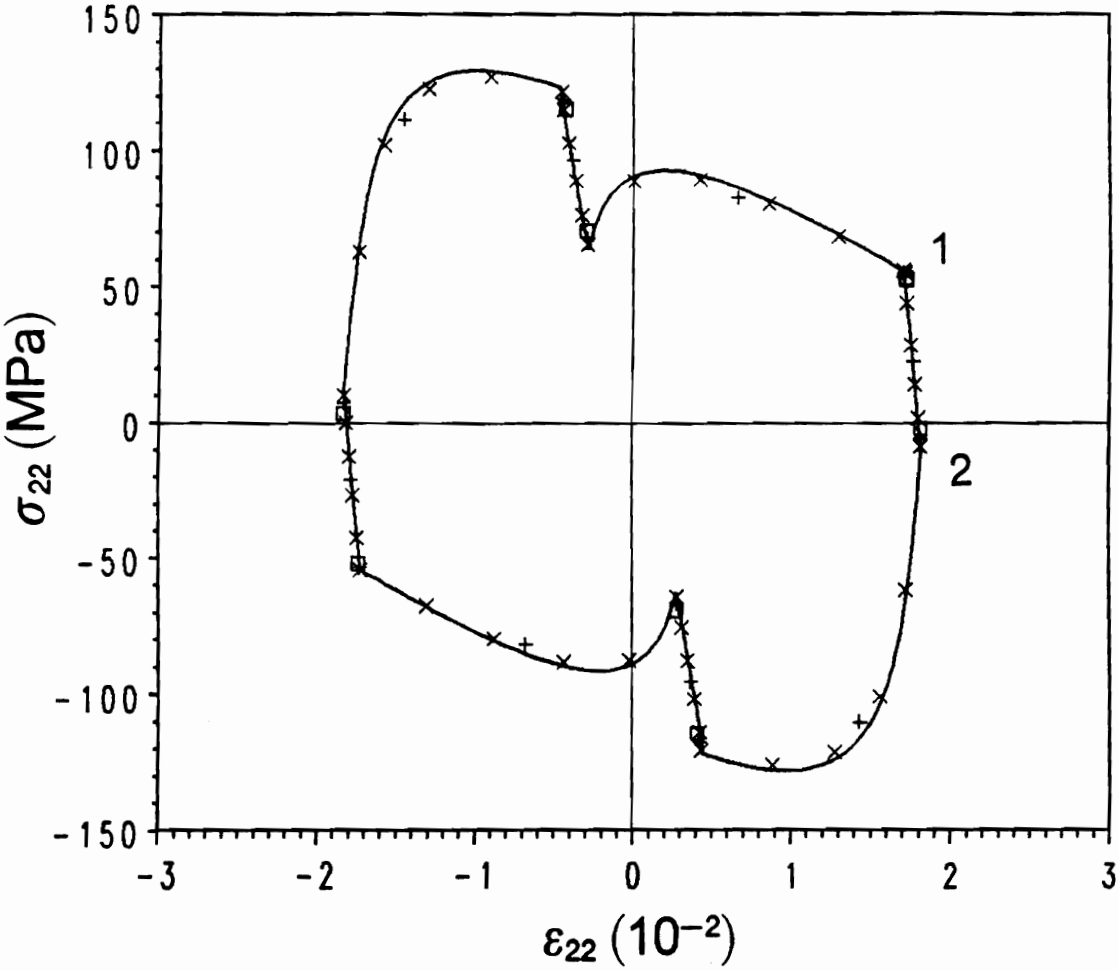

Figure 11d. Micro-Response to Transverse-Normal Longitudinal-Shear Cyclic Loading in Element 52: The predictions using 1, 2, 5, and 50 increments/segment are represented by the square, +, x, and continuous line, respectively.

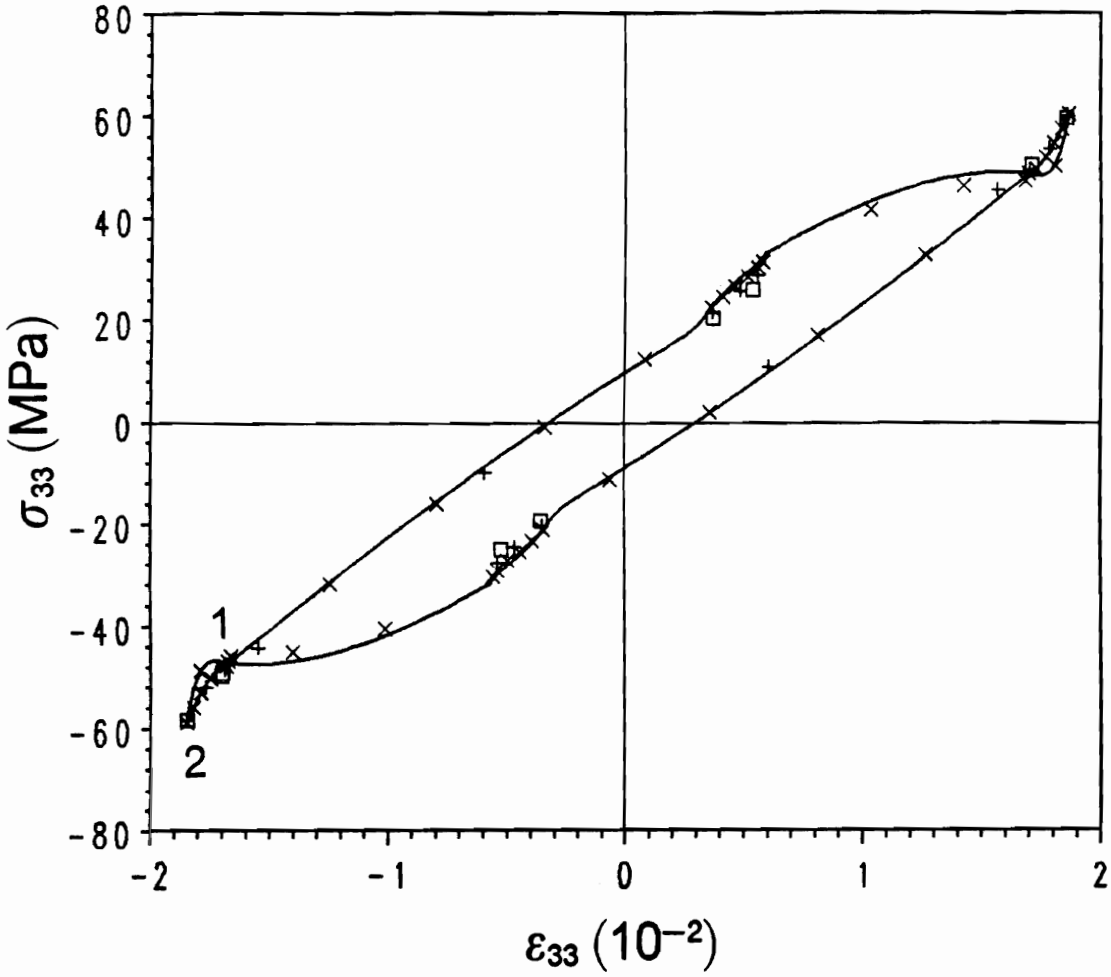

Figure 11e. Micro-Response to Transverse-Normal Longitudinal-Shear Cyclic Loading in Element 52: The predictions using 1, 2, 5, and 50 increments/segment are represented by the square, +, x, and continuous line, respectively.

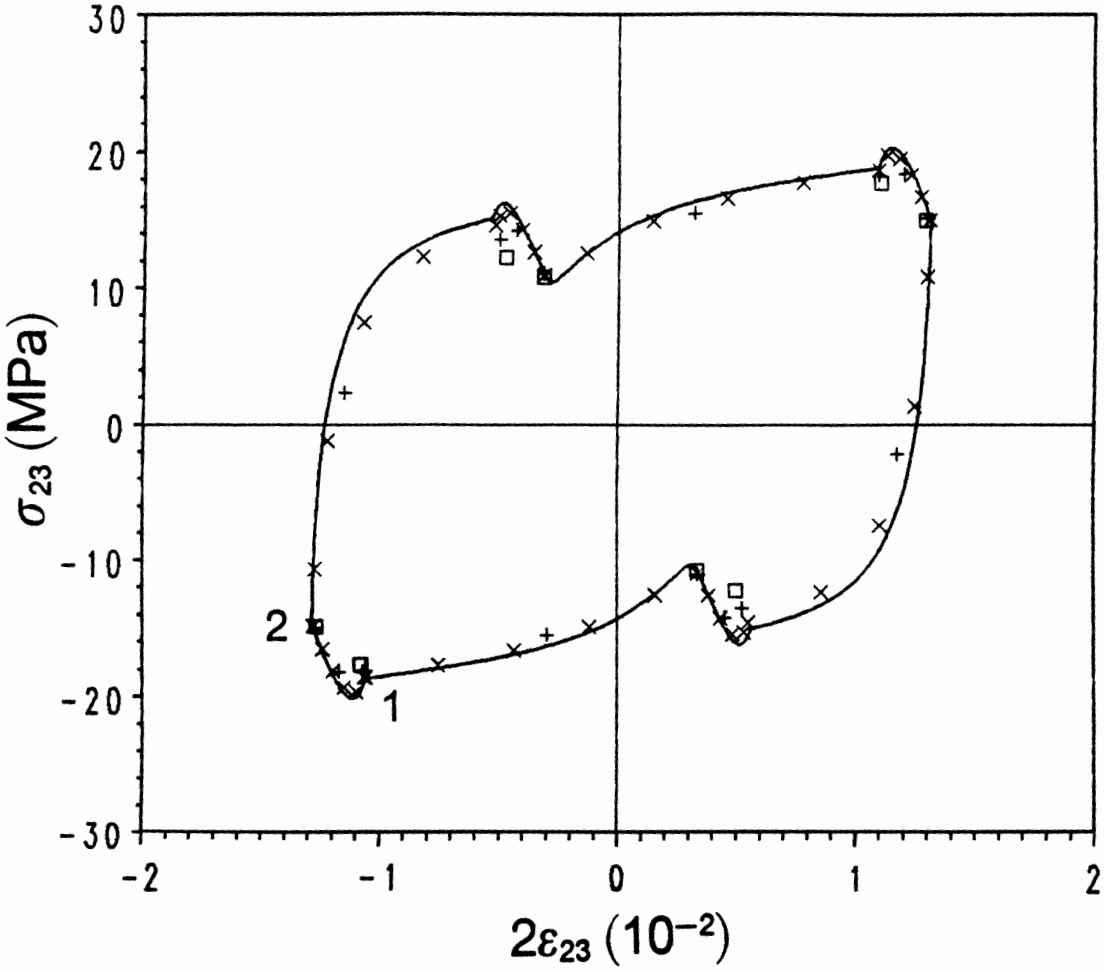

Figure 11f. Micro-Response to Transverse-Normal Longitudinal-Shear Cyclic Loading in Element 52: The predictions using 1, 2, 5, and 50 increments/segment are represented by the square, +, x, and continuous line, respectively.

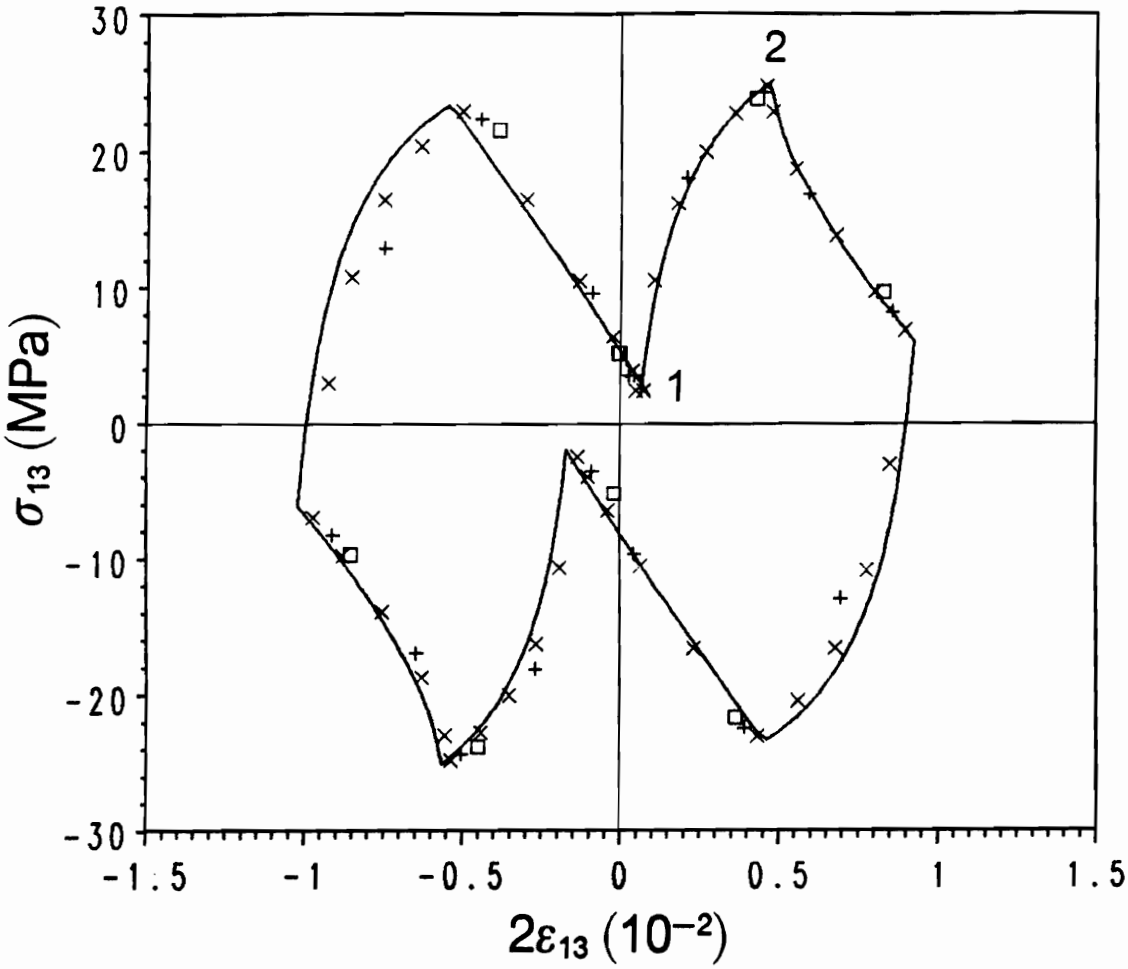

Figure 11g. Micro-Response to Transverse-Normal Longitudinal-Shear Cyclic Loading in Element 52: The predictions using 1, 2, 5, and 50 increments/segment are represented by the square, +, x, and continuous line, respectively.

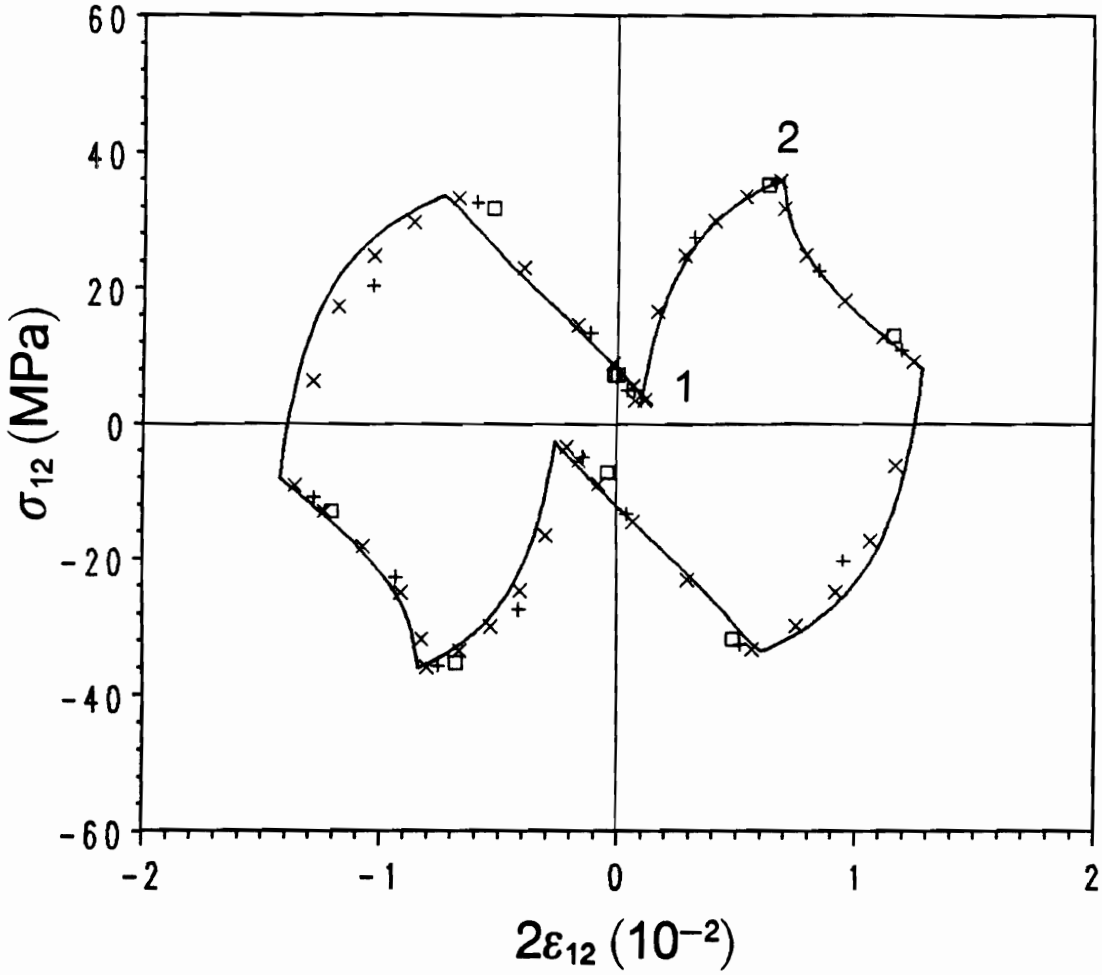

Figure 11h. Micro-Response to Transverse-Normal Longitudinal-Shear Cyclic Loading in Element 52: The predictions using 1, 2, 5, and 50 increments/segment are represented by the square, +, x, and continuous line, respectively.

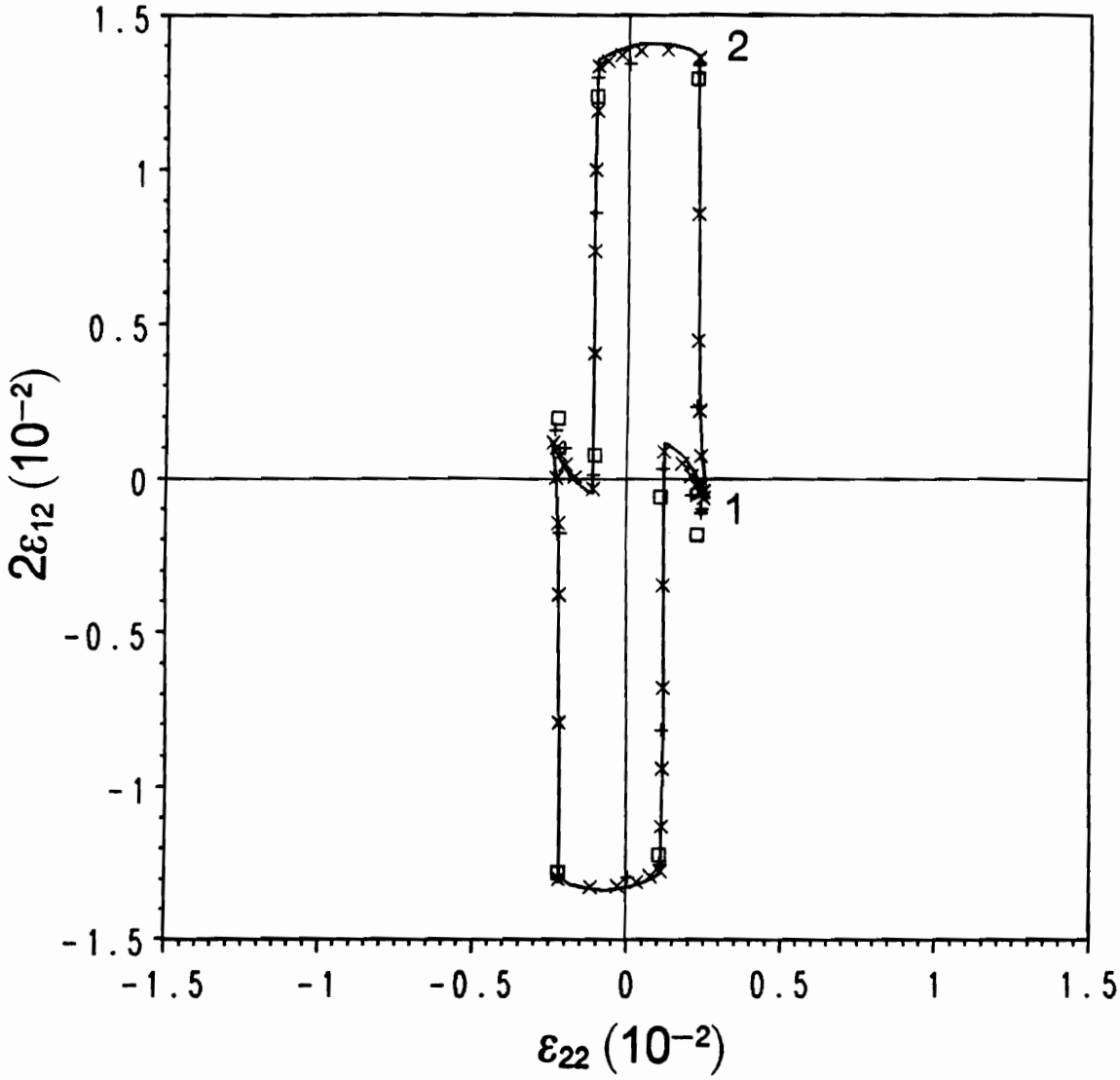

Figure 12a. Micro-Response to Transverse-Normal Longitudinal-Shear Cyclic Loading in Element 72: The predictions using 1, 2, 5, and 50 increments/segment are represented by the square, +, x, and continuous line, respectively.

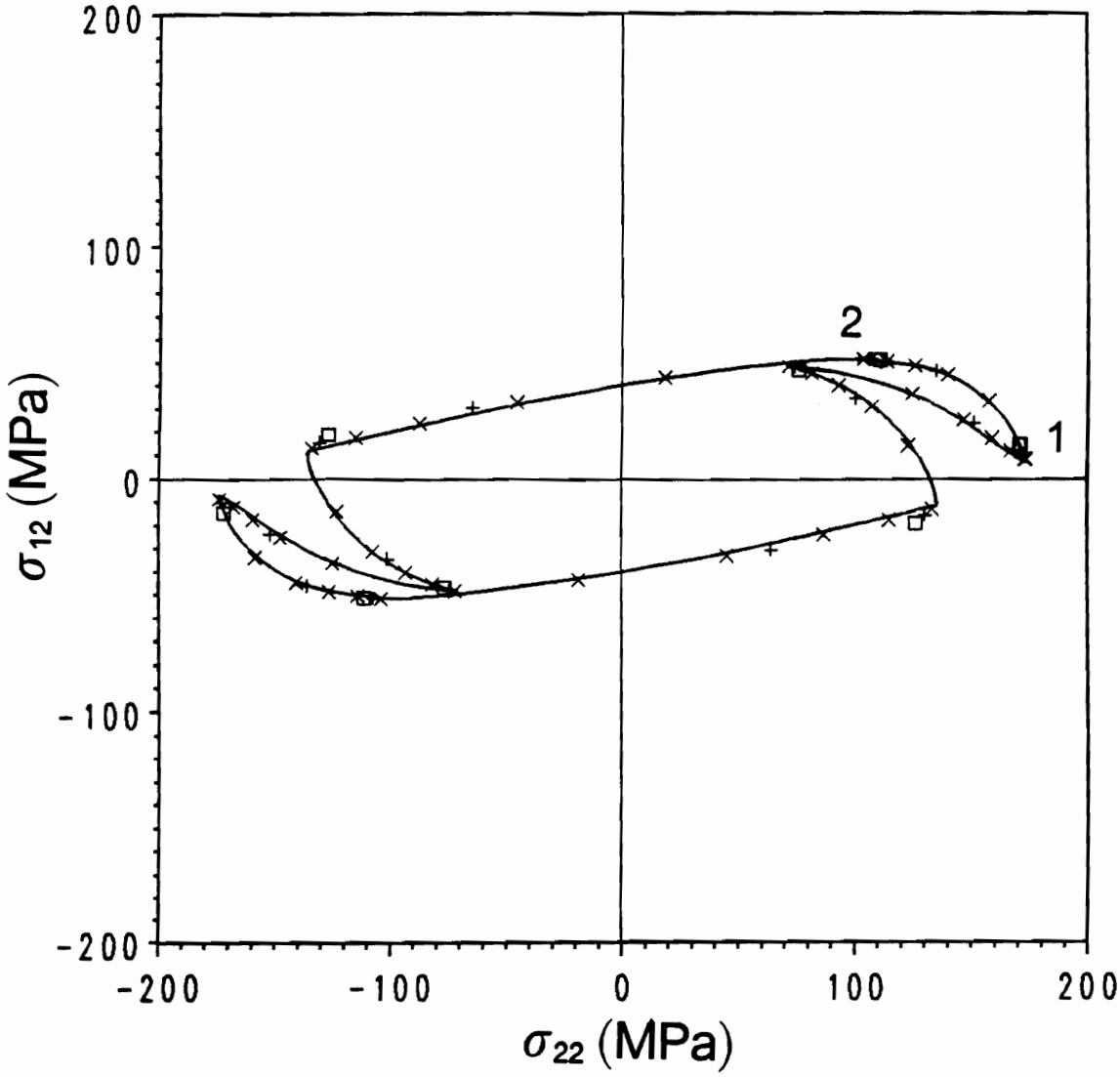

Figure 12b. Micro-Response to Transverse-Normal Longitudinal-Shear Cyclic Loading in Element 72: The predictions using 1, 2, 5, and 50 increments/segment are represented by the square, +, x, and continuous line, respectively.

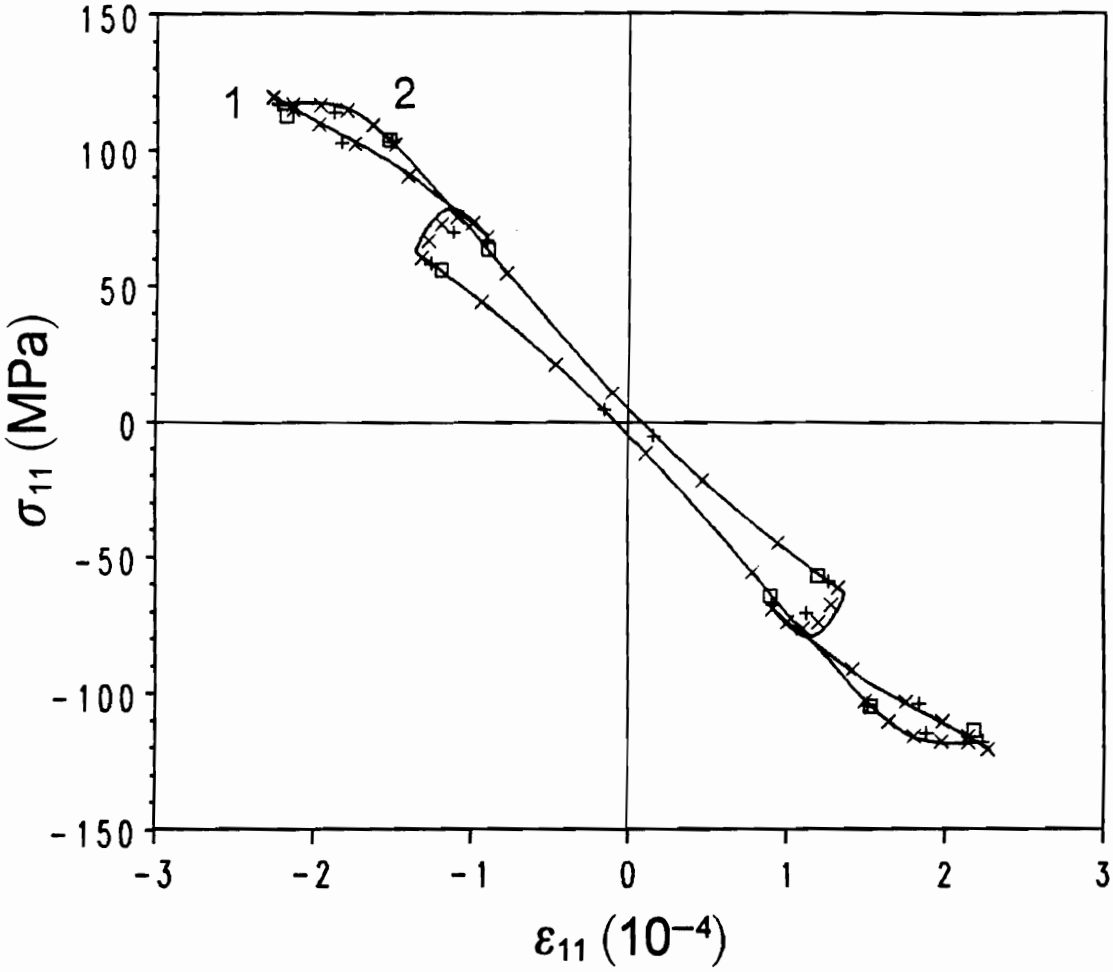

Figure 12c. Micro-Response to Transverse-Normal Longitudinal-Shear Cyclic Loading in Element 72: The predictions using 1, 2, 5, and 50 increments/segment are represented by the square, +, x, and continuous line, respectively.

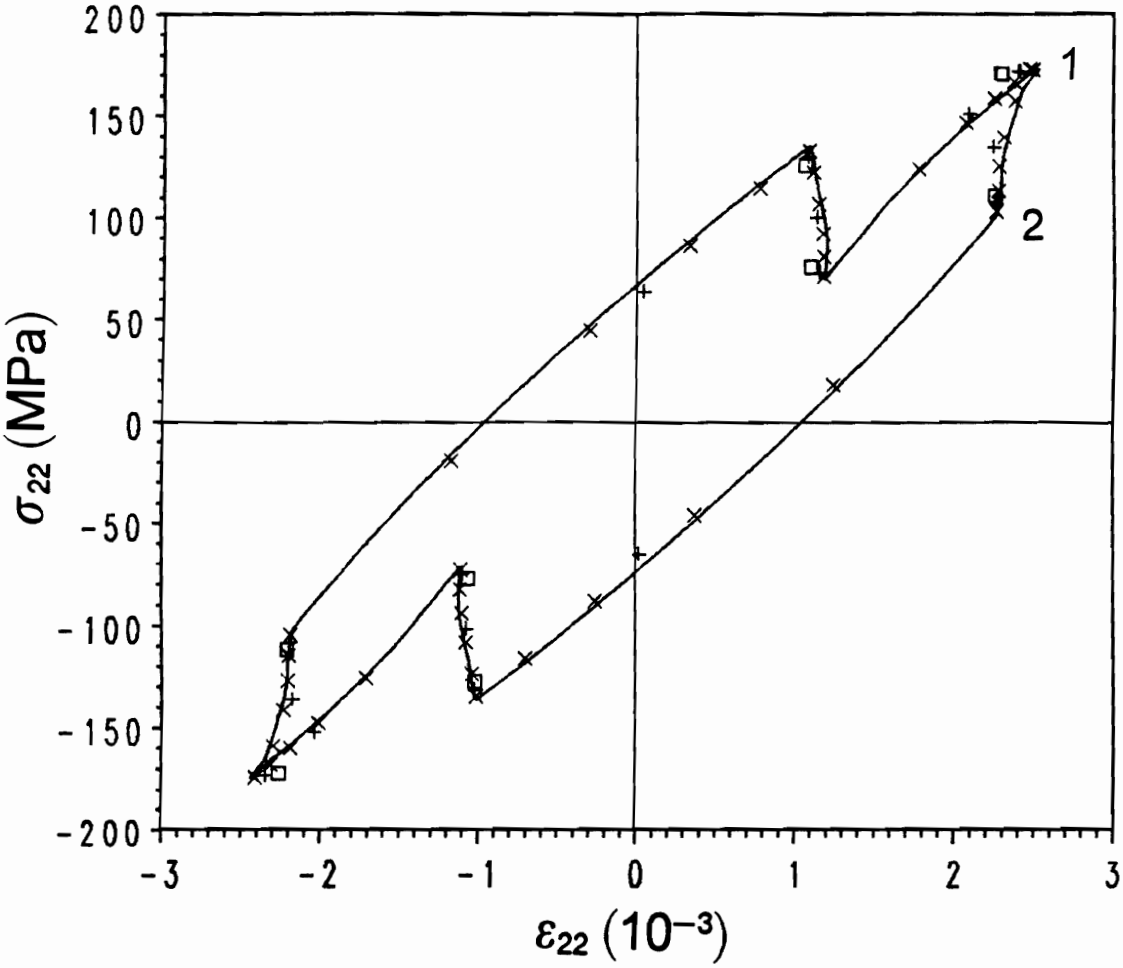

Figure 12d. Micro-Response to Transverse-Normal Longitudinal-Shear Cyclic Loading in Element 72: The predictions using 1, 2, 5, and 50 increments/segment are represented by the square, +, x, and continuous line, respectively.

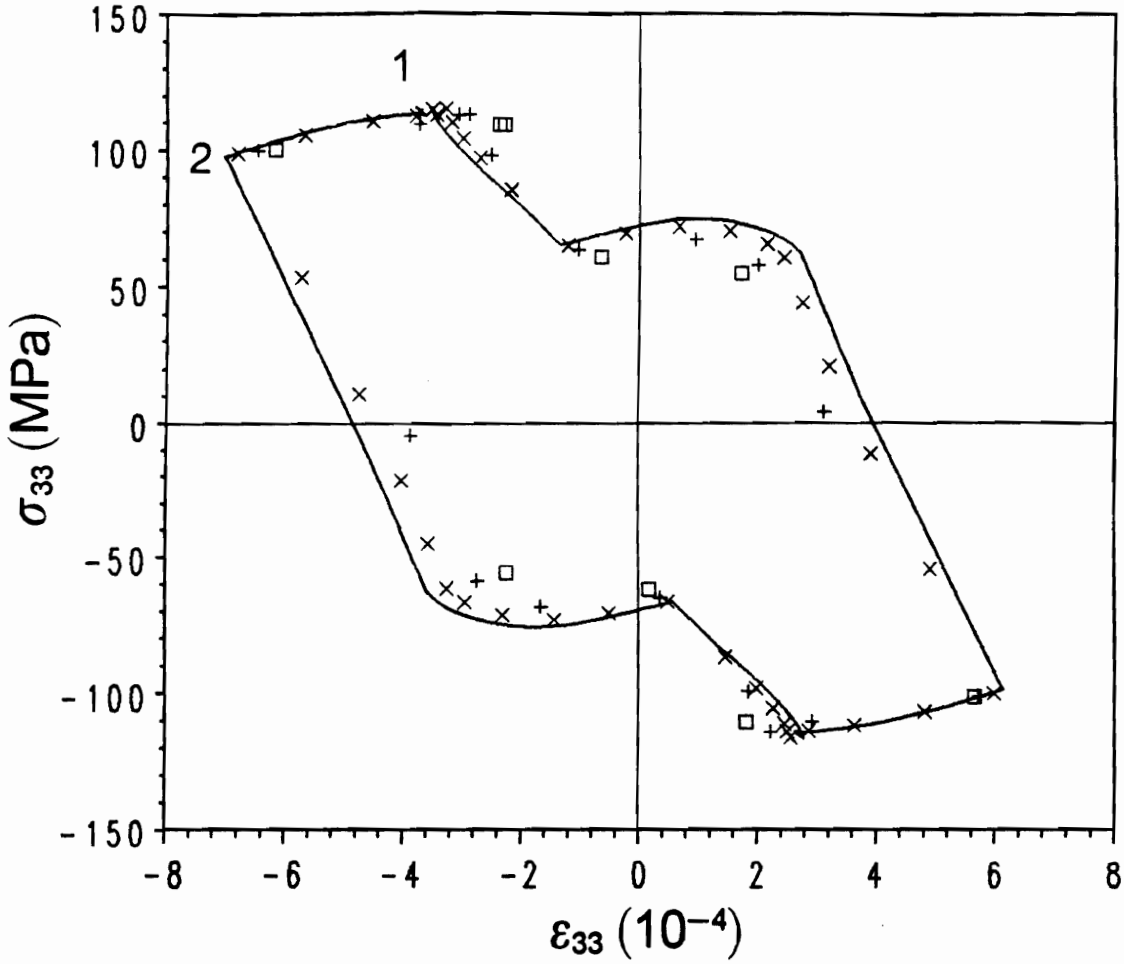

Figure 12e. Micro-Response to Transverse-Normal Longitudinal-Shear Cyclic Loading in Element 72: The predictions using 1, 2, 5, and 50 increments/segment are represented by the square, +, x, and continuous line, respectively.

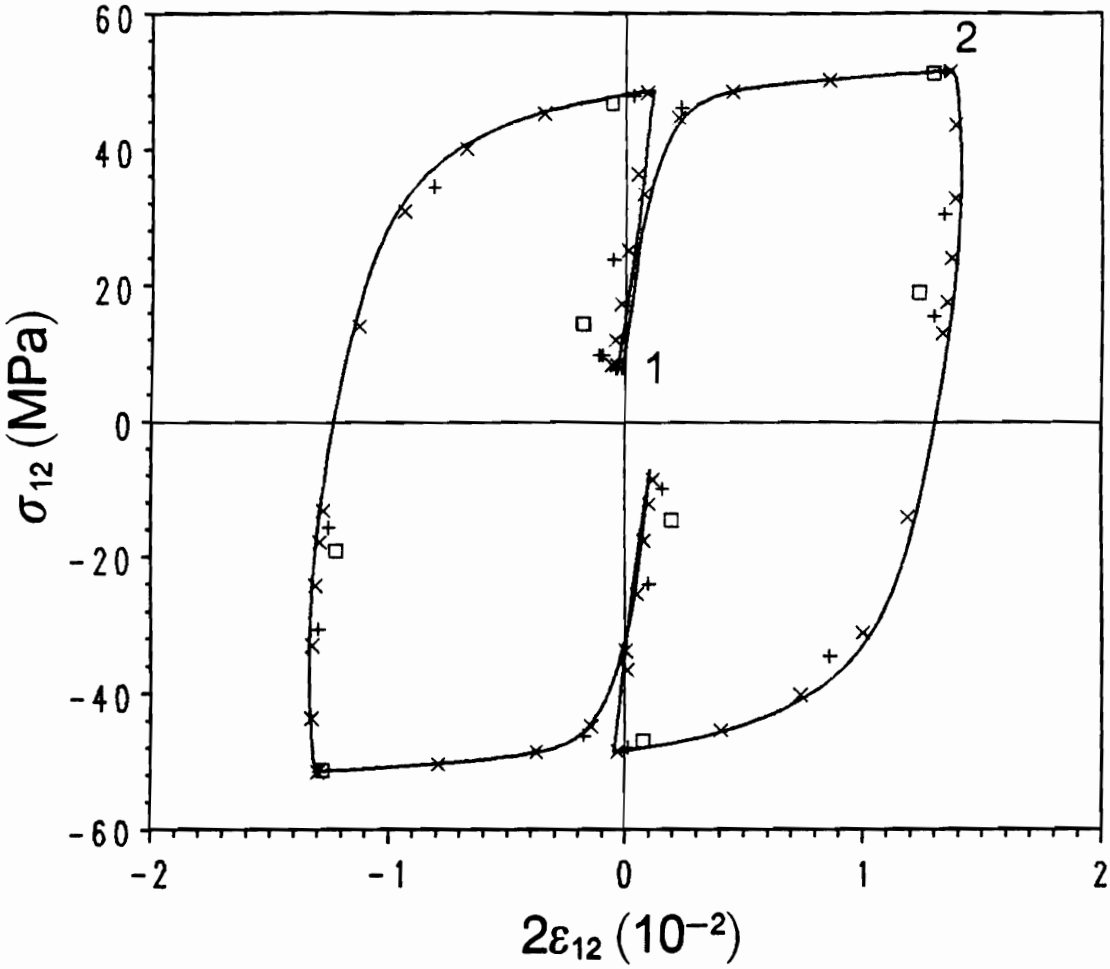

Figure 12f. Micro-Response to Transverse-Normal Longitudinal-Shear Cyclic Loading in Element 72: The predictions using 1, 2, 5, and 50 increments/segment are represented by the square, +, x, and continuous line, respectively.

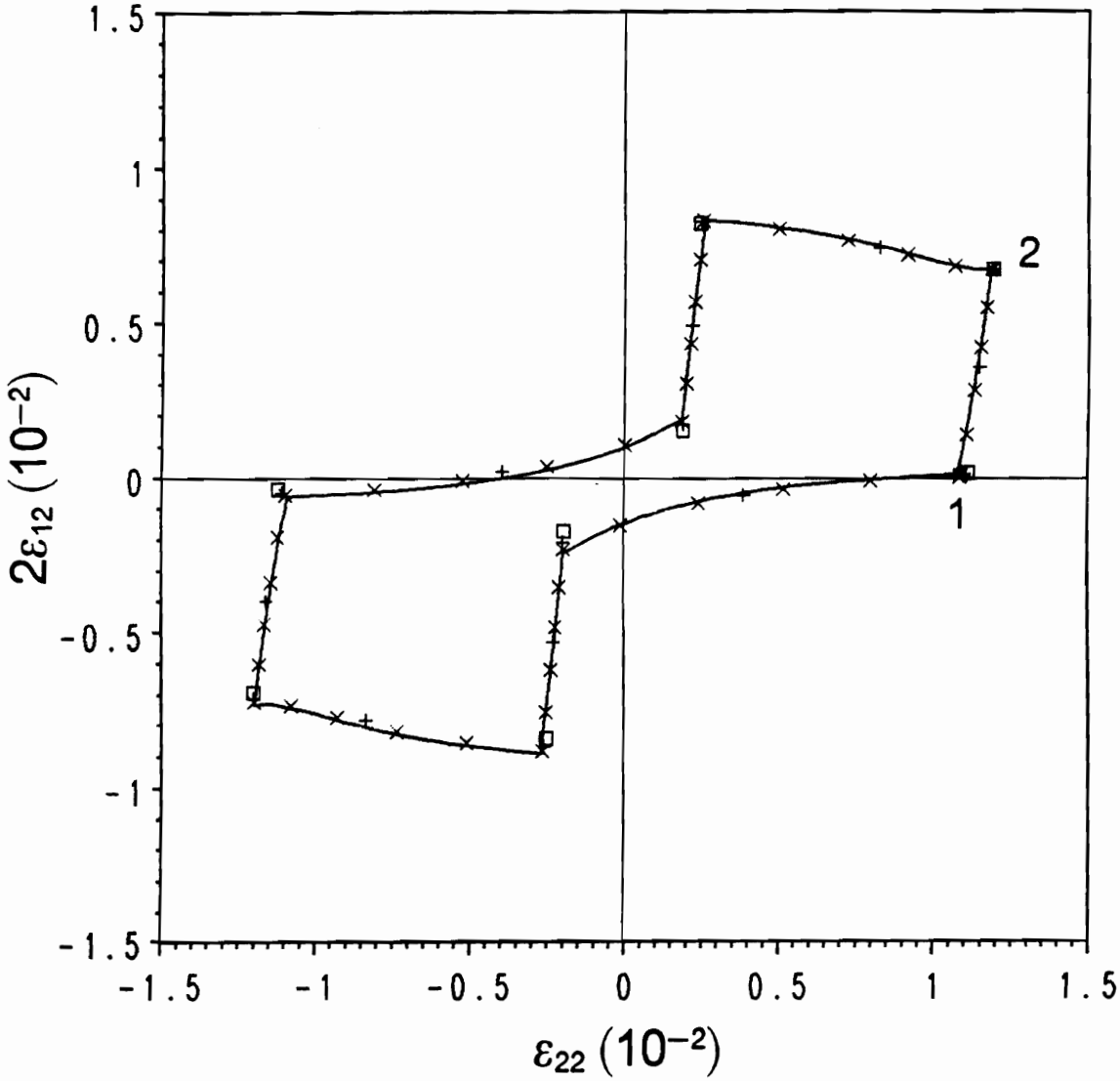

Figure 13a. Micro-Response to Transverse-Normal Longitudinal-Shear Cyclic Loading in Element 216: The predictions using 1, 2, 5, and 50 increments/segment are represented by the square, +, x, and continuous line, respectively.

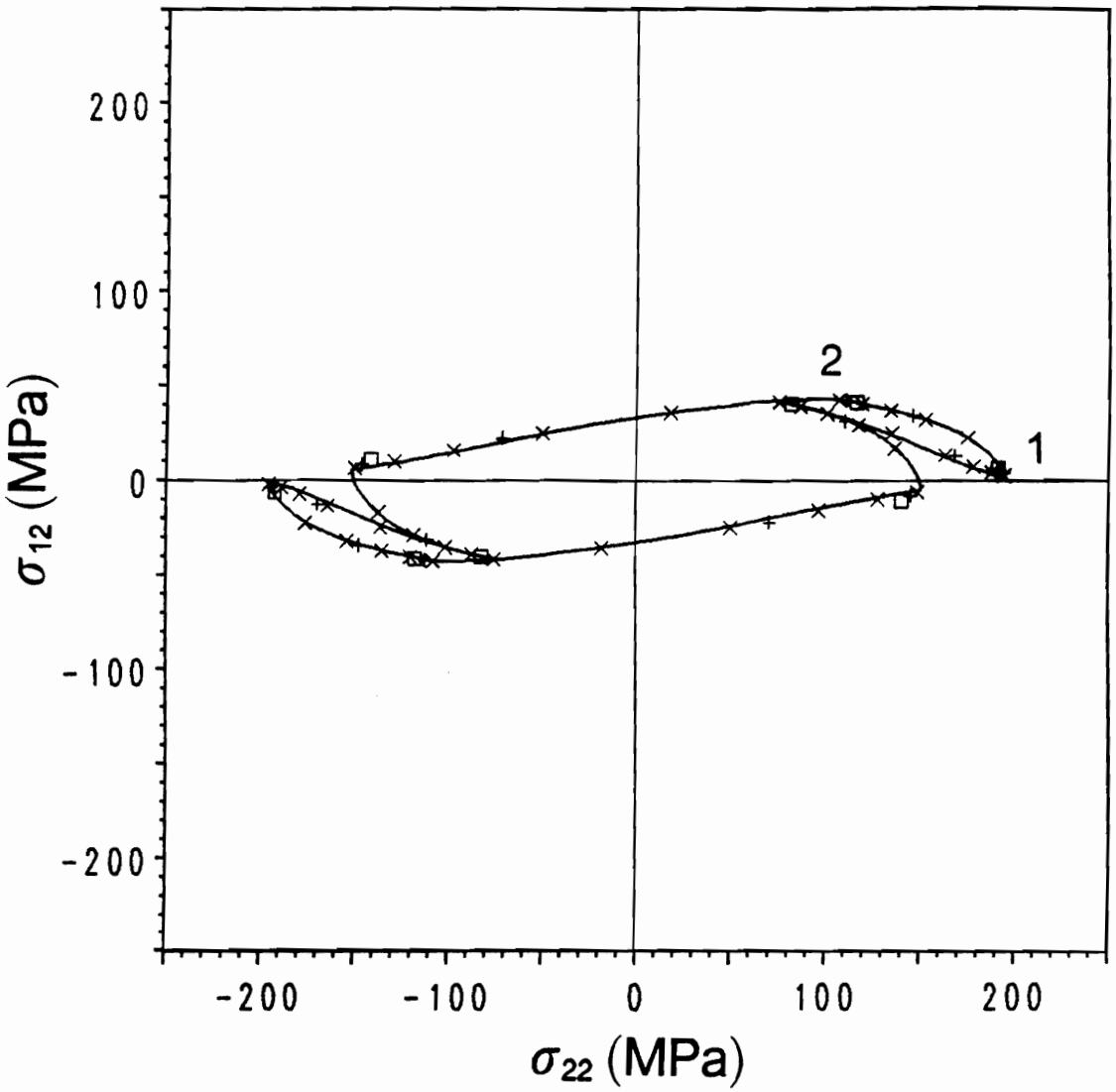

Figure 13b. Micro-Response to Transverse-Normal Longitudinal-Shear Cyclic Loading in Element 216: The predictions using 1, 2, 5, and 50 increments/segment are represented by the square, +, x, and continuous line, respectively.

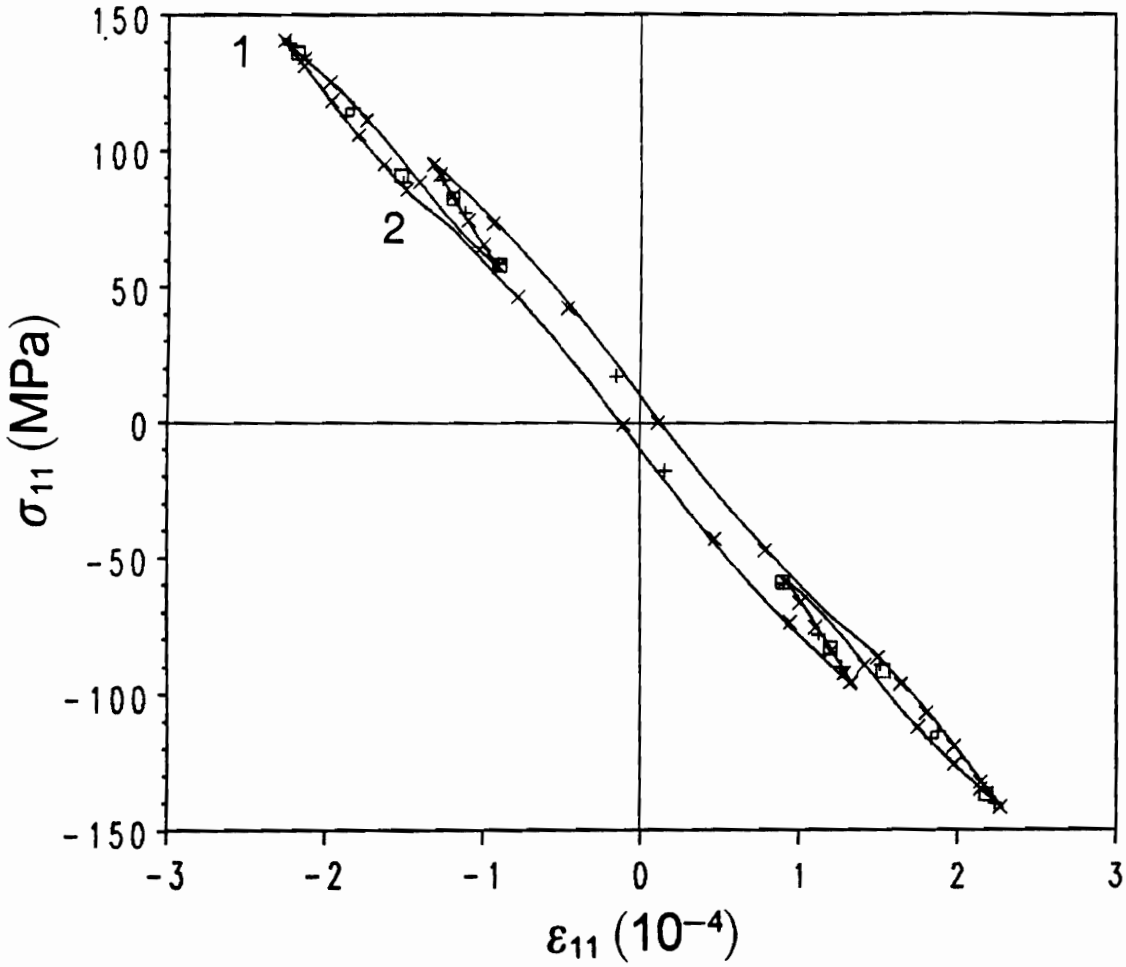

Figure 13c. Micro-Response to Transverse-Normal Longitudinal-Shear Cyclic Loading in Element 216: The predictions using 1, 2, 5, and 50 increments/segment are represented by the square, +, x, and continuous line, respectively.

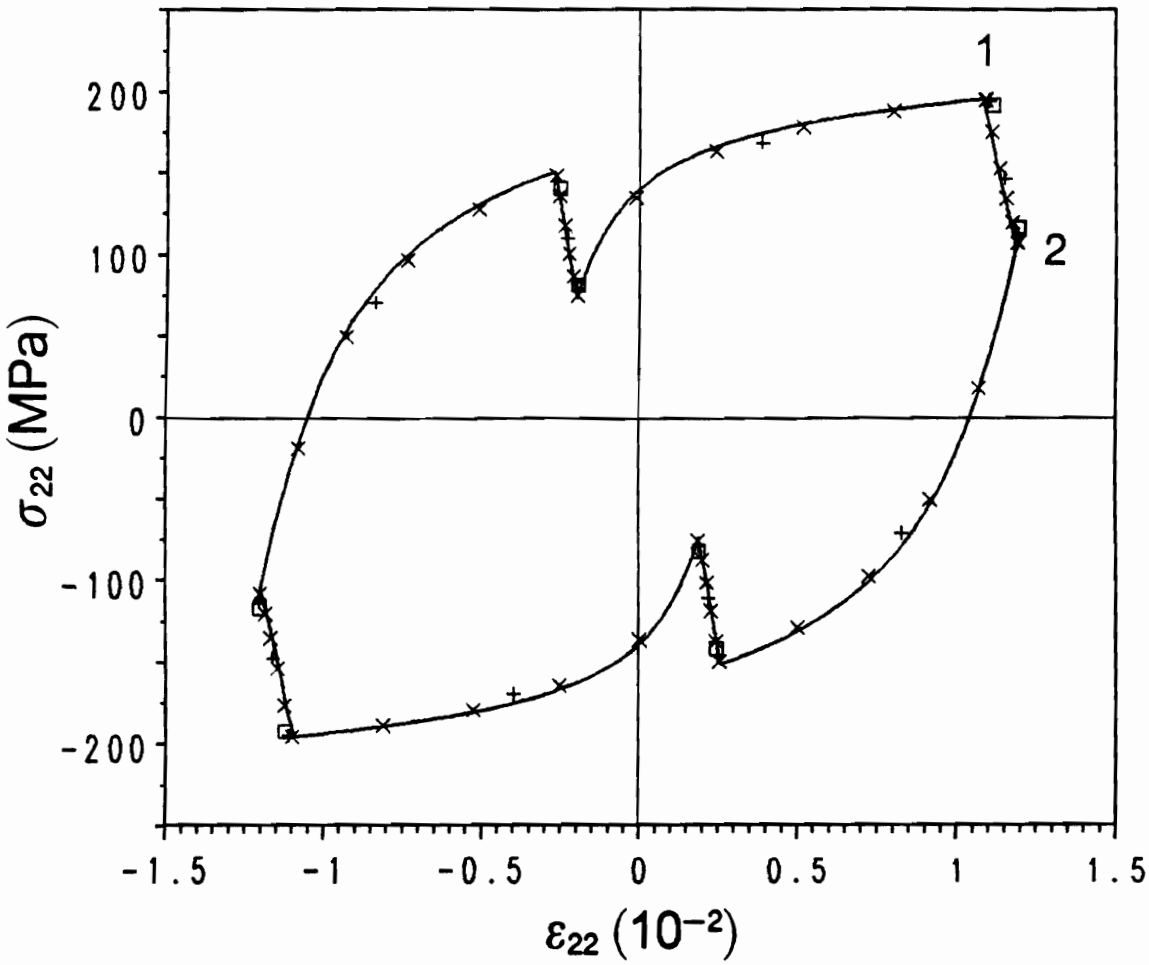

Figure 13d. Micro-Response to Transverse-Normal Longitudinal-Shear Cyclic Loading in Element 216: The predictions using 1, 2, 5, and 50 increments/segment are represented by the square, +, x, and continuous line, respectively.

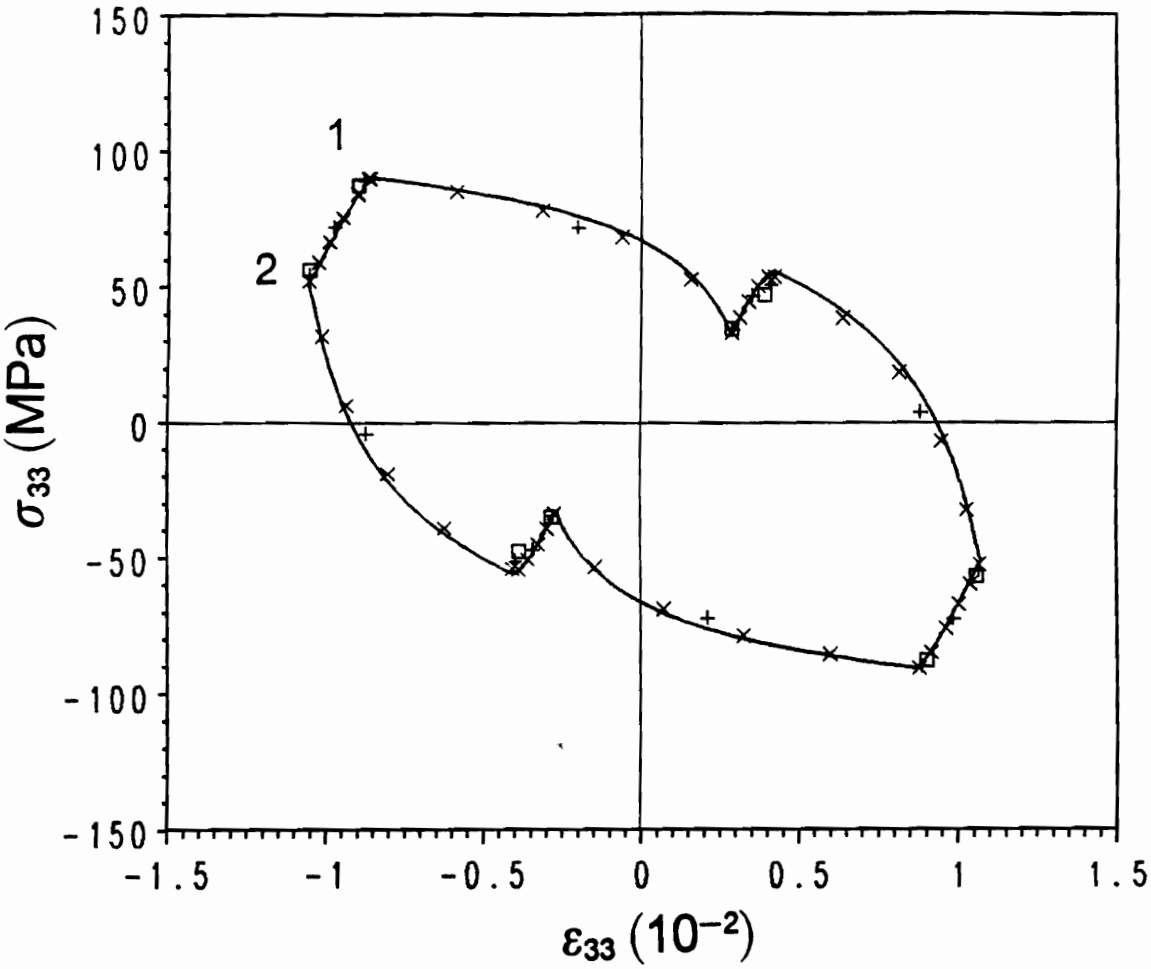

Figure 13e. Micro-Response to Transverse-Normal Longitudinal-Shear Cyclic Loading in Element 216: The predictions using 1, 2, 5, and 50 increments/segment are represented by the square, +, x, and continuous line, respectively.

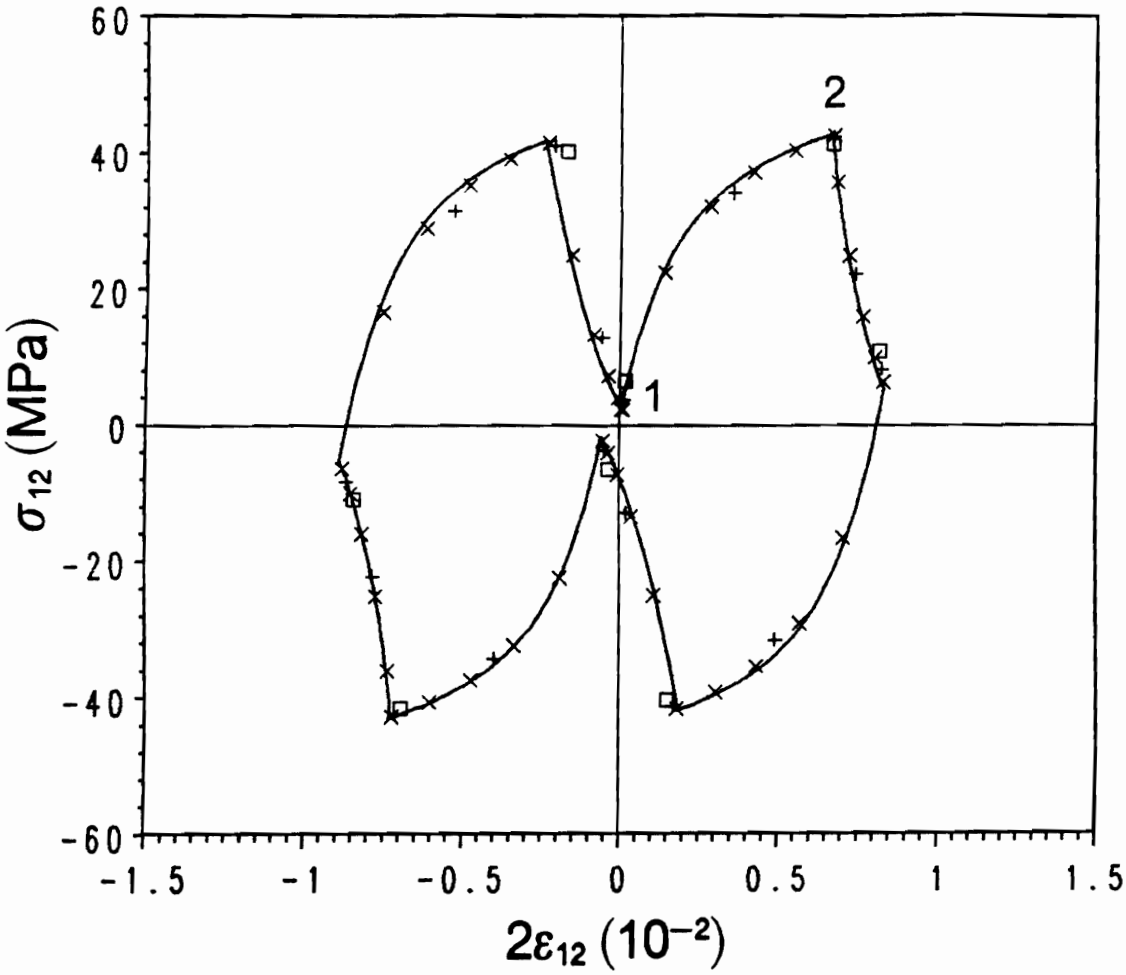

Figure 13f. Micro-Response to Transverse-Normal Longitudinal-Shear Cyclic Loading in Element 216: The predictions using 1, 2, 5, and 50 increments/segment are represented by the square, +, x, and continuous line, respectively.

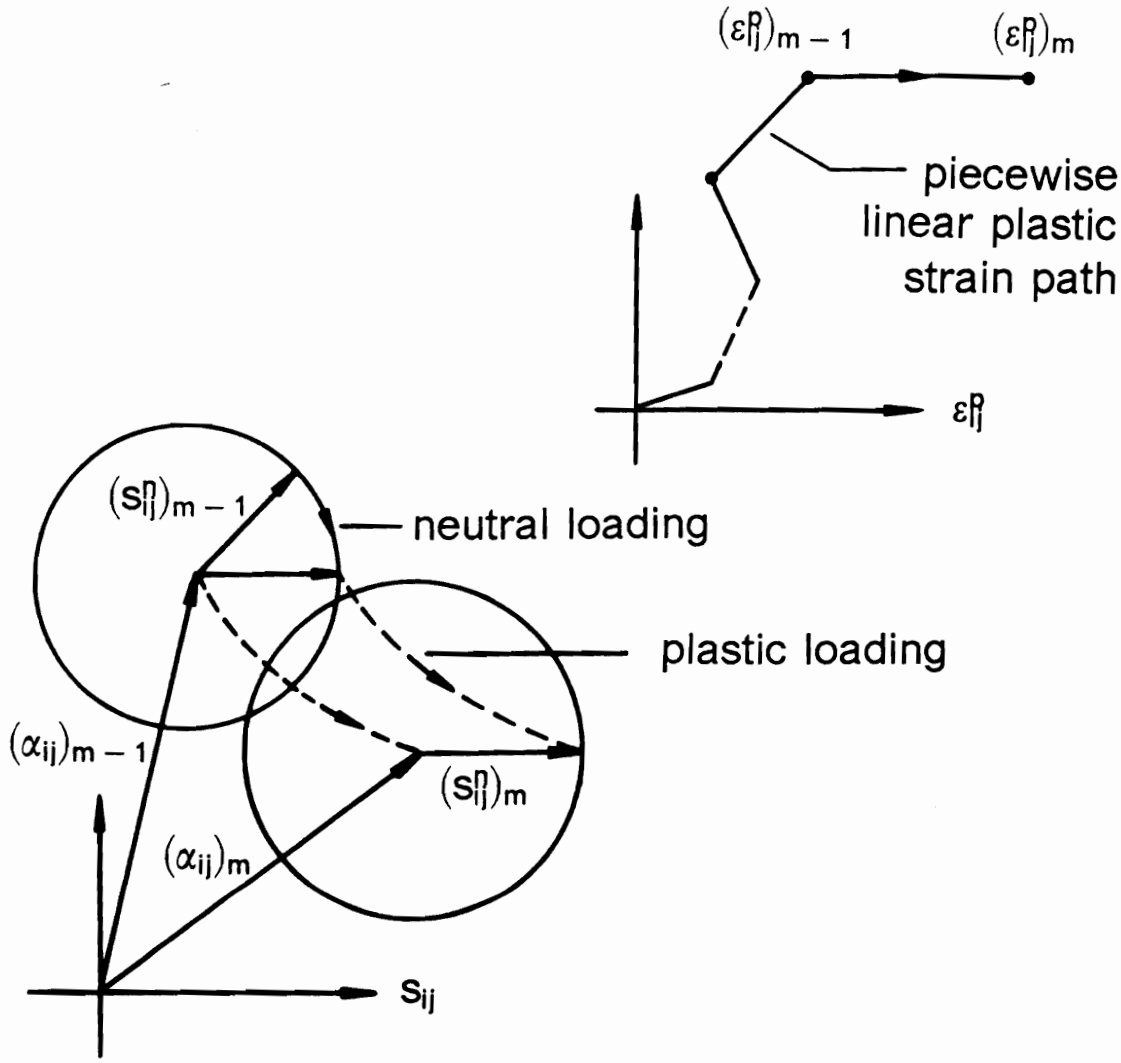

Figure 14. Geometrical Interpretation of Deviatoric Stress Response along Piecewise Linear Plastic Strain Path

Tables

Table 1. Statistics on Simulation of Transverse Normal Cyclic Loading Using (1, 1, 1) Increments

	loading events		
	0-1	1-2	2-3
number of increments	1	1	1
records of iterations	(11, 3) X 1	(5, 1) X 1	(10, 1) X 1
CPU seconds over entire loading history: 8			

Table 2. Statistics on Simulation of Transverse Normal Cyclic Loading Using (2, 1, 3) Increments

	loading events		
	0-1	1-2	2-3
number of increments	2	1	3
records of iterations	(12, 3) X 1 (10, 1) X 1	(4, 1) X 1	(8, 1) X 1 (10, 1) X 2
CPU seconds over entire loading history: 13			

Table 3. Statistics on Simulation of Transverse Normal Cyclic Loading Using (5, 3, 8) Increments

	loading events		
	0-1	1-2	2-3
number of increments	5	3	8
records of iterations	(4, 1) X 1 (9, 1) X 4	(3, 1) X 1 (4, 1) X 1 (5, 1) X 1	(3, 1) X 1 (5, 1) X 1 (10, 1) X 1 (9, 1) X 1 (8, 1) X 4
CPU seconds over entire loading history: 24			

Table 4. Statistics on Simulation of Transverse Normal Cyclic Loading Using (50, 25, 75) Increments

	loading events		
	0-1	1-2	2-3
number of increments	50	25	75
records of iterations	(3, 1) X 5 (4, 1) X 8 (5, 1) X 33 (6, 1) X 4	(2, 1) X 1 (3, 1) X 18 (4, 1) X 6	(3, 1) X 13 (4, 1) X 8 (5, 1) X 19 (6, 1) X 35
CPU seconds over entire loading history: 175			

Table 5. Statistics on Simulation of Transverse-Normal Longitudinal-Shear Cyclic Loading Using 1 Increment/Segment

	loading events			
	5-6	6-7	7-8	8-1
number of increments	1	1	1	1
records of iterations	(8, 1) X 1	(11, 3) X 1	(10, 1) X 1	(11, 3) X 1
CPU seconds over entire loading history: 62				

Table 6. Statistics on Simulation of Transverse-Normal Longitudinal-Shear Cyclic Loading Using 2 Increments/Segment

	loading events			
	5-6	6-7	7-8	8-1
number of increments	2	2	2	2
records of iterations	(8, 1) X 1 (7, 1) X 1	(9, 1) X 1 (11, 3) X 1	(9, 1) X 2	(11, 3) X 1 (10, 1) X 1
CPU seconds over entire loading history: 93				

Table 7. Statistics on Simulation of Transverse-Normal Longitudinal-Shear Cyclic Loading Using 5 Increments/Segment

	loading events			
	5-6	6-7	7-8	8-1
number of increments	5	5	5	5
records of iterations	(11, 4) X 1 (7, 1) X 2 (6, 1) X 2	(4, 1) X 1 (8, 1) X 1 (9, 1) X 3	(6, 1) X 1 (8, 1) X 4	(11, 3) X 1 (10, 1) X 1 (9, 1) X 3
CPU seconds over entire loading history: 180				

Table 8. Statistics on Simulation of Transverse-Normal Longitudinal-Shear Cyclic Loading Using 50 Increments/Segment

	loading events			
	5-6	6-7	7-8	8-1
number of increments	50	50	50	50
records of iterations	(6, 1) X 1 (9, 2) X 2 (12, 4) X 1 (11, 3) X 1 (5, 1) X 44 (4, 1) X 1	(4, 1) X 15 (5, 1) X 17 (6, 1) X 18	(3, 1) X 1 (5, 1) X 49	(8, 2) X 1 (10, 3) X 1 (9, 2) X 1 (12, 4) X 1 (11, 2) X 1 (7, 1) X 1 (6, 1) X 44
CPU seconds over entire loading history: 1374				

II. Simple and Unified Finite Element Formulation for Doubly Periodic Models: Applications to Boron/Aluminum Composites

1. Introduction

Recently, increasing efforts have been made to model inelastic deformation of unidirectionally fiber-reinforced composites for advanced high temperature applications [1 - 10]. Among various approaches, the micromechanics approach is uniquely suitable for development of composite materials, and has the potential for integrated micro-macro analysis of composite structures [11]. In addition, complicated behavior of composites at the macro level, e.g., severely anisotropic inelasticity and thermal-mechanical coupling, may be more easily simulated with material models at the micro-level.

It is well known that stress analysis of inelastic structures relies heavily on numerical methods at least because local material stiffness is subsequently anisotropic and inhomogeneous. Therefore, the versatile finite element (FE) method has been considered the most general approach for micromechanics modeling of inelastic behavior of fiberous composites, e. g., in the earlier work by Adams and his co-workers [12 - 15], and Foye [16 - 18], and the more recent work by Teply and Dvorak [1], Wu et al. [2], and Jansson [7]. The primary concern from the viewpoint of material developers

and structural designers is whether inelastic FE micromechanics modeling is convenient and efficient. In this regard, at least two issues must be considered: (1) the FE formulation for composite geometric models, and (2) the constitutive model for the inelastic matrix of a composite.

Many investigators have successfully applied the FE method using the ordinary nodal displacements as the discrete variables to analyze various representative cells of periodic diamond and periodic rectangular models under plane stress macro-loading. In their analyses, some boundary conditions are in the standard form, and the others are simple algebraic relations between boundary nodal displacements and macro-strains, and between boundary nodal forces and macro-stresses, respectively. The case of 3-D macro-loading is more complicated. With an effort in heavy algebra, Teply and Dvorak [1, 19] derived FE equations for a specialized trial displacement field in a periodic hexagonal model under 3-D macro-loading. Jansson [7] proposed a simple method for admissible FE displacement fields in any doubly periodic model. The displacement field is decomposed into a uniform macro-deformation field, and a fluctuating field represented by the common FE technique. FE equations are obtained by considering the virtual work due to the variation of the fluctuating part of the displacement; and the associated boundary conditions represent antisymmetry of boundary nodal fluctuating displacements, and symmetry of boundary nodal forces. If the uniform macro-deformation is unknown, the relations which straightforwardly represent macro-stresses as volume averages of micro-stresses are used as the additional equations. When higher-ordered finite elements are used, Jansson's method requires considerable modification of standard FE subprograms due to the decomposition of the displacement. Besides, when an FE model contains a number of internal nodes (i.e., nodes not on the boundary), the method demands "extra" com-

putation because the uniform macro-deformation is influential over the entire analyzed region and the macro-stresses are coupled to the fluctuating part of the displacement everywhere. It appears from the literature that a simple and unified weak formulation which is valid for any doubly periodic model under general macro-loading, and serves as a common rational foundation of different FE approaches has not been addressed. A convenient FE implementation of such a weak formulation would be the most desirable.

The overall success of inelastic FE micromechanics modeling also relies on the existence of a constitutive model for the inelastic matrix which has a wide range of predictive capability, and can be implemented in FE analysis conveniently and efficiently. The endochronic theory [20] has been shown able to simulate rate-independent and rate-dependent material responses to nonproportional cyclic loading in a unified framework (for references, see [21]). A rate-dependent theory can also be constructed as an extension of the rate-independent endochronic theory using the concept of over-stress [22]. Besides, a convenient and efficient algorithmic tangent matrix approach has been developed for endochronic FE analysis [23]. The underlying integration algorithm [24], which is derived by piecewise linearization of the plastic strain path, is unconditionally stable [25]. All the above progress favors the selection of the endochronic theory as a local constitutive model in FE micromechanics modeling of fiberous composites.

This paper is aimed at two goals. First, we present, in Section 2, a simple and unified weak formulation for doubly periodic models under general macro-loading conditions, and, in Section 3, a convenient FE implementation of the weak formulation. Second, the algorithmic tangent matrix approach for the endochronic theory has been incor-

porated into the FE formulation in order to model isothermal, rate-independent inelastic macro-deformation of unidirectionally fiber-reinforced composites. As an example, simulation has been performed for unidirectional boron/6061 aluminum composites. We present, in Section 4, theoretical-experimental correlation for the B/6061 Al composites, and, in Section 5, effects of model geometry of a B/6061 Al composite on overall inelastic response.

2. Weak Formulation for Doubly Periodic Models

In this section, we deal with composites whose micro-structure, when referred to a suitable Cartesian coordinate system, x_i, exhibits x_1-independence and double periodicity with respect to two linearly independent base vectors, b_i^1 and b_i^2, on the $x_1 = 0$ plane. The double periodicity of micro-structure with respect to b_i^1 and b_i^2 means that material properties and states at point P are identical to those at point Q if the coordinates of point P, $(x_i)_P$, and of point Q, $(x_i)_Q$, satisfy the following condition with two proper integers, m and n:

$$(x_i)_P - (x_i)_Q = mb_i^1 + nb_i^2 \tag{1}$$

The $x_1 = 0$ plane can be partitioned into parallelogram regions, each of which has four vertices located at $x_i = mb_i^1 + nb_i^2$, $(m+1)b_i^1 + nb_i^2$, $mb_i^1 + (n+1)b_i^2$, and $(m+1)b_i^1 + (n+1)b_i^2$ where m and n are two proper integers. The parallelogram regions on the $x_1 = 0$ plane are referred to as the unit cells of the composite under consideration. For example, a unit cell (the parallelogram region OABC) and the two base vectors (b_i^1 and b_i^2) are shown in Fig. 1. Obviously, any unit cell can be mapped onto any other unit cell by a translation, $mb_i^1 + nb_i^2$, defined with two appropriate in-

tegers, m and n. In addition, fissures and voids are excluded from the present consideration.

According to Hashin [26], local-theory stress-strain relations of a macroscopically homogeneous composite are determined by imposing the following displacement condition on the boundary of a composite volume to induce a uniform macroscopic strain field, ε_{ij}^{o}, and a uniform macroscopic stress field, σ_{ij}^{o}:

$$\mathbf{u} = \mathbf{x}\boldsymbol{\epsilon}^{o} \tag{2}$$

where $\mathbf{u}$ is the column matrix of the displacement components, $\mathbf{u}^T = [u_1\ u_2\ u_3]$, $\boldsymbol{\epsilon}^{o^T} = [\varepsilon_{11}^{o}\ \varepsilon_{22}^{o}\ \varepsilon_{33}^{o}\ 2\varepsilon_{23}^{o}\ 2\varepsilon_{13}^{o}\ 2\varepsilon_{12}^{o}]$, and

$$\mathbf{x} = \begin{bmatrix} x_1 & 0 & 0 & 0 & x_3 & x_2 \\ 0 & x_2 & 0 & x_3 & 0 & 0 \\ 0 & 0 & x_3 & 0 & 0 & 0 \end{bmatrix} \tag{3}$$

The geometry of the composite volume should be such that local-theory constitutive relations between macro-stress and macro-strain can be established. In view of the boundary condition, and the x_1-independence of micro-structure of the present composite model, we consider a composite volume whose geometry leads to dominant generalized plane strain deformation. Therefore, the displacement field can be approximately expressed in the following form:

$$\mathbf{u} = \mathbf{g} + \varepsilon_{11}^{o}\hat{\mathbf{x}} \tag{4}$$

where $\mathbf{g}^T = [g_1\ g_2\ g_3]$,

$$\hat{\mathbf{x}}^T = [x_1\ \ 0\ \ 0] \tag{5}$$

and g_1, g_2, and g_3 are functions of x_2 and x_3. The generalized plane strain deformation also allows us to restrict our discussion of the stress, strain, and displacement fields to the case of $x_1 = 0$ for convenience when the extension to the x_1-independent case is evident. Accordingly, we have $(\bullet)_P$ denote the value of a variable at point P on the $x_1 = 0$ plane, henceforth.

On the other hand, in view of the boundary condition, and the double periodicity of micro-structure of the present composite model, the geometry of the composite volume is further assumed to result in the characteristics of the stress and displacement fields discussed below.

- The stress field is dominated by the double periodicity of micro-structure. Namely, the stress field, σ_{ij}, can be approximately represented by

$$(\sigma_{ij})_P = (\sigma_{ij})_Q \tag{6}$$

  where points P and Q are any two locations that satisfy Eq. 1 with two proper integers, m and n.

- The displacement at the vertices of the unit cells (e.g., the points O, A, B, and C of Fig. 1), i.e., the g_i of Eq. 4 evaluated at the vertices, is a linear function of x_2 and x_3. In addition, the difference between g_i and the linear function is doubly periodic, and hence, has no contribution to the average strain of the displacement field, which must be ε_{ij}^{o}. Therefore, the displacement at the vertices must be represented by Eq. 2 with $x_1 = 0$ to best match the remote boundary condition. It is expedient to recast Eq. 4 into the following form:

$$\mathbf{u} = \mathbf{d} + \mathbf{f}\boldsymbol{\epsilon}^{o} \tag{7}$$

where $\mathbf{d}^T = [d_1\ d_2\ d_3]$,

$$\mathbf{f} = \begin{bmatrix} x_1 & 0 & 0 & 0 & f_3 & f_2 \\ 0 & f_2 & 0 & f_3 & 0 & 0 \\ 0 & 0 & f_3 & 0 & 0 & 0 \end{bmatrix} \tag{8}$$

and d_1, d_2, d_3, f_2, and f_3 are functions of x_2 and x_3. Thus, the characteristics of the displacement field corresponding to the double periodicity of the stress field are satisfied by the the following conditions:

$$\begin{aligned} (d_i)_V &= 0 \\ (f_i - x_i)_V &= 0 \end{aligned} \tag{9a, b}$$

and

$$\begin{aligned} (d_i)_P &= (d_i)_Q \\ (f_i - x_i)_P &= (f_i - x_i)_Q \end{aligned} \tag{10a, b}$$

where point V is any of the vertices of the unit cells, and points P and Q are defined as for Eq. 6.

We further consider the case in which the distribution of material properties and states is not only doubly periodic but also symmetric in a unit cell about its centroid. In this case, the stress and displacement fields exhibit the following characteristics:

- The stress field is symmetric about any of the vertices and centroids of the unit cells, and about any of the mid-points of the edges of the unit cells (e.g., any of the points O, A, B, C, H, D, E, F, and G of Fig. 1). Namely,

$$(\sigma_{ij})_R = (\sigma_{ij})_S \tag{11}$$

where points R and S are any two locations that are symmetric about W, which is any of the vertices and centroids of the unit cells, or is any of the mid-points of the edges of the unit cells. As expected, Eq. 6 is a necessary condition of Eq. 11.

•

$$(g_i)_R + (g_i)_S = 2(g_i)_W \tag{12}$$

where points R, S and W are defined as for Eq. 11. Eq. 12 means the displacement at the vertices, centroids, and midpoints of the edges is a linear function of x_2 and x_3. In addition, the difference between g_i and the linear function is anti-symmetric about the vertices, centroids, and mid-points of the edges, and hence, has no contribution to the average strain of the displacement field. Therefore, Eqs. 7 and 8 are also suitable for the current case, and the characteristics of the displacement field corresponding to the symmetry of the stress field are satisfied by the following conditions:

$$\begin{aligned} (d_i)_W &= 0 \\ (f_i - x_i)_W &= 0 \end{aligned} \tag{13a, b}$$

and

$$\begin{aligned} (d_i)_R &= -(d_i)_S \\ (f_i - x_i)_R &= -(f_i - x_i)_S \end{aligned} \tag{14a, b}$$

where points R, S, and W are defined as for Eq. 11. As expected, Eqs. 9 and 10 are necessary conditions of Eqs. 13 and 14, respectively.

Eq. 6 implies that it is sufficient for the doubly periodic model to analyze the parallelogram region OABC of Fig. 1, or any of its "equivalent regions" of other geometry, which carry the same information about the stress distribution as the parallelogram unit cell because of the double periodicity. On the other hand, Eq. 11 implies that the analysis of the triangular region OAC of Fig. 1, or any of its equivalent regions (e.g., the regions OBC, ODFC, and OIJC of Fig. 1, or I''J'IJ and HIJI'H' of Fig. 2a) is sufficient for the doubly periodic model with material properties and states symmetrically distributed in a unit cell about its centroid. Although there are infinitely many choices of the smallest regions for sufficient analysis, all the boundary conditions are classified into two types. Boundary traction conditions of both types are obtained by the following relation:

$$t_j = \sigma_{ij} n_i \tag{15}$$

where t_j is the boundary traction, and n_i is the unit vector outward normal to a boundary. The two types of boundary conditions are summarized below:

- Type 1: For example, on the boundaries OA and CB of the region OABC, OD and CF of ODFC, and OZ and CJ of OIJC (Fig. 1), and on the boundaries HI and H'I' of the region HIJI'H' (Fig. 2a), the displacement satisfies Eqs. 9 and 10, and the traction satisfies the following condition as a result of Eqs. 6 and 15:

$$(t_i)_P = -(t_i)_Q \tag{16}$$

where points P and Q are any two boundary points of a selected smallest region for sufficient analysis that satisfy Eq. 1 with two proper integers, m and n.

- Type 2: For example, on the boundary CO of the region OAC, OBC, ODFC, or OIJC, and ZI of OIJC (Fig. 1), and on the boundary H'H of the region HIJI'H' (Fig. 2a), the displacement satisfies Eqs. 13 and 14, and the traction satisfies the following condition as a result of Eqs. 11 and 15:

$$(t_i)_R = (t_i)_S \tag{17}$$

where points R and S are any two boundary points of a selected smallest region for sufficient analysis that are symmetric about a vertex or the centroid of a unit cell, or about the mid-point of an edge of a unit cell.

We now consider a cylindrical region, Ω, of which the axis is perpendicular to the $x_1 = 0$ plane. Ω has an axial length of L and two ends parallel to the $x_1 = 0$ plane. The cross-section of Ω on the $x_1 = 0$ plane, which is a selected region for sufficient analysis as discussed above, is denoted by S°, and has an area of A°. The boundary of Ω, which includes the lateral surface and two ends, is denoted by Γ. The equilibrium equation governing the stress field in Ω is

$$\sigma_{ij,i} = 0 \tag{18}$$

In addition, given below are the conditions of macro-stress (or average stress) and of macro-strain (or average strain) [26] which are imposed on Γ because of Eq. 6 or 11.

$$LA^{o}\sigma_{ij}^{o} = \int_{\Gamma} x_i t_j ds \tag{19}$$

and

$$2LA^{o}\varepsilon_{ij}^{o} = \int_{\Gamma} (u_i n_j + u_j n_i) ds \tag{20}$$

where LA^{o} is equal to the volume of Ω, and $\int(\bullet)ds$ denotes the surface integral. It can be shown easily using Gauss' theorem that Eq. 20 is satisfied if the displacement boundary conditions of type 1 or 2 are imposed on the lateral surface. Therefore, the displacement field represented by Eqs. 7 and 8 is governed by Eqs. 18 and 19, the two types of boundary conditions, appropriately specified constitutive equations, and the strain-displacement relation as follows:

$$\varepsilon_{ij} = \frac{1}{2}(u_{i,j} + u_{j,i}) \tag{21}$$

A weak formulation for Eqs. 18 and 19, and the boundary conditions is derived below in preparation for FE analysis.

$$0 = -\int_{\Omega} \sigma_{ij,i}\delta u_j dv + \int_{\Gamma} t_j(\delta u_j - x_i\delta\varepsilon_{ij}^{o})ds + (\int_{\Gamma} x_i t_j ds - LA^{o}\sigma_{ij}^{o})\delta\varepsilon_{ij}^{o} \tag{22}$$

where $\int(\bullet)dv$ denotes the volume integral, and $\delta(\bullet)$ denotes the variation of a function. The first term of Eq. 22 is due to Eq. 18, and the third term is due to Eq. 19. The second term of Eq. 22 represents a surface integral over the lateral surface and two

ends of the considered cylindrical region. The integral over the lateral surface vanishes due to Eqs. 7 and 8, and the two types of boundary conditions. The integral over one end cancels that over the other since $\sigma_{kj}(\delta u_j - x_i \delta \varepsilon_{ij}^{o})$ is x_1-independent. Eq. 22 reduces to

$$
\begin{aligned}
0 &= -\int_{\Omega} \sigma_{ij,i} \delta u_j dv + \int_{\Gamma} t_j \delta u_j ds - LA^{o} \sigma_{ij}^{o} \delta \varepsilon_{ij}^{o} \\
&= \int_{\Omega} \sigma_{ij} \delta \varepsilon_{ij} dv - LA^{o} \sigma_{ij}^{o} \delta \varepsilon_{ij}^{o} \\
&= \int_{S^{o}} \sigma_{ij} \delta \varepsilon_{ij} ds - A^{o} \sigma_{ij}^{o} \delta \varepsilon_{ij}^{o}
\end{aligned}
\tag{23}
$$

Gauss' theorem and Eqs. 15 and 21 have been used to derive the second equality in Eq. 23, which reduces to the last equality because of the x_1-independence. Eq. 23 is valid for the doubly periodic model under uniform 3-D macro-stress and macro-strain no matter whether the distribution of material properties and states is symmetric in a unit cell about its centroid or not.

Finally, we consider the macro-deformation of the periodic diamond and periodic rectangular models (shown in Figs. 2 and 3, respectively) in the absence of ε_{23}^{o} and ε_{13}^{o}, i.e.,

$$
\varepsilon_{23}^{o} = \varepsilon_{13}^{o} = 0 \tag{24}
$$

It is assumed that the distribution of material properties and states is not only doubly periodic but also symmetric in a unit cell with respect to the two straight lines which pass through the centroid of the unit cell, and are parallel with the x_2 and x_3 axes, respectively. We further assume that material properties and states at any point in

a unit cell are invariant under the tensorial transformation corresponding to $x_1' = -x_1$, $x_2' = -x_2$, and $x_3' = x_3$, and under the tensorial transformation corresponding to $x_1' = x_1$, $x_2' = x_2$, and $x_3' = -x_3$. In this case, the stress, strain, and displacement fields exhibit the following characteristics:

- $$(\sigma_{ij})_L = \begin{cases} (\sigma_{ij})_M & \text{if } (i, j) \neq (2, 3), (3, 2), (1, 3), \text{ and } (3, 1) \\ -(\sigma_{ij})_M & \text{if } (i, j) = (2, 3), (3, 2), (1, 3), \text{ or } (3, 1) \end{cases} \tag{25a, b}$$

  where points L and M are two arbitrary locations which are symmetric about any of the two straight lines which pass through any of the vertices and centroids of the unit cells, and are parallel with the x_2 and x_3 axes, respectively. In addition,

  $$(\sigma_{ij})_P = (\sigma_{ij})_Q \tag{26}$$

  where points P and Q are any two locations that are symmetric about V, which is any of the mid-points of the edges of the unit cells. As expected, Eq. 11 is a necessary condition of Eqs. 25 and 26.

- The characteristics of the displacement field corresponding to Eq. 25 are represented by the following:

$$
\begin{aligned}
(g_1)_{L_2} &= (g_1)_{M_2} \\
(g_2)_{L_2} &= (g_2)_{M_2} \\
(g_3)_{L_3} &= (g_3)_{M_3} \\
(g_1)_{L_3} + (g_1)_{M_3} &= 2(g_1)_{Y_3} \\
(g_2)_{L_3} + (g_2)_{M_3} &= 2(g_2)_{Y_3} \\
(g_3)_{L_2} + (g_3)_{M_2} &= 2(g_3)_{Y_2}
\end{aligned}
\tag{27a – f}
$$

and

$$
\begin{aligned}
(g_{1,3})_{Y_3} &= 0 \\
(g_{2,3})_{Y_3} &= 0 \\
(g_{3,2})_{Y_2} &= 0
\end{aligned}
\tag{28a – c}
$$

where points L_i and M_i are two arbitrary locations which are symmetric about the straight line which passes through any of the vertices and centroids of the unit cells, and is parallel with the x_i axis, and point Y_i is the mid-point between L_i and M_i (hence, Y_i is on the straight line parallel with the x_i axis). In addition, the characteristics of the displacement field corresponding to Eq. 26 are represented by the following:

$$
(g_i)_P + (g_i)_Q = 2(g_i)_V \tag{29}
$$

where points P, Q and V are defined as for Eq. 26. As expected, Eq. 12 is a necessary condition of Eqs. 27 - 29. Consequently, Eqs. 7, 8, 13, and 14 are also suitable for the current case. In view of Eqs. 7, 8, 13, and 24, Eq. 28 is satisfied by the following conditions:

$$
\begin{aligned}
(d_1)_{Y_3} &= 0 \\
(d_2)_{Y_3} &= 0 \\
(d_3)_{Y_2} &= 0 \\
(f_2 - x_2)_{Y_3} &= 0 \\
(f_3 - x_3)_{Y_2} &= 0
\end{aligned}
\tag{30a – e}
$$

where point Y_i are defined as for Eq. 28.

Eqs. 25 and 26 imply that the analysis of the triangular region OHC of Fig. 2a or b, or any of its equivalent regions (e.g., the trapezoid region OHIJ of Fig. 2a) is sufficient for the periodic diamond model with the appropriate intrinsic symmetry and distribution symmetry of material properties and states when the macro-deformation displays vanishing ε^{0}_{23} and ε^{0}_{13}. Similarly, the rectangular region ODHG of Fig. 3 is a smallest region for sufficient analysis of the periodic rectangular model. In any case, the foregoing type 2 boundary condition is applicable to any sloping edge such as the edge IJ of Fig. 2a or edge CO of Fig. 2b. Any of the rest of the boundary edges is parallel either with the x_2 or with the x_3 axis. Boundary conditions on such edges are classified as type 3.

- Type 3: On the boundaries which are parallel with the x_2 or x_3 axis, e.g., the boundaries OH, HI, and JO of the trapezoid region OHIJ of Fig. 2a, the displacement satisfies Eqs. 24 and 30, and the traction satisfies the following condition as a result of Eqs. 15 and 25b: On the boundaries parallel with the x_2 axis,

$$t_1 = t_2 = 0 \tag{31}$$

and on the boundaries parallel with the x_3 axis,

$$t_3 = 0 \tag{32}$$

A cylindrical region can be defined for the current case in the same way as for deriving Eq. 23 earlier; the relevant notations (Ω, L, S°, A°, and Γ) are used below correspondingly. The conditions of macro-stress and of macro-strain are imposed on Γ because of Eqs. 25a and 26.

$$LA^\circ \sigma_{ij}^* = \int_\Gamma x_i t_j ds \tag{33}$$

and

$$2LA^\circ \varepsilon_{ij}^* = \int_\Gamma (u_i n_j + u_j n_i) ds \tag{34}$$

where σ_{ij}^* and ε_{ij}^* are the local stress and strain averages over S°, respectively; $\sigma_{ij}^* = \sigma_{ij}^\circ$ and $\varepsilon_{ij}^* = \varepsilon_{ij}^\circ$, $(i, j) \neq (2, 3), (3, 2), (1, 3), (3, 1)$. For example, if the trapezoid region OHIJ of Fig. 2a is chosen as S°, then according to Eq. 25b, the local averages over the region OI''J'H of Fig. 2a should be $-\sigma_{ij}^*$ and $-\varepsilon_{ij}^*$ for $(i, j) = (2, 3), (3, 2), (1, 3), (3, 1)$. Therefore, the overall averages satisfy Eq. 24 and

$$\sigma_{23}^\circ = \sigma_{13}^\circ = 0 \tag{35}$$

It can be shown easily using Gauss' theorem that Eq. 34 with $(i, j) \neq (2, 3), (3, 2), (1, 3), (3, 1)$ is satisfied if the displacement boundary conditions of types 2 and 3 are imposed on the lateral surface of the considered cylindrical region.

An equation similar to Eq. 22 may be established for the periodic diamond and periodic rectangular models in the absence of ε^{o}_{23} and ε^{o}_{13}.

$$0 = -\int_{\Omega} \sigma_{ij,i}\delta u_j dv + \int_{\Gamma} t_j(\delta u_j - x_i\delta\varepsilon^{o}_{ij})ds + (\int_{\Gamma} x_i t_j ds - LA^{o}\sigma_{ij}{}^{*})\delta\varepsilon^{o}_{ij} \tag{36}$$

The second term of Eq. 36 vanishes due to Eqs. 7 and 8, and the boundary conditions of types 2 and 3, and the third term due to Eq. 33. Similarly, Eq. 36 reduces to

$$0 = \int_{S^{o}} \sigma_{ij}\delta\varepsilon_{ij} ds - A^{o}\sigma_{ij}{}^{*}\delta\varepsilon^{o}_{ij} \tag{37}$$

The above methodology for deriving the weak formulation for the periodic diamond and periodic rectangular models in the absence of ε^{o}_{23} and ε^{o}_{13} can also be applied to the case of $\varepsilon^{o}_{23} = \varepsilon^{o}_{12} = 0$. In conclusion, Eqs. 23 and 37 constitute the weak formulation intended for FE analysis of the doubly periodic models. As one can see, there is no formal difference between the two equations. It should be borne in mind that a trial displacement field (in the form defined by Eqs. 7 and 8) must satisfy the appropriate conditions among Eqs. 9, 10, 13, 14, 24, and 30 in order to be admissible to Eq. 23 or 37. A convenient FE implementation of the weak formulation is presented in the next section.

3. Finite Element Implementation

Approximation of the displacement field represented by Eq. 7 can be attained by the finite element technique. A selected smallest region for sufficient analysis, S°, is divided into 2-D conforming finite elements defined by nodes in S° and on its boundary. Such spatially identified nodes are called "real nodes," henceforth, which include "boundary nodes" and "internal nodes." The allocation of the boundary nodes should ensure that Eqs. 9a, 13a and 30a - c can be imposed. On the boundaries where type 1 or 2 boundary conditions are applied, boundary nodes except the vertices and centroids of the unit cells, and except the mid-points of the edges of the unit cells are divided into two groups, i.e., master nodes and slave nodes. Each slave node is dominated by one and only one master node; each master node dominates at least one slave node. A slave and its master are spatially correlated as the points P and Q of Eq. 16, or the points R and S of Eq. 17. The real nodes other than the slave nodes are called "active real nodes." Two "fictitious nodes" are added to a considered FE model to account for the six degrees of freedom in ϵ° (Eq. 7). To facilitate our discussion, we have m denote the number of the active real nodes of a considered FE grid, which are numbered from 1 to m at the global level; and let the $(m+1)$th and

$(m+2)$th nodes be the two fictitious nodes. Therefore, global numbering of the slave nodes should start with $m+3$. The active real nodes and the two fictitious nodes are collectively called "active nodes" of an FE model. A column vector of nodal variables is defined at each active node; at the ith node ($i \leq m+2$), the column vector is denoted by $\bar{\mathbf{a}}_i$. For $i \leq m$, $\bar{\mathbf{a}}_i$ represents the value of $\mathbf{d}$ (Eq. 7) at the ith node, i.e., $\bar{\mathbf{a}}_i = (\mathbf{d})_i$. On the other hand, $\bar{\mathbf{a}}_{m+1}^T = [\varepsilon_{11}^0\ \varepsilon_{22}^0\ \varepsilon_{33}^0]$, and $\bar{\mathbf{a}}_{m+2}^T = [2\varepsilon_{23}^0\ 2\varepsilon_{13}^0\ 2\varepsilon_{12}^0]$. The column vector of all the nodal variables, $\bar{\mathbf{a}}$, is defined as $\bar{\mathbf{a}}^T = [\bar{\mathbf{a}}_1^T\ \bar{\mathbf{a}}_2^T \ldots \bar{\mathbf{a}}_m^T\ \bar{\mathbf{a}}_{m+1}^T\ \bar{\mathbf{a}}_{m+2}^T]$.

In principle, two pieces of information about each finite element need be generated. For the convenience of description, we assume all the elements have the same number of real nodes, say n real nodes, and we consider an element, say element e. The first piece of information is the element connectivity:

$$c(1, e), c(2, e), \ldots, c(n, e)$$

where $c(i, e)$ denotes the global sequential number of the ith real node of element e. The other piece of information indicates the active nodes associated with element e:

$$\phi(1, e), \phi(2, e), \ldots, \phi(n, e), \phi(n+1, e), \phi(n+2, e)$$

where (1) $\phi(i, e) = c(i, e)$, if node $c(i, e)$ is an active real node; (2) $\phi(i, e)$ is set equal to the global sequential number of the master node dominating node $c(i, e)$, if node $c(i, e)$ is considered a slave node due to the boundary conditions of type 1; (3) $\phi(i, e)$ is set equal to the minus global sequential number of the master node dominating node $c(i, e)$, if node $c(i, e)$ is considered a slave node due to the boundary conditions of type 2; (4) $\phi(n+1, e) = m+1$ and $\phi(n+2, e) = m+2$.

For the time being, we assume linear elasticity. The basic FE relations for element e are given as follows:

$$\mathbf{u} = \sum_{i=1}^{n+2} \text{sign}[\phi(i, e)]\overline{\mathbf{N}}_i^e \overline{\mathbf{a}}_{|\phi(i, e)|} \tag{38}$$

$$\boldsymbol{\epsilon} = \sum_{i=1}^{n+2} \text{sign}[\phi(i, e)]\overline{\mathbf{B}}_i^e \overline{\mathbf{a}}_{|\phi(i, e)|} \tag{39}$$

and

$$\overline{\mathbf{K}}^e_{|\phi(i, e)|\,|\phi(j, e)|} = \text{sign}[\phi(i, e)]\text{sign}[\phi(j, e)]\int_{S^e} \overline{\mathbf{B}}_i^{e^T} \mathbf{C} \overline{\mathbf{B}}_j^e ds \qquad i, j = 1, 2, ..., n, n+1, n+2 \tag{40}$$

where $\mathbf{u}$ is the matrix of the displacements (Eq. 2), and $\boldsymbol{\epsilon}^T = [\varepsilon_{11}\ \varepsilon_{22}\ \varepsilon_{33}\ 2\varepsilon_{23}\ 2\varepsilon_{13}\ 2\varepsilon_{12}]$. In Eqs. 38 - 40, for $i \leq n$, $\overline{\mathbf{N}}_i^e$ is the matrix of the usual shape functions of the displacements for the ith real node of element e, and $\overline{\mathbf{B}}_i^e$ is the corresponding matrix for the strains. A comparison of Eqs. 7 and 38 immediately reveals that in element e, $\mathbf{f} = [\overline{\mathbf{N}}_{n+1}^e\ \overline{\mathbf{N}}_{n+2}^e]$. The $|\phi(i, e)|$ in Eqs. 38 - 40 means the absolute value of $\phi(i, e)$; therefore, $\overline{\mathbf{a}}_{|\phi(i, e)|}$ is the column vector of nodal variables at the active node whose global sequential number is $|\phi(i, e)|$. The $\text{sign}[\phi(i, e)]$ in Eqs. 38 - 40 stands for $+1$ in case of $\phi(i, e) > 0$, and stands for -1 in case of $\phi(i, e) < 0$. The $\overline{\mathbf{K}}^e_{|\phi(i, e)|\,|\phi(j, e)|}$ of Eq. 40 stands for the contribution of element e to a sub-matrix of the global stiffness matrix; the sub-matrix represents the interaction between the nodal force at node $|\phi(i, e)|$ and $\overline{\mathbf{a}}_{|\phi(j, e)|}$. The $\mathbf{C}$ of Eq. 40 is the matrix of elastic moduli. The integration

in Eq. 40 is carried out over the region of element e, S^e. Obviously, the global stiffness matrix, $\overline{\mathbf{K}}$, is obtained by assembling all the $\overline{\mathbf{K}}^e_{|\phi(i,e)||\phi(j,e)|}$ matrices in the usual way. In case of Eq. 23, the desired FE equation system is

$$\overline{\mathbf{K}}\,\overline{\mathbf{a}} = \begin{bmatrix} \mathbf{F} \\ A^o \boldsymbol{\sigma}^o \end{bmatrix} \tag{41}$$

where $\mathbf{F}$ is a 3m × 1 column vector, and $\boldsymbol{\sigma}^{o^T} = [\sigma^o_{11}\ \sigma^o_{22}\ \sigma^o_{33}\ \sigma^o_{23}\ \sigma^o_{13}\ \sigma^o_{12}]$. In case of Eq. 37,

$$\overline{\mathbf{K}}\,\overline{\mathbf{a}} = \begin{bmatrix} \mathbf{F} \\ A^o \boldsymbol{\sigma}^* \end{bmatrix} \tag{42}$$

where $\boldsymbol{\sigma}^{*T} = [\sigma_{11}^*\ \sigma_{22}^*\ \sigma_{33}^*\ \sigma_{23}^*\ \sigma_{13}^*\ \sigma_{12}^*]$. The right-hand sides of Eqs. 41 and 42 are the global force vectors due to applied loading.

In view of Eqs. 41 and 42, it is obviously simple to construct the nodal forces at the last two active nodes with specified macro-stress components. Secondly, Eqs. 23 and 37 imply that among the elements of $\mathbf{F}$, those corresponding to unknown nodal variables are zero.

Note that Eqs. 9a and 13a can be applied to Eq. 41 in the usual way, and so can Eqs. 13a, 24, and 30a - c be applied to Eq. 42. On the other hand, the role of $\phi(i, e)$ in Eqs. 38 - 40 reflects the imposition of Eqs. 10a and 14a. Hence, still left intact among the boundary conditions are Eqs. 9b, 10b, 13b, 14b, and 30d and e. These conditions must be imposed by judicious selection of $\overline{\mathbf{N}}^e_{n+1}$ and $\overline{\mathbf{N}}^e_{n+2}$. Three selections are presented in the following paragraphs.

In the first method, $f_i - x_i = 0$ (Eq. 8) in S^e and on its boundary is adopted. Therefore, Eqs. 9b, 10b, 13b, 14b, and 30d and e are automatically satisfied. The $\overline{\mathbf{N}}^e_{n+1}$, $\overline{\mathbf{N}}^e_{n+2}$, $\overline{\mathbf{B}}^e_{n+1}$, and $\overline{\mathbf{B}}^e_{n+2}$ of the first method are defined as follows:

$$\overline{\mathbf{N}}^e_{n+1} = \begin{bmatrix} x_1 & 0 & 0 \\ 0 & x_2 & 0 \\ 0 & 0 & x_3 \end{bmatrix} \tag{43}$$

$$\overline{\mathbf{N}}^e_{n+2} = \begin{bmatrix} 0 & x_3 & x_2 \\ x_3 & 0 & 0 \\ 0 & 0 & 0 \end{bmatrix} \tag{44}$$

$$\overline{\mathbf{B}}^e_{n+1} = \begin{bmatrix} 1 & 0 & 0 \\ 0 & 1 & 0 \\ 0 & 0 & 1 \\ 0 & 0 & 0 \\ 0 & 0 & 0 \\ 0 & 0 & 0 \end{bmatrix} \tag{45}$$

$$\overline{\mathbf{B}}^e_{n+2} = \begin{bmatrix} 0 & 0 & 0 \\ 0 & 0 & 0 \\ 0 & 0 & 0 \\ 1 & 0 & 0 \\ 0 & 1 & 0 \\ 0 & 0 & 1 \end{bmatrix} \tag{46}$$

After substitution of Eqs. 45 and 46 into Eq. 40 for $i = n + 1, n + 2$, the last six equations of Eq. 41 are found to be the condition of average stress in the other form (cf. Eq. 19),

$$LA^{o}\sigma_{ij}^{o} = \int_{\Omega} \sigma_{ij} dv \tag{47}$$

Similarly, for the last six equations of Eq. 42 (cf. Eq. 33),

$$LA^{o}\sigma_{ij}^{*} = \int_{\Omega} \sigma_{ij} dv \tag{48}$$

Therefore, the FE equations resulting from the first method are no different than those from Jansson's method [7]; however, all the present FE equations are derived from a single weak formulation.

In the second method, $f_i - x_i = 0$ (Eq. 8) on the boundary of S^o, and $f_2 = f_3 = 0$ in the elements which contain only internal nodes. Therefore, Eqs. 9b, 10b, 13b, 14b, and 30d and e are automatically satisfied. The requirements on f_i can be easily met with the aid of the shape functions. In element e,

$$\left[\overline{N}_{n+1}^{e} \quad \overline{N}_{n+2}^{e}\right] = \left[\hat{\mathbf{x}} \quad \mathbf{N}^{e}\tilde{\mathbf{x}}^{e}\right] \tag{49}$$

where $\hat{\mathbf{x}}$ has been defined by Eq. 5,

$$\mathbf{N}^{e} = \left[\overline{N}_{1}^{e} \quad \overline{N}_{2}^{e} \quad \ldots \quad \overline{N}_{n}^{e}\right] \tag{50}$$

and

$$\tilde{\mathbf{x}}^{e^T} = \left[\tilde{\mathbf{x}}_1^{e^T} \;\; \tilde{\mathbf{x}}_2^{e^T} \;\; \ldots \;\; \tilde{\mathbf{x}}_n^{e^T}\right] \tag{51}$$

in which (1) if node c(i, e) is an internal node, then $\tilde{\mathbf{x}}_i^e$ is a 3×5 zero matrix; (2) otherwise, node c(i, e) is a boundary node, and

$$\tilde{\mathbf{x}}_i^e = \begin{bmatrix} 0 & 0 & 0 & x_3 & x_2 \\ x_2 & 0 & x_3 & 0 & 0 \\ 0 & x_3 & 0 & 0 & 0 \end{bmatrix} \qquad \text{evaluated at node c(i, e)} \tag{52}$$

If isoparametric elements are used and the boundary geometry of S^e is exactly modeled using the FE technique, then Eqs. 5 and 49 - 52 do lead to the desired properties of **f**. In addition, it is noted that the **f** of this method is C_0 continuous [27]. In view of Eqs. 5 and 49 - 52,

$$\left[\bar{\mathbf{B}}_{n+1}^e \;\; \bar{\mathbf{B}}_{n+2}^e\right] = \left[\hat{\mathbf{I}} \;\; \mathbf{B}^e\tilde{\mathbf{x}}^e\right] \tag{53}$$

where

$$\hat{\mathbf{I}}^T = [1 \;\; 0 \;\; 0 \;\; 0 \;\; 0 \;\; 0] \tag{54}$$

and

$$\mathbf{B}^e = \left[\bar{\mathbf{B}}_1^e \;\; \bar{\mathbf{B}}_2^e \;\; \ldots \;\; \bar{\mathbf{B}}_n^e\right] \tag{55}$$

It is possible to obtain all the matrices $\bar{\mathbf{N}}_i^e$, $\bar{\mathbf{B}}_i^e$, and $\bar{\mathbf{K}}_{|\phi(i,e)||\phi(j,e)|}^e$ (Eqs. 38 - 40) of the second method by simple post-processing of the output from typical FE subroutines for the generalized plane strain problem because the $\tilde{\mathbf{x}}^e$ in Eqs. 49 and 53 is a con-

stant matrix for each individual element. The typical FE relations for the generalized plane strain problem are shown below. For element e,

$$\mathbf{u} = \underline{\mathbf{N}}^{e}\underline{\mathbf{v}}^{e} \tag{56}$$

and

$$\boldsymbol{\epsilon} = \underline{\mathbf{B}}^{e}\underline{\mathbf{v}}^{e} \tag{57}$$

where

$$\underline{\mathbf{N}}^{e} = \left[\mathbf{N}^{e} \;\; \hat{\mathbf{x}}\right] \tag{58}$$

and

$$\underline{\mathbf{B}}^{e} = \left[\mathbf{B}^{e} \;\; \hat{\mathbf{I}}\right] \tag{59}$$

In Eqs 56 and 57, $\underline{\mathbf{v}}^{e^T} = [\mathbf{v}^{e^T} \; \varepsilon_{11}^{e}] = [\mathbf{v}_{c(1,e)}^{T} \; \mathbf{v}_{c(2,e)}^{T} \ldots \mathbf{v}_{c(n,e)}^{T} \; \varepsilon_{11}^{e}]$ where $\mathbf{v}_{c(i,e)}$ represents the value of $\mathbf{g}$ (Eq. 4) at node c(i, e), i.e., $\mathbf{v}_{c(i,e)} = (\mathbf{g})_{c(i,e)}$. Recall that the notation c(i, e) means the global sequential number of the ith real node of element e. The element stiffness matrix for the generalized plane strain problem, $\underline{\mathbf{K}}^{e}$, can be partitioned into four sub-matrices in accordance with Eq. 59, i.e.,

$$\underline{\mathbf{K}}^{e} = \begin{bmatrix} \mathbf{K}^{B^eB^e} & \mathbf{K}^{B^e\hat{I}} \\ \mathbf{K}^{\hat{I}B^e} & \mathbf{K}^{\hat{I}\hat{I}} \end{bmatrix} \tag{60}$$

The $\underline{\mathbf{N}}^{e}$ (Eq. 58), $\underline{\mathbf{B}}^{e}$ (Eq. 59), and $\underline{\mathbf{K}}^{e}$ (Eq. 60) are usually available in the output from typical FE subroutines for the generalized plane strain problem. Using these matrices, the following matrices can be easily constructed:

$$\overline{\mathbf{N}}^e = \left[\mathbf{N}^e \;\; \hat{\mathbf{x}} \;\; \mathbf{N}^e\tilde{\mathbf{x}}^e\right] \tag{61}$$

$$\overline{\mathbf{B}}^e = \left[\mathbf{B}^e \;\; \hat{\mathbf{l}} \;\; \mathbf{B}^e\tilde{\mathbf{x}}^e\right] \tag{62}$$

$$\overline{\mathbf{D}}^e = \begin{bmatrix} \mathbf{K}^{\mathbf{B}^e\mathbf{B}^e} & \mathbf{K}^{\mathbf{B}^e\hat{\mathbf{l}}} & \mathbf{K}^{\mathbf{B}^e\mathbf{B}^e}\tilde{\mathbf{x}}^e \\ \mathbf{K}^{\hat{\mathbf{l}}\mathbf{B}^e} & \mathbf{K}^{\hat{\mathbf{l}}\hat{\mathbf{l}}} & \mathbf{K}^{\hat{\mathbf{l}}\mathbf{B}^e}\tilde{\mathbf{x}}^e \\ \tilde{\mathbf{x}}^{e^T}\mathbf{K}^{\mathbf{B}^e\mathbf{B}^e} & \tilde{\mathbf{x}}^{e^T}\mathbf{K}^{\mathbf{B}^e\hat{\mathbf{l}}} & \tilde{\mathbf{x}}^{e^T}\mathbf{K}^{\hat{\mathbf{l}}\hat{\mathbf{l}}}\tilde{\mathbf{x}}^e \end{bmatrix} \tag{63}$$

Upon retrospecting Eqs. 49 and 50, and Eqs. 53 and 55, one readily finds that partitioning $\overline{\mathbf{N}}^e$, $\overline{\mathbf{B}}^e$, and $\overline{\mathbf{D}}^e$ into 3×3, 6×3, and 3×3 sub-matrices gives all the $\overline{\mathbf{N}}_i^e$ (Eq. 38), $\overline{\mathbf{B}}_i^e$ (Eq. 39), and the integrals for determination of $\overline{\mathbf{K}}^e_{|\phi(i,e)||\phi(j,e)|}$ (Eq. 40), respectively. Further, we recall that $\tilde{\mathbf{x}}^e$ is a zero matrix in the elements which contain only internal nodes; hence, the post-processing is unnecessary for these elements.

The third method applies when all the boundary conditions are of type 2. In the third method, Eqs. 13b and 14b are satisfied, but $f_i - x_i \neq 0$ somewhere, on the boundaries, and $f_2 = f_3 = 0$ in the elements which contain only internal nodes. Eqs. 49 and 53, and the method for obtaining all the matrices $\overline{\mathbf{N}}_i^e$ (Eq. 38), $\overline{\mathbf{B}}_i^e$ (Eq. 39), and $\overline{\mathbf{K}}^e_{|\phi(i,e)||\phi(j,e)|}$ (Eq. 40) from $\underline{\mathbf{N}}^e$ (Eq. 58), $\underline{\mathbf{B}}^e$ (Eq. 59), and $\underline{\mathbf{K}}^e$ (Eq. 60) remain valid for the third method. The only difference lies in the definition of the $\tilde{\mathbf{x}}_i^e$ in Eq. 51. $\tilde{\mathbf{x}}_i^e$ for the third method is defined as follows: (1) If node c(i, e) is an internal node or a master node, then $\tilde{\mathbf{x}}_i^e$ is a 3×5 zero matrix. (2) If node c(i, e) is a slave node, then

$$\tilde{\mathbf{x}}_i^e = 2\begin{bmatrix} 0 & 0 & 0 & x_3 & x_2 \\ x_2 & 0 & x_3 & 0 & 0 \\ 0 & x_3 & 0 & 0 & 0 \end{bmatrix} \quad \begin{matrix}\text{evaluated at the point which} \\ \text{node c(i, e) and its master} \\ \text{node are symmetric about}\end{matrix} \tag{64}$$

(3) Otherwise, node c(i, e) is a vertix or the centroid of a unit cell, or the mid-point of an edge of a unit cell, and $\tilde{\mathbf{x}}_i^e$ is defined by Eq. 52. Note that the point where the $\tilde{\mathbf{x}}_i^e$ of Eq. 64 is evaluated is also a vertix or the centroid of a unit cell, or the mid-point of an edge of a unit cell. Comparing the second method with the third, one can find that the third method may lead to more elements for which the post-processing is unnecessary.

When material behavior is not linearly elastic, FE analysis is usually based on the well-known Newton-Raphson method. All the foregoing theoretical development needs only minor modification in order to be applied in the Newton-Raphson method. Generally, the previous displacement and strain quantities are now replaced with their increments or sub-increments, depending on whether material behavior is path-independent or path-dependent. The **C** matrix in Eq. 40 now should mean the constitutive tangent matrix or algorithmic tangent matrix [28]. Besides, the right-hand sides of Eqs. 41 and 42 are now replaced with the global residual force vector, which represents the global force vector due to applied loading less the one due to internal stress, or the incremental global force vector due to an applied loading increment less the one due to an internal stress increment. Let $\Delta\boldsymbol{\sigma}$ denote the matrix of the components of an internal stress increment, $\Delta\boldsymbol{\sigma}^T = [\Delta\sigma_{11}\ \Delta\sigma_{22}\ \Delta\sigma_{33}\ \Delta\sigma_{23}\ \Delta\sigma_{13}\ \Delta\sigma_{12}]$, and let $\Delta\bar{\mathbf{F}}^e_{|\phi(i,e)|}$ denote the contribution of element e to the incremental nodal force at node $|\phi(i, e)|$ due to $\Delta\boldsymbol{\sigma}$. Thus,

$$\Delta\bar{\mathbf{F}}^e_{|\phi(i,e)|} = \mathrm{sign}[\phi(i, e)]\int_{S^e} \bar{\mathbf{B}}_i^{e^T}\Delta\boldsymbol{\sigma}\,ds \qquad i = 1, 2, ..., n, n+1, n+2 \tag{65}$$

The incremental global force vector due to an internal stress increment is obtained through the usual element-by-element assemblage of $\Delta\bar{F}^{\circ}_{\{\phi(i,e)\}}$. For the second and third methods, all the matrices $\Delta\bar{F}^{\circ}_{\{\phi(i,e)\}}$ (Eq. 65) can also be obtained by utilizing typical FE subroutines for the generalized plane strain problem. Let $\Delta\underline{F}^{e}$ denote the incremental force vector due to an internal stress increment in element e output from the subroutines.

$$\Delta\underline{F}^{e} = \begin{bmatrix} \Delta F^{B^{e}} \\ \Delta F^{\hat{i}} \end{bmatrix} \tag{66}$$

Accordingly, the integrals in Eq. 65 are obtained by partitioning the following matrix into $n+2$ 3×1 vectors:

$$\Delta\bar{L}^{e} = \begin{bmatrix} \Delta F^{B^{e}} \\ \Delta F^{\hat{i}} \\ \tilde{x}^{e^{T}} \Delta F^{B^{e}} \end{bmatrix} \tag{67}$$

The presented FE formulation is convenient for simulation of any type of macro-loading. In linearly elastic analysis, desired macro-strains are imposed on the left-hand side of Eq. 41 or 42; and desired macro-stresses are substituted into the right-hand side. After solving the equation system, unknown macro-strains are directly available from the vectors of nodal variables at the last two active nodes; and unknown macro-stresses are obtained simply by dividing by A^{o} the nodal forces calculated at the last two active nodes due to internal stress. The procedure for analysis with material nonlinearity or path-dependence is similar.

4. Applications to Unidirectional Boron/Aluminum Composites

Assumptions are usually made in micromechanics analysis to replace unknown or complicated distribution of material properties or states. Such assumptions usually leave some geometric or material parameters indeterminate which must be backed out by fitting, with model prediction, certain experimental data of a composite. In the simplest approach, a "nominally" two-phase fibrous composite is idealized as an "exactly" two-phase composite without polycrystalline micro-structure,[1] and all the geometric parameters are assumed a priori. Therefore, an idealized two-phase fibrous composite contains homogeneous fibers and a homogeneous matrix. It is usually a good assumption that elastic properties of fibers of an idealized fibrous composite are independent of composite fabrication, and elastic properties of the matrix of an idealized fibrous composite can be determined by testing pure-matrix specimens which are obtained through a thermomechanical process similar to the

[1] There usually exist more than two phases in a nominally two-phase fibrous composite. Sometimes, a nominal phase does not even imply piecewise homogeneity. Besides, the polycrystalline micro-structure of many fibrous composites is not negligible from a rational viewpoint.

composite fabrication. However, Inelastic properties must be backed out [3, 6]. In a rigorous sense, the simplest approach in connection with the backed-out inelastic properties from a specific fibrous composite may be used to predict unknown macro-response of the specific composite, or of other composites in the same material system but with moderately different fiber volume fractions. The backed-out inelastic properties of a phase (usually, the matrix) of a specific fibrous composite may also be used for other systems containing the same phase if close similarity is expected. Confidence in the approach can be gained only through satisfactory theoretical-experimental correlation. It seems that up to date, such correlation is still insufficient as far as inelastic response of unidirectional fibrous composites[2] to combined loading is concerned.

The above approach has been adopted to model isothermal, rate-independent inelastic macro-response of unidirectionally fiber-reinforced composites with an FE program called TPLAS. TPLAS was developed by use of (1) the first method depicted in Section 3, (2) constant strain, triangular finite elements, and (3) an adaptive iterative numerical scheme reported in Section 4 of [23]. To model a unidirectionally fiber-reinforced composite using TPLAS, a fiber is located at each vertex of the unit cells of a selected doubly periodic model. In general, there are four independent geometric parameters in the micromechanics modeling (e.g., the magnitudes of the two base vectors, the angle between the vectors, and the diameter of fibers), which must be specified a priori. In case of the periodic diamond model, three geometric parameters need be specified; in case of the periodic square model, only two geometric parameters need be specified. The subprograms which have been installed in TPLAS

---

[2] It should be noted that good agreement with experimental tensile data of certain balanced symmetric multidirectional laminates does not necessarily imply good agreement at the level of individual unidirectional laminae.

to calculate local material stiffness and stress response were developed for isothermal simulation by assuming that the elastic behavior of the phases is orthotropic and linear, and the plastic behavior is modeled with the endochronic theory without a yield surface [20]. The algorithmic tangent matrix approach for the endochronic theory [23] has been applied in the material subprograms.

The endochronic constitutive equation for plastically incompressible, rate-independent isotropic materials [20] is recapitulated below.

$$s_{ij} = \int_0^z \rho(z - z') \frac{d\varepsilon_{ij}^p}{dz'} dz' \tag{68}$$

where

$$dz = \frac{d\zeta}{f} \tag{69}$$

and

$$d\zeta = (d\varepsilon_{ij}^p d\varepsilon_{ij}^p)^{1/2} \tag{70}$$

$\rho(z)$ is a material function called the hereditary function. The other material function, f, is called the hardening function, and may be assumed to depend on z. The symbols s_{ij} and ε_{ij}^p are the deviatoric stress and plastic strain tensors, respectively. The parameter z is referred to as the intrinsic time. The kernel function $\rho(z)$ may be represented by an n-term Dirichlet series (not to be confused with the n in Section 3, which denotes the number of real nodes of a finite element),

$$\rho(z) = \sum_{r=1}^{n} C_r e^{-\alpha_r z} \tag{71}$$

with the requirement that $\rho(0)$ be sufficiently large in order to produce instantaneous elastic response at the onset of initial loading or subsequent unloading. C_r and α_r are material constants such that $\alpha_1 = 0$, $C_1 \geq 0$, and α_r and C_r are positive for $r \geq 2$.

Analysis involving material nonlinearity or path-dependence must start with known initial material states. Even in case of linear elasticity, initial material states are needed when one wants to know the total response (e.g., the stress state at a point), not merely the change. Therefore, micromechanics analysis for in-service loading of composites usually has to be extended backward to some point during fabrication where initial material states can be assumed. The present simulation of path-dependent macro-response to isothermal loading is extended backward to include a monotonic uniform cool-down. The cool-down is defined with the equivalent temperature change [3], ΔT, and is hypothetic because the material subprograms installed in TPLAS do not indeed have nonisothermal capability. The initial material states (at the beginning of the cool-down) are assumed as follows: Bonding between the phases is complete, the composite is microscopically stress-free, and each inelastic phase is in the virgin state of the endochronic theory, i.e., $z = 0$. We remark that the present approach may be suitable for prediction of macro-response when local plasticity (and hence, the effect of fading memory) develops noticeably during subsequent in-service loading. It should be borne in mind that the equivalent temperature change, ΔT, can be regarded as a material parameter of the present micromechanics approach, which must be backed out from experimental data of

composites. Linear orthotropic thermal expansion is taken into account by the material subprograms installed in TPLAS to simulate the cool-down.

Each specified thermomechanical loading increment usually necessitates several numerical iterations, each of which generates a sub-incremental solution. In the jth iteration of the ith loading increment, TPLAS constructs the linear FE equations based on the following approximate relation between the sub-incremental stress, $\Delta\boldsymbol{\sigma}^{i,j}$, and the sub-incremental strain, $\Delta\boldsymbol{\epsilon}^{i,j}$:

$$\Delta\boldsymbol{\sigma}^{i,j} = \begin{cases} \mathbf{C}^{e}\Delta\boldsymbol{\epsilon}^{i,j} - \mathbf{C}^{e}\Delta\boldsymbol{\epsilon}^{t,i} & \text{if } j = 1 \\ \mathbf{C}\Delta\boldsymbol{\epsilon}^{i,j} & \text{if } j \geq 2 \end{cases} \tag{72a, b}$$

where $\mathbf{C}^{e}$ is the elastic constitutive matrix; $\mathbf{C}$ is set equal to either $\mathbf{C}^{e}$ or the elastoplastic algorithmic tangent matrix by iteration-by-iteration decision in order to reduce computational time; and $\Delta\boldsymbol{\epsilon}^{t,i}$ is the ith thermal strain increment due to the ith temperature increment. Eq. 72a leads to calculation of incremental nodal forces due to an applied temperature increment, which are identical to those defined by Eq. 65 except that the $\Delta\boldsymbol{\sigma}$ of Eq. 65 is now replaced with $\mathbf{C}^{e}\Delta\boldsymbol{\epsilon}^{t,i}$. For more details regarding the numerical procedure, readers are referred to [23].

In the following, we compare our theoretical predictions against the experimental data of unidirectional boron/6061 aluminum composites reported by Becker et al. [29] and by Dvorak et al. [30]. TPLAS and the above-mentioned material sub-programs were used to carry out the simulation based on the simplest micromechanics approach.

The nominal fiber diameter (d) and volume fraction (v_f) were used to define the idealized micro-structure of each investigated B/Al composite. Micrographs of the B/Al composites [29, 30] suggest the very reasonable use of the periodic diamond model of Fig. 2a, where for the present cases, the center of a fiber is located at each vertex of the unit cells. The third (last) independent geometric parameter was selected as the monolayer thickness (the h in Fig. 4), and was estimated from the micrograph of a composite. Fig. 4 shows the idealized micro-structure in detail.

The mechanical behavior of the boron fibers is elastic and isotropic with the elastic bulk modulus, K_f, and the elastic shear modulus, G_f. The 6061 aluminum alloy matrix shows elastoplastic behavior. The elastic behavior of the matrix is isotropic with the elastic bulk modulus, K_m, and the elastic shear modulus, G_m. The thermal expansion of both phases is also isotropic with the coefficient of thermal expansion of the fibers, β_f, and of the matrix, β_m. $f \equiv 1$ (Eq. 69) was taken for the matrix in the simulation because the 6061 aluminum alloy does not show significant cyclic hardening. It has been found that the regular 6061-O aluminum alloy can be accurately modeled using a four-term Dirichlet series (Eq. 71) with $C_1 = 8.40 \times 10^2$ MPa, $\alpha_1 = 0$, $C_2 = 4.80 \times 10^3$ MPa, $\alpha_2 = 3.2 \times 10^2$, $C_3 = 1.16 \times 10^5$ MPa, $\alpha_3 = 3.6 \times 10^3$, $C_4 = 2.81 \times 10^6$ MPa, and $\alpha_4 = 4.0 \times 10^5$. The α_r, $r = 1, 2, 3, 4$, for the regular aluminum alloy were applied to the matrix, but the C_r, $r = 1, 2, 3, 4$, for the matrix must be determined from experimental data of the B/Al composites.

First, we consider a series of on-axis and off-axis tensile tests on unidirectional B/6061 Al coupons performed by Becker et al. [29]. The mid-plane of each tensile coupon was found to be parallel to the $x_3 = 0$ plane of Fig. 2a. Therefore, it suffices to analyze the trapezoid region OHIJ of the periodic diamond model (Fig. 2a) sub-

jected to proportional, monotonic plane stress loading with specified σ°_{11}, σ°_{22}, and σ°_{12}. To facilitate our discussion, another Cartesian coordinate system, (x, y, z), such that $z = x_3$ and the x axis is in the loading direction is established for each specimen.[3] The geometric parameters used for modeling the specimens are $v_f = 0.46$, $d = 0.142$ mm, and $h = 0.173$ mm, which define a periodic diamond model very close to a periodic hexagonal model. The trapezoid region for sufficient analysis was discretized into finite elements as shown in Fig. 5. The elastic material parameters are $K_f = 222.22 \times 10^3$ MPa, $G_f = 166.67 \times 10^3$ MPa, $K_m = 70.98 \times 10^3$ MPa, and $G_m = 27.22 \times 10^3$ MPa. The coefficients of thermal expansion are as follows: $\beta_f = 2.8 \times 10^{-6}\,(^\circ\,F)^{-1}$ and $\beta_m = 13.0 \times 10^{-6}\,(^\circ\,F)^{-1}$. Apparent tensile and compressive yield stresses were reported for different fiber angles in [29]. However, the results from 90° specimens appear to be the most reliable both in tension and in compression (i.e., the yield stresses in σ°_{22} tension and in σ°_{22} compression). The elastic FE analysis by Dvorak et al. [31] suggests that for the B/6061 Al system, the size of elastic range in σ°_{22} is insensitive to elastic cool-down. As a result, the mean of the stress levels of apparent tensile and compressive yielding (48 MPa and 40 MPa, respectively) of the 90° specimens is a good estimate of the apparent elastic limit of the model before the cool-down. By temporarily taking the endochronic material parameter $C_1 = C_2 = C_3 = 0$, the C_4 of the matrix which results in the TPLAS prediction of the desired apparent elastic limit before the cool-down (44 MPa), can be determined quickly. Note that the endochronic memory function which contains only the fast-decaying term, $C_4 e^{-\alpha_4 z}$, corresponds to a nearly perfectly plastic model for the matrix. Then, the equivalent temperature change, ΔT, which results in the desired apparent tensile yield stress after the cool-down (48 MPa), can be quickly determined using

---

[3] When a tensor which has been defined in reference to the (x_1, x_2, x_3) coordinate system previously is referred to the (x, y, z) coordinate system in the following, we will continue to use the previous tensorial notation except its subscripts. The subscripts will be rewritten in terms of x, y, and z.

TPLAS. ΔT was found to be $-10°$ F.[4] Shown in Fig. 6 are the theoretical transverse tensile responses with the preceding cool-down (the continuous line)[5] and without the cool-down (the broken line), respectively. Having ΔT and C_4, we can add one exponential term at a time to the memory function in order to produce further hardening. Since among the reported tensile curves of 0°, 10°, 15°, 30°, 45°, 60°, and 90° specimens, the 10° curve is the most sensitive to the nonlinear shear response of the matrix, the experimental tensile data of the 10° specimen (the squares in Fig. 7) were selected for determination of C_1, C_3, and C_2 in turn. First, C_1 was determined to generate curve 1 of Fig. 7 so that the desired asymptotic slope was obtained (at this moment, $C_3 = C_2 = 0$). Subsequently, an appropriate C_3 was chosen to generate curve 2 of Fig. 7 which matches the lower knee portion of the experimental data (at this moment, $C_2 = 0$). Finally, C_2 was backed out, and the "buildup" of the theoretical response (curve 3 of Fig. 7) was completed with $C_1 = 8.43 \times 10^2$ MPa, $C_2 = 5.12 \times 10^3$ MPa, $C_3 = 8.00 \times 10^4$ MPa, and $C_4 = 1.78 \times 10^7$ MPa. Shown in Fig. 8 are respective stress-strain curves of the regular 6061-O aluminum alloy (the broken line) and 6061 aluminum alloy matrix (the continuous line), both represented by the endochronic theory. The squares in the figure are experimental data of the regular aluminum alloy. Note that each simulation for determining C_1, C_2, or C_3 started at the beginning of the cool-down, and required approximately 15 CPU seconds on an IBM 3090-300E computer. We also emphasize that the trial-and-error procedure for determining the

---

[4] Another estimate of ΔT can be obtained by fitting the apparent compressive yield stress. When considerable difference occurs, an average can be adopted. The average can even be used to redetermine C_4; thus, an iterative procedure can be devised. Practically, no improvement of C_4 or ΔT is necessary for the B/6061 Al system.

[5] At the end of the cool-down, the normal macro-strains are negative because of the thermal contraction of both phases. In Fig. 6 and in any following figure where subsequent change in macro-strain due to mechanical loading is shown, the macro-strain is offset so that it reads as zero at the beginning of the mechanical loading.

plastic material parameters and effective temperature change is systematic and efficient because of the use of the endochronic theory.

We are ready to simulate isothermal inelastic behavior of a unidirectionally fiber-reinforced composite when all the model parameters, as in the above, are in hand. The continuous lines in Figs. 9 - 15 are the TPLAS predictions for the tensile tests reported in [29], which were obtained by using the above parameters. The symbols in the figures represent the experimental data. In general, good agreement has been consistently achieved in both the axial and the Poisson's responses from one fiber angle to another when the axial strain $\varepsilon^{\circ}_{xx} < 0.25\%$. The consistency suggests the use of experimental data from the convenient tests on 90° specimens to determine all the material parameters.

We next consider a stress-controlled tension-torsion experiment on a unidirectional B/6061 Al tube performed by Dvorak et al. [30]. The fibers are in the axial direction of the tube; and the local radial direction of the tube was found to be parallel with the x_3 axis of Fig. 2a. Therefore, it suffices to analyze the trapezoid region OHIJ of the periodic diamond model (Fig. 2a) subjected to a loading history of σ°_{11} and σ°_{12}. The geometric parameters used for modeling the composite are $v_f = 0.45$, $d = 0.142$ mm, and $h = 0.194$ mm. The FE grid is shown in Fig. 16. The elastic moduli of the fibers are $K_f = 240.44 \times 10^3$ MPa, and $G_f = 180.33 \times 10^3$ MPa. In addition, K_m, G_m, β_f, and β_m are the same as used for the foregoing application. The experimental loading path and response are shown by the squares in Fig. 17a and Figs. 17b - d, respectively. Because the measured shear response (Fig. 17d) exhibits uncertain unsymmetry, the simulation was performed by specifying σ°_{11} and ε°_{12} throughout the loading history in order to attain a meaningful comparison. Another procedure for determination of the

endochronic material parameters C_r of the matrix and the equivalent temperature change ΔT was employed for lack of necessary experimental data. First, we note that the cyclic ratcheting of ε_{11}^{o} during the initial pure shear loading and subsequent reverse loading (Fig. 17b) is due to compressive longitudinal stress in the fibers induced by the cool-down. Let $\varepsilon_{11}^{o,c}$ denote ε_{11}^{o} at the end of the cool-down, and let $\Delta\varepsilon_{11}^{o,r}$ denote the saturated growth of the ratcheting strain. The simple strength-of-materials analysis for balance of the longitudinal forces gives

$$E_f(\varepsilon_{11}^{o,c} - \Delta T\beta_f)v_f + E_m(\varepsilon_{11}^{o,c} - \Delta T\beta_m)(1 - v_f) = 0 \tag{73}$$

where E_f and E_m are the Young's moduli of the fibers and matrix, respectively. Since the compressive longitudinal thermal stress in the fibers is almost completely relaxed when the saturation of cyclic ratcheting is reached, the following approximation can be made:

$$(\varepsilon_{11}^{o,c} + \Delta\varepsilon_{11}^{o,r}) - \Delta T\beta_f = 0 \tag{74}$$

Judging from Fig. 17b, if the saturation had been reached, $\Delta\varepsilon_{11}^{o,r}$ should have been approximately 120×10^{-6}, which can be used to solve Eqs. 73 and 74 to get the estimate $\Delta T = -70°$ F. Then, C_4, C_1, C_3, and C_2 were determined in turn so as to fit the experimental data of the last reverse shear loading (Fig. 17d). The response to the last reverse shear loading (Fig. 17d) was chosen for curve-fitting because of its proximity to the cyclically stable response, the uncertain unsymmetry in the measured shear deformation, and the observed minor cyclic hardening. The C_r for the current demonstration were obtained as follows: $C_1 = 6.72 \times 10^2$ MPa, $C_2 = 4.80 \times 10^3$ MPa, $C_3 = 1.16 \times 10^5$ MPa, and $C_4 = 1.26 \times 10^7$ MPa. Shown in Fig. 18 are respective stress-strain curves of the regular 6061-O aluminum alloy (the broken line) and 6061 aluminum alloy matrix (the continuous line). The theoretical responses to the initial

shear loading in Fig. 17d with the preceding cool-down (the continuous line) and without the cool-down (the broken line), respectively, are shown in Fig. 19. Recall that cyclic hardening has been neglected in the present model for the B/6061 Al system by assuming $f \equiv 1$. No matter whether cyclic hardening of a composite is considerable or not, C_r obtained by fitting a stabilized stress-strain loop under a strain-controlled cyclic loading with a constant amplitude of either ε_{22}^{g} or ε_{12}^{g} and a zero mean should be suitable for prediction of long-term behavior, which is the primary concern in many cases.

The model response shown by the continuous lines in Figs. 17a - d displays more qualitative regularity than the experimental data. There seems to be some uncertainty about experimental reproducibility of the test data. The present model has shown the potential for quantitative characterization of complicated cyclic behavior; however, it is clear that more comparions with cyclic test results, especially from strain-controlled tests, are indeed required.

5. Effects of Model Geometry on Overall Plastic Response

We recall that the foregoing simulation of the experiments of Becker et al. [29] employed the Periodic Diamond Model with Circular Fibers (PDMCF) as suggested by the micrographs. One may question the possibility of obtaining similar or even better theoretical-experimental agreement if using another set of plastic material parameters in conjunction with the Periodic Square Model with Circular Fibers (PSMCF).

On the other hand, a higher-ordered continuum theory for the Periodic Rectangular Model with Rectangular Fibers (PRMRF) has been derived by Aboudi [32]. Surmising that under uniform macro-loading: (1) the overall behavior of PSMCF is nearly the same as that of the Periodic Square Model with Square Fibers (PSMSF) if both types of fibers have an identical cross-sectional area, and (2) the overall behavior of PSMSF can be well represented by first-ordered approximation, Aboudi and his co-workers have applied a first-ordered theory to model inelastic macro-response of various composites, all of which are actually reinforced with circular fibers (e.g., [3, 4]). Good

agreement has been found between the overall inelastic response of PSMSF predicted using Aboudi's first-ordered theory and that of PSMCF predicted using the FE method [33, 34]. However, the above two conjectures have not been directly justified.

Motivated by the questions, we used TPLAS and the same fiber diameter, fiber volume fraction, elastoplastic material parameters, and equivalent temperature change, as for the B/Al composite specimens of Becker et al. [29], to simulate the overall responses of PSMCF and PSMSF to transverse tensile and longitudinal shear loadings. The FE grids are shown in Figs. 20 and 21. The transverse tensile responses are shown in Figs. 22a and b, and the longitudinal shear responses in Fig. 23. Also shown in Figs. 22 and 23 for comparison are the TPLAS predictions for the previous PDMCF. The simulation was repeated using the endochronic memory function which contains only the $C_4e^{-\delta_4 z}$ term; the results are shown in Figs. 24 and 25. Simulation of the longitudinal tensile responses of PSMCF and PSMSF was also performed; virtually, no difference among PDMCF, PSMCF, and PSMSF was observed for this case.

Three conclusions can be drawn from the results of the above numerical experiments. The conclusions should be valid if fibers are much stiffer under transverse tension and longitudinal shear than the matrix.

1. The PSMCF curve is considerably above the PDMCF curve in Fig. 22a, but the opposite situation is seen in Fig. 23.

2. That the difference in elastic transverse tensile response (Figs. 22a and b) and in longitudinal shear response (Fig. 23) between PSMSF and PSMCF is negligible is confirmed. However, the difference in plastic transverse tensile response is by no means negligible; PSMSF shows very strong constraint hardening.

3. Since the overall behavior of PSMSF predicted using Aboudi's first-ordered theory is in good agreement with that of PSMCF predicted using the FE method, the first-ordered representation of the plastic transverse tensile response of PSMSF must seriously deviate from a higher-ordered representation which is accurate enough for PSMSF.

Thus, regarding the on-axis and off-axis tests of Becker et al. [29], it is impossible to attain similar or better theoretical-experimental agreement if using another set of plastic material parameters in conjunction with PSMCF. For comparison, the various on-axis and off-axis tensile curves of PSMCF, obtained with the same parameters, are shown in Figs. 9 - 15 (the broken lines). On the other hand, PSMSF is unrealistic for modeling the macroscopic plastic behavior of the B/6061 Al composite of [29]. Interestingly, one can expect that if using Aboudi's theory to model the B/6061 Al composite of [29], the higher the order of the representation, the worse the theoretical-experimental correlation.

As a final remark on Aboudi's first-ordered theory for PRMRF, we show in the following that Aboudi's first-ordered approximation is equivalent to an FE approximation using four nonconforming, constant strain, triangular finite elements in conjunction with the first method of Section 3. The four triangular elements, shown in Fig. 26, make up a smallest region for sufficient analysis of PRMRF by using Eqs. 38 - 41 and 43 - 46. $\bar{\mathbf{a}}_i$, $i = 1, 2, ..., 8$, are defined at the mid-points of the edges of the four triangular elements, and $\bar{\mathbf{a}}_9$ and $\bar{\mathbf{a}}_{10}$ represent the average strain, $\boldsymbol{\epsilon}^o$. Since there is no master or slave node, $\phi(i, e)$ is of no use and Eqs. 38 - 40 can be simplified. All the boundary conditions are of type 2, and the displacement boundary conditions are satisfied simply by imposing $\bar{\mathbf{a}}_i = \mathbf{0}$ at nodes O, D, H, and G (Fig. 26). The equivalence

between the FE approximation and Aboudi's first-ordered theory is evidenced by the following features of the FE model: (1) The model contains 12 degrees of freedom for 3-D strain-controlled simulation, and 18 degrees of freedom for 3-D stress-controlled simulation. (2) The displacement field is linear in each element, and displacement continuity along an element interface is guaranteed only at its mid-point. (3) Traction continuity is satisfied along any of the four element interfaces.

6. Concluding Remarks

The simple and unified weak formulation and its convenient FE implementation have been proposed. The weak formulation is valid for any doubly periodic model under general macro-loading, and serves as a common rational foundation of different FE approaches. The algorithmic tangent matrix approach for the endochronic theory has been incorporated into the FE formulation to model isothermal, rate-independent plastic macro-deformation of unidirectional fibrous composites using the simplest micromechanics approach. The methods for determining the associated inelastic material parameters have been established. The numerical results for the B/6061 Al composite of [29] under proporional monotonic plane stress loading are in good agreement with the experimental data. The micromechanics model also shows the potential for quantitative characterization of complicated cyclic behavior. It was found for the B/6061 Al composite of [29] that PSMSF is unrealistic, and the use of PSMCF will deteriorate the quality of theoretical-experimental correlation no matter how the plastic material parameters are adjusted. In addition, if Aboudi's theory is used to model the B/6061 Al composite of [29], the higher the order of the representation, the worse the theoretical-experimental correlation.

Future research is recommended as follows:

1. Recent advancement [35] indicates that the accurate overall plastic response of a composite model, such as used in Section 4, can be obtained with a small number of degrees of freedom if the approximate displacement field is admissible to Eq. 23 or 37, the fibers are modeled as hexagonal cylinders, and plastic locking is avoided. Therefore, numerical efficiency can be further greatly improved by judicious selection and discretization of a smallest region for sufficient analysis. When testing a mini model, the presented FE solutions can be considered the base-line solutions. It is believed that the culmination of the numerical techniques for computing macro-response is reached when the algorithmic tangent matrix approach and a successful mini model are employed simultaneously. Such implementation would be promising for integrated micro-macro inelastic analysis of composite structures.

2. Further verification for strain-controlled cyclic loading and for other material systems is needed before a general evaluation of the simplest micromechanics approach in conjunction with the endochronic FE analysis can be made.

3. The algorithmic tangent matrix approach for the endochronic theory has the potential for straightforward extension to viscoplasticity. Since rate-dependent behavior of unidirectional fibrous composites is usually a concern in advanced high temperature applications, the extension deserves future efforts.

References

1. Teply J. L. and Dvorak, G. J., "Bounds on Overall Instantaneous Properties of Elastic-Plastic Composites," *Journal of the Mechanics and Physics of Solids*, Vol. 36, 1988, pp. 29 - 58.

2. Wu, J. F., Shephard, M. S., Dvorak, G. J., and Bahei-El-Din, Y. A., "A Material Model for the Finite Element Analysis of Metal Matrix Composites," *Composites Science and Technology*, Vol. 35, 1989, pp. 347 - 366.

3. Pindera, M-J., Herakovich, C. T., Becker, W., and Aboudi, J., "Nonlinear Response of Unidirectional Boron/Aluminum," *Journal of Composite Materials*, Vol. 24, 1990, pp. 2 - 21.

4. Aboudi, J., "Micromechanical Characterization of the Non-linear Viscoelastic Behavior of Resin Matrix Composites," *Composites Science and Technology*, Vol. 38, 1990, pp. 371 - 386.

5. Ha, S. K., Wang, Q., and Chang, F. K., "Modeling the Viscoplastic Behavior of Fiber-Reinforced Thermoplastic Matrix Composites at Elevated Temperatures," *Journal of Composite Materials*, Vol. 25, 1991, pp. 334 - 374.

6. Sun, C. T. and Chen, J. L., "A Micromechanical Model for Plastic Behavior of Fibrous Composites," *Composites Science and Technology*, Vol. 40, 1991, pp. 115 - 129.

7. Jansson, S., "Mechanical Characterization and Modeling of Non-linear Deformation and Fracture of a Fiber Reinforced Metal Matrix Composite," *Mechanics of Materials*, Vol. 12, 1991, pp. 47 - 62.

8. Stango, R. J., Wang, S. S., and Nelson, C. R., "A Note on Analytical Representation of Anisotropic Viscoelastic Constitutive Equations for Fiber-Reinforced Composites," *Composites Science and Technology*, Vol. 35, 1989, pp. 273 - 282.

9. Robinson, D. N. and Duffy, S. F., "Continuum Deformation Theory for High-Temperature Metallic Composites," *Journal of Engineering Mechanics*, Vol. 116, 1990, pp. 832 - 844.

10. Yoon, K. J. and Sun, C. T., "Characterization of Elastic-Viscoplastic Properties of an AS4/PEEK Thermoplastic Composite," *Journal of Composite Materials*, Vol. 25, 1991, pp. 1277 - 1296.

11. Rosen, B. W., "Materials by Design," *ASTM Standardization News*, October 1987, pp. 40 - 43.

12. Adams, D. F., "Inelastic Analysis of a Unidirectional Composite Subjected to Transverse Normal Loading," *Journal of Composite Materials*, Vol. 4, 1970, pp. 310 - 328.

13. Adams, D. F. and Miller, A. K., "Hygrothermal Microstresses in a Unidirectional Composite Exhibiting Inelastic Material Behavior," *Journal of Composite Materials*, Vol. 11, 1977, pp. 285 - 299.

14. Miller, A. K. and Adams, D. F., "Inelastic Finite Element Analysis of a Heterogeneous Medium Exhibiting Temperature and Moisture Dependent Material Properties," *Fibre Science and Technology*, Vol. 13, 1980, pp. 135 - 153.

15. Adams, D. F. and Crane, D. A., "Combined Loading Micromechanical Analysis of a Unidirectional Composite," *Composites*, Vol. 15, 1984, pp. 181 - 191.

16. Foye, R. L., "Theoretical Post-Yielding Behavior of Composite Lamintes: Part I - Inelastic Micromechanics," *Journal of Composite Materials*, Vol. 7, 1973, pp. 178 - 193.

17. Foye, R. L., "Theoretical Post-Yielding Behavior of Composite Lamintes: Part II - Inelastic Macromechanics," *Journal of Composite Materials*, Vol. 7, 1973, pp. 310 - 319.

18. Foye, R. L., "Inelastic Micromechanics of Curing Stresses in Composites," *Inelastic Behavior of Composite Materials*, ASME AMD-Vol. 13, Herakovich, C. T., ed., 1975, pp. 177 - 211.

19. Teply J. L. and Dvorak, G. J., "Dual Estimates of Overall Instantaneous Properties of Elastic- Plastic Composites," Proceedings, *5th International Symposium on Continuum Models of Discrete Systems*, Spencer, A. J. M., ed., Nottingham, UK, 1985, pp. 205 - 216.

20. Valanis, K. C., "Fundamental Consequences of a New Intrinsic Time Measure: Plasticity as a Limit of the Endochronic Theory," *Archives of Mechanics*, Vol. 32, 1980, pp. 171 - 191.

21. Sugiura, K., Lee, G. C., and Chang, K. C., "Endochronic Theory for Structural Steel under Nonproportional Loading," *Journal of Engineering Mechanics*, Vol. 113, 1987, pp. 1901 - 1917.

22. Malvern, L. E., "The Propagation of Longitudinal Waves of Plastic Deformation in a Bar of Material Exhibiting a Strain-Rate Effect," *Journal of Applied Mechanics*, Vol. 18, 1951, pp. 203 - 208.

23. Hsu, S. Y. and Griffin, O. H., Jr., "Efficient Endochronic Finite Element Analysis: an Example of a Cyclically Loaded Boron/Aluminum Composite," Technical Report VPI-E-92-08, College of Engineering, Virginia Polytechnic Institute and State University, Blacksburg, Virginia, 1992.

24. Hsu, S. Y., Jain, S. K., and Griffin, O. H., Jr., "Verification of Endochronic Theory for Nonproportional Loading Paths," *Journal of Engineering Mechanics*, Vol. 117, 1991, pp. 110 - 131.

25. Hsu, S. Y. and Griffin, O. H., Jr., "On Stability and Efficiency of Numerical Integration of Endochronic Constitutive Equations," *Computers and Structures*, Vol. 44, 1992, pp. 657 - 665.

26. Hashin, Z., "Analysis of Composite Materials - A Survey," *Journal of Applied Mechanics*, Vol. 50, 1983, pp. 481 - 505.

27. Zienkiewicz, O. C., Section 3.2, *The Finite Element Method*, McGraw-Hill Book Company, Maidenhead, Berkshire, UK, 1977.

28. Lubliner, J., Section 4.5, *Plasticity Theory*, Macmillan Publishing Company, New York, 1990.

29. Becker, W., Pindera, M. J., and Herakovich, C. T., "Mechanical Response of Unidirectional Boron/Aluminum under Combined Loading," Technical Report VPI-E-87-17, College of Engineering, Virginia Polytechnic Institute and State University, Blacksburg, Virginia, 1987.

30. Dvorak, G. J., Bahei-El-Din, Y. A., Macheret, Y., and Liu, C. H., "An Experimental Study of Elastic-Plastic Behavior of a Fibrous Boron-Aluminum Composite," Technical Report to Office of Naval Research, Contract No. N00014-85-K-0247, and U. S. Army Research Office, Contract No. DAAG29-85-K-0011, Department of Civil Engineering, Rensselaer Polytechnic Institute, Troy, New York, 1988.

31. Dvorak, G. J., Rao, M. S. M., and Tarn, J. Q., "Yielding in Unidirectional Composites under Exteral Loads and Temperature Changes," *Journal of Composite Materials*, Vol. 7, 1973, pp. 194 - 216.

32. Aboudi, J., "A Continuum Theory for Fiber-Reinforced Elastic-Viscoplastic Composites," *International Journal of Engineering Science*, Vol. 20, 1982, pp. 605 - 621.

33. Aboudi, J., "Effective Behavior of Inelastic Fiber-Reinforced Composites," *International Journal of Engineering Science*, Vol. 22, 1984, pp. 439 - 449.

34. Aboudi, J., "The Effective Thermomechanical Behavior of Inelastic Fiber-Reinforced Materials," *International Journal of Engineering Science*, Vol. 23, 1985, pp. 773 - 787.

35. Dvorak, G. J., Bahei-El-Din, Y. A., Shah, R. S., and Nigam, H., "Experiments and Modeling in Plasticity of Fibrous Composites," *Inelastic Deformation of Composite Materials*, Dvorak, G. J., ed., Springer-Verlag New York, Inc., New York, 1991, pp. 283 - 306.

Figures

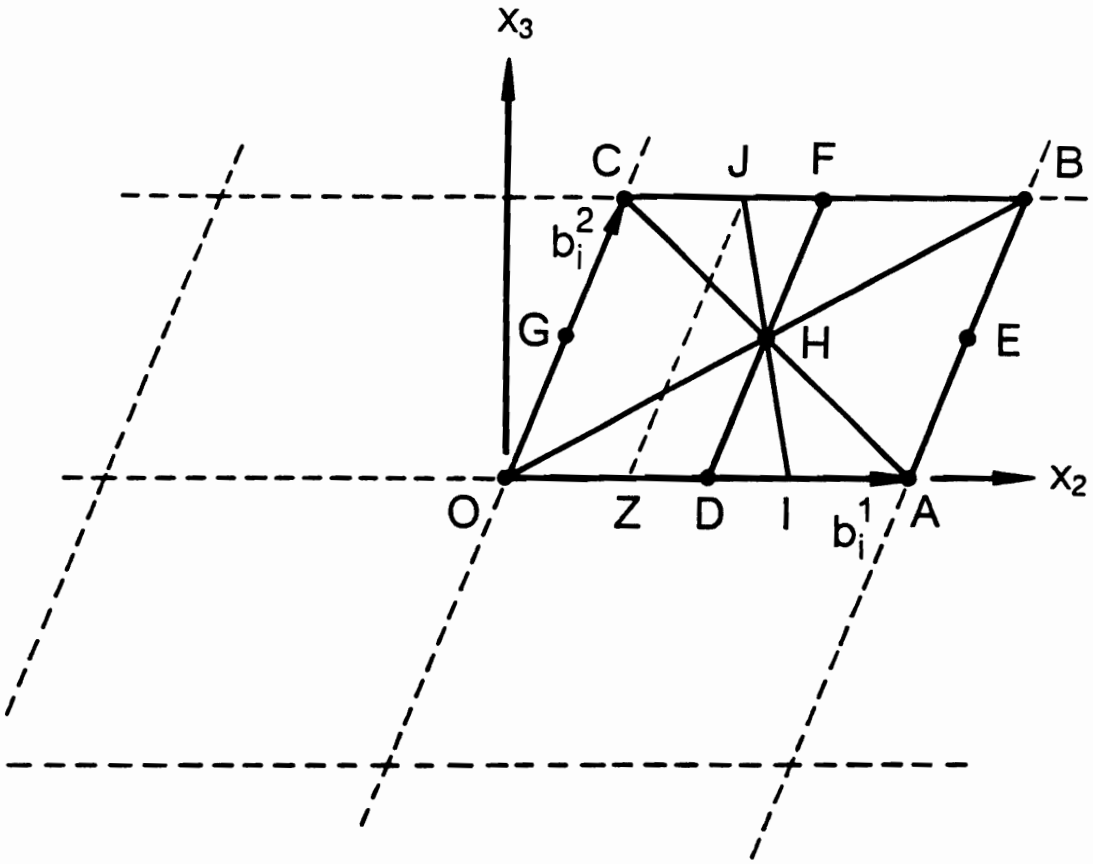

Figure 1. Doubly Periodic Model

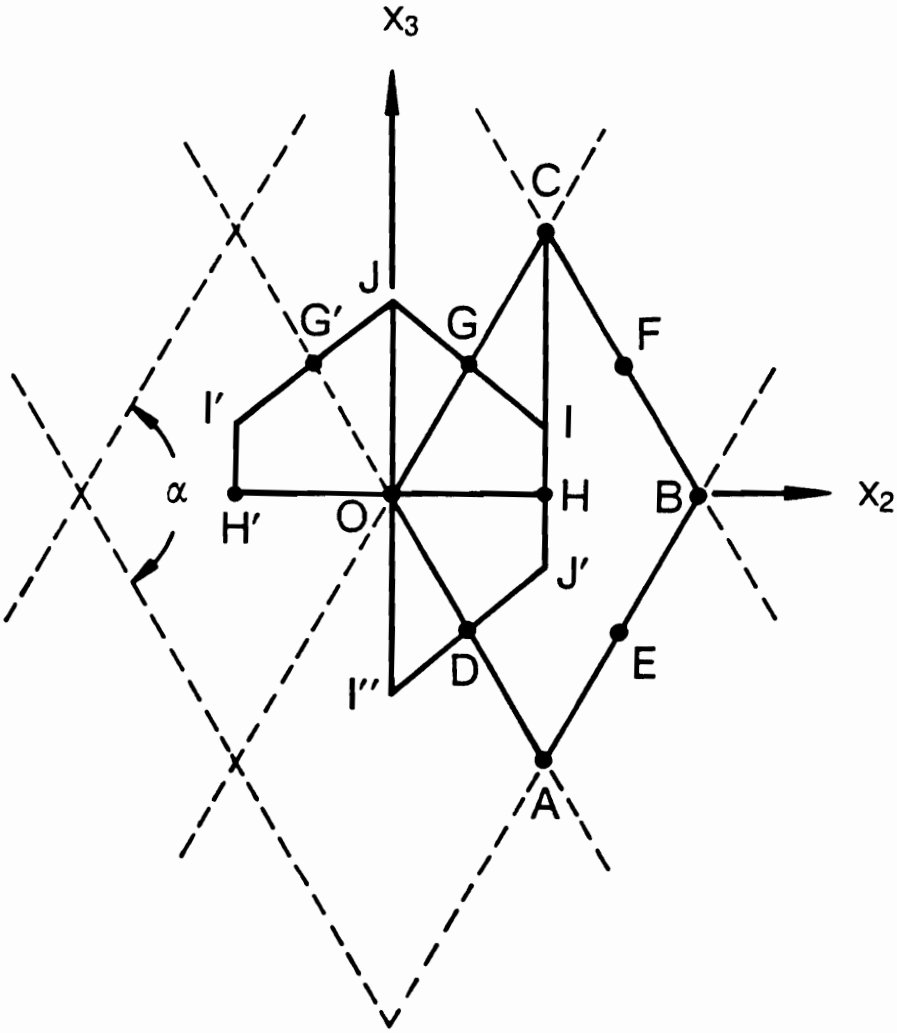

Figure 2a. Periodic Diamond Model: $90° < \alpha < 180°$

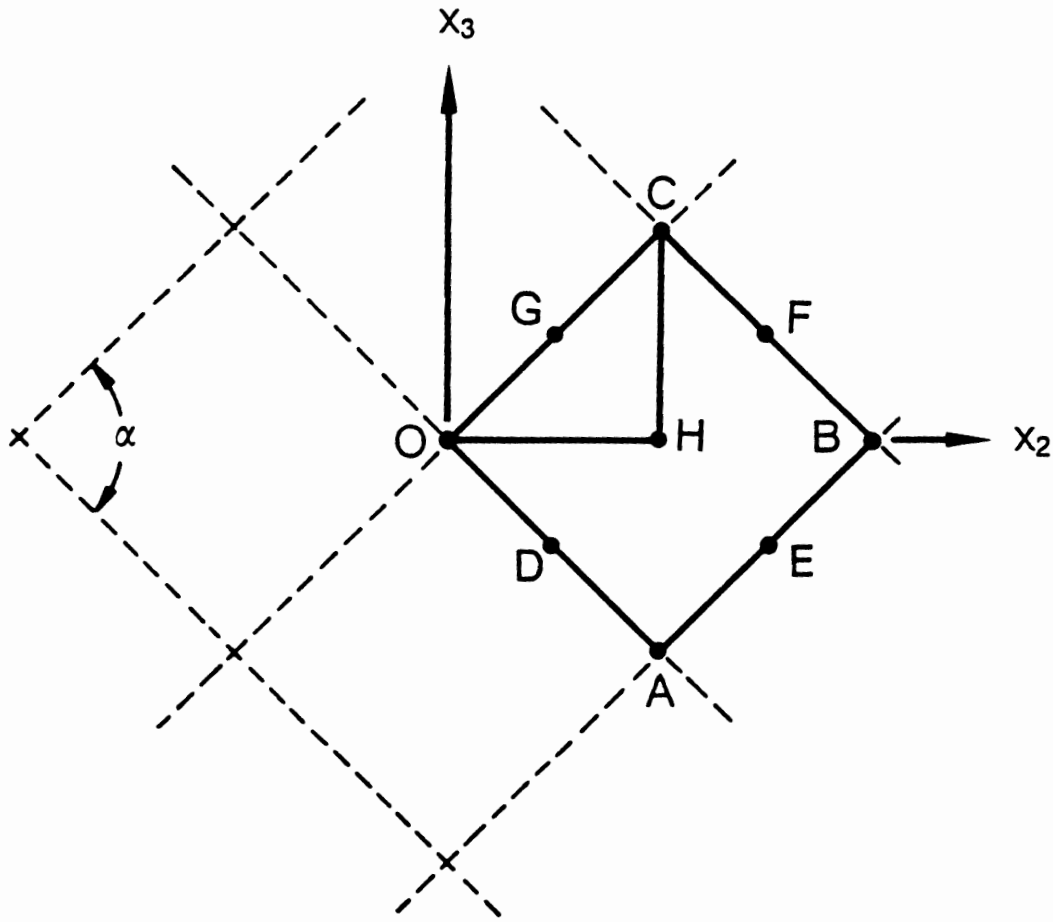

Figure 2b. Periodic Diamond Model: $\alpha = 90°$

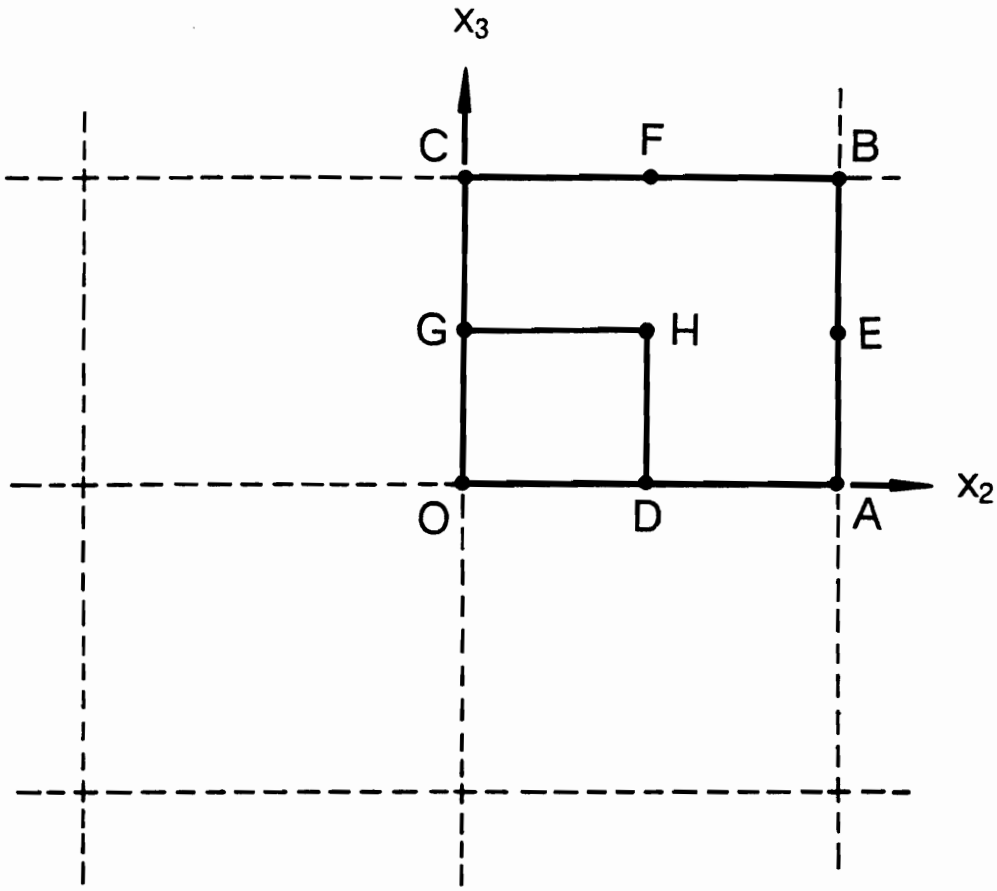

Figure 3. Periodic Rectangular Model

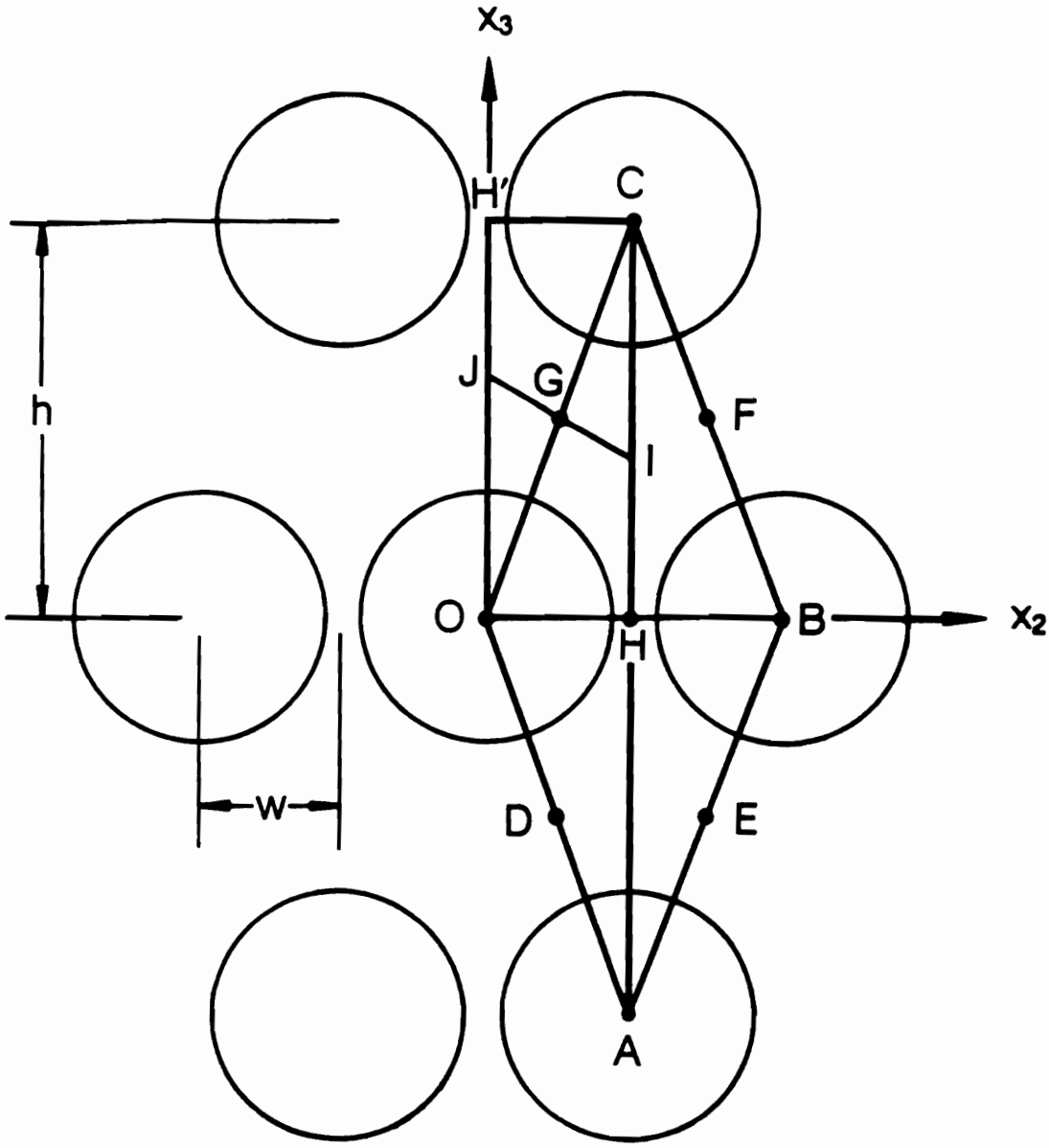

Figure 4. Idealized Micro-structure of B/6061 Al Composites

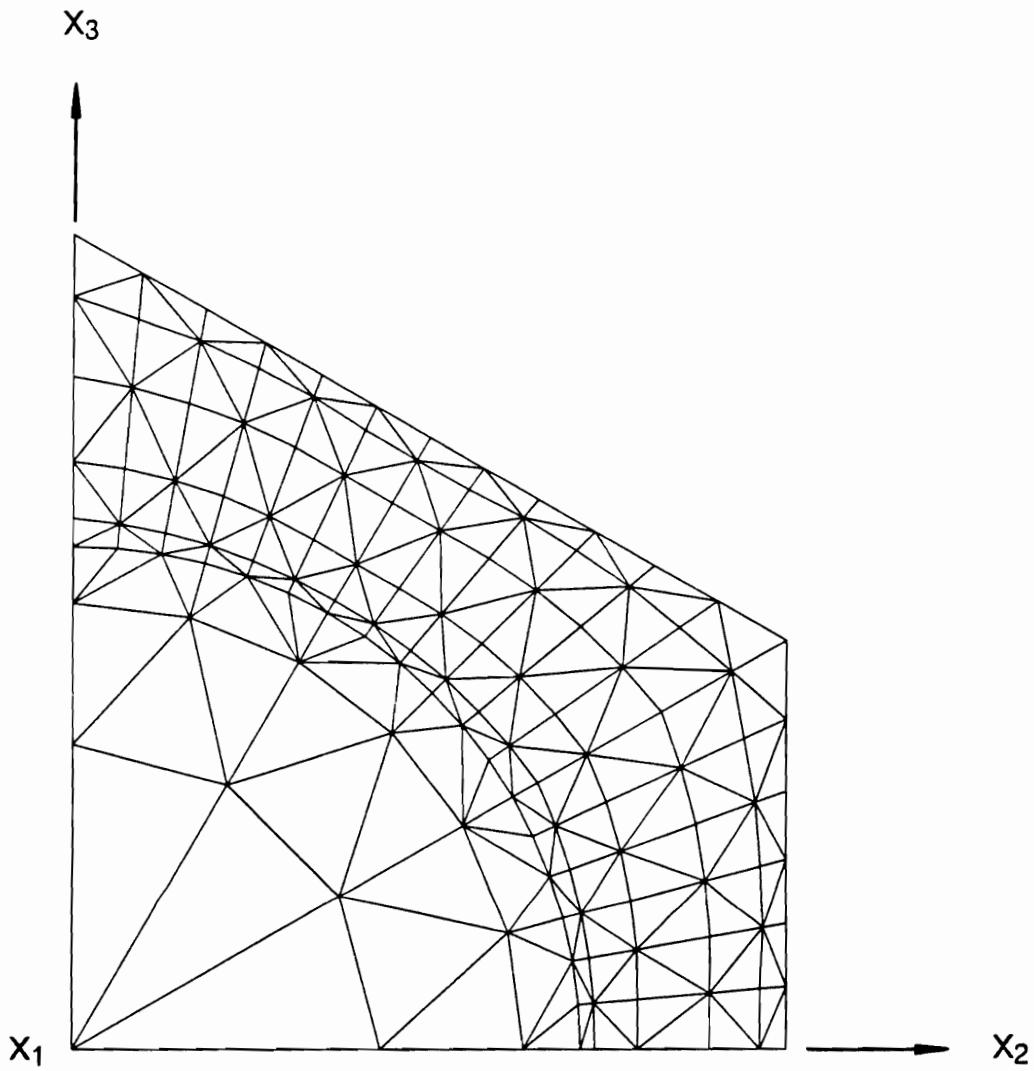

Figure 5. Finite Element Grid for Modeling B/6061 Al Composite of [29]

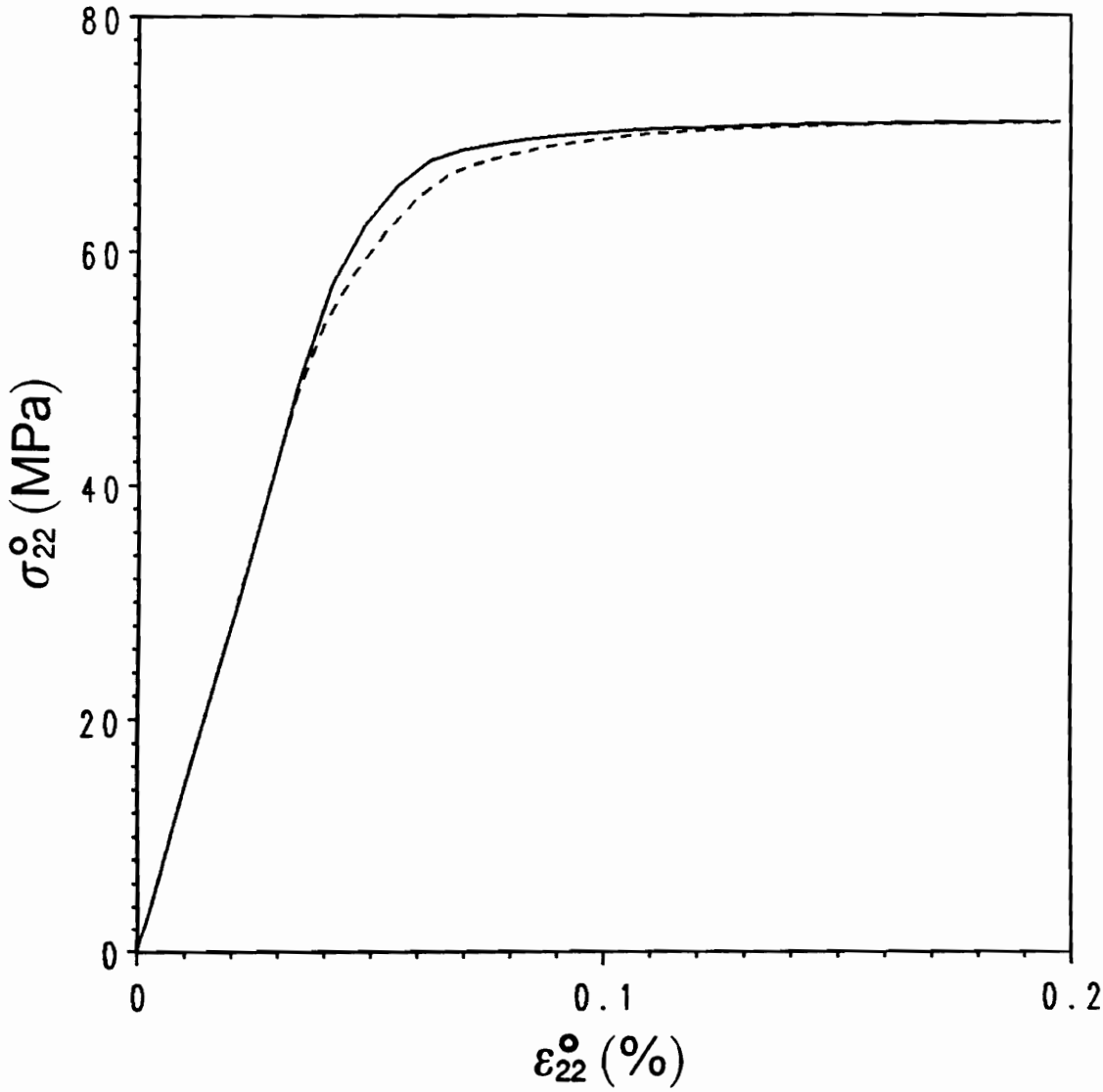

Figure 6. Illustrating Determination of Material Parameters: First, C_4 was determined so that the TPLAS prediction (the broken line) shows an apparent elastic limit of 44 MPa before the cool-down. By using C_4, ΔT was determined to obtain the TPLAS prediction (the continuous line) showing an apparent elastic limit of 48 MPa.

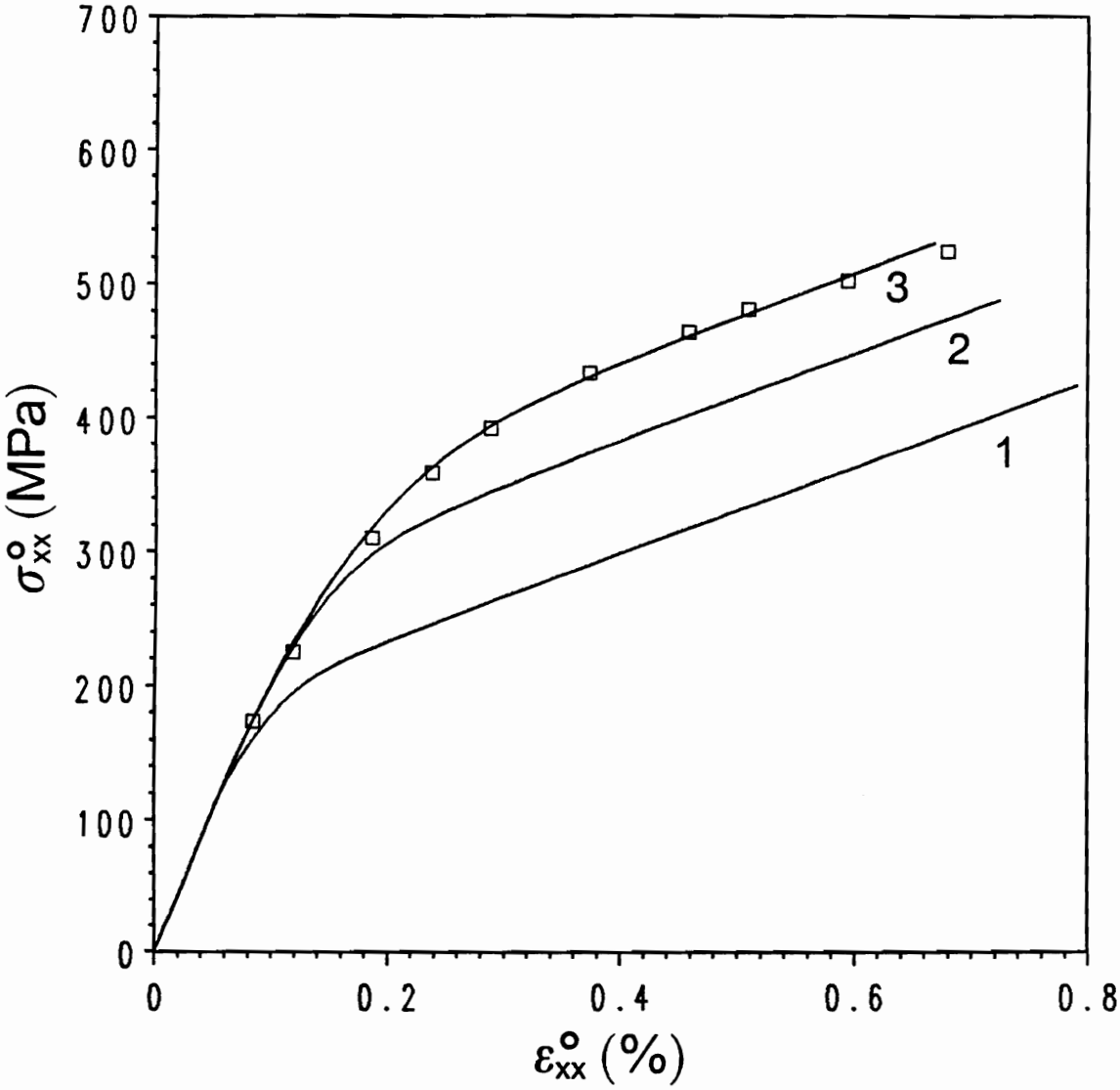

Figure 7. Illustrating Determination of Material Parameters: The squares represent the experimental 10° off-axis tensile data from [29]. By using C_4 and ΔT, C_1 was chosen to obtain the desired asymptotic slope (curve 1). Then, C_3 was chosen to produce the lower knee portion (curve 2), and finally, C_2 to produce the upper knee portion (curve 3).

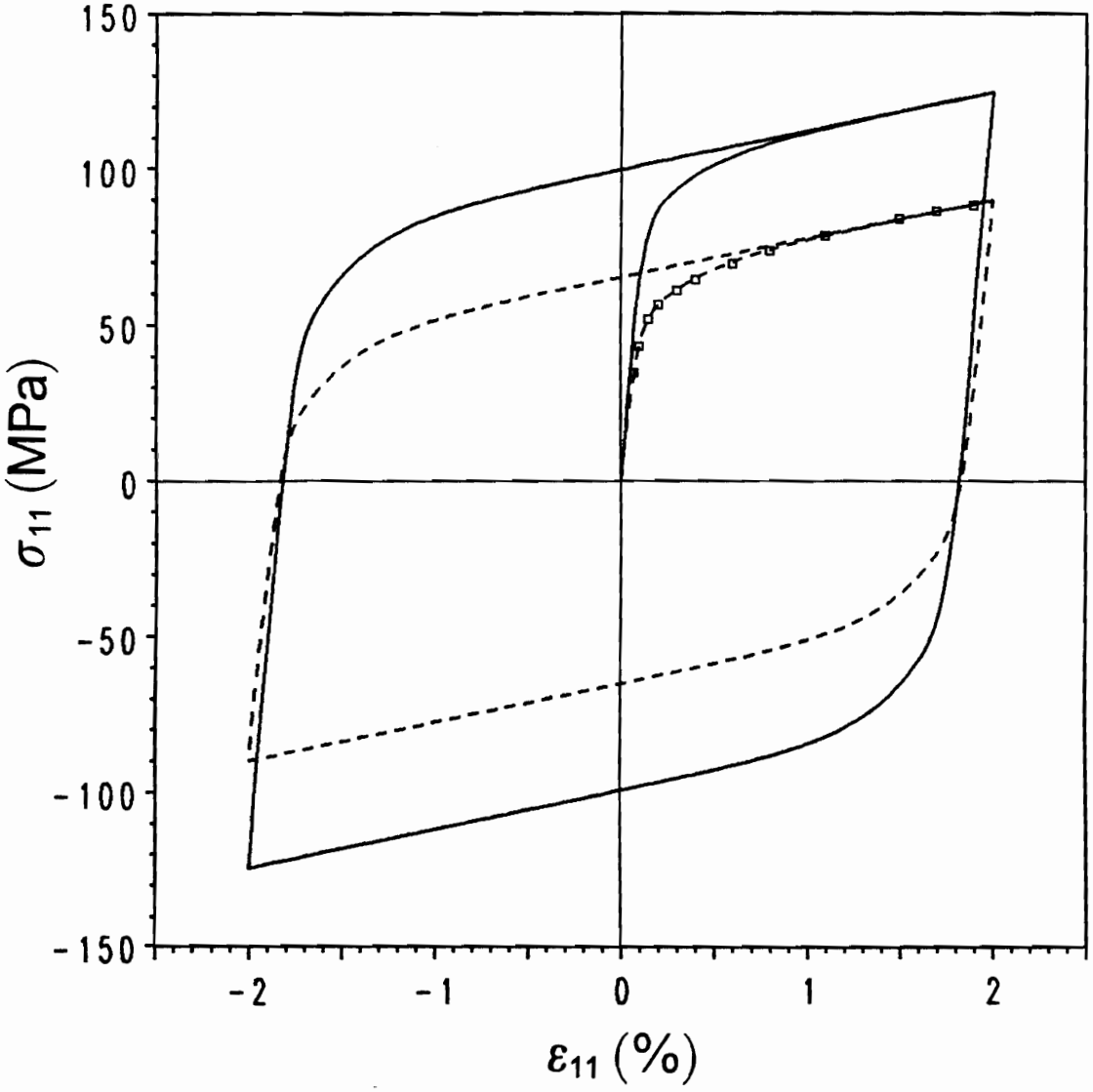

Figure 8. Stress-Strain Curves of Regular 6061-O Aluminum Alloy and 6061 Aluminum Alloy Matrix: The broken line represents the model response of the regular aluminum alloy, and the continuous line the aluminum alloy matrix of [29]. The squares represent the experimental data of the regular aluminum alloy.

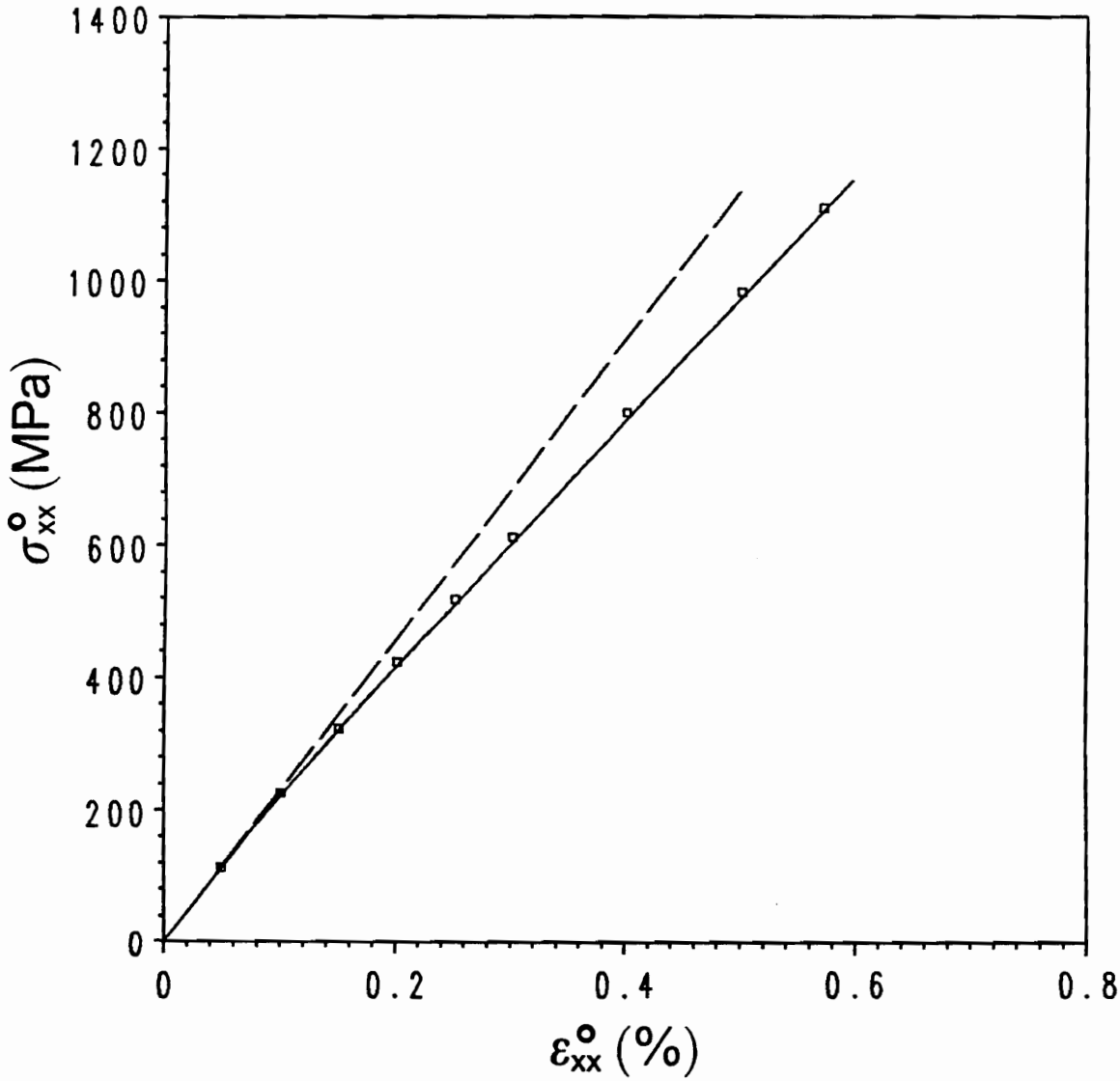

Figure 9a. Axial Response of 0° Specimen: The predictions using the periodic diamond model and periodic square model are represented by the continuous line and short broken line, respectively, and are virtually indistinguishable for the 0° specimen. The squares represent the experimental data from [29], and the long broken line indicates the experimental initial linearity.

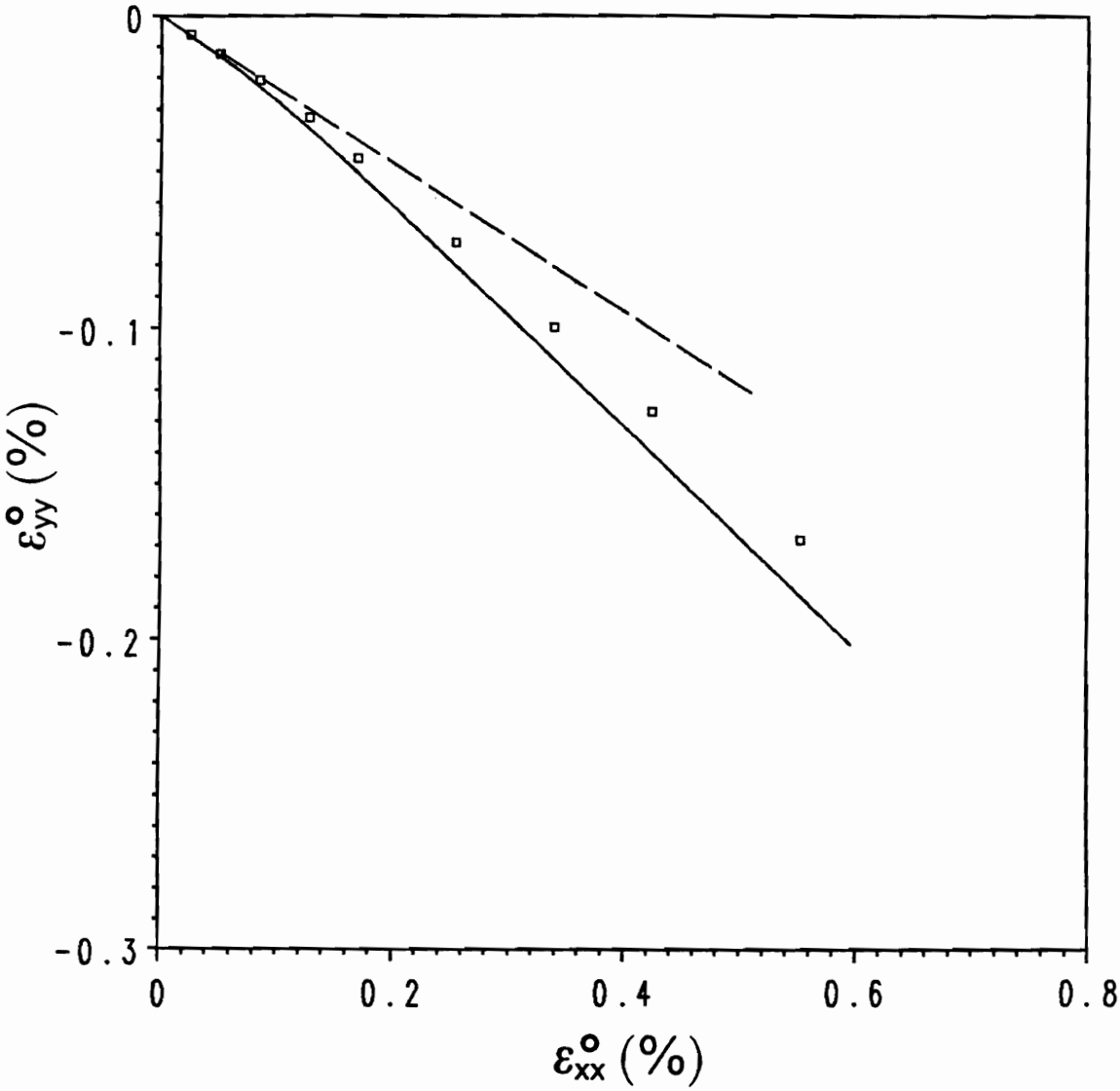

Figure 9b. Poisson's Response of 0° Specimen: The predictions using the periodic diamond model and periodic square model are represented by the continuous line and short broken line, respectively, and are virtually indistinguishable for the 0° specimen. The squares represent the experimental data from [29], and the long broken line indicates the experimental initial linearity.

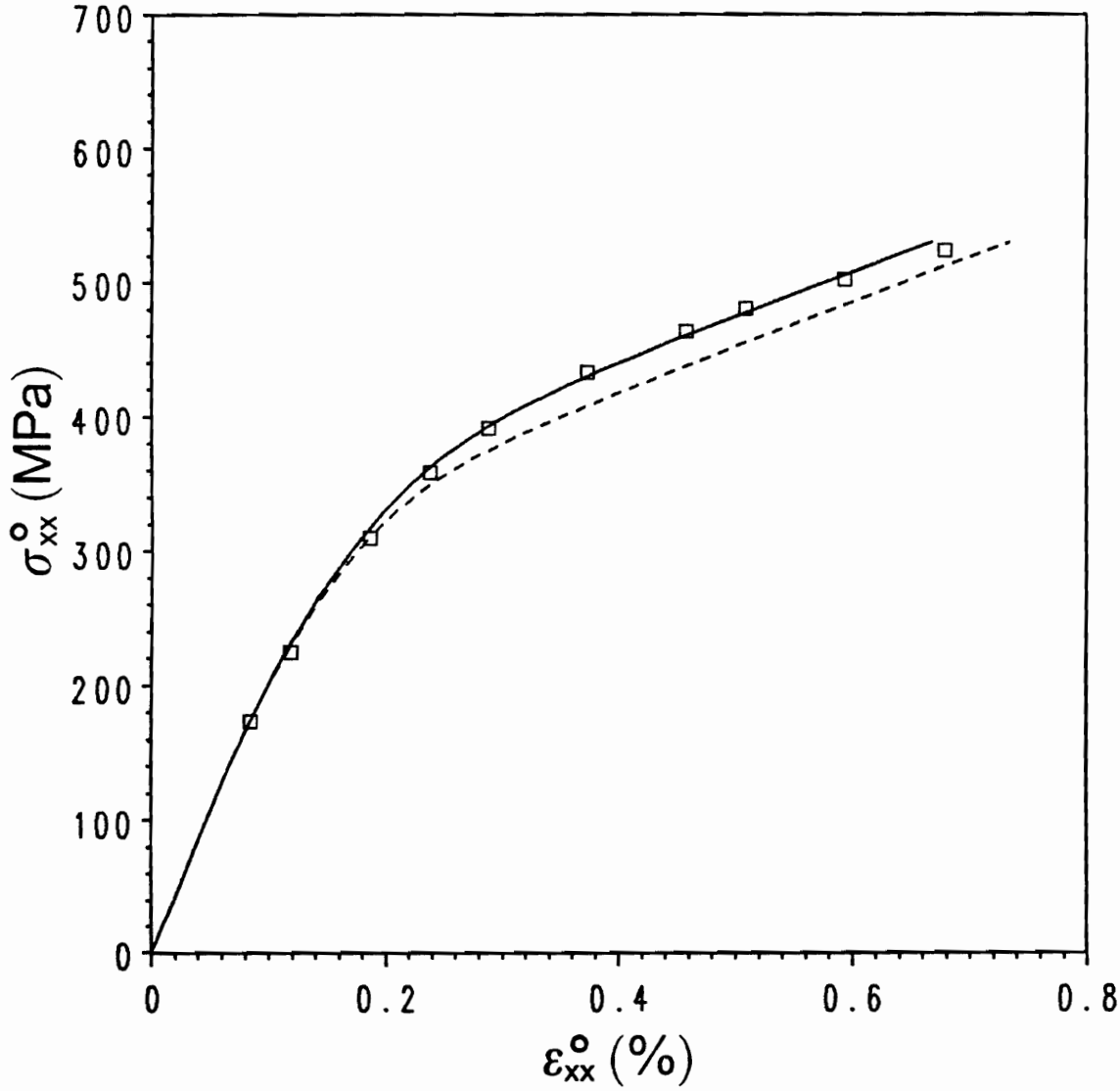

Figure 10a. Axial Response of 10° Specimen: The continuous line represents the prediction using the periodic diamond model, and the broken line the periodic square model. The squares represent the experimental data from [29].

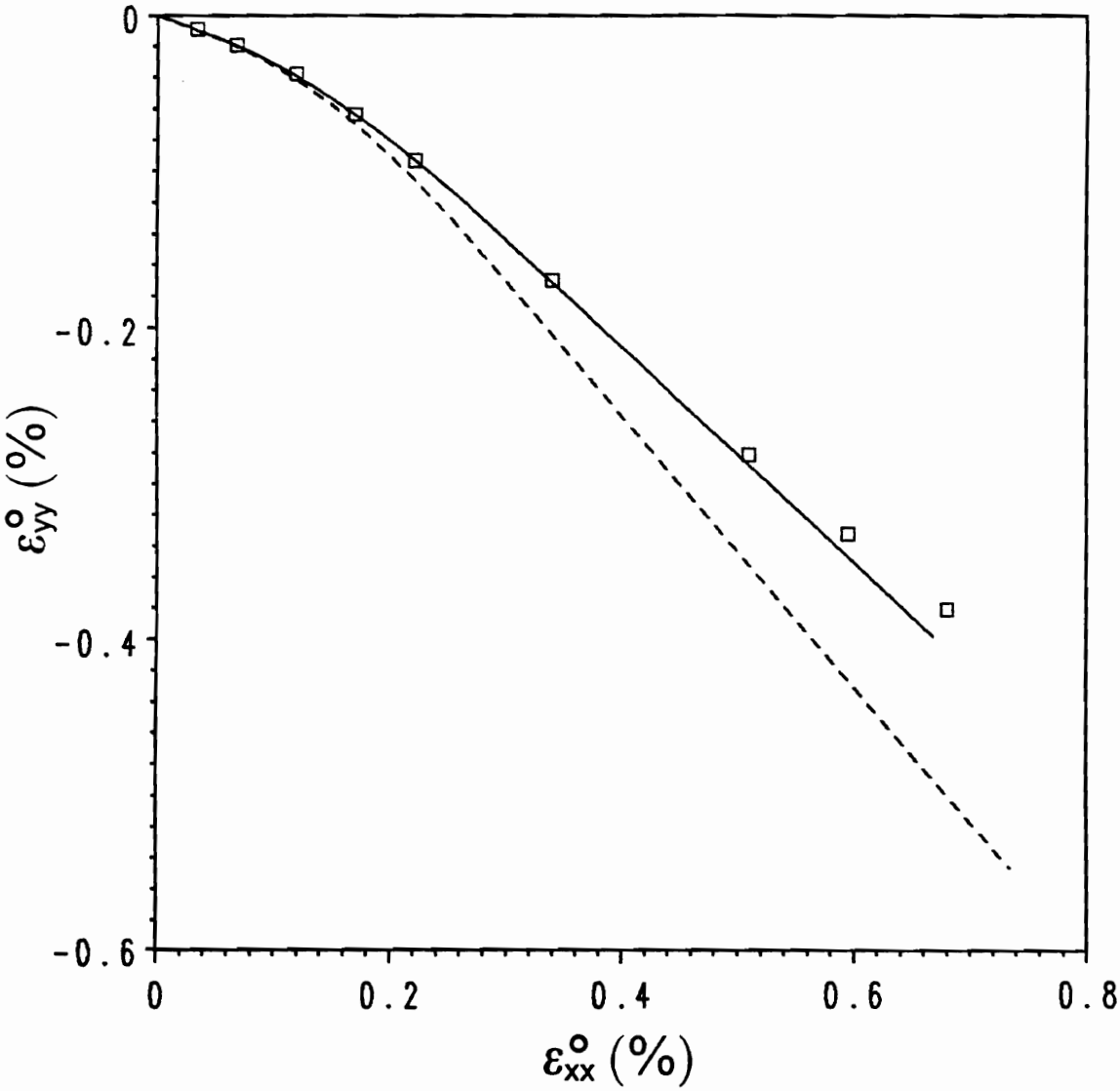

Figure 10b. Poisson's Response of 10° Specimen: The continuous line represents the prediction using the periodic diamond model, and the broken line the periodic square model. The squares represent the experimental data from [29].

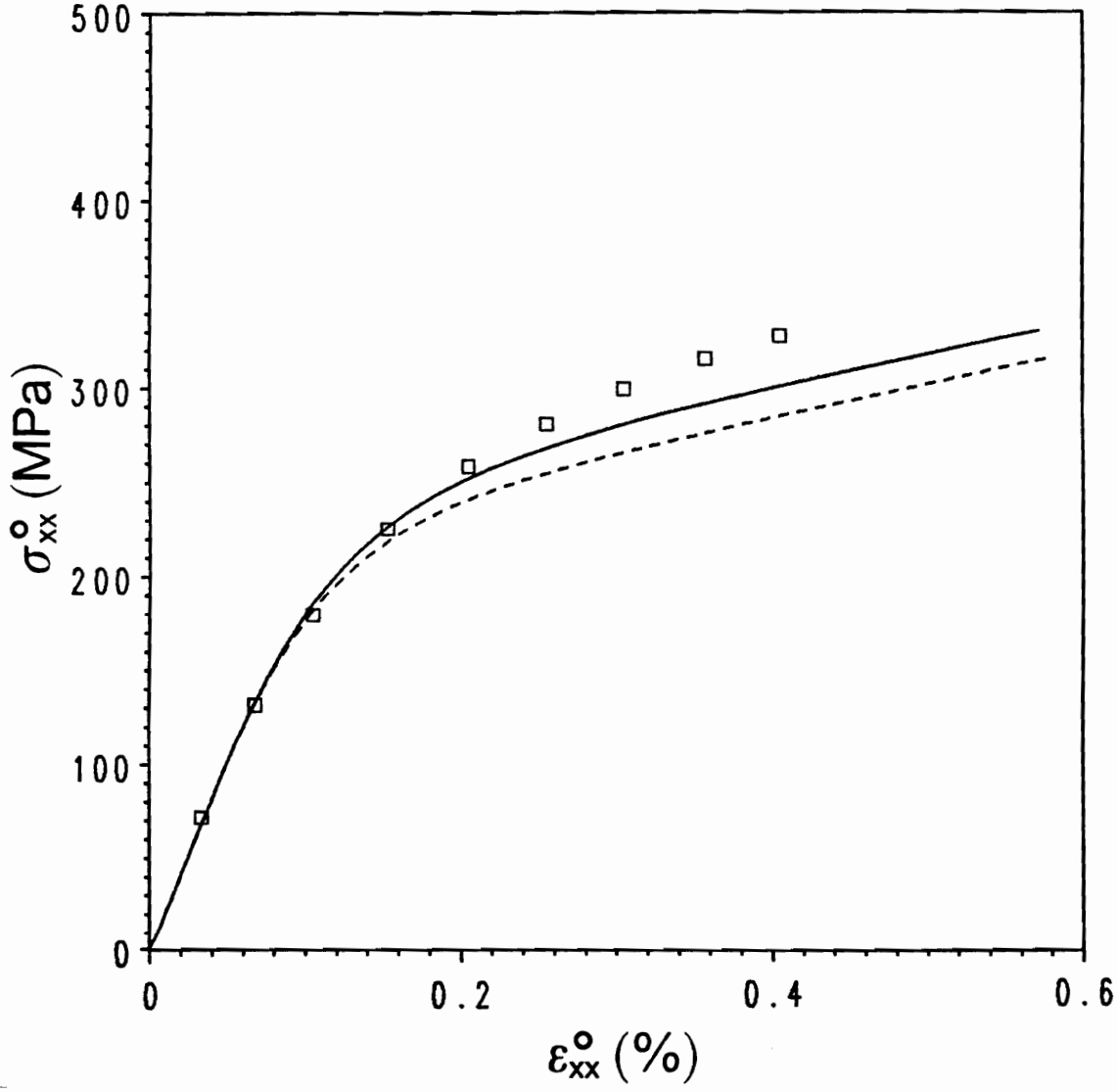

Figure 11a. Axial Response of 15° Specimen: The continuous line represents the prediction using the periodic diamond model, and the broken line the periodic square model. The squares represent the experimental data from [29].

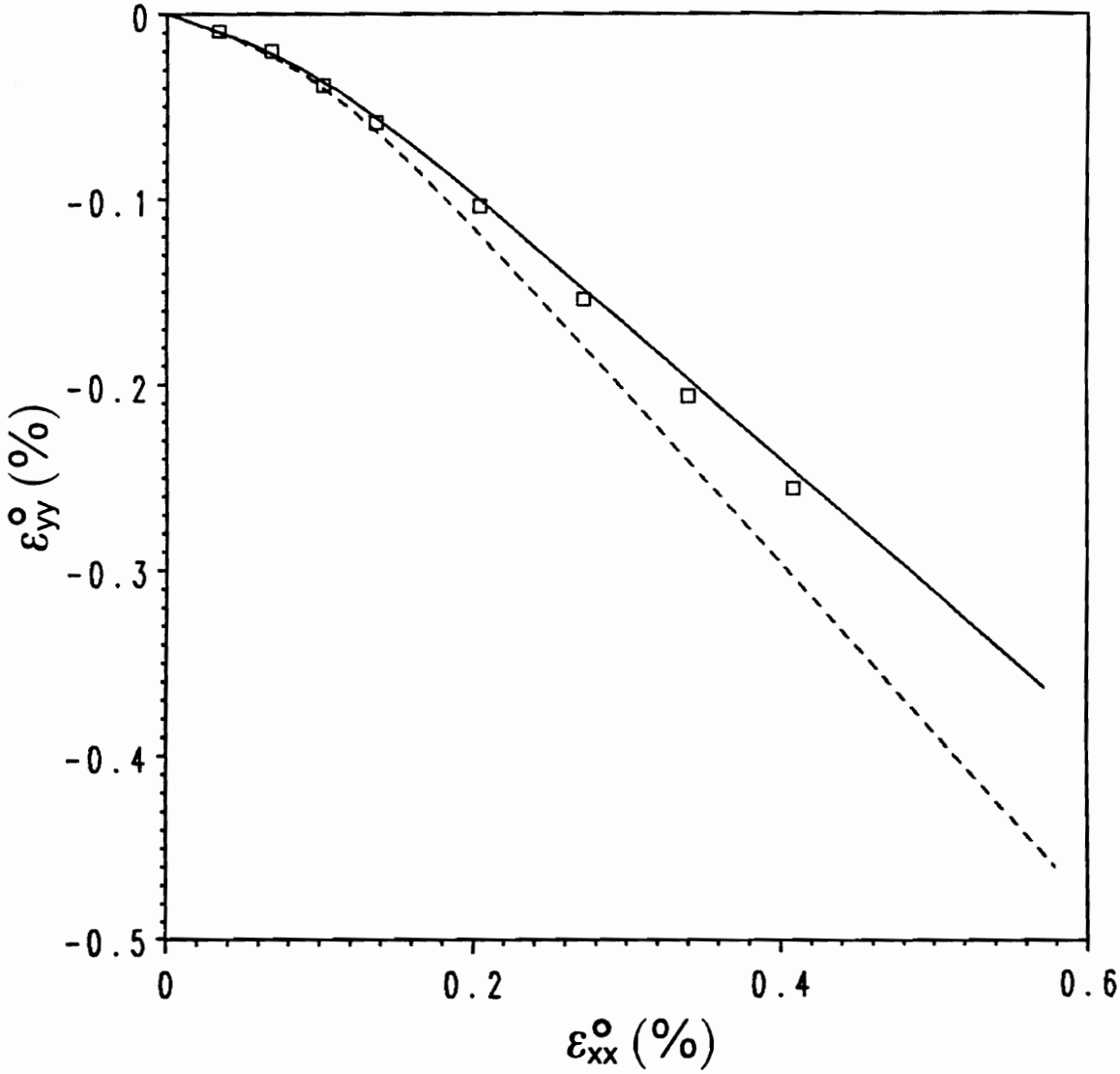

Figure 11b. Poisson's Response of 15° Specimen: The continuous line represents the prediction using the periodic diamond model, and the broken line the periodic square model. The squares represent the experimental data from [29].

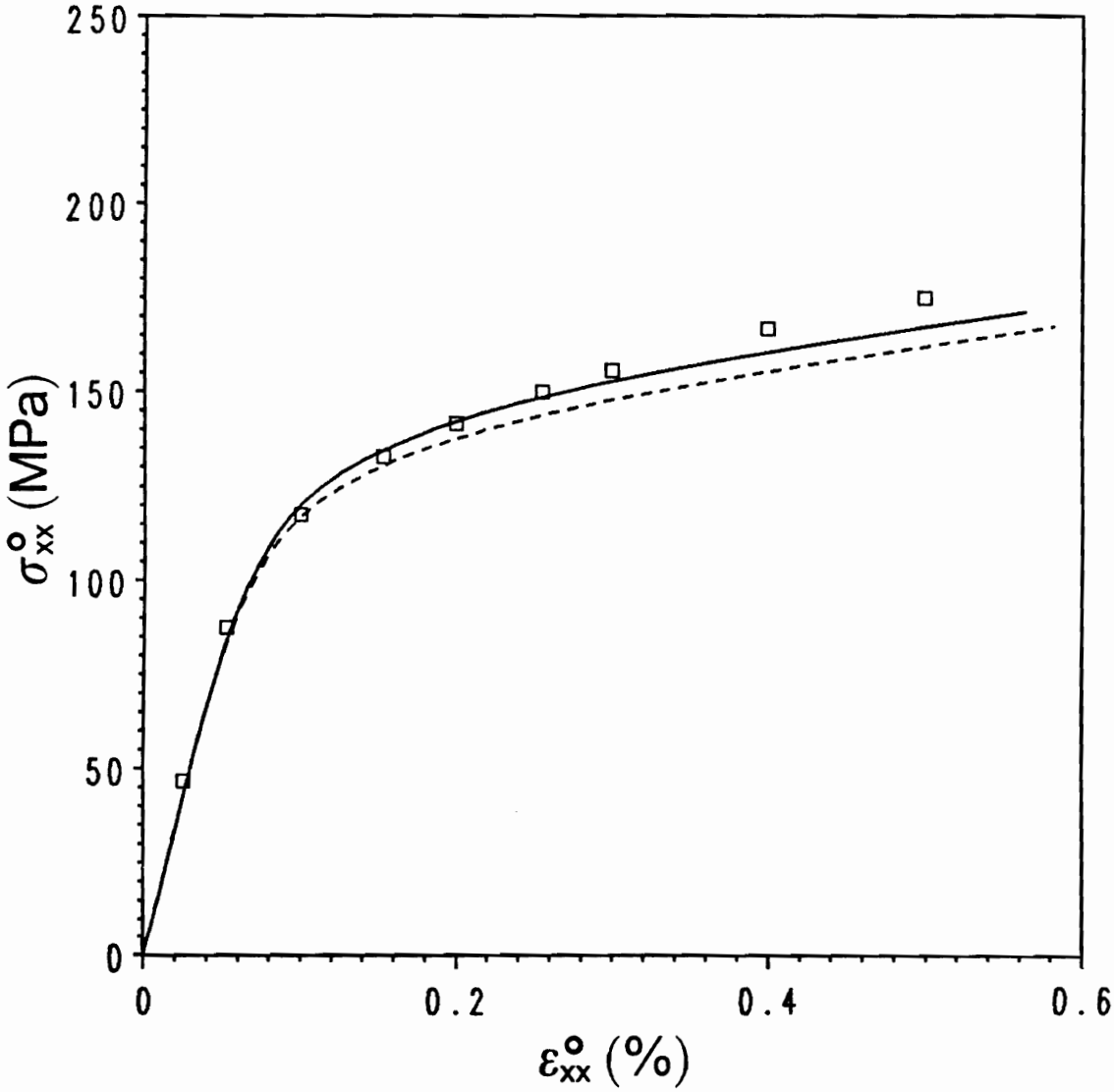

Figure 12a. Axial Response of 30° Specimen: The continuous line represents the prediction using the periodic diamond model, and the broken line the periodic square model. The squares represent the experimental data from [29].

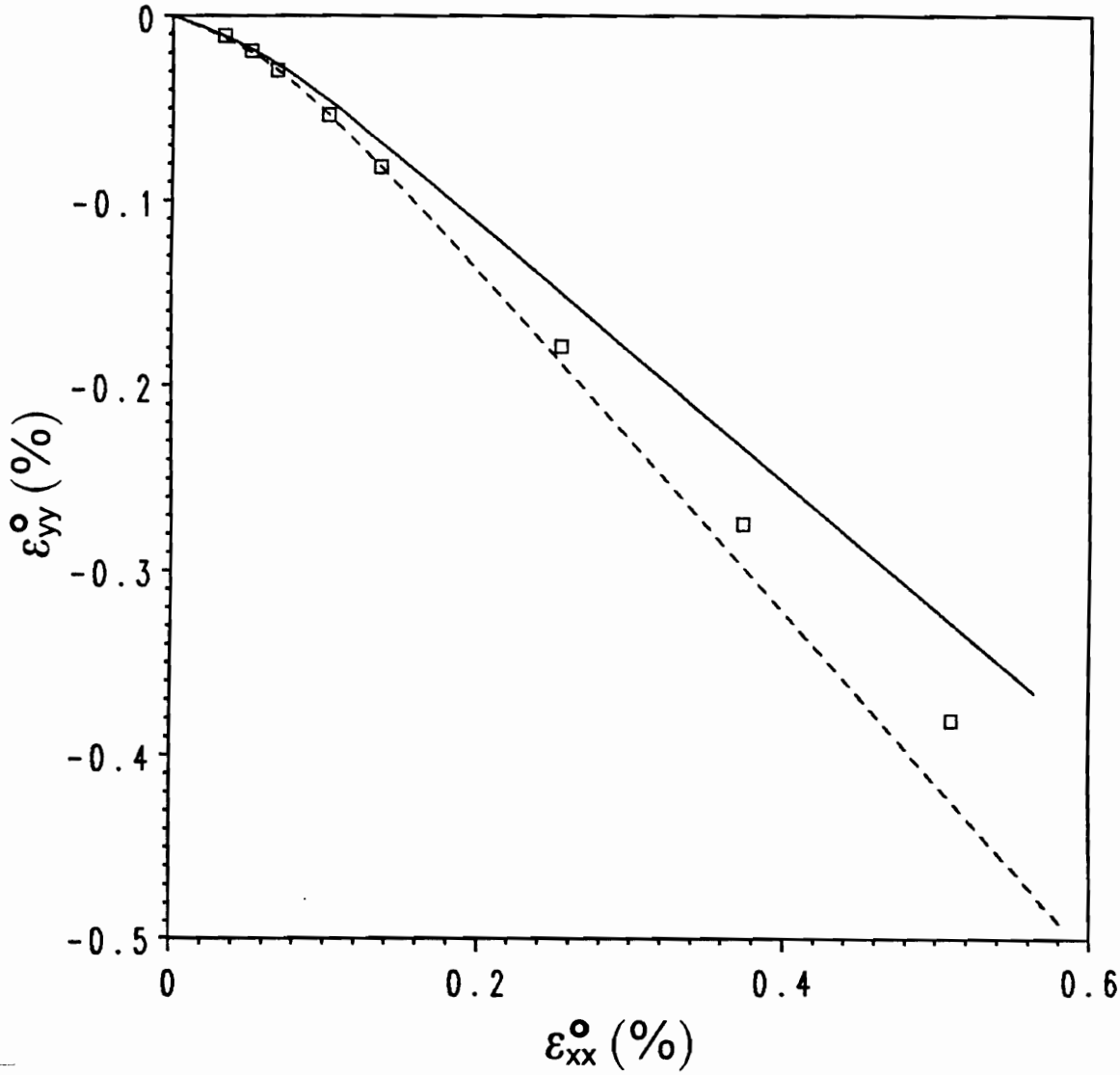

Figure 12b. Poisson's Response of 30° Specimen: The continuous line represents the prediction using the periodic diamond model, and the broken line the periodic square model. The squares represent the experimental data from [29].

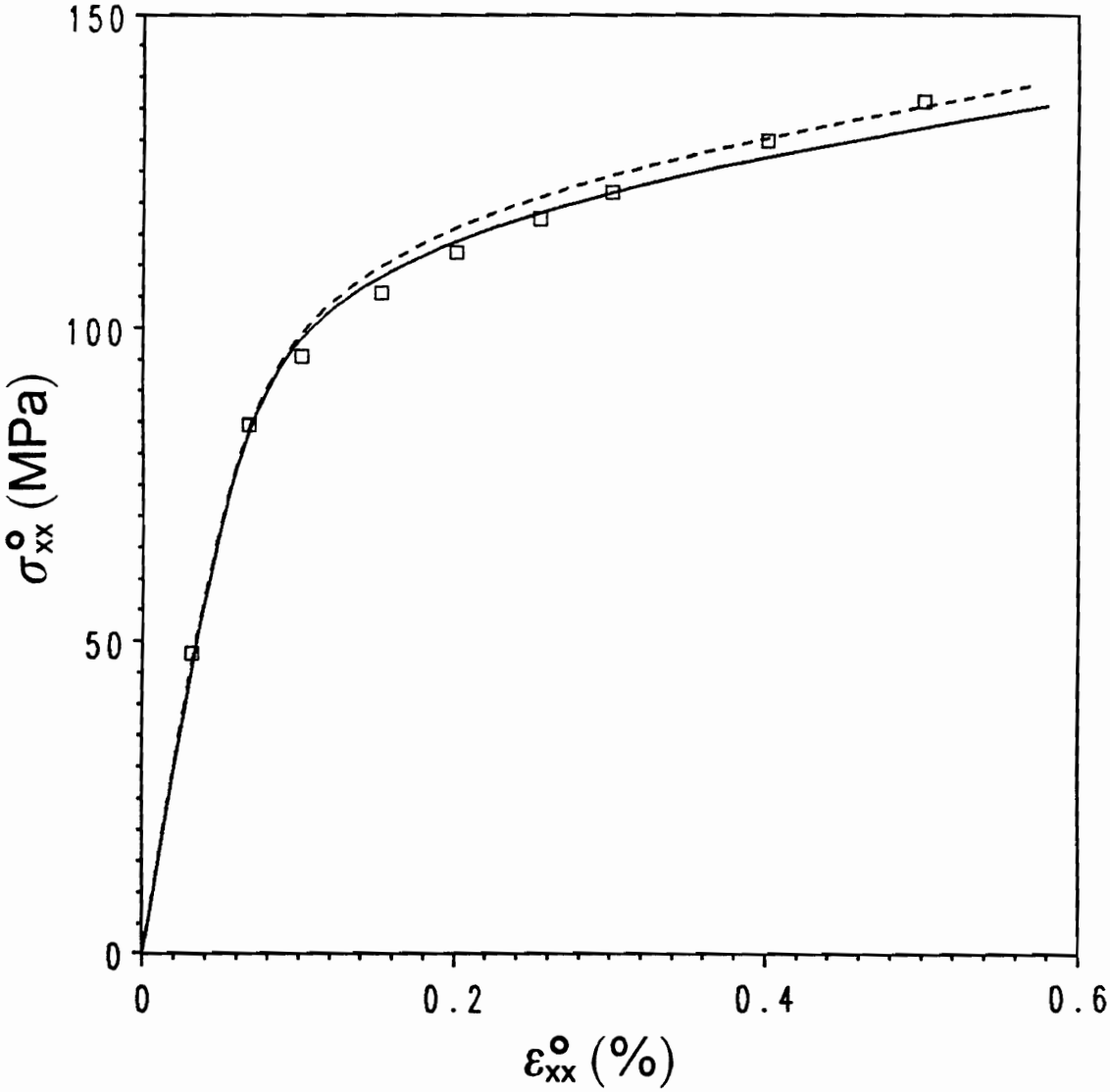

Figure 13a. Axial Response of 45° Specimen: The continuous line represents the prediction using the periodic diamond model, and the broken line the periodic square model. The squares represent the experimental data from [29].

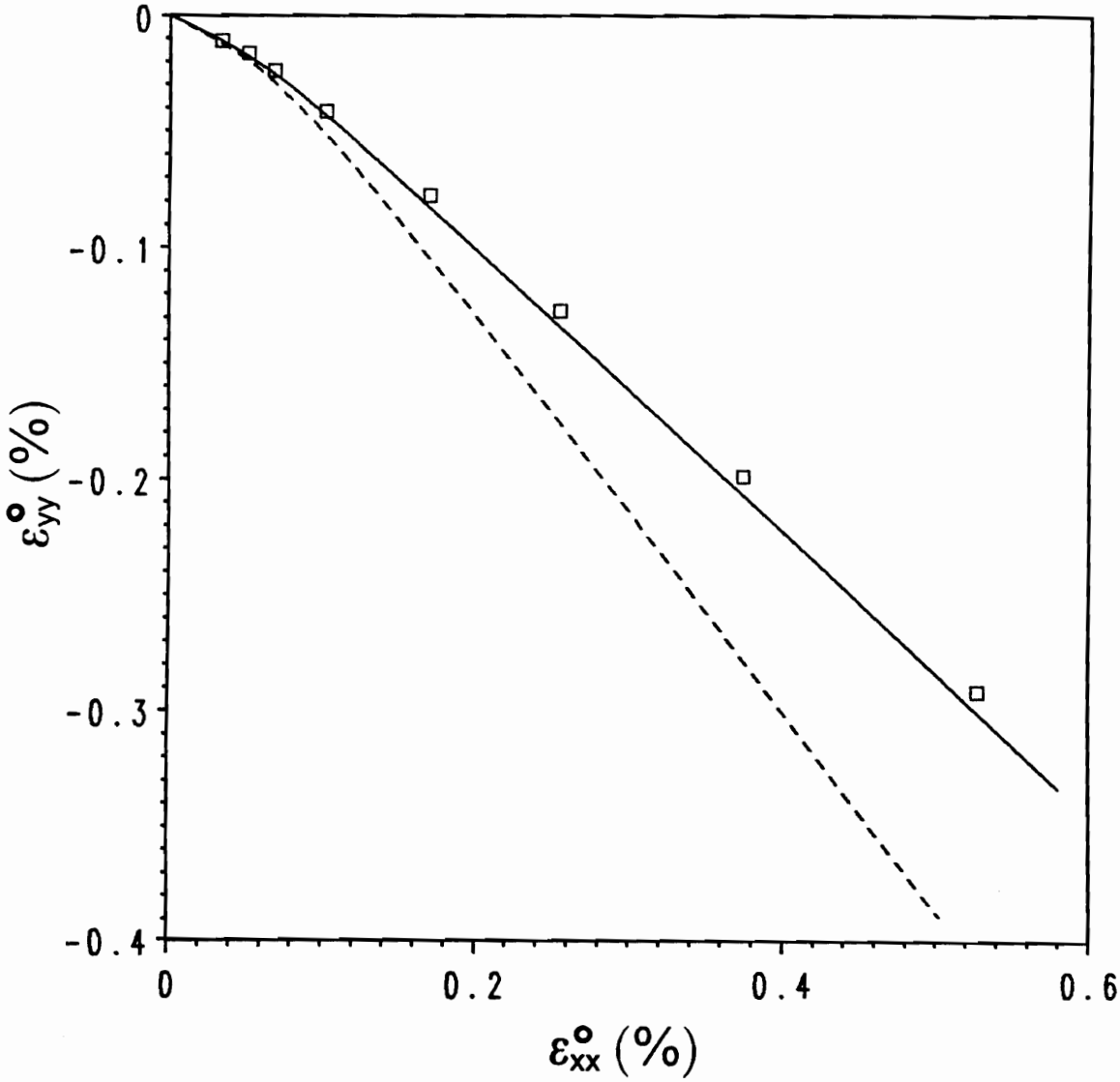

Figure 13b. Poisson's Response of 45° Specimen: The continuous line represents the prediction using the periodic diamond model, and the broken line the periodic square model. The squares represent the experimental data from [29].

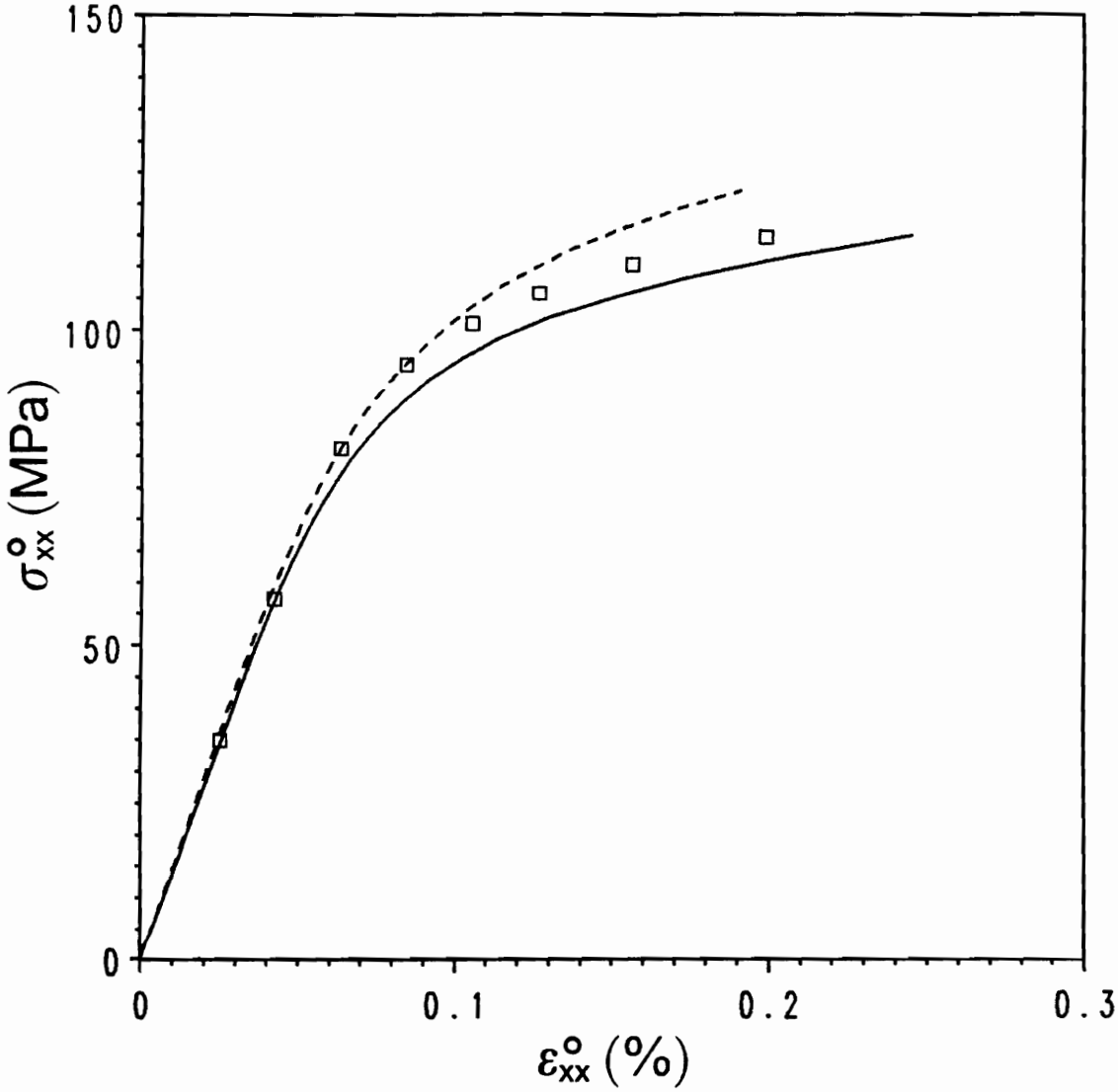

Figure 14a. Axial Response of 60° Specimen: The continuous line represents the prediction using the periodic diamond model, and the broken line the periodic square model. The squares represent the experimental data from [29].

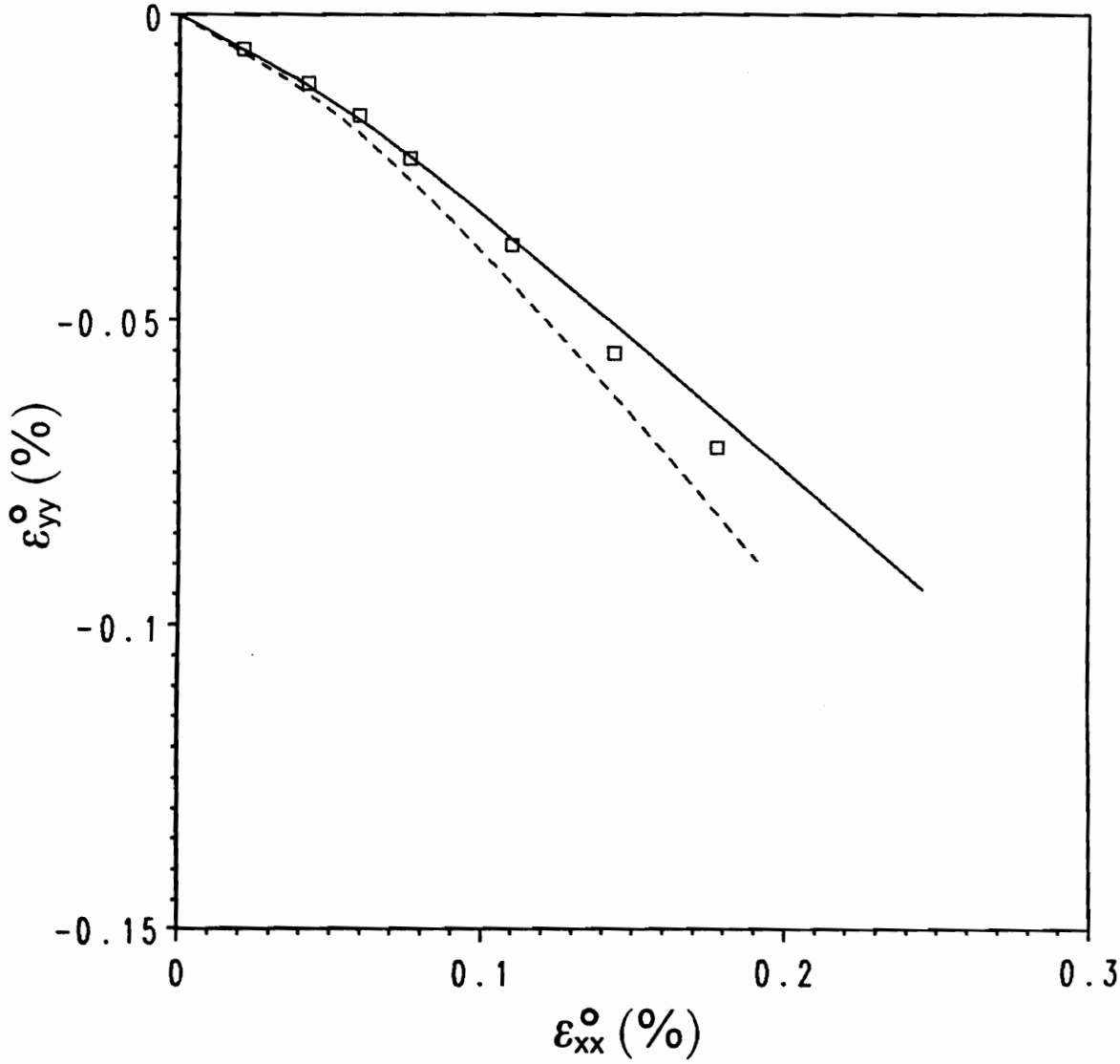

Figure 14b. Poisson's Response of 60° Specimen: The continuous line represents the prediction using the periodic diamond model, and the broken line the periodic square model. The squares represent the experimental data from [29].

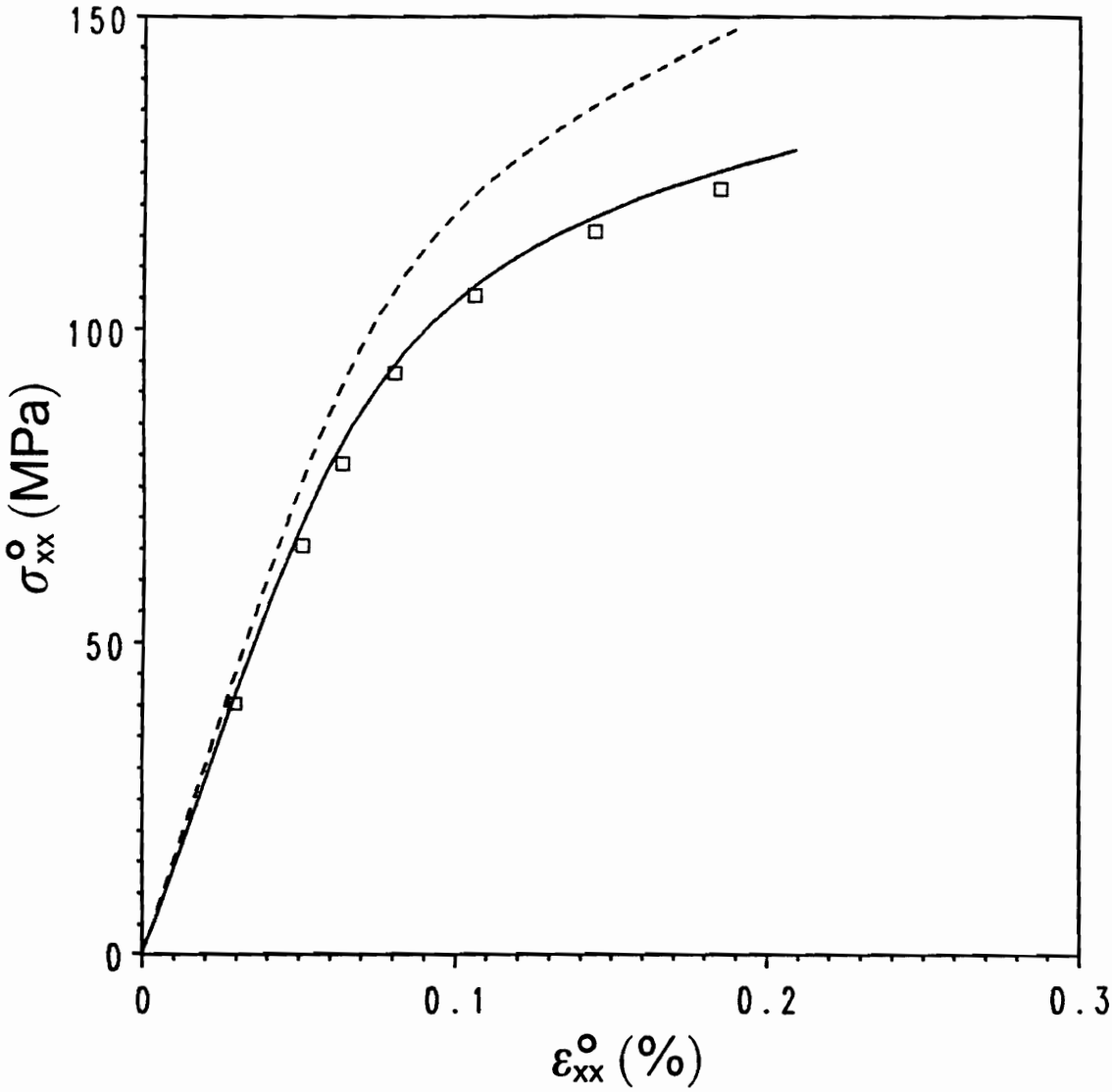

Figure 15a. Axial Response of 90° Specimen: The continuous line represents the prediction using the periodic diamond model, and the broken line the periodic square model. The squares represent the experimental data from [29].

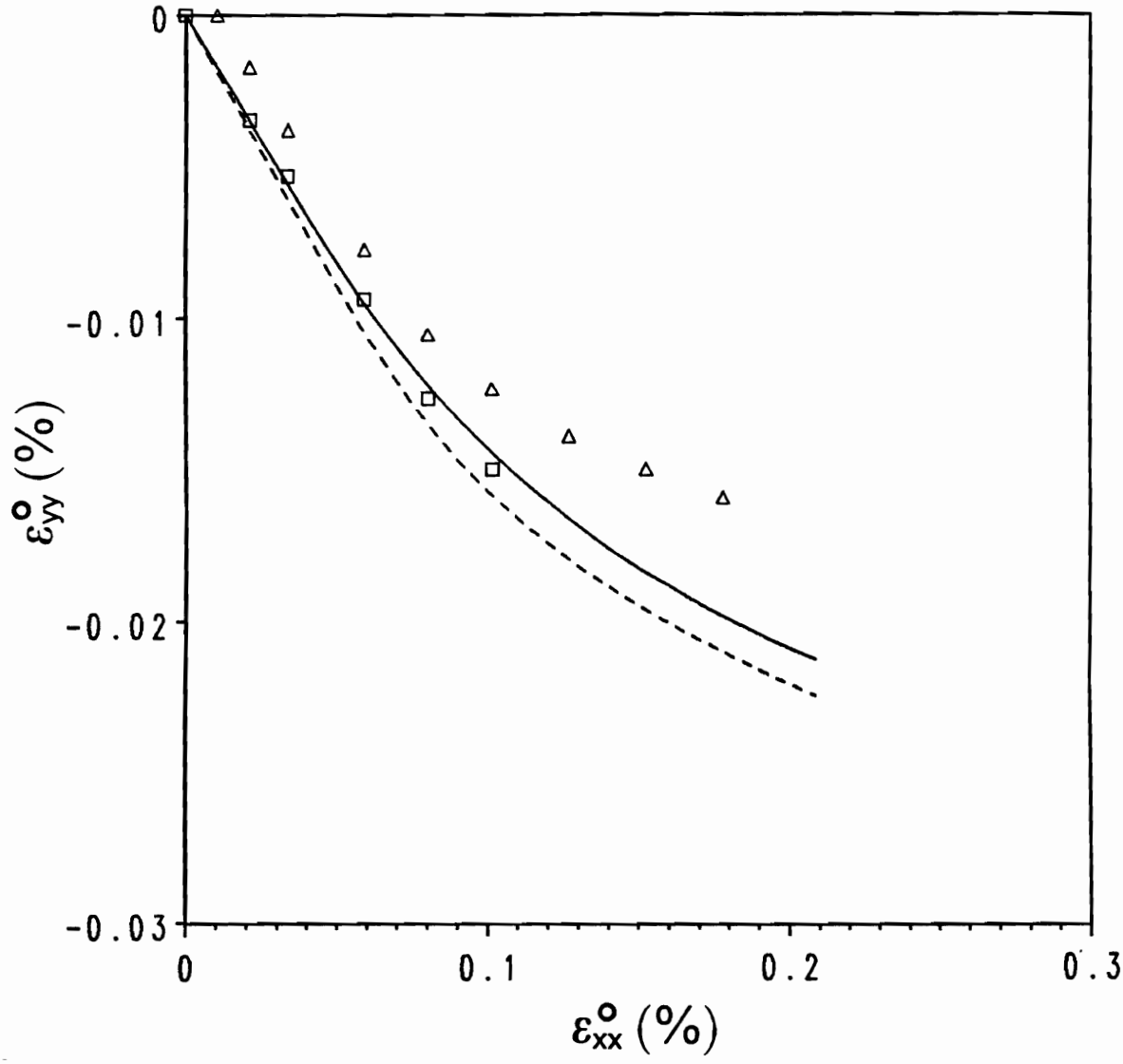

Figure 15b. Poisson's Response of 90° Specimen: The continuous line represents the prediction using the periodic diamond model, and the broken line the periodic square model. The squares represent the experimental data from [29]. For comparison, experimental data (the triangles) from another specimen of [29] are shown in spite of a certain error in strain measurement.

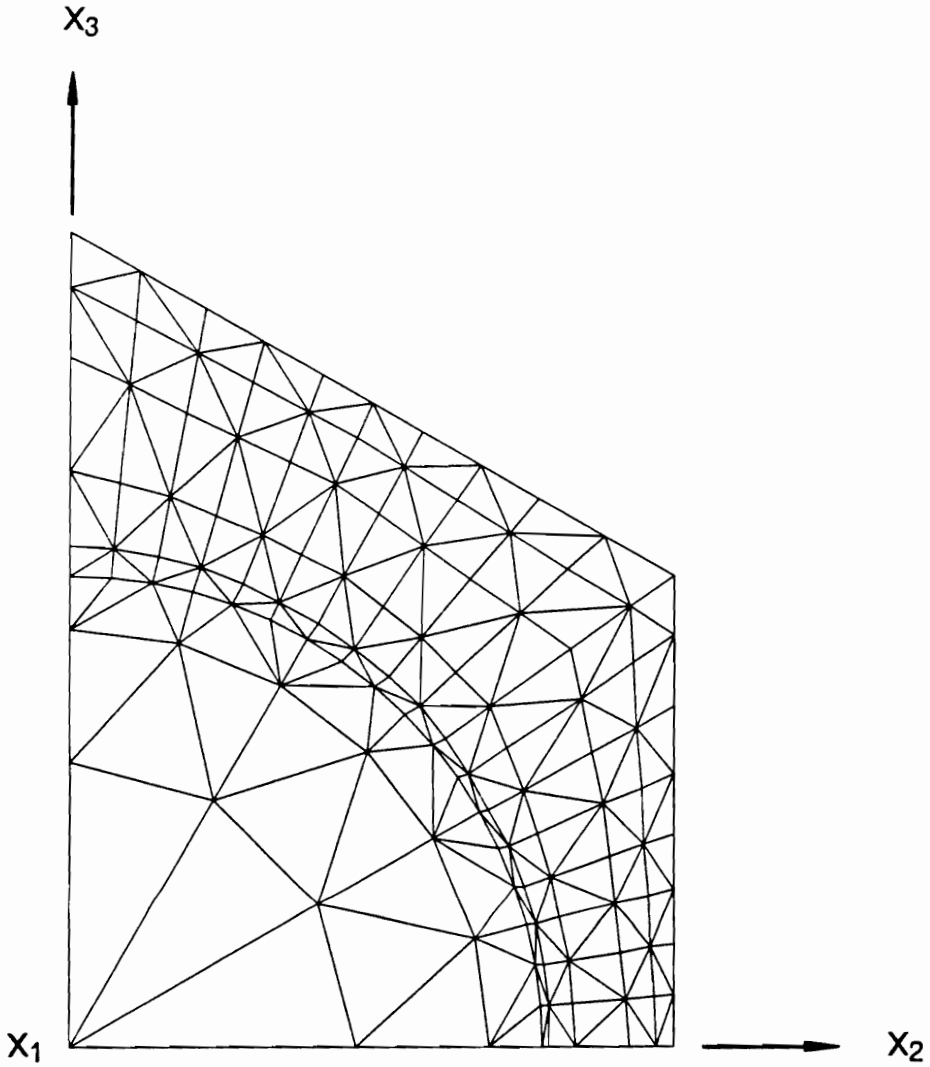

Figure 16. Finite Element Grid for Modeling B/6061 Al Composite of [30]

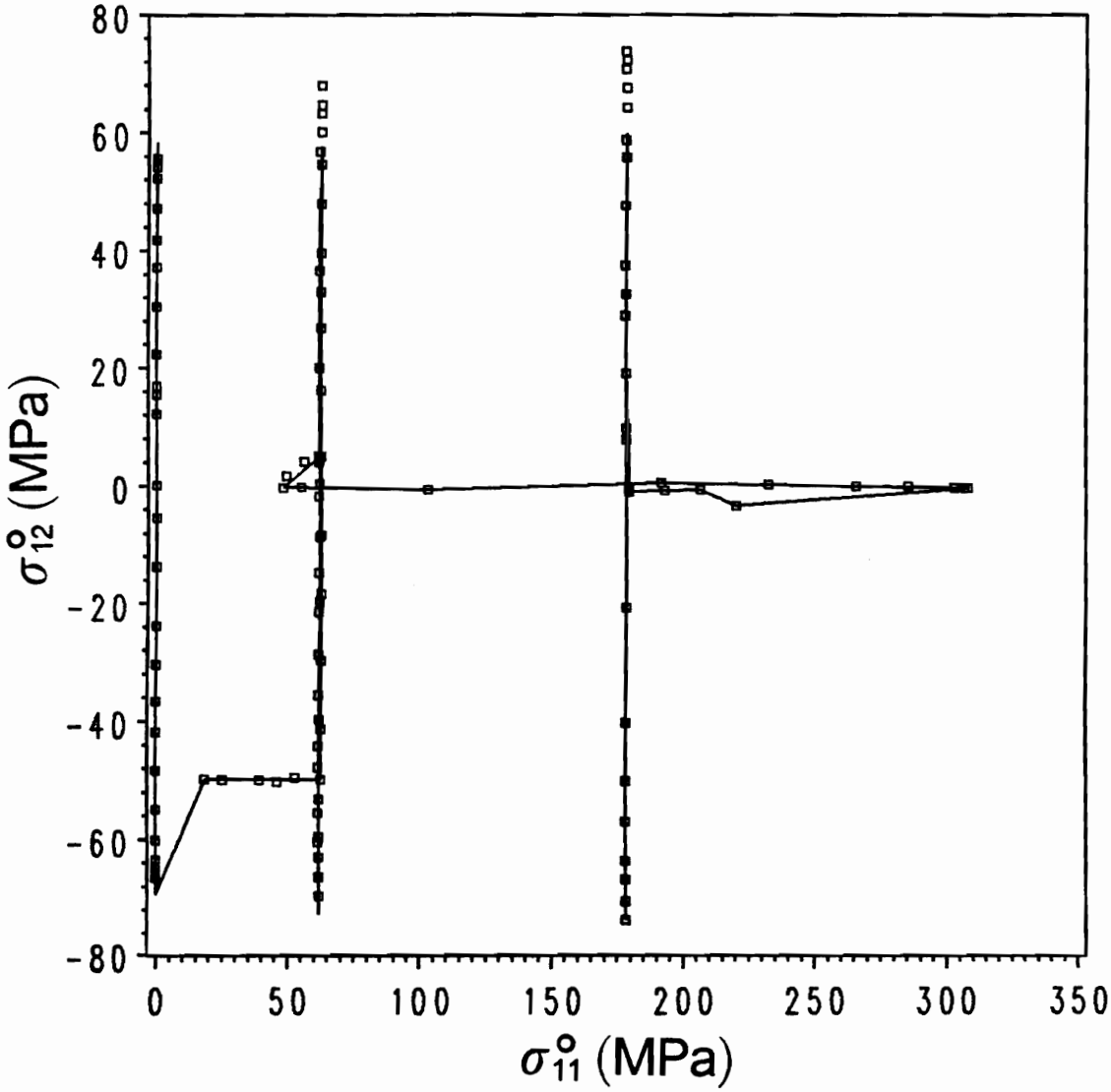

Figure 17a. Stress Response of Composite Tube to Tension-Torsion Loading: The continuous line represents the TPLAS simulation. The squares represent the experimental data from [30].

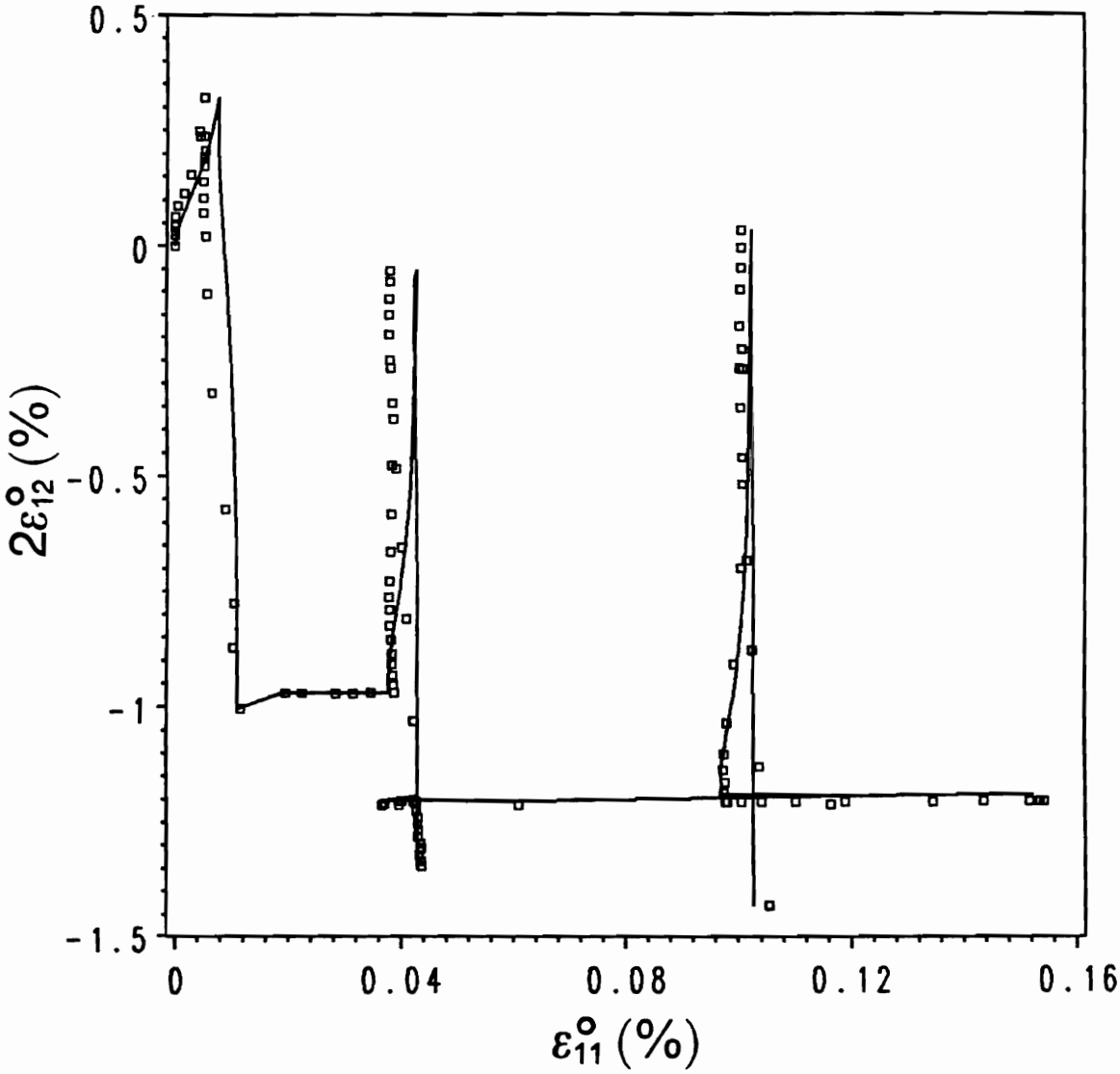

Figure 17b. Strain Response of Composite Tube to Tension-Torsion Loading: The continuous line represents the TPLAS simulation. The squares represent the experimental data from [30].

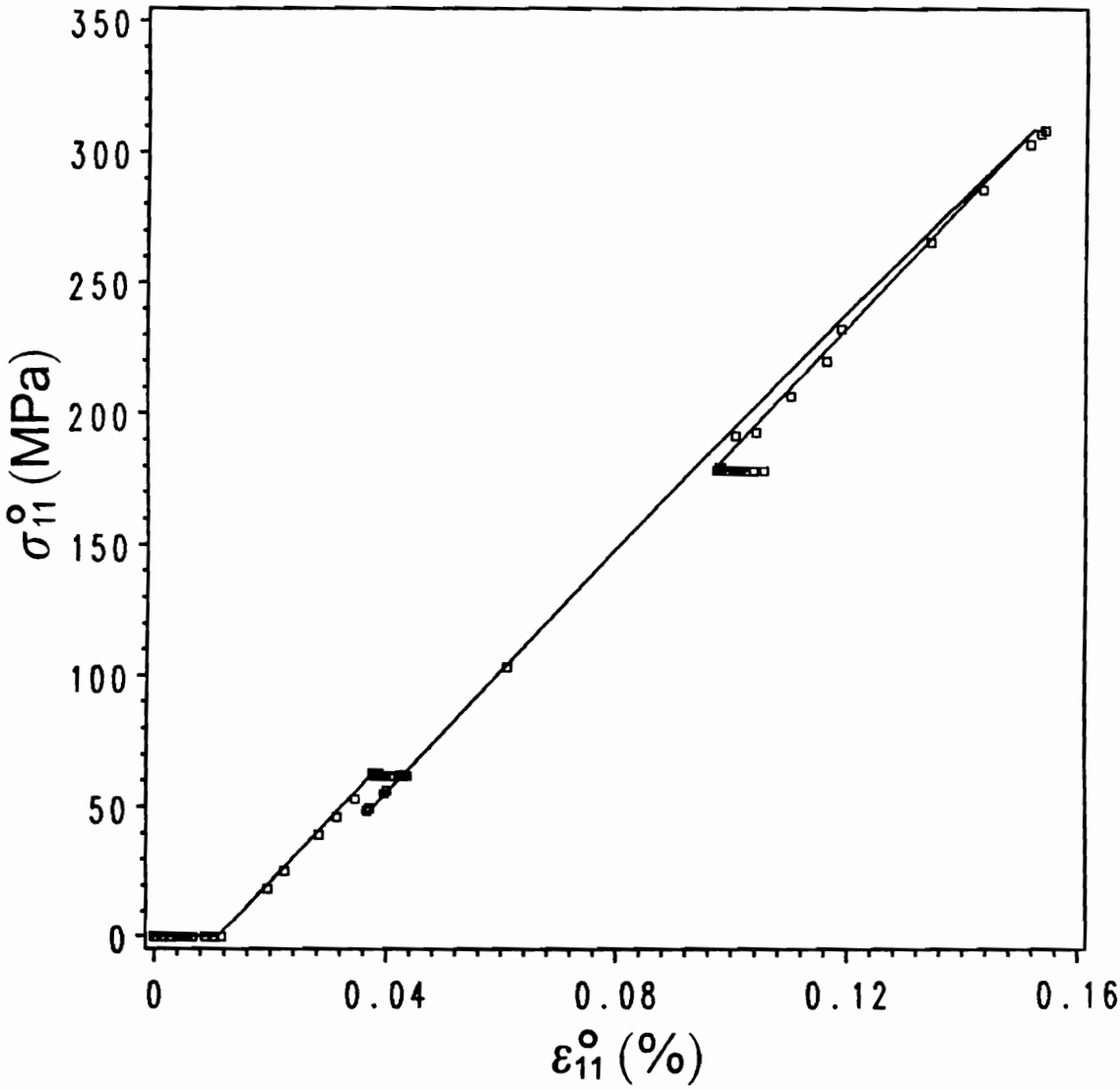

Figure 17c. Tensile Response of Composite Tube to Tension-Torsion Loading: The continuous line represents the TPLAS simulation. The squares represent the experimental data from [30].

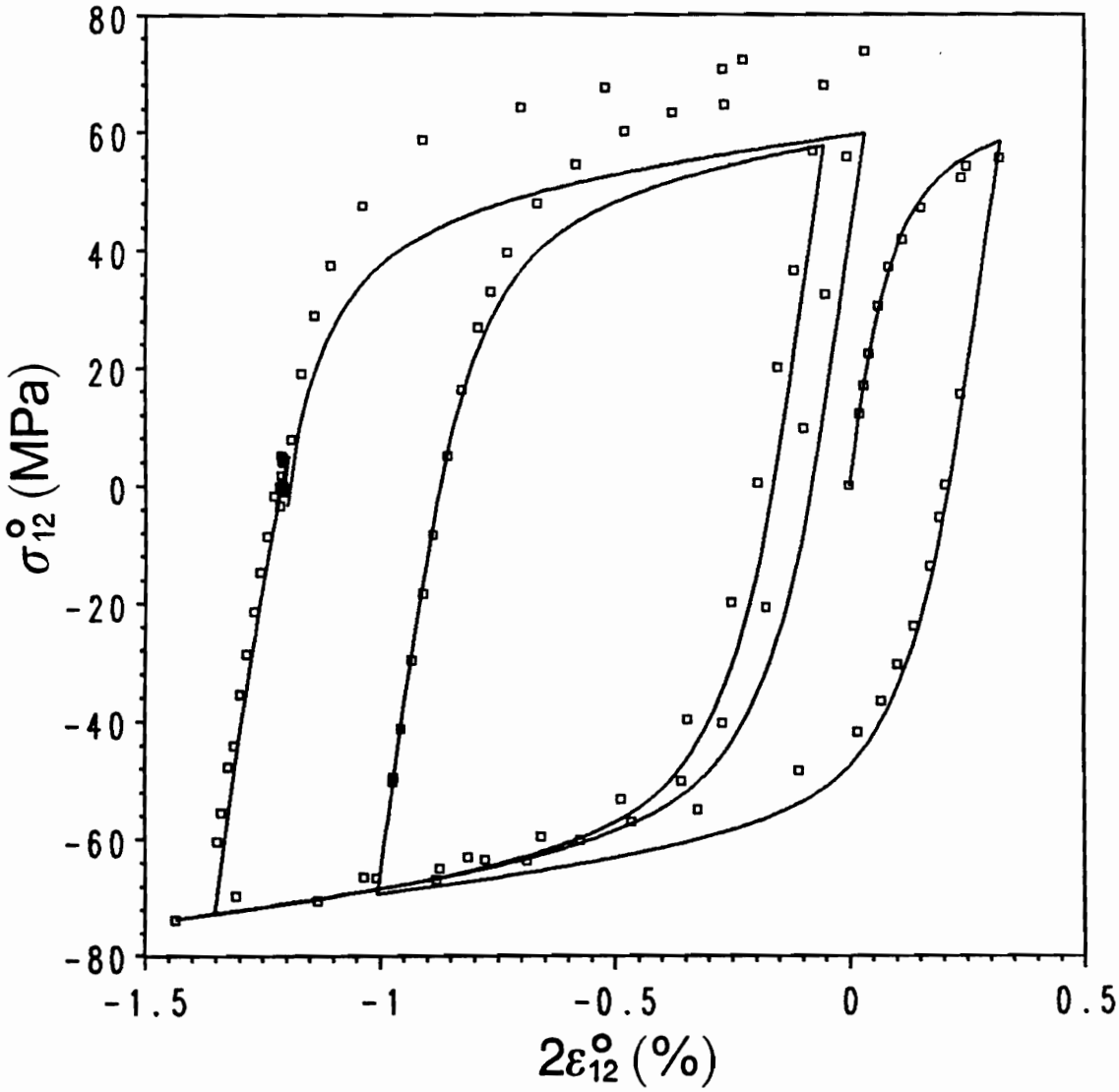

Figure 17d. Shear Response of Composite Tube to Tension-Torsion Loading: The continuous line represents the TPLAS simulation. The squares represent the experimental data from [30].

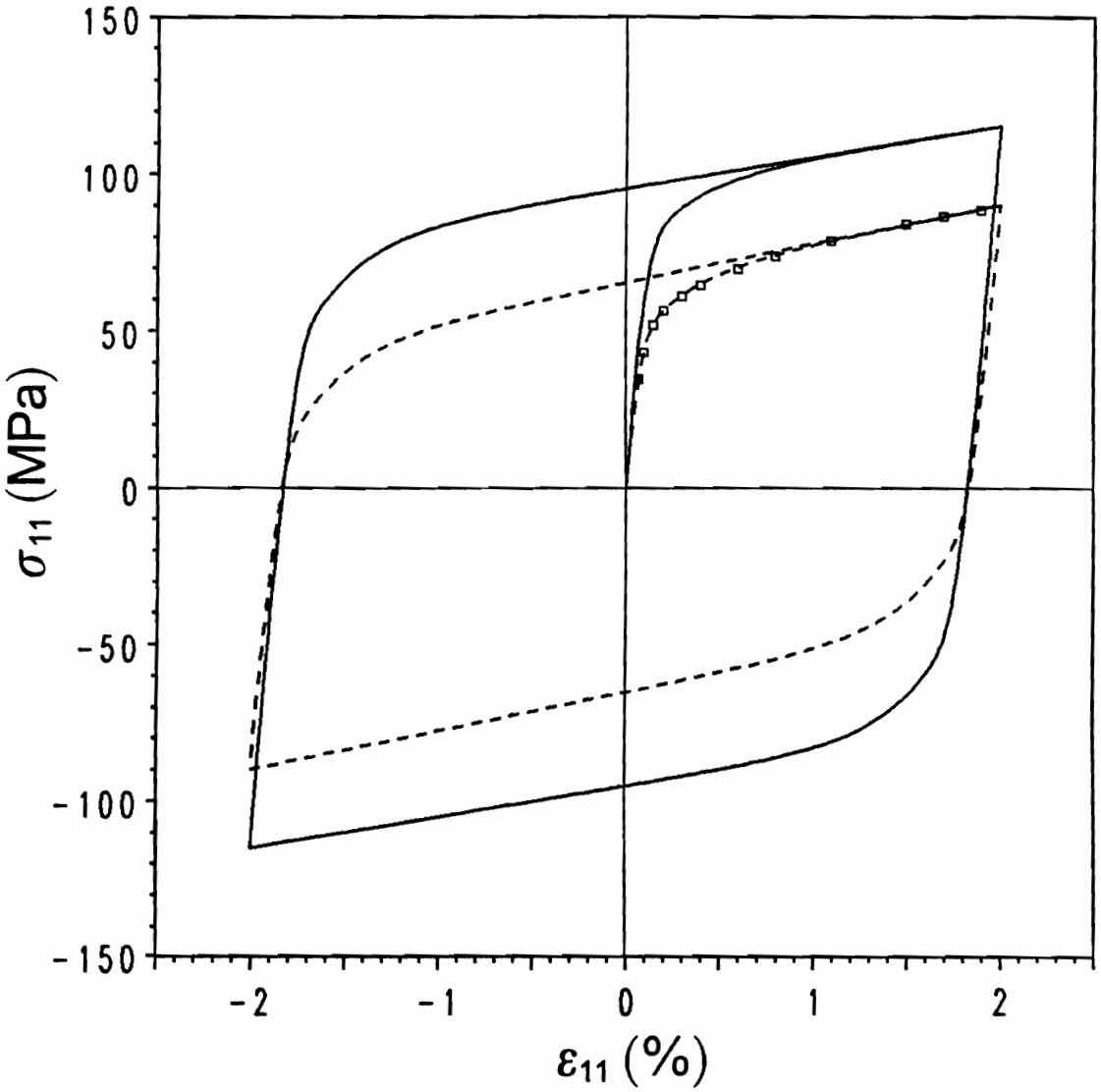

Figure 18. Stress-Strain Curves of Regular 6061-O Aluminum Alloy and 6061 Aluminum Alloy Matrix: The broken line represents the model response of the regular aluminum alloy, and the continuous line the aluminum alloy matrix of [30]. The squares represent the experimental data of the regular aluminum alloy.

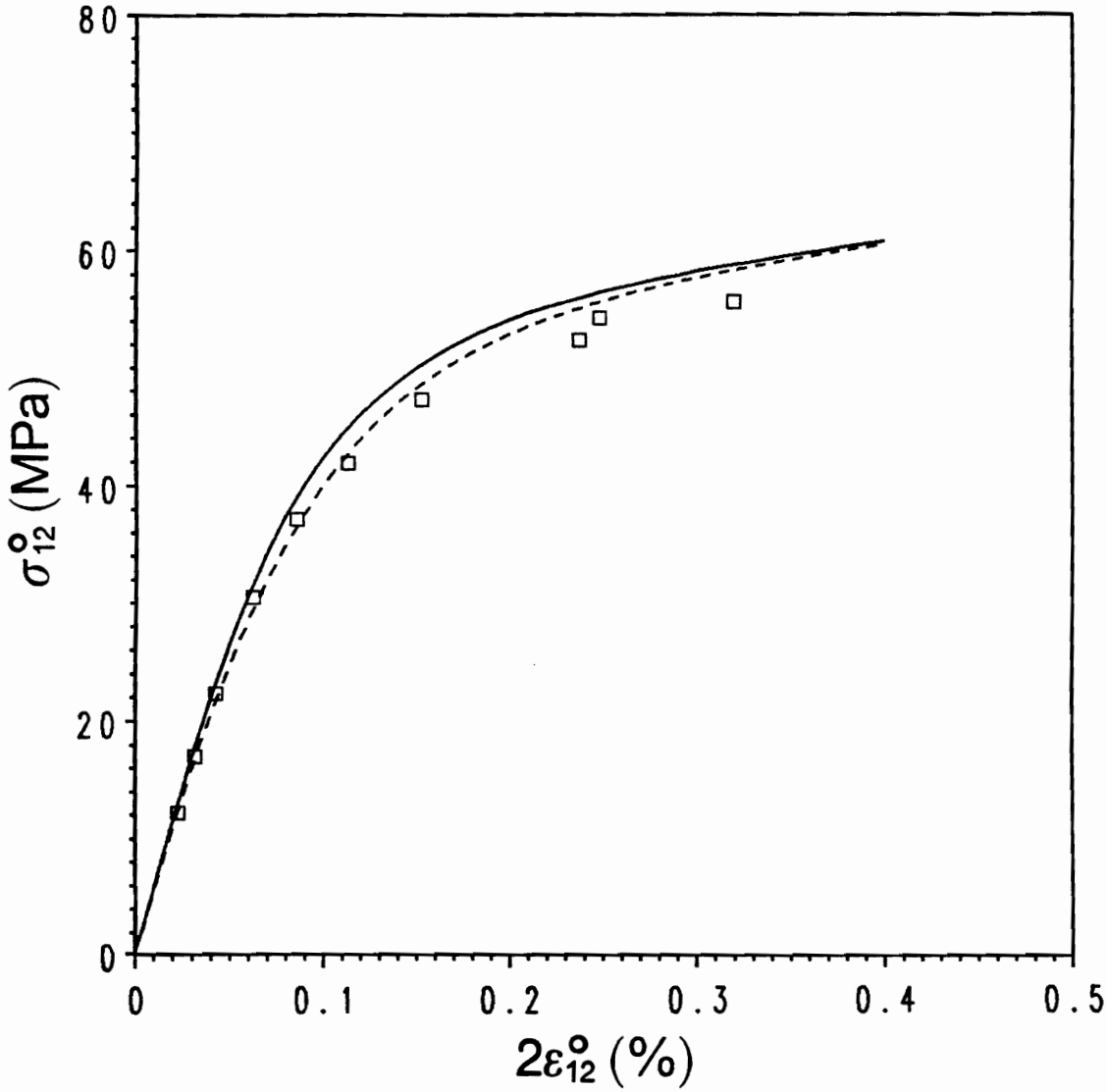

Figure 19. Illustrating Influence of Cool-Down on Initial Shear Response: The broken line represents the TPLAS simulation without the cool-down, and the continuous line with the cool-down. The squares represent the experimental data from [30].

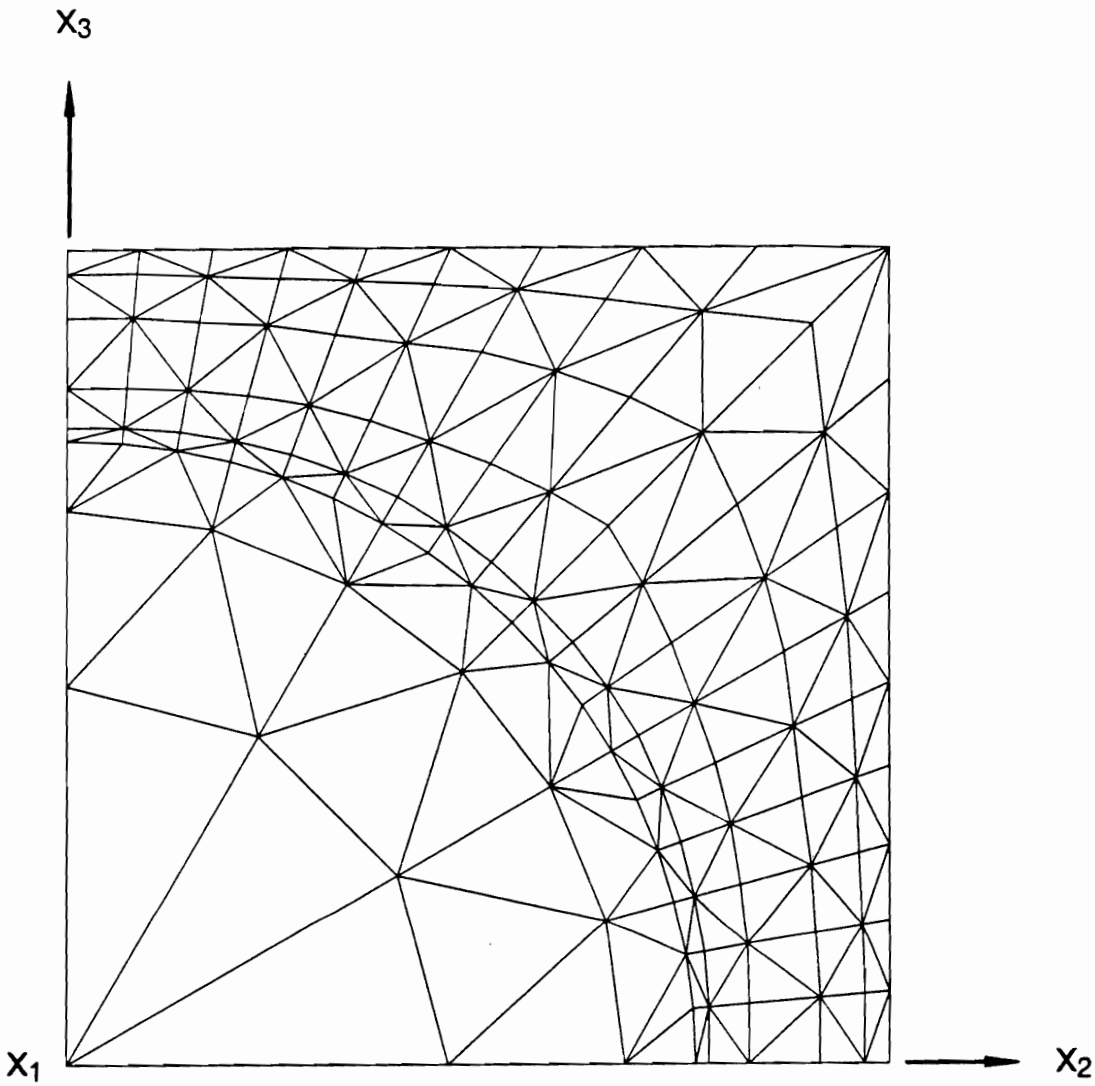

Figure 20. Finite Element Grid of PSMCF for Modeling B/6061 Al Composite of [29]

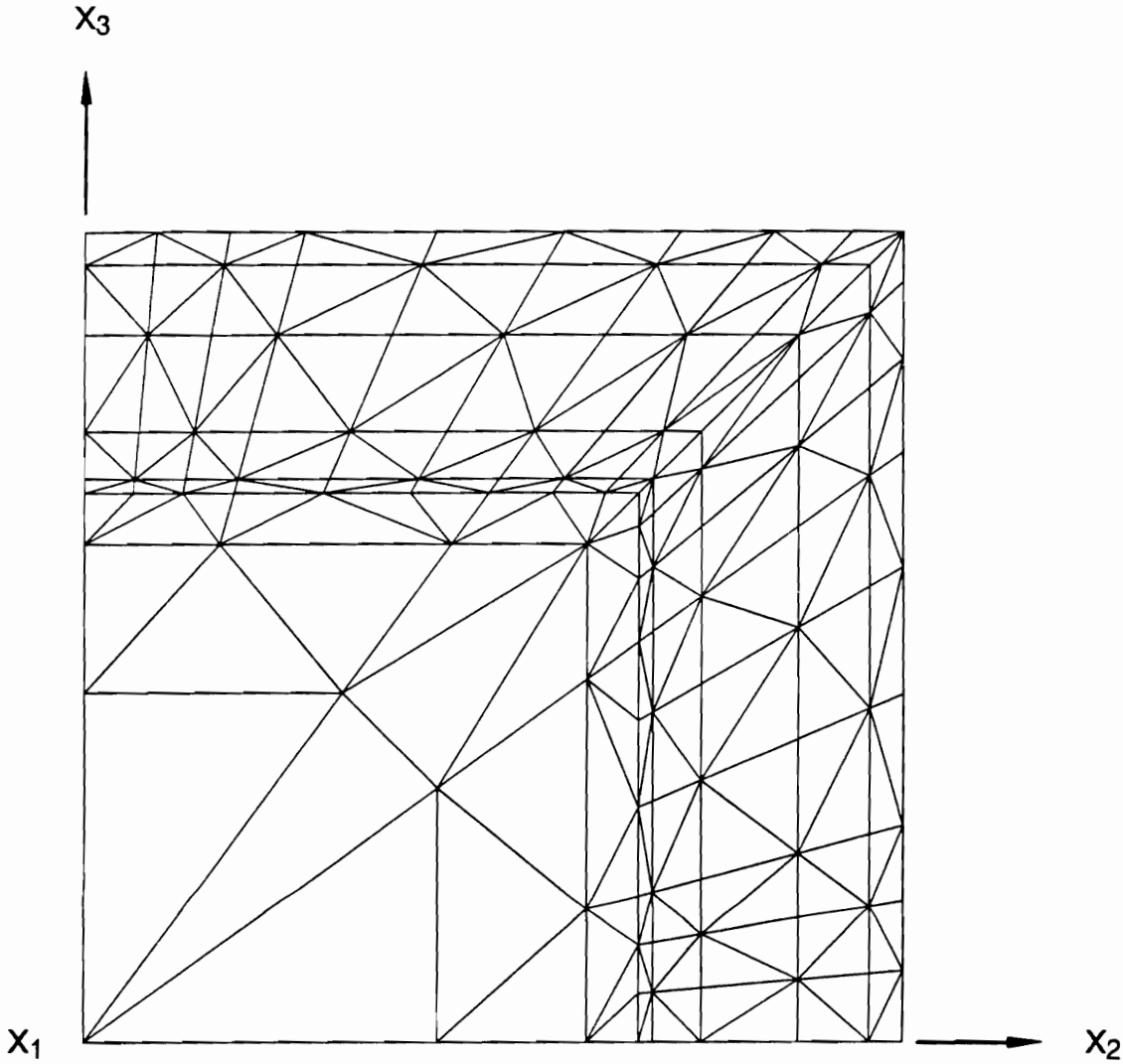

Figure 21. Finite Element Grid of PSMSF for Modeling B/6061 Al Composite of [29]

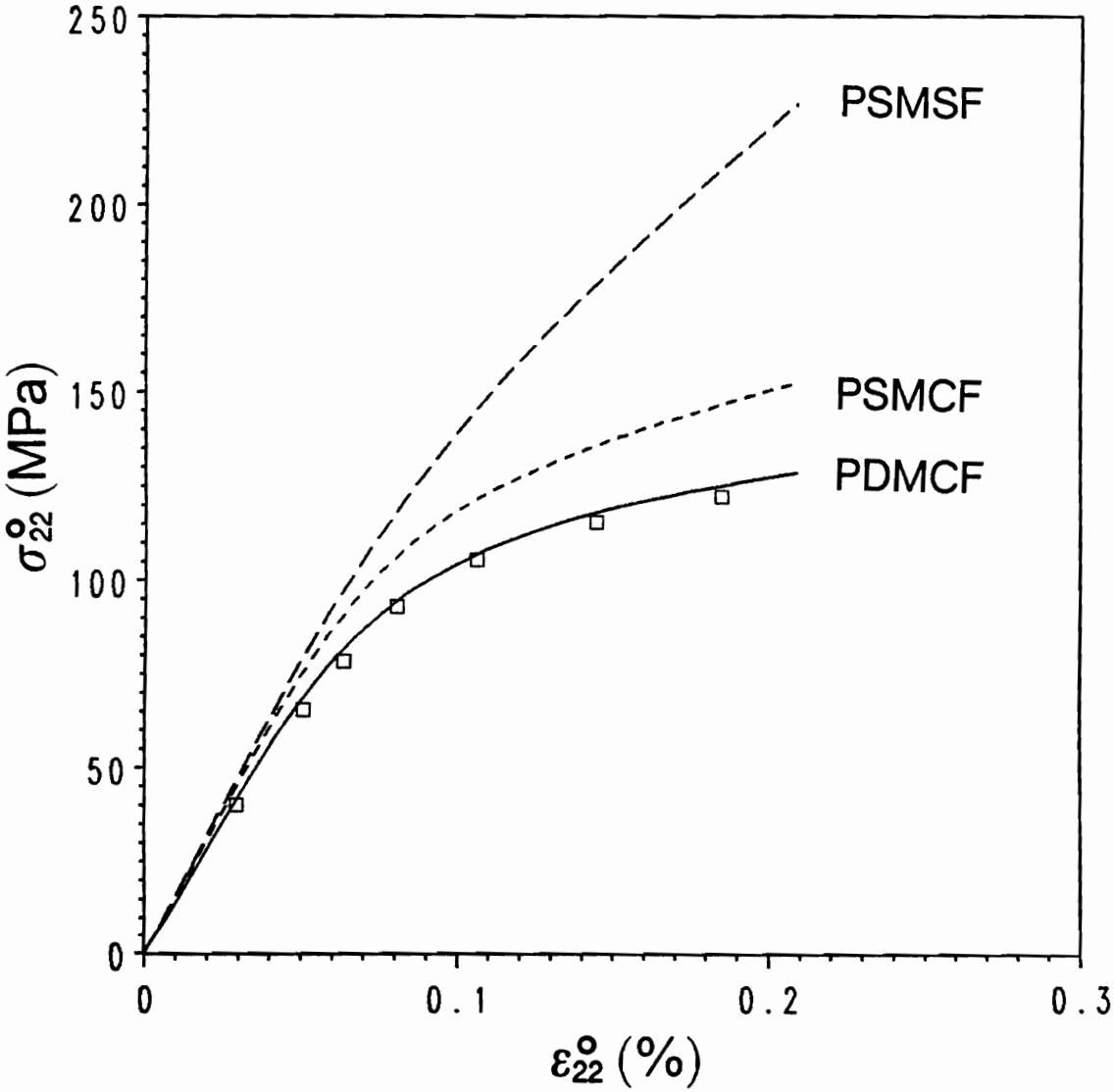

Figure 22a. Transverse Tensile Responses of PDMCF, PSMCF, and PSMSF: The squares represent the experimental data from [29].

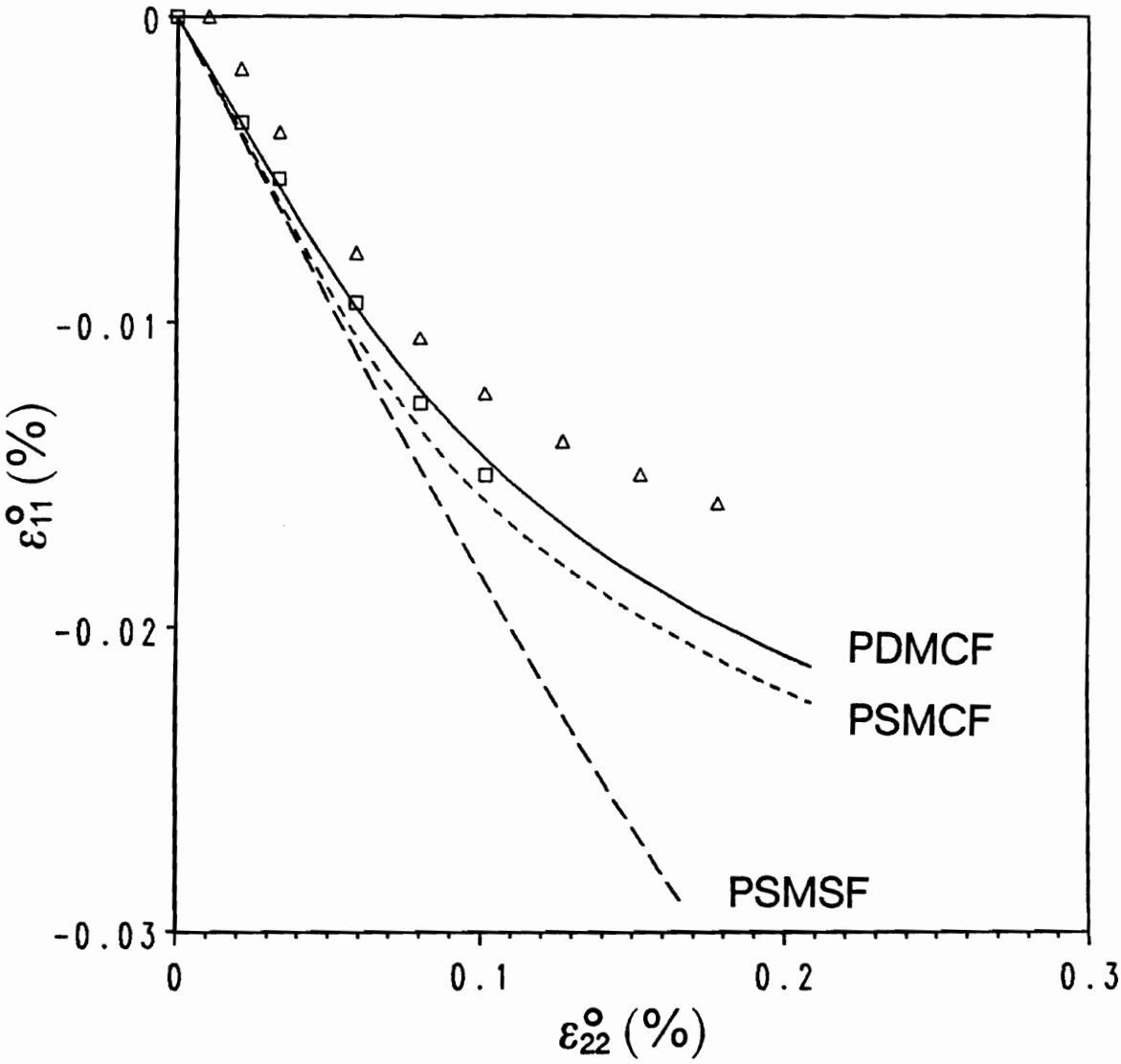

Figure 22b. Transverse Tensile Responses of PDMCF, PSMCF, and PSMSF: The squares represent the experimental data from [29]. For comparison, experimental data (the triangles) from another specimen of [29] are shown in spite of a certain error in strain measurement.

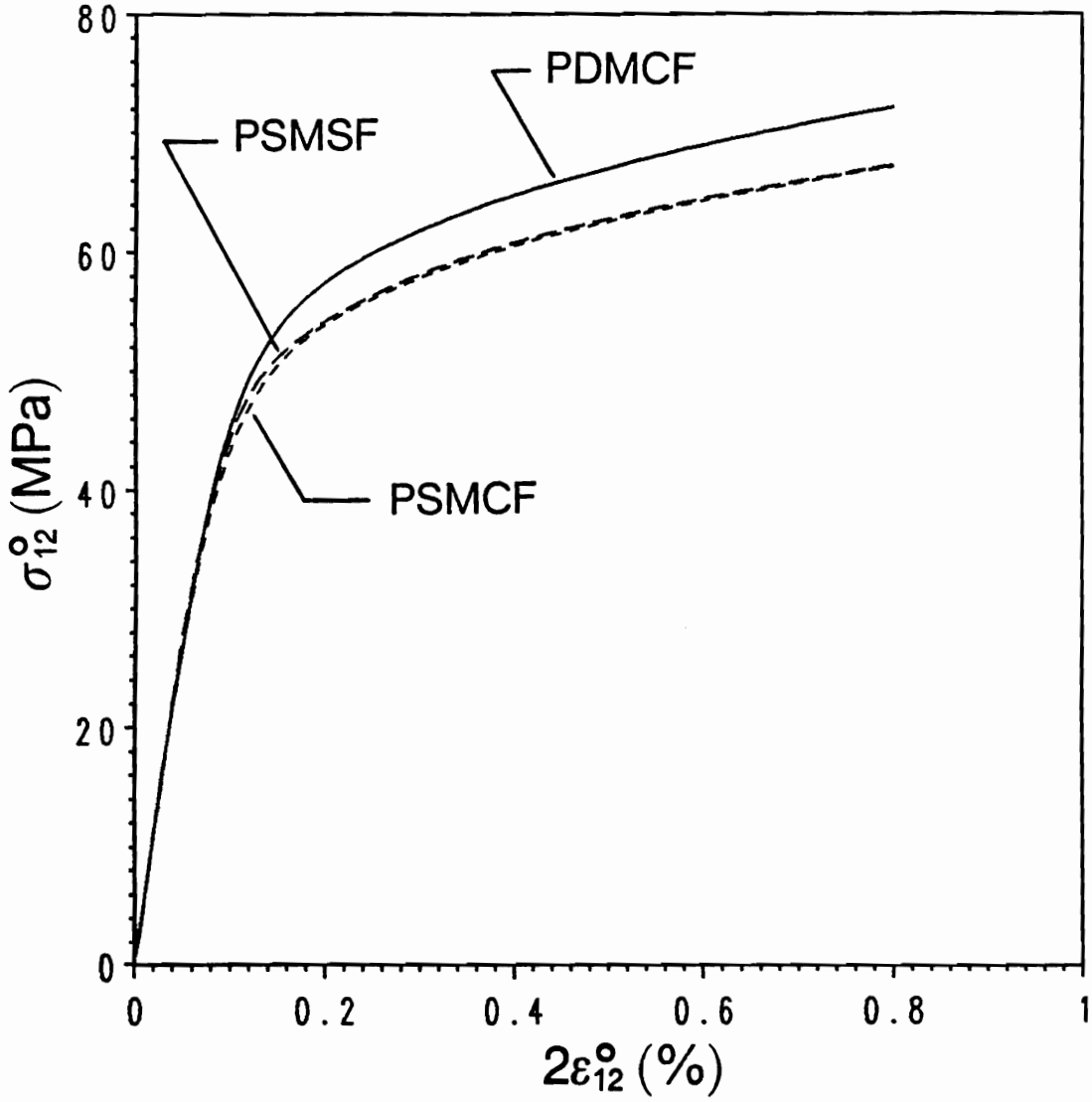

Figure 23. Longitudinal Shear Responses of PDMCF, PSMCF, and PSMSF

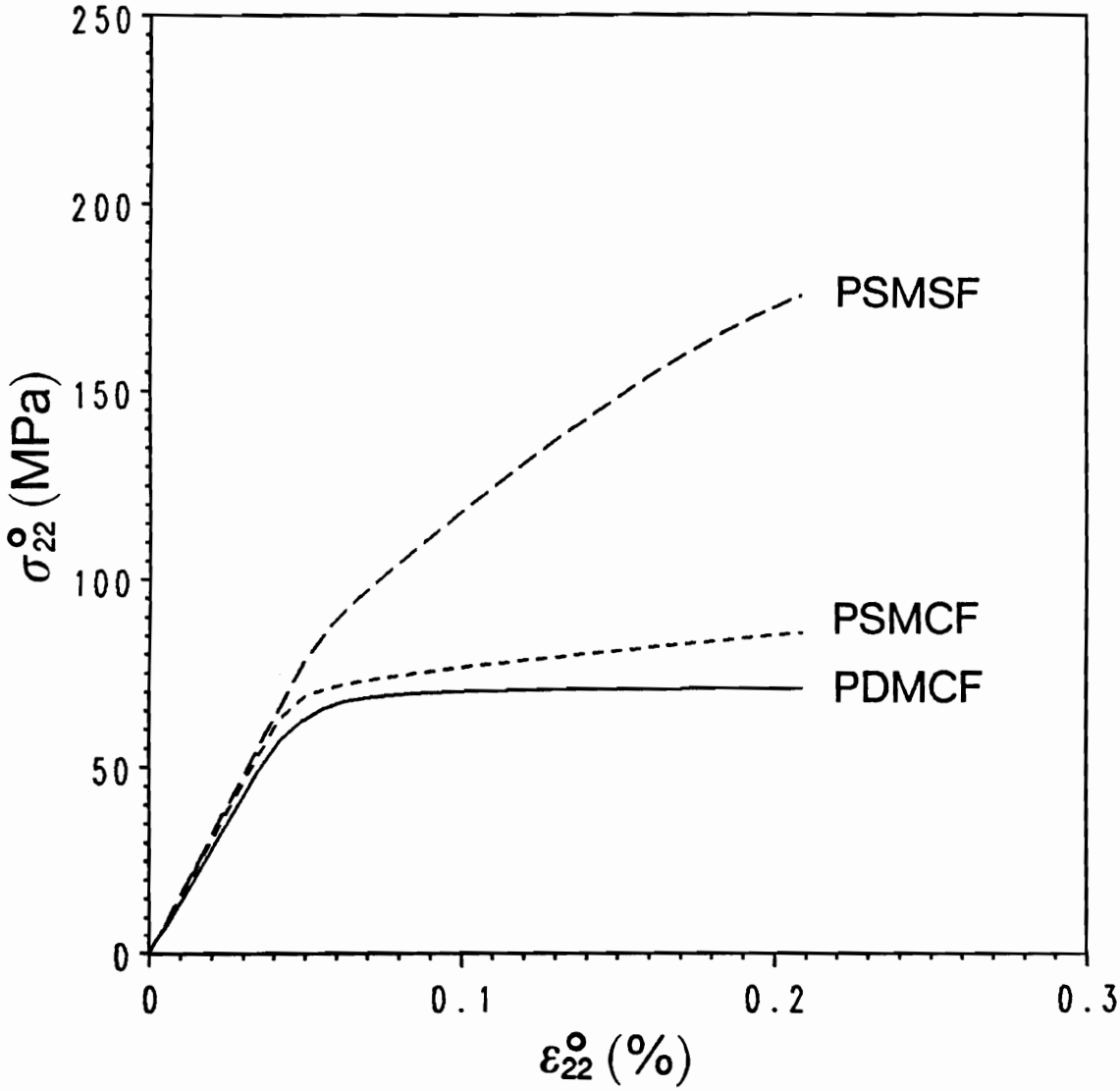

Figure 24a. Transverse Tensile Responses of PDMCF, PSMCF, and PSMSF Obtained with Nearly Perfectly Plastic Model for Matrix

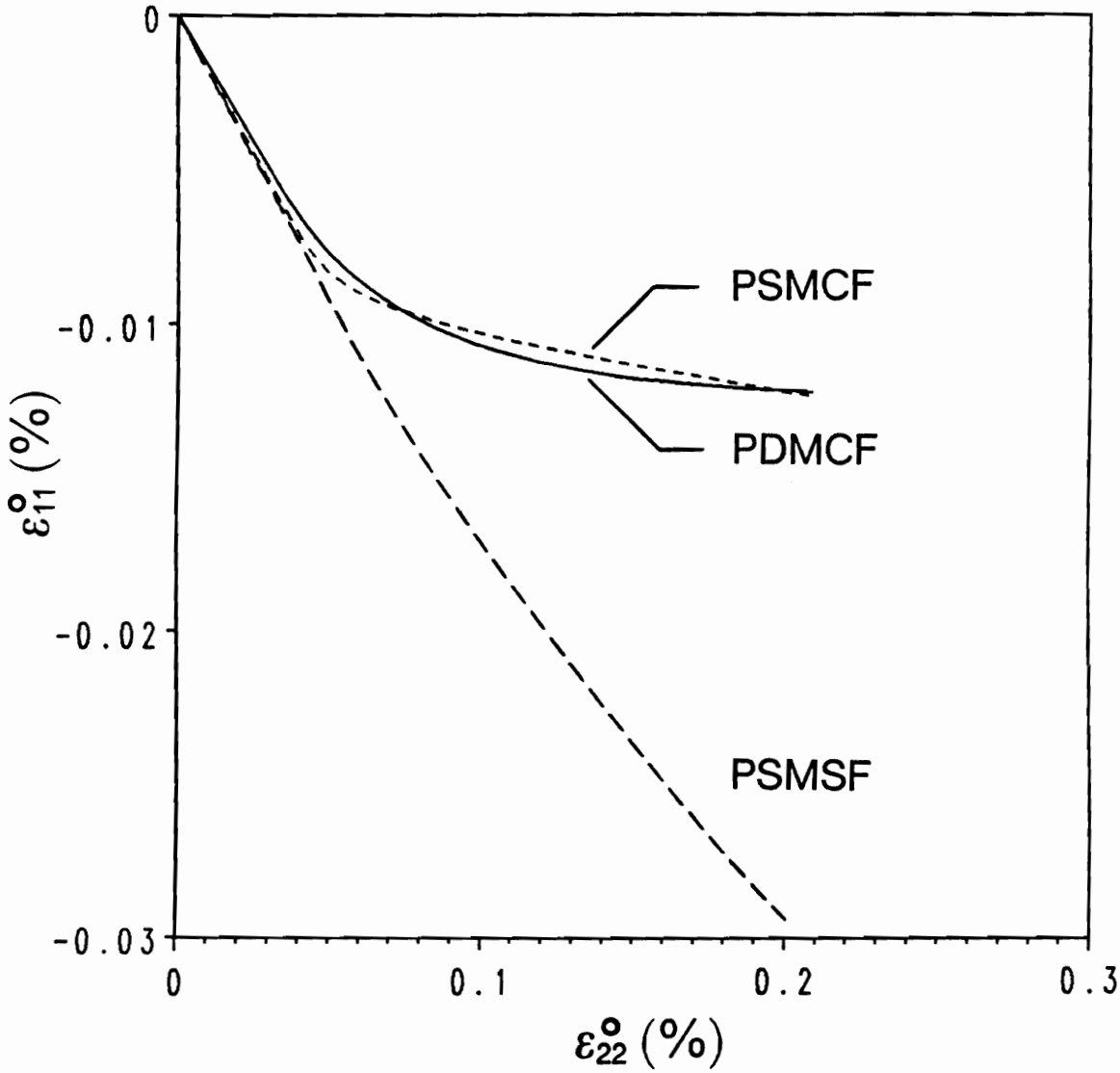

Figure 24b. Transverse Tensile Responses of PDMCF, PSMCF, and PSMSF Obtained with Nearly Perfectly Plastic Model for Matrix

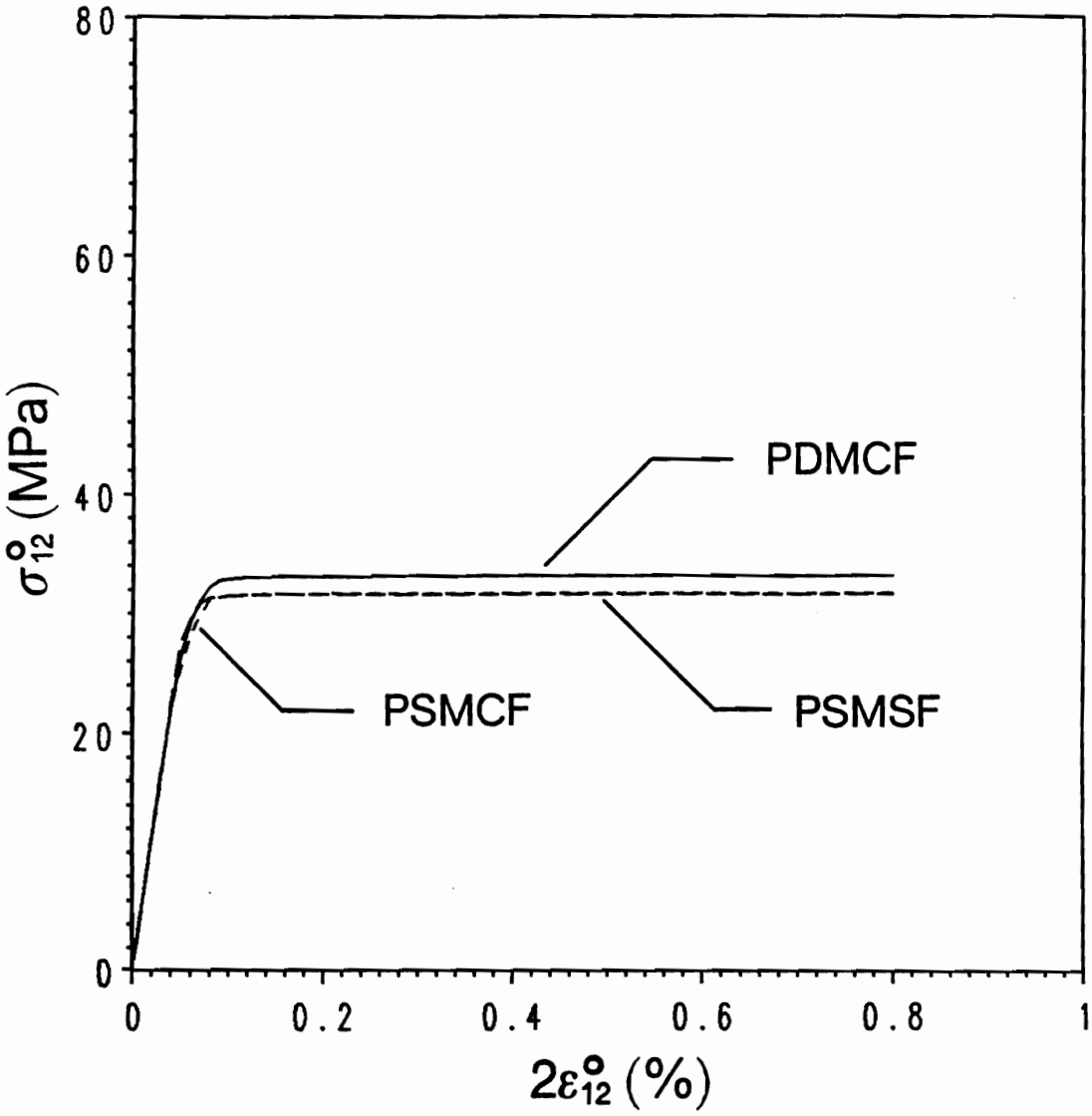

Figure 25. Longitudinal Shear Responses of PDMCF, PSMCF, and PSMSF Obtained with Nearly Perfectly Plastic Model for Matrix

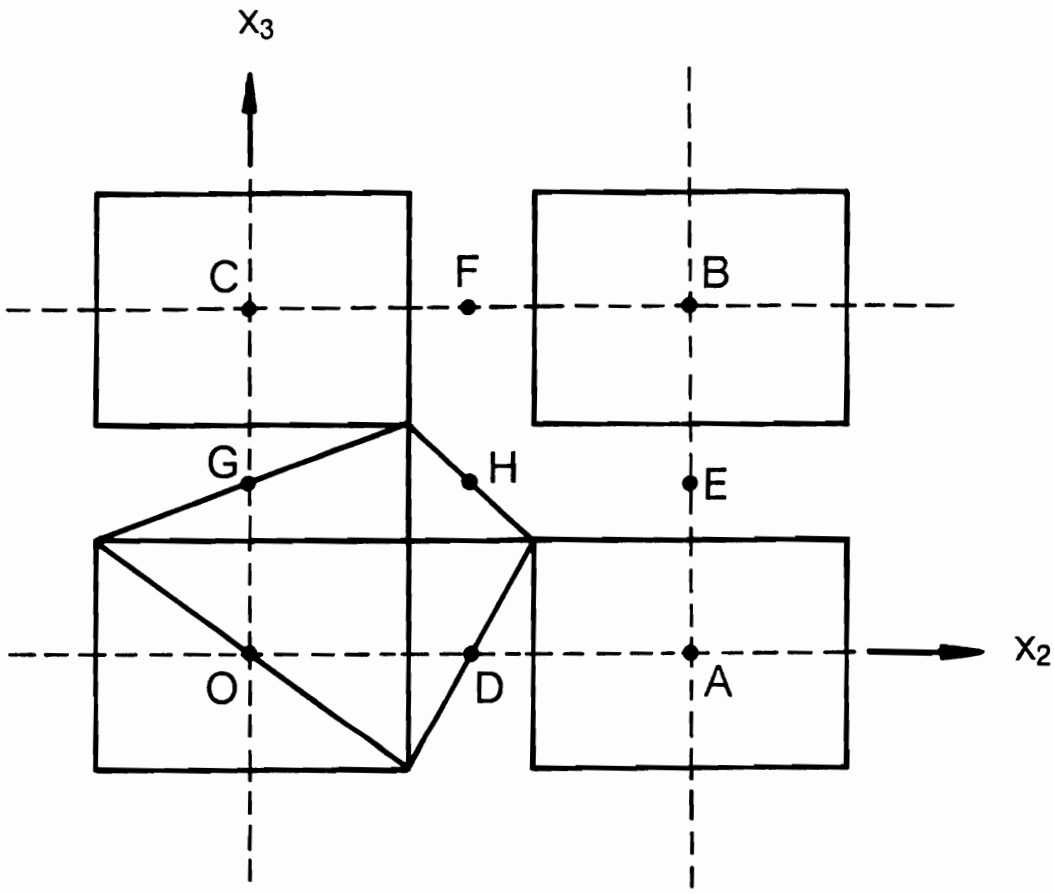

Figure 26. Aboudi's First-Ordered Model

Vita

Su-Yuen Hsu was born in Taipei, Taiwan on November 25, 1959. He acquired his B.S. and M.S. degrees in Mechanical Engineering from Chung Yuan University in 1981 and National Chiao Tung University in 1983, respectively. He served the Taiwanese Army as a second lieutenant during 1983 - 1985. He married Shu-Man Chien on July 27, 1985. On July 11, 1986, Su-Yuen, with Shu-Man, left his family in Japan in order to join the Ph.D. program in the Engineering Science and Mechanics Department at Virginia Polytechnic Institute and State University. Their daughter, Ina, was born in 1988.

After graduation, the author plans to continue his association with his advisor, Dr. O. H. Griffin, Jr., on post doctoral research.